The University of Manchester

UNDERSTANDING THE NUCLEATION OF ICE PARTICLES IN POLAR CLOUDS

A THESIS SUBMITTED TO THE UNIVERSITY OF MANCHESTER
FOR THE DEGREE OF DOCTOR OF PHILOSOPHY
IN THE FACULTY OF SCIENCE AND ENGINEERING

2016

Gillian Young
School of Earth and Environmental Sciences

Contents

Word count 78589

The University of Manchester

Gillian Young
Doctor of Philosophy
Understanding the Nucleation of Ice Particles in Polar Clouds
December 12, 2016

Arctic clouds are poorly represented in numerical models due to the complex, small-scale interactions which occur within them. Modelled cloud fractions are often significantly less than observed in this region; therefore, the radiative budget is not accurately simulated and forecasts of the melting cryosphere are fraught with uncertainty. Our ability to accurately model Arctic clouds can be improved through observational studies. Recent in situ airborne measurements from the springtime Aerosol-Cloud Coupling and Climate Interactions in the Arctic (ACCACIA) campaign are presented in this thesis to improve our understanding of the cloud microphysical interactions unique to this region.

Aerosol-cloud interactions – where aerosol particles act as ice nucleating particles (INPs) or cloud condensation nuclei (CCN) – are integral to the understanding of clouds on a global scale. In the Arctic, uncertainties caused by our poor understanding of these interactions are enhanced by strong feedbacks between clouds, the boundary layer, and the sea ice.

In the Arctic spring, aerosol-cloud interactions are affected by the Arctic haze, where a stable boundary layer allows aerosol particles to remain in the atmosphere for long periods of time. This leads to a heightened state of mixing in the aerosol population, which affects the ability of particles to act as INPs or CCN. Aerosol particle compositional data are presented to indicate which particles are present during the ACCACIA campaign, and infer how they may participate in aerosol-cloud interactions. Mineral dusts (known INPs) are identified in all flights considered, and the dominating particle classes in each case vary with changing air mass history. Mixed particles, and an enhanced aerosol loading, are identified in the final case. Evidence is presented which suggests these characteristics may be attributed to biomass burning activities in Siberia and Scandinavia.

Additionally, in situ airborne observations are presented to investigate the relationship between the Arctic atmosphere and the mixed-phase clouds – containing both liquid cloud droplets and ice crystals – common to this region. Cloud microphysical structure responds strongly to changing surface conditions, as strong heat and moisture fluxes from the comparatively-warm ocean promote more turbulent motion in the boundary layer than the minimal heat fluxes from the frozen sea ice. Observations over the transition from sea ice to ocean show that the cloud liquid water content increases four-fold, whilst ice crystal number concentrations, N_{ice}, remain consistent at $\sim 0.5\,L^{-1}$. Following from this study, large eddy simulations are used to illustrate the sensitivity of cloud structure, evolution, and lifetime to N_{ice}. To accurately model mixed-phase conditions over sea ice, marginal ice, and ocean, ice nucleation must occur under water-saturated conditions. Ocean-based clouds are found to be particularly sensitive to N_{ice}, as small decreases in N_{ice} allow glaciating clouds to be sustained, with mixed-phase conditions, for longer. Modelled N_{ice} also influences precipitation development over the ocean, with either snow or rain depleting the liquid phase of the simulated cloud.

Declaration

No portion of the work referred to in the thesis has been submitted in support of an application for another degree or qualification of this or any other university or other institute of learning.

Copyright Statement

Acknowledgements

First and foremost, I would like to thank my supervisors – Tom, Martin, and Paul – for their continual support throughout the last three years, and for not saying "no" when I asked to go to *yet another* conference. The highlight of my PhD by far was going to Svalbard and seeing the Arctic first-hand. I'll never forget hiking to Hansbreen glacier, seeing a polar bear, and meeting so many other Arctic researchers who share my interests. The last three years have been incredible, and I would like to thank NERC for funding my work; these experiences simply would not have happened without it.

There are numerous others who deserve thanks: from those in the weekly polar and modelling meetings to the room 1.03 contingent, you have actually made this... dare I say it... *fun*. To single out a few people, Hazel, Jonny, and Keith deserve a mention for always giving good, constructive advice whenever I've needed it.

It is safe to say I would not be where I am now if it hadn't been for my mum and dad; they have always encouraged my obsession with academia. Last but not least, Callum deserves the biggest thanks of all... he has put up with an extensive amount of moaning throughout this PhD, has endured endless grammar-checking requests, and has been extremely patient while I've been writing up. I suspect he'll never want to hear about Oxford commas ever again.

1 Introduction

1.1 Motivation

Global warming is felt strongly at the polar regions of our planet. The Arctic is responding to climate change at a heightened pace (Curry et al. 1996), with surface air temperatures rising quicker than anywhere else on the globe. This phenomenon is known as Arctic amplification (ACIA 2005; Serreze and Barry 2011). From the Greenland Ice Sheet to the annually-forming sea ice, this anthropogenically-induced warming is having a devastating impact on the cryosphere (Stocker et al. 2014). Record-breaking sea ice melts are becoming more frequent in recent decades (e.g. 2004, 2007, and 2012, Stroeve et al. 2005; Perovich et al. 2008; Parkinson and Comiso 2013). Forecasts of the melting sea ice – and predictions for the first ice-free Arctic summer – are highly variable, as are predictions of atmospheric temperature trends and the rising sea level (Stocker et al. 2014). Large uncertainties in models affect forecasts of sea ice volume, cloud fractions, and thermodynamic interactions in the boundary layer (BL, Tjernström et al. 2005).

As the Arctic sea ice retreats further, ocean-atmosphere interactions will become more important. Providing heat and moisture fluxes to the atmosphere, the warm ocean will have an increasing influence on atmospheric circulation and heat distribution in the Arctic (Wu and Lee 2012). Cloud radiative forcing (CRF) has been modelled to increase with decreasing sea ice extent (Walsh et al. 2009; Abe et al. 2016). Increased springtime cloudiness has been found to correlate well with decreased sea ice cover during the summer (Kapsch et al. 2013). Incorrectly simulating this fraction affects surface heating and top-of-the-atmosphere radiative predictions in the Arctic (Morrison et al. 2012). Between clear-sky and cloudy conditions, the net longwave (LW) radiation can vary by 30-40 $\mathrm{W\,m^{-2}}$ (Morrison et al. 2012),

based on winter and springtime measurements during the Surface HEat Budget of the Arctic Ocean campaign (SHEBA[1], Intrieri et al. 2002). Accurate predictions of Arctic cloud fractions therefore have significant consequences for the modelled radiative budget (Prenni et al. 2007).

The variability in climate predictions can be largely associated with the poor performance of unresolved, sub-grid scale processes in global climate models (GCMs, Boucher et al. 2014). Our basic knowledge of these processes is partly responsible for this poor representation. Significant feedbacks in GCMs are caused by inaccurately modelling processes dependent on these small-scale interactions; feedbacks which enhance perturbations and cause divergent solutions. For example, aerosol-cloud interactions are both poorly understood and poorly represented in GCMs (Seinfeld et al. 2016). If the processes governing cloud droplet and ice crystal formation in clouds are unrepresentative, the cloud microphysics will be inaccurately modelled, leading to incorrect feedbacks on the radiative budget and precipitation predictions. These uncertainties are enhanced in the Arctic. With weak solar heating, a stable boundary layer, and vastly changing surface conditions, this unique environment is particularly susceptible to positive feedbacks in models. To improve our forecasts of how these processes may change in the future, we need to develop our understanding of the microphysical interactions that occur in the Arctic atmosphere today. However, in situ observational studies in this region are scarce due to the remote, inhospitable location (Tjernström et al. 2004), leading to an inadequate understanding of these unique atmospheric interactions (de Boer et al. 2014).

1.1.1 Aerosol-cloud interactions

Aerosol particles influence atmospheric radiative interactions. Particles can directly absorb or scatter incident solar radiation, leading to local atmospheric heating or cooling. The radiative impact of an aerosol population is governed in part by their size distribution: numerous, small aerosol particles are more efficient at scattering radiation directly, whilst larger particles are more susceptible to cloud activation as cloud condensation nuclei (CCN) or ice nucleating particles (INPs, Dusek et al. 2006; Formenti et al. 2011). The process by which aerosol particles can affect cloud

[1]Cited measurement campaigns are summarised in Appendix A.

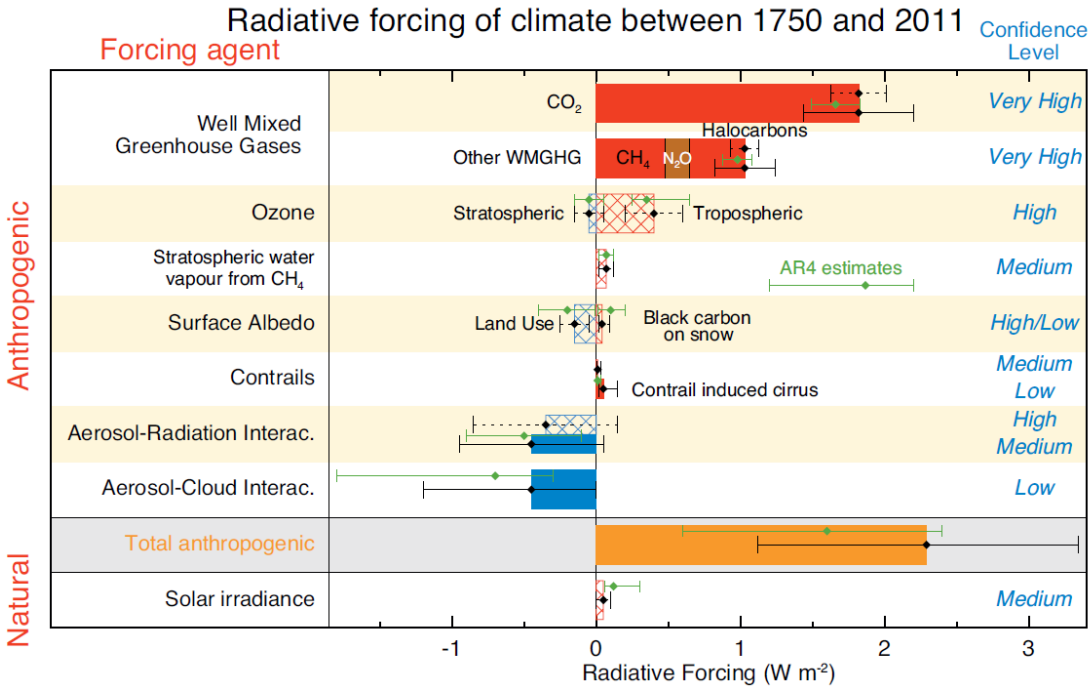

Figure 1.1: *Adapted from* Stocker et al. (2014) Fig. TS.6: Summary of climate radiative forcing (RF) since 1750, determined by the change in concentration since pre-industrial periods. Contributions from natural and anthropogenic sources are shown. Green error bars represent estimates placed by the previous IPCC report (AR4, 2007). A variety of information is illustrated; however, the large uncertainty interval associated with aerosol-cloud interactions (third from bottom), and our low level of confidence in these processes, is the focus of this thesis.

microphysical structure – the aerosol indirect effect – likely has a cooling effect on the atmosphere; however, the extent of this cooling is poorly quantified (Boucher et al. 2014).

Aerosol-cloud interactions contribute towards a large uncertainty in climate forecasts and predictions (Boucher et al. 2014; Seinfeld et al. 2016). Our poor understanding of the processes by which aerosol particles can act as CCN or INPs, and contribute towards cloud microphysical structure, hinders our ability to accurately model clouds. This is a global problem; however, this significant uncertainty is particularly pronounced in the Arctic due to enhanced feedbacks between clouds, the boundary layer, and the surface. Figure 1.1 illustrates our current estimate of the uncertainties associated with aerosol-cloud interactions. Realistic treatments of both aerosol-cloud interactions and cloud microphysics are required to constrain the large uncertainties, and inter-model discrepancies, associated with modelling Arctic radiative interactions (Tjernström et al. 2005).

GCMs often use the same representation of ice nucleation and microphysical interactions in the Arctic as they do in the mid-latitudes (Morrison and Pinto 2006; Prenni et al. 2007). However, the Arctic experiences a unique annual cycle of variable cloud (Intrieri et al. 2002) and aerosol (Ström et al. 2003; Tunved et al. 2013) properties; therefore, it requires a unique treatment of aerosol-cloud interactions (Prenni et al. 2007).

1.2 Thesis overview

Our understanding of aerosol-cloud interactions is poor on a global scale. Uncertainties in these sub-grid scale processes contribute towards unconstrained climate forecasts in the Arctic. Model development is required to improve our understanding of aerosol-cloud interactions; development which requires observations for validation.

This thesis seeks to better understand the nucleation of ice particles in Arctic clouds by utilising in situ observations from the Aerosol-Cloud Coupling and Climate Interactions in the Arctic (ACCACIA) campaign of 2013. Springtime cloud microphysical measurements in the vicinity of Svalbard, Norway are used to achieve this goal. By considering characteristics of the aerosol particles present in the Arctic boundary layer, investigating the distribution of ice crystals and liquid cloud droplets in the clouds sampled, and testing the sensitivity of modelled cloud structure to changing microphysics, details of the underlying processes and physical interactions are revealed.

This thesis is presented in Alternative Format as three inter-connected studies of Arctic cloud microphysics have been conducted, each with independent goals. For context, a review of current knowledge of Arctic clouds – from observational and modelling studies – and the underlying physics involved is presented in Chapter 2. An overview of the ACCACIA campaign, and details of the laboratory and modelling techniques used, follow in Chapter 3. The three journal articles integral to this thesis are detailed in Chapters 4, 5, and 6. To close, a summary and final conclusions are presented in Chapter 7.

2 Polar clouds

2.1 Arctic mixed-phase stratocumulus

Mixed-phase clouds – containing both liquid cloud droplets and ice crystals – are common in the Arctic (Shupe et al. 2008; Vihma et al. 2014), particularly during the winter and transition seasons (Pinto 1998; Shupe et al. 2006; Verlinde et al. 2007; McFarquhar et al. 2011; Vihma et al. 2014). These low altitude, boundary layer clouds are typically capped by a strong temperature and humidity inversion (Curry et al. 2000; Kay and Gettelman 2009; Solomon et al. 2011), caused by a stably stratified boundary layer (Barrie 1986), and are long-lived (Verlinde et al. 2007; Shupe et al. 2006). The weak solar heating experienced by the Arctic for most of the year, coupled with other unique factors such as variable surface fluxes from the annual melting and refreezing of the sea ice, causes these mixed-phase clouds to behave differently to their mid-latitude counterparts (Verlinde et al. 2007).

2.1.1 Cloud microphysics

Mixed-phase stratocumulus (MPS) contain both liquid cloud droplets and ice crystals, and can occur in single or multiple layers. Single-layer MPS are particularly common in the Arctic, and are therefore focused on in this thesis. These typically have a supercooled liquid layer at cloud top with ice formation, aggregation, and precipitation below (Hobbs and Rangno 1998; Shupe et al. 2006; Verlinde et al. 2007; Shupe et al. 2008; McFarquhar et al. 2011; Jackson et al. 2012). Mixed-phase clouds are particularly difficult to represent as the small-scale interactions which occur within them, which are crucial for their structure and lifetime, are on spatial and temporal scales too small to be resolved by global climate models (GCMs); they are

sub-grid scale processes (Korolev and Field 2008).

With cloud top temperatures typically warmer than -30 °C (Verlinde et al. 2007), these clouds are formed by aerosol-cloud interactions. In supersaturated conditions, where the relative humidity of air exceeds 100%, it is energetically favourable for water vapour to be in a liquid or solid phase, dependent on ambient temperatures (Pruppacher and Klett 1997). As a result, liquid cloud droplets and ice crystals form as excess water vapour condenses onto cloud condensation nuclei (CCN) or ice nucleating particles (INPs). This mechanism is known as heterogeneous nucleation, and is the process by which the majority of low-altitude clouds form (Pruppacher and Klett 1997).

Mixed-phase clouds are inherently unstable (e.g. Korolev and Field 2008). At sub-zero temperatures, the saturation vapour pressure over ice is lower than over liquid, allowing ice crystals to form, grow, and act as a sink of water vapour within mixed-phase clouds. The vapour field is depleted by the efficient crystal growth, leading to water sub-saturated conditions; however, the inherent difference in saturation vapour pressures between liquid and ice can allow ice supersaturation to be maintained. Below water saturation, the liquid droplets evaporate. Liquid droplets are therefore depleted in the vicinity of growing ice crystals in mixed-phase conditions (Pruppacher and Klett 1997; Pinto 1998). This physical process is known as the Wegener-Bergeron-Findeisen (WBF, Wegener 1911; Bergeron 1935; Findeisen 1938) mechanism, and it governs MPS structure and evolution (Korolev and Isaac 2003; Korolev and Field 2008). One might expect mixed-phase clouds to glaciate quickly by this mechanism, with the complete depletion of the liquid phase, but Arctic MPS have been observed to persist for long periods of time (Verlinde et al. 2007; Shupe et al. 2006).

Microphysical interactions are thought to be responsible for the long lifetime of Arctic MPS (Verlinde et al. 2007). Figure 2.1 illustrates these processes. Rising parcels of air expand and cool as they ascend, allowing water supersaturation to be attained. Droplets are nucleated at the lifting condensation level, and grow with increasing altitude (Jackson et al. 2012), causing the liquid water content (LWC) of the cloud to increase (Hobbs and Rangno 1998; Jackson et al. 2012). Latent heat is released by droplet nucleation and growth, thus strengthening the updraught.

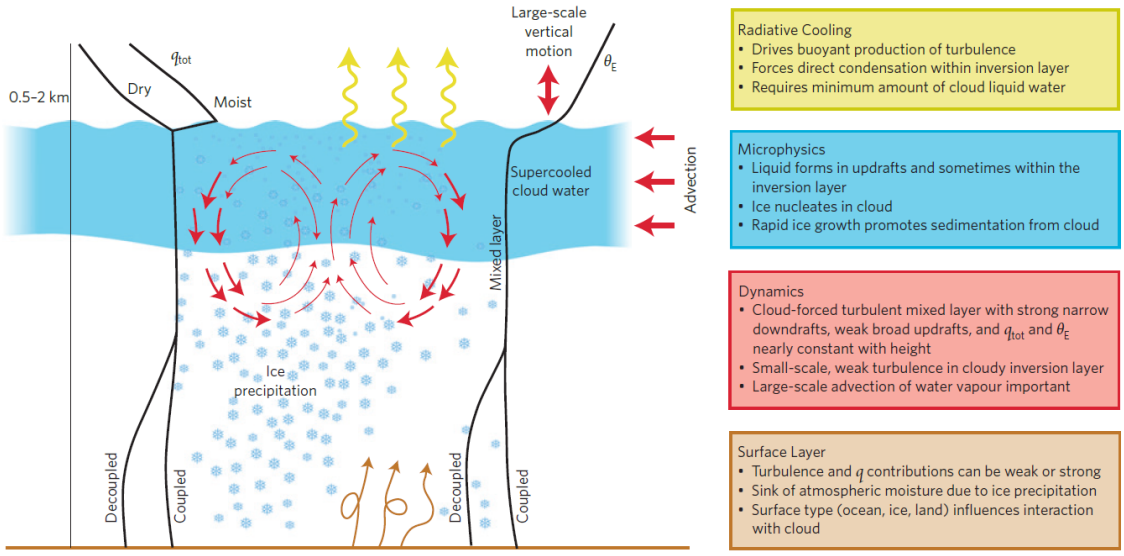

Figure 2.1: Morrison et al. (2012) Fig. 3: Schematic summarising the key processes involved in maintaining Arctic mixed-phase clouds. Example profiles of total water mixing ratio (q_{tot}) and equivalent potential temperature (θ_E) are shown. Total water refers to the combined contributions of vapour, liquid, and ice. Rising warm parcels of air attain water saturation upon cooling, allowing for droplet nucleation and growth. Subsequent latent heat release strengthens these updraughts. Ice nucleates within the cloud at sub-zero temperatures if ice nucleating particles (INPs) are available, and subsequent growth and aggregation leads to snow precipitation from the cloud. In-cloud turbulence is driven by radiative cooling at cloud top, which drives negatively buoyant motion within the cloud layer. The surface layer can affect cloud microphysical interactions through heat and moisture fluxes, which induce turbulence in the boundary layer from below. The surface-induced and cloud-driven turbulence can mix, causing the cloud to become coupled to the surface. Advection of moist or dry air can promote cloud persistence through increased availability of water vapour, or cause the break up of the cloud or glaciation by lowering the relative humidity within the cloud.

Cloud top is defined by a strong temperature inversion at the top of the boundary layer (BL), which halts the parcel ascent. Strong cloud top radiative cooling produces negatively-buoyant parcels of air which fall downwards adjacent to the updraught column. These cooler downdraughts allow water supersaturated conditions to be maintained (Pinto 1998), promoting further droplet formation. With colder temperatures, ice nucleation, growth, and aggregation can occur if INPs are available. Observations have indicated that ice number concentrations are generally isolated to downdraughts (Verlinde et al. 2007). However, modelling simulations have shown that ice crystal growth also occurs in updraughts (Solomon et al. 2011). Latent heating from hydrometeor growth drives the updraughts, and the

enhanced liquid phase reinforces radiative cooling at cloud top, strengthening adjacent downdraughts (Pinto 1998). This dynamical motion is thought to sustain the mixed-phase conditions for a prolonged time (Korolev and Isaac 2003).

Arctic MPS are often decoupled from the surface, isolating the cloud layer from surface heat and moisture fluxes (Fig. 2.1, Sotiropoulou et al. 2014). Turbulence within these decoupled clouds is driven by this cloud top radiative cooling (Solomon et al. 2015). Decoupled MPS are more common in the Arctic than their coupled counterparts (Sotiropoulou et al. 2014). If these clouds form at low altitudes, the cloud-driven dynamic motions may extend downwards and combine with the induced turbulence from surface heat and moisture fluxes, coupling the clouds to the surface (Sotiropoulou et al. 2014). Decoupled clouds are often sustained through the introduction of moist air from above, as humidity inversions are often observed, accompanying the temperature inversions defining cloud top (Solomon et al. 2011). Advection and entrainment of this moist air at the lateral and upper boundaries of the cloud – and little precipitation depleting the cloud liquid water content – are thought to contribute towards the persistence of these Arctic MPS (Solomon et al. 2011, 2015).

Cloud lifetime is related to the number concentration of ice particles in MPS. Dynamics can sustain the mixed-phase conditions if the number of ice particles is low; however, if appreciable ice number concentrations accumulate, the cloud will likely glaciate through the WBF mechanism. Large ice number concentrations are typically not observed in Arctic MPS for this reason, and both ice and droplet number concentrations are often low in single-layer Arctic MPS (Verlinde et al. 2007; McFarquhar et al. 2011; Jackson et al. 2012). Ice formation is regularly overpredicted in modelled Arctic MPS, causing rapid glaciation and cloud dissipation. By representing an over-active ice formation process, the modelled Arctic cloud fractions are often significantly less than are observed (e.g. de Boer et al. 2014).

Measured ice crystal number concentrations are often much greater than corresponding measurements of INPs (e.g. Mossop 1985; Pruppacher and Klett 1997; Verlinde et al. 2007; DeMott et al. 2011), suggesting additional processes can contribute

to the ice phase in clouds. Ice crystals can also be produced through secondary processes, where primary ice crystals shatter or promote splinter production. An efficient method of secondary ice production, called rime-splintering and commonly known as the Hallet-Mossop mechanism, originates from a coating of grain-like ice known as rime (Pruppacher and Klett 1997). Cloud droplets freeze quickly upon impact with ice crystals and can remain as a fragile frozen coating (rime) on the crystal surface (Pruppacher and Klett 1997). Hallett and Mossop (1974) demonstrated that the presence of rime can facilitate the growth of secondary daughter particles from the parent ice crystal: the efficiency of production is closely related to the growth rate of the rime coating and the number of crystals created per milligram of rime accreted. The process is active in clouds with temperatures between -8°C and -3°C, with an optimal rate at approximately -5°C (Hallett and Mossop 1974). At this temperature, growth is favoured along the crystal's longest dimension, promoting the development of columnar or needle-like crystal habits (Hallett and Mossop 1974). The Hallet-Mossop mechanism can produce ice crystal number concentrations of hundreds per litre of air (Mossop 1985). Other secondary processes, such as crystal fragmentation from ice-ice collisions (Schwarzenboeck et al. 2009) and droplet shattering upon freezing (Hobbs and Alkezweeny 1968), may also contribute to the population. Although different mechanisms may be involved, secondary ice production fundamentally involves the breakup of existing crystals and subsequent growth of the shattered artefacts (Seinfeld and Pandis 1998).

Consequently, ice crystal number concentrations typically decrease with decreasing temperatures in moderately supercooled mixed-phase clouds, due to the strong influence of secondary ice production at warm sub-zero temperatures. Correlations between ice crystal number concentrations and large drizzle drops (200-500 µm, Hobbs and Rangno 1998) have been previously identified, as drizzle is an efficient source of riming particles upon freezing (Pruppacher and Klett 1997). Similarly, high ice number concentrations have been identified in cases where large droplets (>23 µm) form in concentrations of $\sim$15 cm^{-3} between -8 °C and -2.5 °C. Therefore, such large droplets are also thought to contribute towards the rime-splintering process (Hobbs and Rangno 1998; Rangno and Hobbs 2001).

2.1.2 Seasonal influences

The Arctic environment changes significantly throughout the year due to the cyclical influence of the Sun. During the polar night, the Sun does not rise above the horizon and surface temperatures plummet. The sea ice extent reaches its maximum during this time, and the clouds which form do not interact with shortwave (SW) solar radiation. Widespread MPS decks are common. Longwave (LW) radiation at the surface dominates during the polar night, causing a warming effect (Intrieri et al. 2002; Serreze and Barry 2011).

In contrast, the polar day experiences 24 hour solar heating, a minimal sea ice extent, and the domination of incident SW radiation. With increased solar heating from above and warmer boundary layer temperatures from below, summertime clouds are more likely to be multi-layered and produce precipitation (Barrie 1986; Curry et al. 1988). Additionally, low-altitude clouds often form; mean cloud base height was found to be approximately 100 m during the summertime Arctic Ocean Experiment (AOE-2001, Tjernström et al. 2004). These low-altitude clouds reflect incident solar radiation more effectively than the low-albedo ocean below them, leading to surface cooling (Intrieri et al. 2002; Shupe and Intrieri 2003). Despite this, upwelling LW radiation, and weak solar heating, dominates for the majority of the year in the Arctic, causing a net warming effect at the surface (Intrieri et al. 2002).

Cloud base temperatures are significantly colder during the winter and spring with comparison to the summer (with minima of -36 °C, -30 °C and -10 °C, respectively measured during SHEBA, Shupe and Intrieri 2003; Shupe et al. 2006). Consequently, ice number concentrations are typically lower in the colder springtime clouds than the warmer summertime clouds (Hobbs and Rangno 1998), due to the influence of secondary ice production in the summer (Lloyd et al. 2015).

The winter and springtime Arctic BL is very stable, capped by strong temperature inversions, thus vertical mixing with the free troposphere is inhibited (Shaw 1995). Snow precipitation is typically light over the Arctic winter and spring, allowing for aerosol accumulation in the BL (see Sect. 2.2, Shaw 1995; Tunved et al. 2013). Low ice number concentrations ($0.27 \pm 0.26\,\mathrm{L}^{-1}$, with $\mathrm{D_P}$ >125 µm) and moderate droplet number concentrations ($93 \pm 81\,\mathrm{cm}^{-3}$) were measured at Barrow, Alaska

during the Indirect and Semi-Direct Aerosol Campaign (ISDAC, McFarquhar et al. 2011) in the spring of 2008. These ISDAC cases were identified to be polluted, with heightened aerosol number concentrations measured below cloud (Jackson et al. 2012). Enhanced competition for water vapour between more CCN suppresses droplet growth and subsequent secondary ice production, allowing primary ice nucleation to solely contribute to the ice number concentration in these cases (Jackson et al. 2012).

In contrast, pristine autumnal conditions were sampled near Barrow, Alaska during the Mixed-Phase Arctic Cloud Experiment (M-PACE, Verlinde et al. 2007). Higher ice number concentrations ($2.52 \pm 6.45\,\mathrm{L}^{-1}$, with $\mathrm{D_P} > 125\,\mu\mathrm{m}$) and lower droplet number concentrations ($46 \pm 30\,\mathrm{cm}^{-3}$) were found on average (Jackson et al. 2012). With fewer droplets nucleated by the pristine, low CCN-environment, there is less competition for water vapour and droplets grow to large sizes (mean effective radius approximately $>10\,\mu\mathrm{m}$, Jackson et al. 2012). These large drops are susceptible to freezing, promoting secondary ice production through break up (Hobbs and Alkezweeny 1968), shattering (Mossop 1985) or as riming particles (Hobbs and Rangno 1998; Rangno and Hobbs 2001). Known as the thermodynamic indirect effect (Jackson et al. 2012), fewer droplets in the autumn promote higher ice number concentrations than the greater droplet number concentrations during the spring will allow. Polluted clouds, such as those typically measured during ISDAC, would reflect more incident solar radiation – through an increased albedo – and be optically thicker than their clean counterparts (Twomey 1974).

With warmer atmospheric and cloud temperatures, Arctic MPS typically contain greater number concentrations of ice attributable to secondary processes. During the summer, median ice crystal number concentrations measured at Svalbard were approximately $3\,\mathrm{L}^{-1}$ (Lloyd et al. 2015). Lloyd et al. (2015) found that the summertime ice number concentrations measured were greater than INP number concentrations predicted by the DeMott et al. (2010) parameterisation, which is evaluated using aerosol particle number concentrations and temperature. These observations are comparable to the mean ice number concentrations measured during M-PACE (Jackson et al. 2012). Verlinde et al. (2007) also found that the mean measured INP number concentrations did not adequately match the measured ice in these clouds,

and Jackson et al. (2012) concluded that these autumnal observations had been enhanced by secondary processes. Even larger ice crystal number concentrations have been observed in MPS at Svalbard during the late spring (up to $50\,L^{-1}$, Gayet et al. 2009), suggesting that secondary ice production can have a significant influence on these clouds.

Variable meteorological and aerosol properties are a significant factor influencing single-layer Arctic MPS (Earle et al. 2011). Droplet number concentrations within mixed-phase clouds are sensitive to air mass history, as both Verlinde et al. (2007) and Lloyd et al. (2015) observed cases with mean droplet number concentrations $>300\,cm^{-3}$, when the typical measurements were $<100\,cm^{-3}$. The typically low droplet (ice) number concentrations of Arctic MPS makes them vulnerable to pollution plumes of CCN (INPs) from anthropogenic sources (Hobbs and Rangno 1998). Not all springtime observations of Arctic MPS are heavily polluted (Lloyd et al. 2015), and some clean cases were observed during ISDAC (Earle et al. 2011). Despite this, observations of ice crystal number concentrations during the early spring are often low (Hobbs and Rangno 1998; McFarquhar et al. 2011), suggesting primary ice formation is solely involved. Therefore, observations of springtime Arctic mixed-phase clouds, such as those made during ISDAC, provide a valuable dataset for investigating aerosol-cloud interactions involving both CCN and INPs.

2.1.3 Interaction with the environment

Mixed-phase clouds strongly influence Arctic radiative interactions (Morrison et al. 2012). Globally, clouds cool the atmosphere by reflecting incident radiation from the Sun (Boucher et al. 2014). Their cooling influence makes them a key component of the climate system to better understand (Fig. 1.1). Clouds also act to cool the atmosphere in the Arctic; however, their net impact is outweighed by their ability to efficiently trap upwelling terrestrial radiation and promote surface warming (Boucher et al. 2014).

In contrast to lower latitudes, Arctic clouds provide a net positive LW forcing at the surface for the majority of the year, and only act to cool the whole Arctic system for a short period during the summer when the incident solar SW influence is strong (Intrieri et al. 2002; Shupe and Intrieri 2003). This warming effect results

from weak solar heating for much of the year, low surface temperatures and humidity in the boundary layer, and strong temperature inversions, amongst other unique properties (Intrieri et al. 2002; Tjernström et al. 2004). Positive cloud radiative forcing enhances the melt of the Greenland Ice Sheet (van Tricht et al. 2016), and similarly influences the freezing and melting processes of the Arctic sea ice (Kapsch et al. 2013). The positive feedback between clouds and sea ice is strongly felt in the autumn (Kay and Gettelman 2009), where the increasing cloud fraction over the open water efficiently traps upwelling LW radiation, thus warming the surface and affecting sea ice formation. Arctic MPS are a significant source of surface warming during the Arctic winter and spring (Intrieri et al. 2002). Satellite observations indicate that both the autumnal low cloud fraction and the surface air temperature increased over the decade from 2000-2010 (Wu and Lee 2012), indicating a causal link.

The cold sea ice acts to minimise moisture and heat transfer from the ocean to the atmosphere, thus restricting turbulent motions and producing a stable BL (Wu and Lee 2012). Surface heat fluxes affect the atmosphere over the ocean, enhancing turbulent kinetic energy (TKE) and influencing cloud microphysics (Tjernström et al. 2004; Wu and Lee 2012). Therefore, with a declining sea ice extent, the increased availability of open water will strongly influence cloud and BL structure (Wu and Lee 2012). Cloud fraction correlates with open water; either as the open ocean, or leads or polynas in the ice pack (Curry et al. 2000; Kay and Gettelman 2009). Over the marginal ice zones (MIZ) – the region of broken ice at the edge of the ice pack – cloud fractions have been found to be typically about 10-15% greater than over the sea ice (Palm et al. 2010). This fraction often increases to 100% over the open ocean (Palm et al. 2010).

The surface conditions strongly affect the low-cloud fraction (Kay and Gettelman 2009); however, large-scale atmospheric circulation has also been found to contribute to the cloud evolution in the Arctic. Off-ice air flows – or, cold air outbreaks (CAOs) – are affected by the strong changes in surface fluxes, and often convective roll clouds are observed downstream over the ocean in these scenarios (Hartmann et al. 1997; Kay and Gettelman 2009). Increased sensible and latent

heat fluxes over the ocean cause roll convection to develop in the warming, unstable boundary layer (Hartmann et al. 1997). Roll vortices form under conditions of high wind speeds ($\sim$10 m s^{-1}) and small air-sea temperature differences ($\sim$4 °C, Grossman 1982). These structures can transition to convective cells with increasing boundary layer instability (Grossman 1982; Hartmann et al. 1997). Precipitation influences this convection by warming the cloud layer, depleting the cloud liquid water, and promoting cloud break up (Ovchinnikov et al. 2011). With depletion of liquid water from the cloud layer, the influence of radiative cooling, downdraughts, and updraughts decrease, thus removing the positive feedback on the liquid phase within the cloud layer (Jiang et al. 2000). Understanding the development of cloud microphysics in these scenarios may indicate how Arctic cloud fractions may evolve with a decreasing sea ice surface in the future.

2.2 Arctic aerosol particles

The Arctic boundary layer is characterised by aerosol particle number concentrations which vary significantly with season (Seinfeld and Pandis 1998; Tunved et al. 2013). The Arctic aerosol particle population typically has a bimodal size distribution, dominated by Aitken-mode (0.06 µm $<$ D_P, particle diameter) and accumulation-mode particles (0.1 µm $<$ D_P $<$ 1.0 µm, Tunved et al. 2013). The shape of the aerosol particle size distribution varies with season (Ström et al. 2003).

The Arctic aerosol population comprises a variety of species, from organic material and continental pollutants to minerals from across the globe (Barrie 1986; Hara et al. 2003; Behrenfeldt et al. 2008; Geng et al. 2010; Weinbruch et al. 2012). A wide range of geographical sources affect this region; from Europe, Siberia and Asia to North America (Barrie 1986; Seinfeld and Pandis 1998; Behrenfeldt et al. 2008; Weinbruch et al. 2012; Tunved et al. 2013, amongst others). To improve the representation of aerosol-cloud interactions in the Arctic, more information is required about the properties of Arctic aerosol particles in the context of measured cloud microphysics. As mixed-phase clouds are particularly sensitive to the ice phase, focus is placed upon species that may act as INPs.

2.2.1 Seasonal characteristics and the Arctic haze

The annual variability in Arctic aerosol particle concentration is dominated by a yearly phenomenon called the Arctic haze where, during late winter to early spring, the Arctic receives an influx of aerosol from continental sources (Shaw 1995; Tunved et al. 2013). This pollution has been widely documented since the 1950s (e.g. Shaw 1995) and anthropogenic particles – including black carbon (BC), sulphates, and nitrates – are major constituents in this phenomena (Korhonen et al. 2008). The springtime Arctic aerosol population is heavily influenced by the accumulation-mode particles associated with this haze, leading to a larger mass concentration during these months than at other times of the year (on average, approximately $0.8\,\mathrm{ng\,m^{-3}}$ compared with $0.1\,\mathrm{ng\,m^{-3}}$ for Mar and Sep respectively, Tunved et al. 2013). Minimal precipitation leads to inefficient aerosol scavenging, allowing these large aerosol to persist (Tunved et al. 2013). BC mass concentrations also follow this relationship, varying from $80\,\mathrm{ng\,m^{-3}}$ to 0–$10\,\mathrm{ng\,m^{-3}}$ between the haze months and the summer respectively (Eleftheriadis et al. 2009). Springtime plumes of BC, associated with burning activities, often come from Eurasia (Wang et al. 2011). Figure 2.2 shows monthly mean aerosol size distributions measured on Svalbard during Mar 2000 – Mar 2001, and the increased mass (related to the volume density distribution) peaks during the spring. Particle growth by condensation and new particle formation are inefficient during the Arctic spring due to weak solar heating and the extensive sea ice cover, which restricts heat and moisture fluxes from the ocean (Ström et al. 2003; Tunved et al. 2013). The stable boundary layer, and inefficient aerosol scavenging and growth processes, allows various particle species to accumulate and interact with each other, producing a springtime aerosol particle population with a large fraction of mixed particles (Weinbruch et al. 2012).

Previous studies have shown little diurnal variability with the accumulation-mode particles common in the springtime Arctic atmosphere, suggesting a consistent source (Tunved et al. 2013). Long-range transport from continental, mid-latitude regions is a likely source of these particles (Tunved et al. 2013). Particle number concentrations have been found to be greater at higher altitudes; further evidence of long-range high-altitude transport from distant sources (Curry et al.

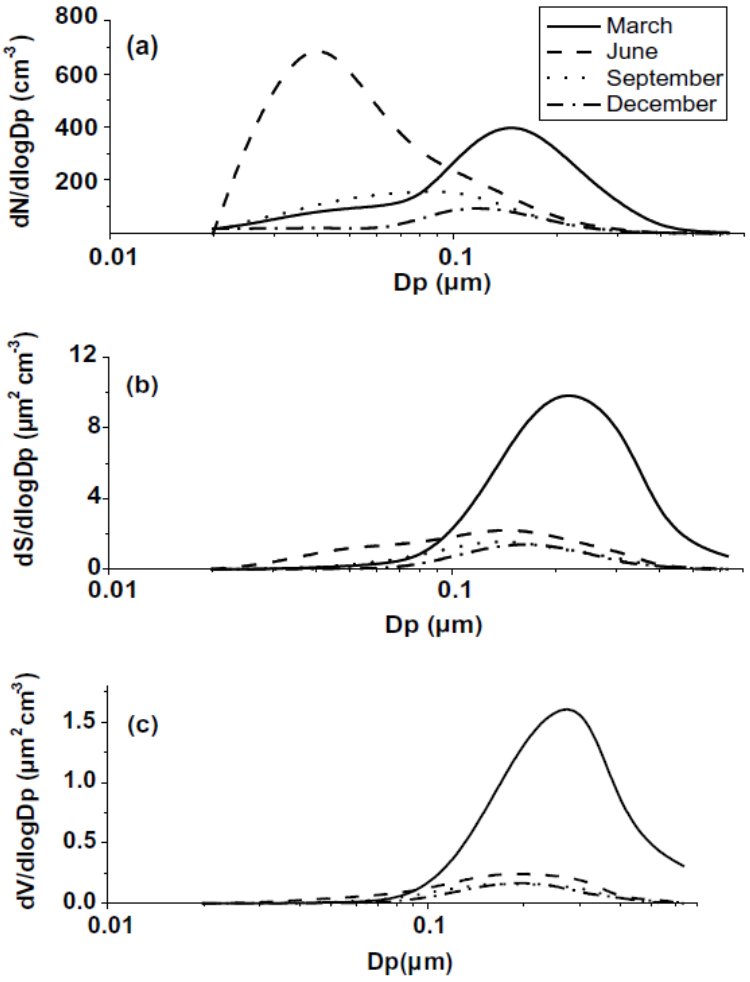

Figure 2.2: Ström et al. (2003) Fig. 1: Monthly averaged size distributions from measurements made at the Zeppelin research station on Svalbard (see Appendix A). Mean distributions from March, June, September, and December are shown against particle diameter, D_P. **Top panel:** number size distribution ($dN/dlogD_P$), **middle panel:** surface area density distribution ($dS/dlogD_P$), and **bottom panel:** volume density distribution ($dV/dlogD_P$).

2000). However, previous studies have also shown that the ocean – as indicated by the relative quantities of Na^+ ions measured at Zeppelin, Svalbard (Ström et al. 2003) – constitutes an influential source of aerosol particles during the winter and spring months (Weinbruch et al. 2012), indicating that not all of this accumulation-mode haze aerosol is transported from far afield. The larger aerosol particles ($D_P >$ 1 µm) associated with the haze tend to have natural origins, and typically include mineral dusts from arid regions, sea salt from the oceans or spores and other biological particles from vegetation and soils (Seinfeld and Pandis 1998). These large particles are of particular interest when considering aerosol-cloud interactions (see

Sect. 2.2.2).

The Arctic haze phenomenon results from the position of the polar air mass: the polar dome extends down to encompass mid-latitude industrial regions which produce significant quantities of anthropogenic pollution. This pollution can then move northwards easily (Shaw 1995). Pollutants are then able to accumulate in the stable Arctic atmosphere due to the position of the polar front (Ström et al. 2003). The haze behaves similarly to clouds in radiative interactions, and produces a net warming effect at the surface (Shaw 1995). Modelling simulations based on observations from the Arctic Research of the Composition of the Troposphere from Aircraft and Satellites (ARCTAS, Jacob et al. 2010) campaign estimate an additional surface radiative forcing of $1.2\,\mathrm{W\,m^{-2}}$ from BC deposition on snow alone (Wang et al. 2011). This warming is offset by a minor cooling effect as the haze particles scatter the minimal springtime solar radiation (Shaw 1995). As the amount of solar radiation increases with time of year, these aerosol particles have an increasing cooling effect as they scatter more incident SW radiation (Shaw 1995).

During the summer months, efficient aerosol scavenging by precipitation (Ström et al. 2003; Browse et al. 2012) and new particle formation events (e.g. Leck and Bigg 1999; Allan et al. 2015) lead to a depleted accumulation-mode and high number concentrations of small, Aitken-mode particles (Fig. 2.2). These processes produce a significantly smaller particle mass concentration compared with the spring (Ström et al. 2003; Tunved et al. 2013). Particle formation events are typically observed during the summer months only, when the Arctic environment is influenced by the Sun (Tunved et al. 2013), suggesting that they are photochemical in nature (Ström et al. 2003). An abundance of photochemically-active compounds are able to build up in the BL during the Arctic night, and these become active again once the sunlight returns (Barrie et al. 1988; Shaw 1995). Within a few days, ozone concentrations at Alert, Canada have been observed to decrease rapidly from 30-40 to 0 parts per billion (by volume, Mar 1985, Barrie et al. 1988) with the polar sunrise. In the summer, the newly-exposed Arctic ocean – and, possibly, the Siberian tundra (Ström et al. 2003) – acts as a source of precursor gases (e.g. SO_2, Engvall et al. 2008), promoting these interactions (Ström et al. 2003). Secondary aerosol particles dominate the sub-micron particle population (Weinbruch et al. 2012). Mixing also

plays a key role in both the summer and autumn, where these precursors interact with local aerosol particles at the surface (Leck et al. 1996). Sea salt remains a large fraction of the aerosol particle population during these months (Weinbruch et al. 2012) and aged sea salt fractions increase during this time, likely produced through interactions with sulphate gases from the ocean (Geng et al. 2010; Weinbruch et al. 2012).

Seasonal characteristics linking the different aerosol properties and polluted conditions to air mass history can be identified. During the haze months, air masses arriving at Svalbard, Norway have typically travelled over the frozen Arctic Ocean (Tunved et al. 2013) or the European continent (Behrenfeldt et al. 2008). These trajectories carry aerosol particles from Europe and Siberia to the Arctic (Tunved et al. 2013); aerosol with a potentially strong anthropogenic influence. However, during summer, the typical transport pathways change to the southwest, over the Atlantic Ocean (Behrenfeldt et al. 2008; Tunved et al. 2013). However, this link can be drawn into question as transport pathways are similar between March and October and these months display different aerosol characteristics (Tunved et al. 2013). Possible explanations could include the heightened biomass burning activity undergone in Siberia during the spring months (Wang et al. 2011; Tunved et al. 2013). As a result, studies have often found it difficult to conclude a robust relationship between back trajectories and polluted air masses (e.g. Ström et al. 2003).

2.2.2 Cloud condensation nuclei and ice nucleating particles

Aerosol particles interact with clouds as CCN or INPs, allowing liquid cloud droplets and ice crystals to form respectively. INPs, and the ice crystals they produce, are of particular interest in this study as the ice phase greatly affects the structure and lifetime of Arctic MPS.

Aerosol particles typically interact with clouds from below: as an air parcel rises, expands, and cools, the aerosol particles within it are exposed to supersaturated conditions and thus activate to form cloud droplets or ice crystals. Aerosol particles can also interact on the periphery of clouds: for example, entrainment of aerosol from above cloud can introduce aerosol particles which nucleate at cloud

top. These could be CCN or INPs (Jackson et al. 2012). Entrainment has likely occurred in a cloud layer with a sub-adiabatic liquid water content profile: dry air moves in from the top or side of the cloud, feeding sub-saturated air into the cloud and causing the evaporation of cloud droplets. However, stable stratification – as commonly observed in the Arctic spring – limits the effect of cloud top entrainment and droplet number concentrations typically correlate strongly with below-cloud aerosol particle number concentrations (Hobbs and Rangno 1998). During ISDAC, accumulation-mode particle number concentrations below cloud compared well with droplet number concentrations within cloud (Jackson et al. 2012). This correlation suggests that the majority of aerosol particles in the detected size limit (approximately 0.1 µm to 3 µm) were acting as CCN.

Nucleation is more efficient on larger curvatures, and this size dependence influences the formation of clouds in the atmosphere: water vapour condenses on to larger particles at lower levels of supersaturation than required for smaller particles, thus removing large CCN and INPs from the aerosol population first (Pruppacher and Klett 1997). CCN are hydrophilic and small in size (approximately D_P <130 nm, Dusek et al. 2006), and various species may act as CCN in the atmosphere (Rogers and Yau 1989). Known CCN include sea salt, non-sea salt sulphate (NSS) and secondary organic aerosol (SOA) particles (amongst others, Pruppacher and Klett 1997). However, Dusek et al. (2006) demonstrated that particle size is the primary defining factor in CCN ability and particle species takes a secondary role. Cloud droplets are typically more numerous than ice crystals as CCN are more plentiful in the atmosphere than INPs.

INPs are more selective and must be insoluble, large, have a similar molecular structure to ice (Seinfeld and Pandis 1998), and have the potential to produce chemical bonds with ice molecules at their surface (Murray et al. 2012). INPs are typically thought to be of coarse-mode sizes, and DeMott et al. (2010) specifically suggest particle sizes >0.5 µm. Coarse-mode aerosol particles are typically mineral dusts, fly ash, biological particles, or sea salts (Seinfeld and Pandis 1998). Estimated number concentrations of known INPs with decreasing temperatures are illustrated in Fig. 2.3.

Mineral dust is a significant component of the global mass of aerosol, quoted to

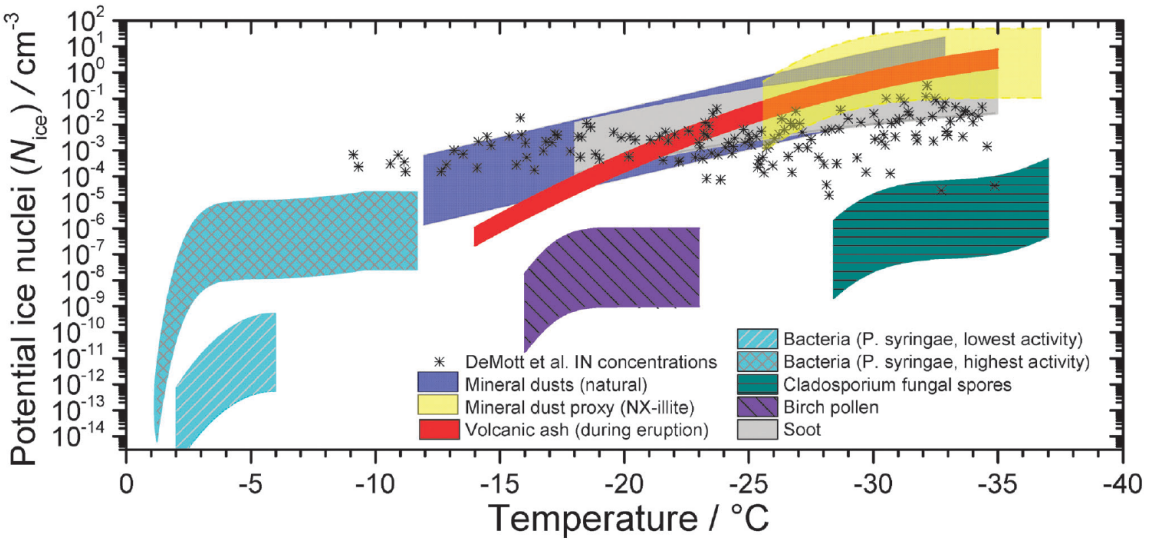

Figure 2.3: Murray et al. (2012) Fig. 19: Overview of known ice nucleating particle (INP) species, using data from various studies. Estimated number concentrations of INPs are shown as a function of temperature. Predicted INP number concentrations using the DeMott et al. (2010) parameterisation are also shown as black asterisks for comparison with the observed data.

be approximately 45% (Caquineau et al. 2002). Dusts are efficient INPs and tend to be active in the atmosphere at temperatures below approximately -10 °C. Hematite, clay minerals (especially kaolinite and illite) and feldspars have been observed to be effective INPs, nucleating ice at temperatures between -12°C and -9°C (Zimmermann et al. 2008). Clay minerals are thought to be the most effective INPs below approximately -12°C (Zimmermann et al. 2008; Formenti et al. 2011); therefore, they may nucleate a substantial fraction of observed atmospheric primary ice particles in moderately supercooled clouds. However, some studies have suggested that it is not the clay minerals themselves which are the most efficient INPs: the presence of feldspar inclusions on clay particles has been found to increase their ice nucleating efficiency at warm sub-zero temperatures (Atkinson et al. 2013; Yakobi-Hancock et al. 2013). As consequence, K-feldspar is commonly identified as the most efficient dust INP (Atkinson et al. 2013).

Soot, bacteria, pollen, and volcanic ash also facilitate ice formation in the atmosphere (Murray et al. 2012). Biological particles have been found to be ice-active at warm sub-zero temperatures, promoting ice formation in a temperature range warmer than possible for mineral dusts (>-10°C, Möhler et al. 2007; Ariya et al.

2009). However, questions remain about their ability to take part in cloud interaction; for example, are the concentrations large enough to produce the ice concentrations observed at such warm temperatures (Möhler et al. 2007)? There are limited in situ data of the direct interaction between biological INPs and clouds (e.g. Pratt et al. 2009); therefore, this question remains unanswered.

Sulphates, metal oxides, sea salt, and carbonate minerals are amongst those species identified to be inefficient INPs (Yakobi-Hancock et al. 2013). Yakobi-Hancock et al. (2013) suggest that the inefficiency of the minerals may be due to the lack of a surface charge; a charge that some efficient INPs possess, such as illite and feldspars.

The ability of an aerosol particle to nucleate ice is dependent on its composition and mixing state, as differing compositions imply differing particle structures and shapes. Several studies (e.g. Mamane and Noll 1985; Zimmermann et al. 2008; Kandler et al. 2011) have observed surface coatings on aerosol particles; thin layers of other minerals, elements, or compounds which may ultimately affect the nucleating ability of the parent particle. For example, Kandler et al. (2009) identified hematite coatings on dust particles in their study; coatings which could either enhance or weaken the nucleating ability of the parent particle dependent on its composition. Ice-active coatings may enhance the nucleating ability of a previously inactive INP in a similar manner to the biological coatings observed by O'Sullivan et al. (2013). Additionally, bacteria – known INPs (Möhler et al. 2007; Hoose and Möhler 2012) – can also survive on the surface of dust particles over long range transport (Yamaguchi et al. 2012). Conversely, organic coatings can suppress the nucleating ability of a previously efficient INP (Primm et al. 2016). Mixed-particles which contain some soluble and insoluble component can act as giant CCN (GCCN), and their influence in cloud microphysical interactions is poorly understood (Khain et al. 2000). GCCN have been modelled to significantly augment the warm rain process if their INP component is ignored (Levin et al. 2005). For example, such particles could be mixes of sea salt and mineral dust (Levin et al. 2005).

In the Arctic, studies have suggested that leads or polynas in the ice (Curry et al. 2000) and the ocean (e.g. Bigg 1996; Leck et al. 1996; Bigg and Leck 2001) could act as sources of INPs. Schnell and Vali (1976) suggested that it is the phytoplankton in the

open water that nucleates ice. Wilson et al. (2015) found that organic material in sea spray, specifically diatom exudates, nucleates ice under atmospherically-relevant conditions and suggest that phytoplankton exudates in general could similarly nucleate ice.

2.2.3 Primary ice nucleation

There are two pathways of ice nucleation; homogeneous and heterogeneous freezing (Pruppacher and Klett 1997). Homogeneous freezing occurs in the absence of an INP: cloud droplets may freeze once a threshold temperature of approximately -38°C is attained (Pruppacher and Klett 1997). As a stochastic process, random motions of supercooled droplets promote grouping into clusters; clusters, or ”germs”, which freeze upon reaching a critical size (Pruppacher and Klett 1997). The rate of homogeneous nucleation can therefore be inferred via the combined number of these ice embryos and the diffusion rate of supercooled droplets to these structures. This mechanism of ice nucleation does not often occur within low-altitude clouds, yet it becomes important in cirrus clouds: at high altitudes where there are depleted number concentrations of aerosol particles, the required combination of high supersaturations and low temperatures can develop and facilitate the formation of ice germs (Pruppacher and Klett 1997). Arctic MPS typically have cloud top temperatures above -30 °C (Verlinde et al. 2007); therefore, homogeneous nucleation unlikely contributes towards the ice phase in these clouds.

When an INP is involved in ice crystal formation, this process is known as heterogeneous freezing (Pruppacher and Klett 1997). There are two proposed mechanisms by which this may occur; the stochastic and singular approaches (Connolly et al. 2009). The first is time-dependent, whereas the second considers the process to occur at a fixed temperature. The stochastic approach treats nucleation as a random process which becomes more efficient with the addition of more INPs and longer timescales (Niedermeier et al. 2011). Conversely, the singular approach treats ice nucleation as approximately instantaneous once a threshold freezing temperature is attained (Connolly et al. 2009). This threshold is determined by the number of ice-nucleating sites present on the particle surface, and freezing occurs once the site with the warmest threshold temperature (T_S) nucleates ice (Niedermeier et al.

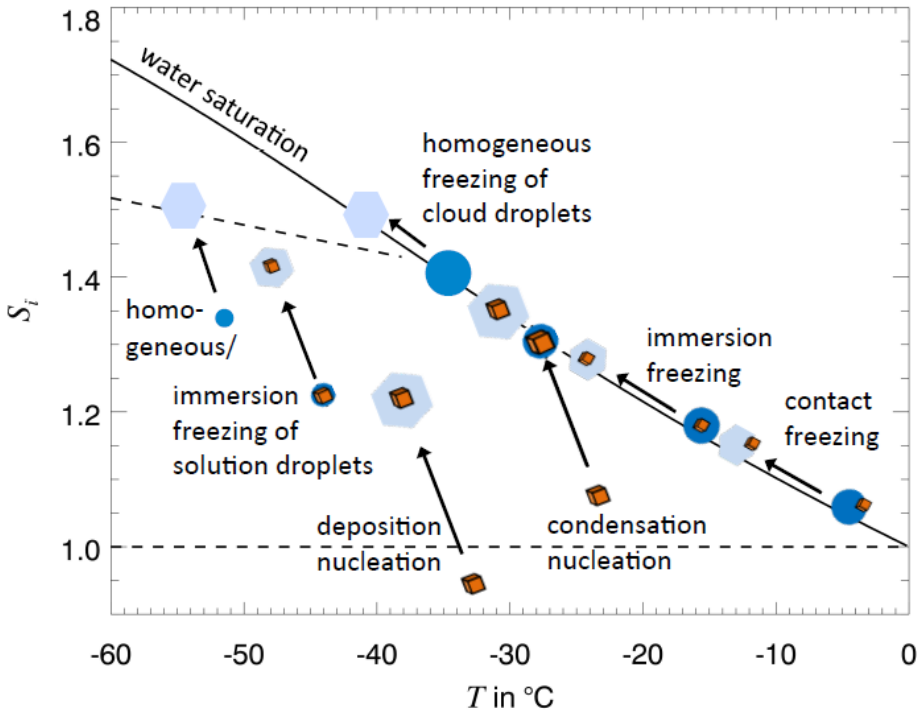

Figure 2.4: Hoose and Möhler (2012) Fig. 1: Schematic illustrating the different modes of ice nucleation, where supersaturation with respect to ice (S_i) is plotted against temperature. Contact-, immersion-, and homogeneous freezing occur at water saturation. Deposition-freezing occurs below the water saturation line in ice supersaturated conditions. Homogeneous freezing is not considered in this thesis as the minimum temperatures reached in Chapters 4, 5, and 6 do not fall below -22 °C. Heterogeneous freezing is solely considered here. As suggested by this diagram, immersion- and contact-freezing – at water saturation – are thought to be the most active ice nucleation mechanisms at temperatures >-20 °C.

2011). An ice-active surface site density, $n_S(T)$, follows from this hypothesis (Connolly et al. 2009). The number of active sites, and probability for freezing, increases with decreasing temperature (Connolly et al. 2009). Both of these nucleation mechanisms have support from different studies (Niedermeier et al. 2011) and are not explicitly considered in this thesis.

Heterogeneous primary ice nucleation may occur through four different pathways: the deposition-, condensation-, contact- and immersion-freezing mechanisms (Rogers and Yau 1989; Pruppacher and Klett 1997; Khain et al. 2000). Vapour may freeze as it directly deposits onto an INP surface in ice supersaturated conditions (deposition), or it can freeze through the formation of a liquid layer first (condensation). Particles of a mixed composition, with soluble and insoluble fractions, can activate to form a cloud droplet in water-saturated conditions and subsequently

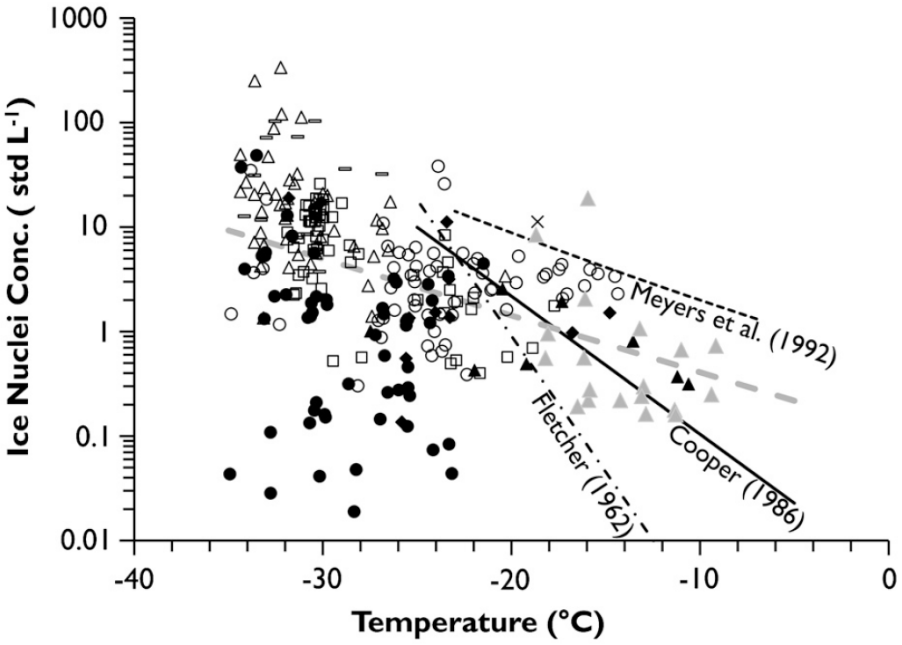

Figure 2.5: DeMott et al. (2010) Fig. 2: Measured INP number concentrations from a variety of geographical locations (legend not shown) and their dependence on temperature. Measurements were made using a Continuous Flow Diffusion Chamber (CFDC). The grey dashed line illustrates a fit to these data, and the derived DeMott et al. (2010) parameterisation is applied in Chapters 5 and 6 to predict INP number concentrations, based on aerosol particle number concentrations and temperature. The Fletcher (1962), Cooper (1986), and Meyers et al. (1992) parameterisations are also shown. Global measurements are shown; however, the data represented by the black triangles were collected near Barrow, Alaska during M-PACE (Verlinde et al. 2007), and thus are of particular interest to the study of Arctic INPs.

freeze if these conditions change to favour ice (immersion), and supercooled liquid droplets can freeze upon collision with an INP (contact). A summary schematic of these four ice nucleation mechanisms are illustrated in Fig. 2.4.

INPs constitute a small fraction of the aerosol population, with <1 INP for every 10^6 aerosol particles (DeMott et al. 2011). These low number concentrations can be below the background level of detection for some INP instruments (Rogers and Yau 1989; DeMott et al. 2011). Significant developments in INP measurements have been made possible in recent years due to improved instrument capabilities (Prenni et al. 2007; DeMott et al. 2010; DeMott et al. 2011). Figure 2.5 highlights an issue with INP observations: measurements are highly variable, covering several orders of magnitude, causing large uncertainties to be associated with derived parameterisations. The vast measurement range is partly a result of the four freezing mechanisms, which are active in different conditions. Mode-dependent

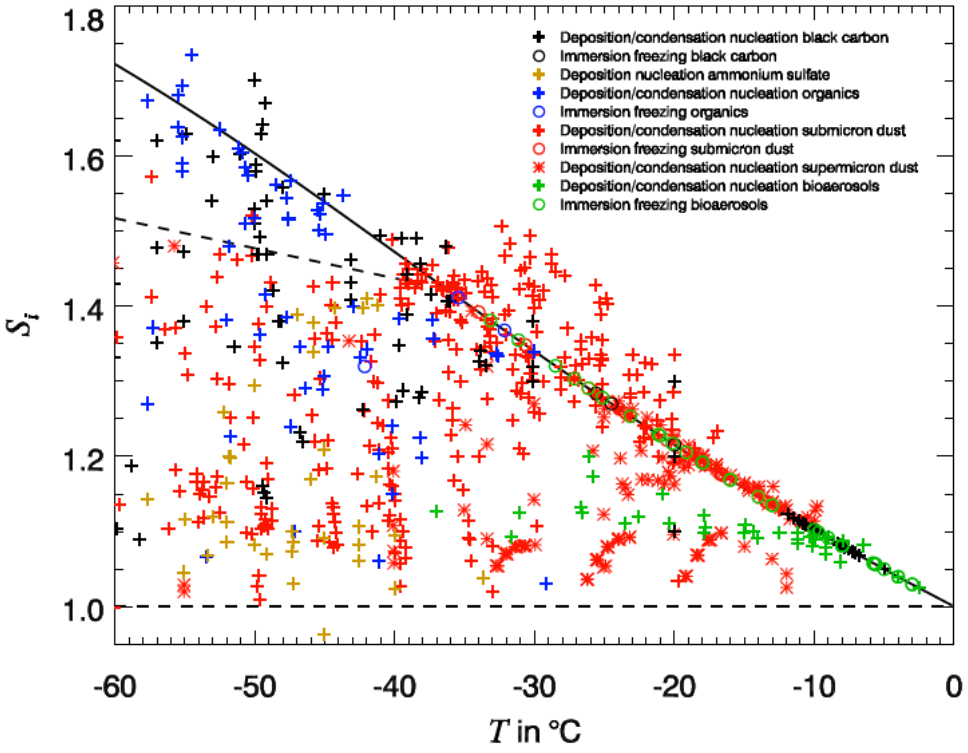

Figure 2.6: Hoose and Möhler (2012) Fig. 2: A review of the onset conditions of measured INPs is illustrated. As illustrated, temperature and ice saturation ratio are important dependencies for primary ice nucleation. Deposition and immersion ice nucleation are indicated by crosses and circles respectively, with different colours for different species. **Black:** black carbon, **gold:** ammonium sulphate, **blue:** organics, **red:** (sub-micron) mineral dust, and **green:** bioaerosols. Deposition-condensation freezing of super-micron mineral dust is shown separately by a red asterisk.

INP measurements are difficult to obtain; for example, Continuous Flow Diffusion Chambers (CFDC), as used by DeMott et al. (2010), measure INPs activated at water-saturation in immersion-freezing conditions. INPs which may activate in deposition-condensation conditions may not nucleate as efficiently in immersion-freezing conditions. Measuring the number of INPs in one nucleation mode does not necessarily represent the INP population (DeMott et al. 2011), and a wide range of measurements can be obtained when measuring the same mode (see Fig. 2.6). Additionally, ice nucleation occurs within short spatial and temporal windows, making it a difficult process to measure. Therefore, it is still not well known which particle species, in which mixing states, act as INPs in the atmosphere (Pruppacher and Klett 1997). A mixture of field-, laboratory- and theory-based studies, such as those conducted by Prenni et al. (2007), Niemand et al. (2012), and Hoose et al. (2010) respectively, are required to learn more about INPs in our atmosphere.

In the field, the conditions required for correlating INP and ice crystal number concentrations are often not sustained; clouds often evolve past the point of primary ice nucleation reasonably quickly (DeMott et al. 2011). Mean measured INP number concentrations during M-PACE did not adequately match the measured ice in the clouds, and this is a common observation from Arctic observational campaigns (e.g. Curry et al. 2000; Rangno and Hobbs 2001; Verlinde et al. 2007). This discrepancy is likely due in part to the difficulty in measuring INP number concentrations in situ (DeMott et al. 2010). Consistent primary ice number concentrations are required to test derived relationships between aerosol particles – as INPs – and ice crystals: with persistent, mixed-phase clouds containing low (likely primary) ice number concentrations, the springtime Arctic provides a good atmospheric test bed for testing field- and laboratory-derived ice nucleation parameterisations (e.g. DeMott et al. 2010; Niemand et al. 2012)

2.3 Modelling Arctic mixed-phase clouds

2.3.1 Overview of modelling knowledge

Numerical models fail to accurately simulate Arctic MPS on various scales (e.g. Curry et al. 2000; Jiang et al. 2000; Klein et al. 2009; Morrison et al. 2011; de Boer et al. 2014). In cloud-resolving models (CRMs), bulk treatments of microphysical interactions are used. Sub-grid scale processes are represented by parameterisations; empirically-derived relationships which make a prediction based on simulated properties. Key sub-grid scale microphysical interactions – such as primary ice nucleation, droplet activation, the coalescence of droplets to form raindrops, and the vapour growth of ice crystals – are often represented (e.g. Morrison et al. 2005). Particle size distributions are assumed to follow a functional form (for example, a gamma or exponential function of particle size), which can then be used to calculate changes in bulk properties (for example, mass mixing ratios). Cloud microphysics is often simplified further in GCMs: these models frequently do not resolve hydrometeor number concentrations and often only the ice and liquid water paths (IWP/LWP) are simulated due to computational cost (e.g. Harrington and

Olsson 2001; Klein et al. 2009).

Resulting from these simplified treatments of microphysical interactions, GCMs often underestimate the fraction of and liquid water path in low-altitude Arctic MPS; for example, the Community Atmosphere Model (CAM5, Neale et al. 2010) produces a reduced low cloud fraction in the Arctic with comparison to observations made during the Arctic Summer Cloud Ocean Study (ASCOS, de Boer et al. 2014; Tjernström et al. 2014). The resulting effect is net longwave fluxes at the surface which are too small, and net SW fluxes which are too large. Conversely, simulations using the Met Office Unified Model (MetUM, Staniforth et al. 2006) show an inability to reproduce clear sky conditions, with reference to the same ASCOS observations, by modelling over-active BL mixing (Birch et al. 2012). Reanalysis data are often used to initialise GCMs; however, initial cloud fractions can vary widely between analysis products (Walsh et al. 2009; de Boer et al. 2014). Therefore, it can be difficult to determine whether model output inaccuracies are due to the reanalysis products used or the model itself (de Boer et al. 2014).

To minimise error from initialisation data and improve model validation and development, observations of Arctic cloud microphysical interactions are required. There has been an increased effort to collect concentrated, high resolution data from observational campaigns in recent decades, and our knowledge of the microphysical properties and radiative implications of Arctic MPS has improved as a result. By developing models to improve agreement with observations, they can be used more effectively for sensitivity and forecast studies with decreased uncertainty.

By understanding how processes within the model need to be adapted to agree with observations, details of the physical interactions involved can be inferred. For example, predicted ice and droplet number concentrations, $\mathrm{N_{ice}}$ and $\mathrm{N_{drop}}$ respectively, liquid mass mixing ratio, $\mathrm{Q_{liq}}$, and liquid fraction modelled by the System for Atmospheric Modelling (SAM, Fan et al. 2009) 3-D model were found to agree well with observations made during ISDAC (McFarquhar et al. 2011). This was achieved through the use of a detailed spectral bin microphysics scheme; a microphysical representation that resolves aerosol-cloud interactions and tracks the activation and growth of hydrometeors. In contrast to bulk schemes, no assumptions are made about the underlying particle size distributions. However, with increased

complexity comes heightened computational cost; therefore, these detailed schemes are not included in large-scale models. Bin schemes are often used to investigate the physics of aerosol-cloud interactions and inform how they can be parameterised for use in bulk microphysics schemes, which are less computationally expensive. Bulk schemes are often not as accurate in representing microphysical interactions as bin schemes; however, they can provide good agreement with observations if appropriate representations of hydrometeor properties, informed by bin schemes, are used (Harrington and Olsson 2001).

A common issue with these numerical models is a reduced cloud fraction and depleted liquid phase due to an overpredicted ice phase (e.g. Pinto 1998; Harrington et al. 1999; Jiang et al. 2000; Harrington and Olsson 2001; Prenni et al. 2007; Morrison et al. 2012). Studies have been conducted to improve the physical representation of each phase in models; for example, liquid has been theorised to form in the presence of ice only when both a vertical velocity and an altitude threshold are reached (Korolev and Field 2008), and these droplets must undergo activation and evaporation cycles with the convective motion of air parcels within the mixed-phase cloud to promote persistence (Korolev and Isaac 2003). Such turbulent motion allows the mean LWP and IWP of mixed-phase clouds, modelled with a 1-D adiabatic model, to reach a steady state (Korolev and Isaac 2003). The relationship between turbulence and the liquid phase is key to sustained mixed-phase conditions: Hill et al. (2014) found that both the LWC and liquid fraction of modelled mixed-phase clouds increased with increasing TKE and temperature using large eddy simulations coupled with a bulk microphysics scheme. With increasing temperatures, the difference between ice and water supersaturation is reduced, ice crystal growth becomes less efficient, and further droplet nucleation and growth can occur in warm supercooled mixed-phase clouds (Hill et al. 2014). The liquid phase is positively forced by strong cloud top radiative cooling, which strengthens downdraughts and promotes further droplet activation within the cloud layer (Morrison et al. 2011).

Intercomparisons of CRMs and single column models (SCMs), with reference to M-PACE observations, have shown that models can capture the IWP of Arctic MPS; however, significant deficiencies in LWP compared with observations (up to

3× less) are common (Klein et al. 2009). Some models do better than others to recreate the liquid phase under the same large-scale forcing and imposed surface fluxes (Klein et al. 2009). The LWP deficiencies are largely due to the representation of ice and liquid interactions in these models, where a strong WBF mechanism acts to deplete the liquid phase more so than is observed (Klein et al. 2009). Whilst the IWPs are often comparable with observations, the absolute number concentration of ice crystals, $\mathrm{N_{ice}}$, is often highly variable (Klein et al. 2009). Cloud phase is particularly sensitive to $\mathrm{N_{ice}}$, and rapid glaciation has been observed to occur within models when the simulated ice number concentrations are increased (Pinto 1998; Harrington et al. 1999; Jiang et al. 2000; Prenni et al. 2007; Morrison et al. 2011).

2.3.2 Cloud persistence

Single-layer Arctic MPS are often long-lived (e.g. Shupe et al. 2006; Verlinde et al. 2007). Clouds observed during the SHEBA campaign were observed to have a mean lifetime of 12 h; however, observed cloud persistence extended up to a maximum of 153 h (Shupe et al. 2006). Models often do not reproduce these characteristics, simulating much lower cloud fractions than observed (Klein et al. 2009; de Boer et al. 2014; Tjernström et al. 2014).

Figure 2.7 summarises the microphysical interactions which occur within these clouds. Liquid water within modelled Arctic MPS is dependent on ice number concentrations, temperature, turbulent motions, and the representation of ice crystal habit (Harrington and Olsson 2001). By the WBF mechanism, high ice crystal number concentrations cause the rapid depletion of liquid water from mixed-phase clouds, and this interaction is poorly represented in models (Khain et al. 2000). Jiang et al. (2000) showed that modelled cloud microphysics is highly sensitive to the number of ice crystals predicted, with variability of $\mathrm{N_{ice}}$ by a factor of 2–3 significantly influencing the cloud structure and phase. Ovchinnikov et al. (2011) found that increasing $\mathrm{N_{ice}}$ from $0.5\,\mathrm{L^{-1}}$ to $2\,\mathrm{L^{-1}}$ caused their modelled LWP to decrease by a factor of 2 within two hours of simulation time. Additionally, this increase quickened the glaciation time of their simulated MPS (Ovchinnikov et al. 2011).

Several methods of simulating ice nucleation in Arctic MPS have thus far successfully modelled the persistence that is commonly observed. Studies have been

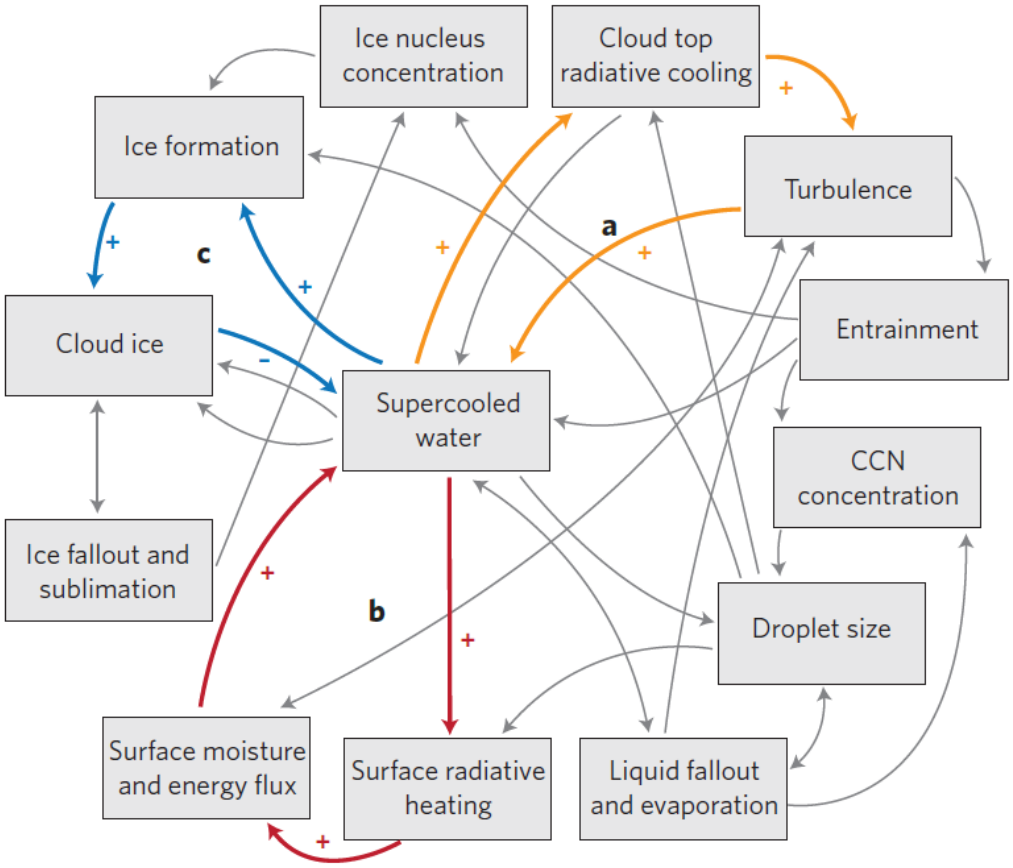

Figure 2.7: Morrison et al. (2012) Fig. 2: Key processes and microphysical interactions associated with Arctic mixed-phase clouds. Three main feedback processes are highlighted. **(a):** Cloud droplet formation within a rising air parcel induces radiative cooling at cloud top. Cooling causes negative buoyancy and colder temperatures within the descending air parcel, promoting further droplet formation through increased water saturation. **(b):** Supercooled liquid droplets within clouds trap upwelling longwave radiation efficiently, leading to heating at the surface. With warmer surface temperatures, stronger heat and energy fluxes are released into the boundary layer, promoting stronger updraughts and enhanced droplet formation within the cloud layer. **(c):** Supercooled liquid within the cloud layer can freeze if the air temperatures are cold enough (homogeneous freezing) or there are INPs available to promote contact-, immersion- or condensation-freezing (heterogeneous freezing). Ice formation processes add to the ice crystal number concentrations within the mixed-phase cloud. By the WBF mechanism (see text), ice crystals grow more efficiently than droplets at sub-zero temperatures. Droplets then evaporate to maintain stability in the increasingly sub-saturated (with respect to water) conditions.

able to reproduce sustained mixed-phase conditions by simulating INP depletion as the microphysical interactions progress (Prenni et al. 2007), employing time-dependent nucleation to represent the spectrum of INP efficiencies in an aerosol population (Savre and Ekman 2015), or by limiting ice nucleating parameterisations to water-saturated conditions and removing the influence of deposition-freezing (de Boer et al. 2011).

The INP depletion hypothesis follows from processes inferred by observations. Low number concentrations of ice crystals in Arctic MPS (e.g. Prenni et al. 2007; Jackson et al. 2012; McFarquhar et al. 2011), especially during the spring, suggest that INP number concentrations are equally low (Bigg 1996). These INPs would activate, microphysically interact in the cloud, grow, and precipitate from the cloud layer (Prenni et al. 2007). In this scenario, the most active INPs would nucleate and be removed from the cloud layer first (Harrington et al. 1999; Harrington and Olsson 2001; Prenni et al. 2007). Rapid INP depletion can occur through this process; therefore, Arctic INP populations must be reintroduced to the system to sustain the persistent mixed-phase clouds we commonly observe. One possible pathway is sedimentation of long-range transported particles from above (Harrington and Olsson 2001; Prenni et al. 2007). Arctic MPS may be particularly sensitive to transported, anthropogenic plumes of INPs for this reason (Pinto 1998; Jiang et al. 2000).

Prenni et al. (2007) simulated a mixed-phase cloud which persisted for 48 h by using an empirically-derived estimate of INPs from M-PACE and allowing INP depletion in their regional model. The cloud top liquid layer that is commonly observed was successfully simulated using this technique. Similarly, Harrington et al. (1999) and Harrington and Olsson (2001) demonstrated that INP depletion is crucial to enhancing modelled mixed-phase cloud lifetime by using bin and bulk microphysics schemes respectively. Depleting INP number concentrations predicted by the Meyers et al. (1992) parameterisation by 30% and increasing large-scale advection by $3\times$ allowed Jiang et al. (2000) to accurately simulate the observed autumnal Arctic MPS observed by Pinto (1998).

INP depletion is often not represented in large-scale models, and Prenni et al. (2007) found that their modelled MPS rapidly glaciated through the accumulation of ice when depletion was not represented. Ice nucleation parameterisations in bulk

microphysics schemes often predict an ice number concentration based on either temperature (e.g. Cooper 1986) or supersaturation with respect to ice (e.g. Meyers et al. 1992). Therefore, these relationships predict the same ice number concentration based on the same thermodynamic conditions; a prediction that does not account for spatial and temporal variability of INP number concentrations in the atmosphere (Prenni et al. 2007). Despite this, studies which utilise a prognostic representation of INPs, which is allowed to deplete, can simulate too few ice crystals within cloud, causing their INP supply to be quickly used up (e.g. Harrington and Olsson 2001).

INP recycling has followed on from these hypotheses, and has been shown to affect modelled Arctic MPS: ice crystals fall from the mixed-phase cloud into the sub-saturated layer below, evaporate, and resupply the sub-cloud layer with INPs (e.g. Fan et al. 2009; Solomon et al. 2015). These INPs then get lofted back into the cloud and nucleate ice once again. This recycling effect has been similarly postulated for droplets freezing upon evaporation and INP formation from droplet residues (Beard 1992; Bigg 1996; Fan et al. 2009).

Time-dependent ice nucleation, relating to the ice-nucleating ability of the aerosol particle population, has been shown to simulate sustained mixed-phase conditions (Westbrook and Illingworth 2013; Savre and Ekman 2015). Savre and Ekman (2015) found that a classical nucleation theory (CNT) representation allowed $\mathrm{N_{ice}}$, LWP, and IWP to be modelled with reasonable agreement with ISDAC observations. Westbrook and Illingworth (2013) suggest that this time-dependency could manifest physically as a spectrum of nucleation efficiencies in the particle population, or it could be a result of contact-freezing of cloud droplets by ambient aerosol at random.

At temperatures greater than -20 °C, mixed-phase conditions are typically dominant in low-altitude clouds (de Boer et al. 2011; Westbrook and Illingworth 2011), especially in the Arctic (de Boer et al. 2009, 2011; Shupe et al. 2011; Vihma et al. 2014). Theoretically, primary ice nucleation via the deposition of water vapour should cause rapid glaciation in this temperature range due to the differences in saturation vapour pressure over ice and liquid water (Pruppacher and Klett 1997). Westbrook and Illingworth (2011) propose that freezing occurs through the liquid phase in

supercooled mixed-phase clouds warmer than -20 °C due to the inefficiency of deposition ice nucleation in this temperature range. Ice clouds are infrequent at low altitudes in the Arctic, supporting the hypothesis of nucleation via liquid pathways (de Boer et al. 2011). Despite this, low altitude ice clouds are often modelled in this regime. Adding a water-saturation restriction to ice formation parameterisations allows a greater mixed-phase cloud fraction and increased LWP to form (Morrison and Pinto 2006). Physically, this limitation acts to restrict primary ice nucleation to occur only when liquid water droplets are also present.

Ice nucleation at water-saturation is hypothesised to be of importance in the Arctic as the aerosol particle population is often well-mixed (de Boer et al. 2011). With enhanced mixing, co-existing soluble and insoluble fractions can promote a two-stage, immersion-freezing process; droplet activation upon 100% relative humidity (RH) conditions and subsequent freezing upon supercooling. Soluble coatings on ice-active particles are also thought to promote this freezing pathway (Bigg and Leck 2001).

Immersion-freezing is typically represented by the Bigg (1953) parameterisation, which describes the rate at which supercooled raindrops freeze. More recently, Diehl and Wurzler (2004) developed this stochastic method to produce a freezing rate of cloud droplets containing an insoluble aerosol particle. Freezing was modelled to depend on the most efficient ice-active site available within the droplet, irrespective of the total number of insoluble particles (Diehl and Wurzler 2004). More generally, de Boer et al. (2011) suggest that limiting traditional parameterisations (e.g. Cooper 1986; Meyers et al. 1992) to water-saturated conditions can provide ice number concentrations and liquid water contents in reasonable agreement with observations.

These methods of restricting the ice number concentrations in Arctic MPS are all based on physical interactions that have either been observed or theorised to occur. All have restricted N_{ice} in modelled Arctic single-layer MPS sufficiently to allow the liquid phase to compete and sustain cloud lifetime. It is likely that a combination of these processes contribute to the mechanisms by which cloud ice forms and is depleted in Arctic single-layer MPS.

2.4 Thesis aims and structure

Much is to be learned about how the ice phase forms and evolves in Arctic single-layer mixed-phase stratocumulus (MPS). Our limited understanding of the microphysical interactions within these clouds prevents us from accurately reproducing them with numerical models. This thesis seeks to develop our current understanding of ice nucleation in Arctic MPS through the use of laboratory techniques, in situ observations, and modelling studies.

Detailed in situ observations of aerosol and cloud properties are required to improve our microphysical understanding of Arctic MPS and the role of aerosol-cloud interactions in this region. The key areas addressed here are: better quantifying the ice phase in these clouds; inferring how these ice crystals form; and investigating how mixed-phase conditions are sustained against the WBF mechanism. This thesis has been dissected into three inter-connected studies to address these issues.

1. Chapter 4 details an investigation of large aerosol particle composition in the Arctic atmosphere, using scanning electron microscopy (SEM). These particles are likely candidates for INPs; therefore, any further knowledge of what particle species are present and studying how their average composition can change with size, day, and position with respect to cloud could inform which of these may be acting as INPs.

   The article titled ”Size-segregated compositional analysis of aerosol particles collected in the European Arctic during the ACCACIA campaign” has been published in the ACCACIA Special Issue of the Atmospheric Chemistry and Physics research journal. This journal maintains Open Access for all publications. Citation is as follows:

   - Young, G., Jones, H. M., Darbyshire, E., Baustian, K. J., McQuaid, J. B., Bower, K. N., Connolly, P. J., Gallagher, M.W., and Choularton, T.W.: Size-segregated compositional analysis of aerosol particles collected in the European Arctic during the ACCACIA campaign, Atmospheric Chemistry and Physics, 16, 4063-4079, doi:10.5194/acp-16-4063-2016, 2016.

2. Chapter 5 presents in situ observations of Arctic MPS cloud microphysics in the context of the thermodynamic boundary layer structure. By investigating cloud microphysical structure and evolution over the transition from sea ice to ocean, the radiative interactions of these clouds with their environment may be inferred.

   The article titled "Observed microphysical changes in Arctic mixed-phase clouds when transitioning from sea ice to open ocean" has been published in the ACCACIA Special Issue of the Atmospheric Chemistry and Physics research journal. Citation is as follows:

   - Young, G., Jones, H. M., Choularton, T. W., Crosier, J., Bower, K. N., Gallagher, M. W., Davies, R. S., Renfrew, I. A., Elvidge, A. D., Darbyshire, E., Marenco, F., Brown, P. R. A., Ricketts, H. M. A., Connolly, P. J., Lloyd, G., Williams, P. I., Allan, J. D., Taylor, J. W., Liu, D., and Flynn, M. J.: Observed microphysical changes in Arctic mixed-phase clouds when transitioning from sea ice to open ocean, Atmospheric Chemistry and Physics, 16, 13 945–13 967, doi:10.5194/acp-16-13945-2016, 2016.

3. Chapter 6 investigates primary ice formation within Arctic MPS. Large eddy simulations (LES) are used to infer which nucleation pathways are active within the observed clouds. A key factor to address is the persistence of Arctic MPS, which is intricately linked to the ice phase; therefore, the sensitivity of the modelled cloud microphysics to ice crystal number concentrations is tested by comparing with in situ observations.

   The article titled "Microphysical sensitivity of coupled springtime Arctic clouds to modelled primary ice formation over the ice pack, marginal ice, and ocean" has been submitted to the ACCACIA Special Issue of the Atmospheric Chemistry and Physics research journal. Citation is as follows:

   - Young, G., Connolly, P. J., Jones, H. M., and Choularton, T. W.: Microphysical sensitivity of coupled springtime Arctic stratocumulus to modelled primary ice over the ice pack, marginal ice, and ocean, Atmospheric

Chemistry and Physics Discussions, doi:10.5194/acp-2016-898, in review, 2016.

3 Methods

An investigation of ice particles in Arctic mixed-phase clouds is detailed herein. Recent observations from the ACCACIA campaign form the basis for the three studies detailed in Chapters 4, 5, and 6; therefore, an overview of the project is provided for context.

3.1 ACCACIA campaign

Our ability to accurately forecast how Arctic warming will progress is hindered by our treatment of atmospheric aerosol-cloud interactions in numerical models. The scarcity of in situ atmospheric measurements in this region causes a substantial hurdle in this effort and, to address this, the ACCACIA campaign was conducted in the European Arctic during the spring (Mar-Apr) and summer (Jul) of 2013. These campaign periods allowed for atmospheric measurements to be made when the sea ice volume was close to its maximum and minimum extent respectively.

The primary objective of the ACCACIA campaign was to improve our knowledge of, and reduce the uncertainty in, the influence of aerosol and clouds on the Arctic energy budget. Two separate measurement platforms were used; airborne- and ship-based. The airborne data are of particular interest to this project as the conducted flight plans sampled below, within, and above cloud layers to directly measure the related aerosol and microphysical properties.

Two cruise ships were used during the ACCACIA campaign: the RV Lance and RRS James Clark Ross during the spring and summer respectively. Fitted with a range of instrumentation, the aim was to study the interaction between the ocean surface and the atmosphere. The cruises primarily sampled to the south and west of Svalbard, in the Greenland sea and Fram Strait, to investigate coastal dependencies

on the aerosol, biological, and atmospheric data collected. Co-located ship and aircraft measurements were not collected; therefore, the ship-based measurements could not be directly linked to cloud properties. As this thesis seeks to investigate cloud microphysical sensitivities to ice crystal and aerosol number concentrations, data from the ship-based segment of the campaign are not discussed.

Two aircraft were used to provide in situ atmospheric measurements. During the springtime campaign, detailed observations were made using the Facility for Airborne Atmospheric Measurements' British Aerospace 146 (FAAM BAe-146) and the British Antarctic Survey's Twin Otter Meteorological Airborne Science INstrumentation (BAS MASIN) aircraft. Meteorology, boundary layer, aerosol, and cloud microphysics measurements were made using both of these aircraft; however, a more comprehensive suite of instrumentation was available on the FAAM aircraft due to its larger size, allowing more detailed measurements to be taken. For example, the FAAM aircraft could additionally measure trace gases and launch dropsondes during the ACCACIA campaign. The BAe-146 flight paths were restricted to the close vicinity of Svalbard; it could not travel too far north over the ice pack due to navigation restrictions. Therefore, the BAS MASIN aircraft was used to conduct observations over a greater geographical range whilst the FAAM aircraft made more detailed, structured flights to sample key areas of interest. The FAAM aircraft was only used during the spring campaign, whilst the BAS MASIN aircraft collected measurements in both segments. In situ observations from the FAAM aircraft of the springtime ACCACIA campaign are used extensively in the studies detailed herein.

Liu et al. (2015) identified Asian plumes as a significant source of black carbon (BC) to the Arctic troposphere from airborne aerosol measurements made during the springtime campaign. This finding is crucial given the widespread fossil fuel activity in Asia, and suggests that the Arctic may be directly affected by the increasing emissions in this region. BC is poorly constrained in the Arctic, and it can have significant radiative impacts as a radiation-absorber when suspended in the atmosphere or as an albedo-reducer when deposited on the snow/ice surface. The identification of these plumes also has possible implications for the laboratory study detailed in Chapter 4, as it may be possible for other aerosol particle species

to travel to the Arctic via the pathways identified by Liu et al. (2015).

Detailed cloud microphysical measurements were made during the springtime ACCACIA campaign, and these are used extensively in the studies detailed herein. Lloyd et al. (2015) compared the cloud structure measured during two of these FAAM flights – flights not considered in Chapters 5 or 6 – and two MASIN summertime flights, and identified a seasonally consistent ice phase accompanied by significantly different cloud droplet number concentrations. Median ice number concentrations were approximately $0.5\,\mathrm{L}^{-1}$ during the springtime and $\sim 3\,\mathrm{L}^{-1}$ during the summer. Secondary ice production, via the Hallet-Mossop mechanism, was identified in the warmer summer clouds, whereas primary ice formation dominated in the springtime. This result proved crucial for the studies detailed in Chapters 4, 5, and 6: with only primary ice formation influencing the clouds, the relationship between aerosol, cloud microphysics, and boundary layer structure could be investigated in isolation from secondary ice enhancement.

In addition to aerosol and cloud microphysics studies, it was also an important goal of the ACCACIA campaign to investigate boundary layer structure and its variability across the ice edge. Elvidge et al. (2016) developed a new parameterisation of surface roughness based on FAAM aircraft measurements during the spring campaign. The surface roughness was at its smoothest over the sea ice pack and ocean, with maxima in the air drag coefficient identified at marginal ice fractions between 60% and 80%. These data have implications for cloud microphysics, as boundary layer structure and stability – which can be greatly affected by roughness and deformities at the surface – can affect the growth and development of clouds that may form within it. The relationship between boundary layer thermodynamic properties and cloud microphysical structure is addressed here in Chapters 5 and 6.

Three goals of the ACCACIA campaign are addressed in this thesis:

1. "What are the microphysical properties of remote Arctic stratus and their relationship with different aerosol sources?"

2. "How do aerosol and cloud properties vary with the extent of sea ice cover?"

3. "Develop and test new process models and parameterisations specific to the Arctic for cloud microphysics"

By studying the compositional characteristics of aerosol particles present in the Arctic atmosphere, and inferring ice nucleating potential, we can make suggestions as to which particles may be ice-active within the clouds observed. Investigating the microphysical properties of the clouds, and the distribution of the liquid and ice phases, can allow derived aerosol-cloud relationships (such as primary ice nucleation parameterisations) to be evaluated and directly compared with observations. Taking these data further in process models, and testing the microphysical sensitivities to such parameterisations, can indicate which representation agrees best with observations and identify pathways of improvement for larger-scale, regional models. Chapters 4, 5, and 6 address this research pathway, and details of the instruments and models used to do so are listed as follows.

3.1.1 FAAM BAe-146 aircraft instrumentation

Several instruments were used to investigate cloud microphysics, aerosol properties, and boundary layer structure in the studies detailed herein. Data from the Cloud Droplet Probe, 2-Dimensional Stereo imaging probe, Cloud Imaging Probes, Passive-Cavity Aerosol Spectrometer Probe, and Cloud Aerosol Spectrometer with Depolarisation are used extensively in Chapters 4, 5, and 6. The capabilities of these instruments are detailed as follows, and a summary of all instrumentation used is included in Table 3.1.

Cloud microphysics

Data from the Cloud Droplet Probe (CDP-100 Version 2, Droplet Measurement Technologies (DMT), Lance et al. 2010) are used in Chapters 4, 5, and 6. This wing-mounted instrument measures the size distribution of liquid cloud droplets from 3 µm to 50 µm in size.

Figure 3.1 illustrates the internal interactions which occur within the CDP when measuring a particle. The CDP has two external arms, across which a laser beam is fired. An open sample area exists between the arms, with detection optics housed in one arm and a laser diode in the other. As particles pass through this sample area, the incident laser light is scattered (Lance et al. 2010). Light scattered in the forward direction (through angles 4-12°, Rosenberg et al. 2012) is used to derive

Table 3.1: List of instruments on the FAAM BAe-146 aircraft from which data have been used herein. **T:** temperature, Θ**:** potential temperature, **Q:** mixing ratio, **U:** W-E wind component, **V:** N-S wind component.

Category	Name	Full Name	Measurement details	Comment	Data included in Chapter:
Aerosol	Aircraft Filters	Nuclepore polycarbonate filters	1 µm, 10 µm pore filter pair Aerosol particles: ∼0.1–10 µm	Internal, modified inlet	4, 5
	C-ToF-AMS	Compact Time of Flight Aerosol Mass Spectrometer	Sub-micron non-refractory aerosol composition	Internal, Rosemount inlet	5
	SP2	Single Particle Soot Photometer	Black carbon mass loading	Internal, Rosemount inlet	5
	CPC	TSI 3786-LP ultrafine Condensation Particle Counter	Aerosol particles: 3 nm–3 µm	Internal, Rosemount inlet	5
	PCASP-100X	Passive-Cavity Aerosol Spectrometer Probe	Aerosol particles: 0.1–3 µm	Wing-mounted, starboard	4, 5, 6
	CAS-DPOL	Cloud Aerosol Spectrometer with Depolarisation	Aerosol and cloud particles: 0.6–50 µm	Wing-mounted, starboard	4, 5
Cloud	CDP-100	Cloud Droplet Probe	Cloud particles: 3–50 µm	Wing-mounted, port	4, 5, 6
	2DS	2-Dimensional Stereo particle imaging probe	Cloud particles: 10–1280 µm	Wing-mounted, starboard	5, 6
	CIP-15	Cloud Imaging Probe-15	Cloud particles: 15–930 µm	Wing-mounted, starboard	5
	CIP-100	Cloud Imaging Probe-100	Cloud particles: 100–6200 µm	Wing-mounted, port	5
	CPI	Cloud Particle Imager	Cloud particles: 15–2500 µm	Wing-mounted, starboard	5
Meteorology	GPS-aided inertial navigation system		Altitude	Antenna	4, 5, 6
	Rosemount de-iced temperature sensor		Air temperature	Nose, inlet	4, 5, 6
	Buck CR2		Dew point/Humidity	Nose, inlet	4
	5-hole turbulence radome		Wind components (3D)	Nose-mounted	5
	AIMMS20AQ turbulence probe		Vertical wind velocity	Wing-mounted, port	5
	Dropsondes		T, Θ, P, Q_{vapour}, Q_{liquid}, U, V	Launcher	5, 6
Remote Sensing	Lidar	FAAM Non-Core Mini-Lidar Leosphere ALS450	Backscatter and depolarisation	Downwards-facing	5

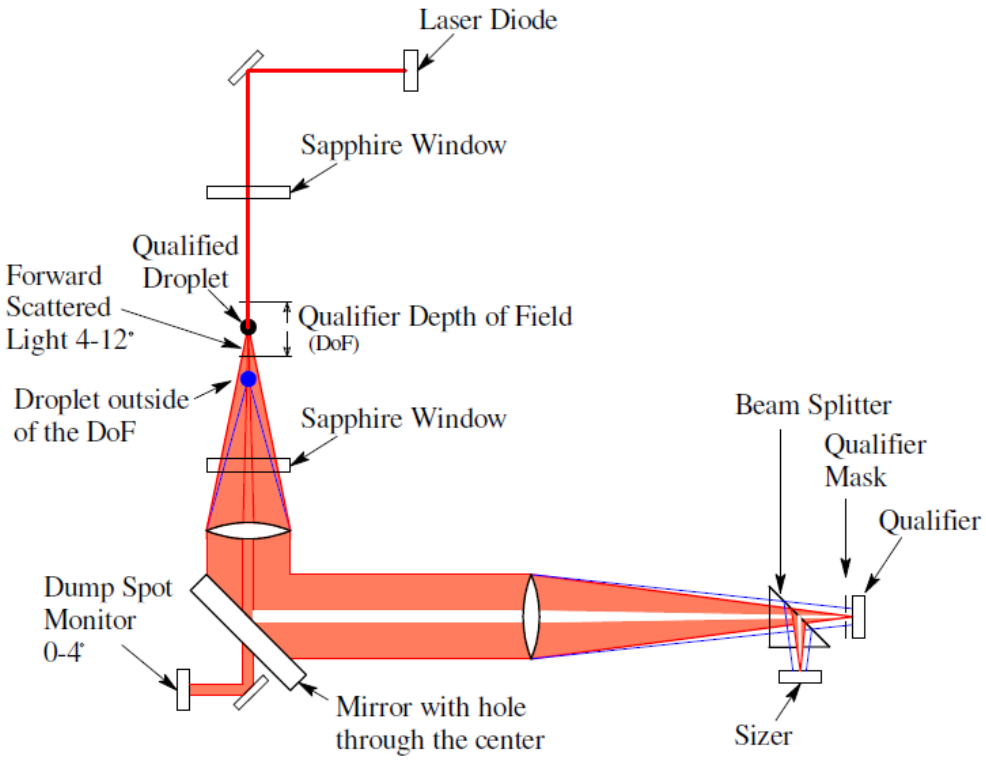

Figure 3.1: Lance et al. (2010) Fig. 1: Schematic of the Cloud Droplet Probe (CDP) detection optics. Scattered light is fed through the optics, and split equally onto two detectors – the sizer and qualifier – to produce size information and qualify true particle events respectively. Rays of laser light indicated in red illustrate the path of a particle detected within the sample volume, whilst blue rays indicate the path of one outwith the depth of field. The red signals are amplified by the qualifier mask (RHS of figure) to log a particle event, whilst the blue signals are removed by the qualifier mask and not counted. All signals are logged by the sizer. Unscattered light is removed by the dump spot monitor (bottom LHS of figure).

size and number information about the particles sampled. Both the scattered and unscattered light pass through to the opposite arm, and the signals are separated using beam splitters: the unscattered light leaves the system while the scattered light is focused on to two detectors to qualify the signal (qualifier) and record size information (sizer, Lance et al. 2010). Only signals scattered from within the sample volume are counted by the qualifier, via the use of a signal-qualifying mask, whilst the sizer measures all incoming signals (Lance et al. 2010).

The 2-Dimensional Stereo (2DS, SPEC inc., Lawson et al. 2006) imaging probe and Cloud Imaging Probes (CIPs, Baumgardner et al. 2001) are optical array probes

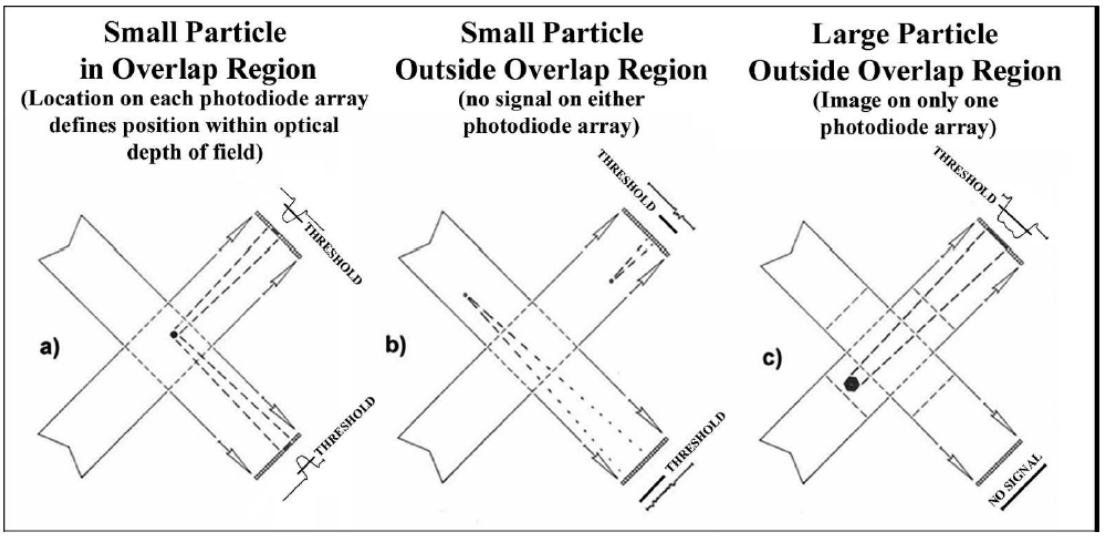

Figure 3.2: Lawson et al. (2006) Fig. 2: Summary of 2DS particle detection scenarios. Arrows indicate the direction of each laser. **(a):** Particle is detected within the overlapping region of the detectors. **(b):** Small particle is within the range of one detector but not the other, and its shadow is not intense enough to trigger a particle event. **(c):** Large particle within the range of one detector and the shadow cast has sufficient intensity to be logged as a particle detection.

(OAPs) also used during ACCACIA. Data from these instruments are used in Chapters 5 and 6 to give a quantitative measure of the ice crystal number concentrations within the clouds sampled.

The 2DS images cloud particles from 10 µm to 1280 µm. Two orthogonal lasers, crossing within the imaging cavity, allow a stereoscopic image of each detected particle to be constructed. 128-photodiode arrays are located at the extremes of these lasers to log particle events (Lawson et al. 2006). The sample area is defined by the region of overlap between the lasers and both detectors record images of the same particle when activated. Particles may be detected if only one laser is triggered; however, only a single image is taken in this case (Lawson et al. 2006). Figure 3.2 illustrates the requirements for particle detection in the 2DS. A positive detection is initiated when the shadow cast across the photodiode arrays is greater than a threshold value – 50% of the background level – and completes when the laser intensity detected at the array returns to 100% (Lawson et al. 2006).

The CIP15 and CIP100 measure cloud particles from 15 µm to 930 µm and 100 µm to 6200 µm respectively. These instruments are useful for identifying properties of ice crystals in mixed-phase clouds. The detection system of the CIPs is summarised

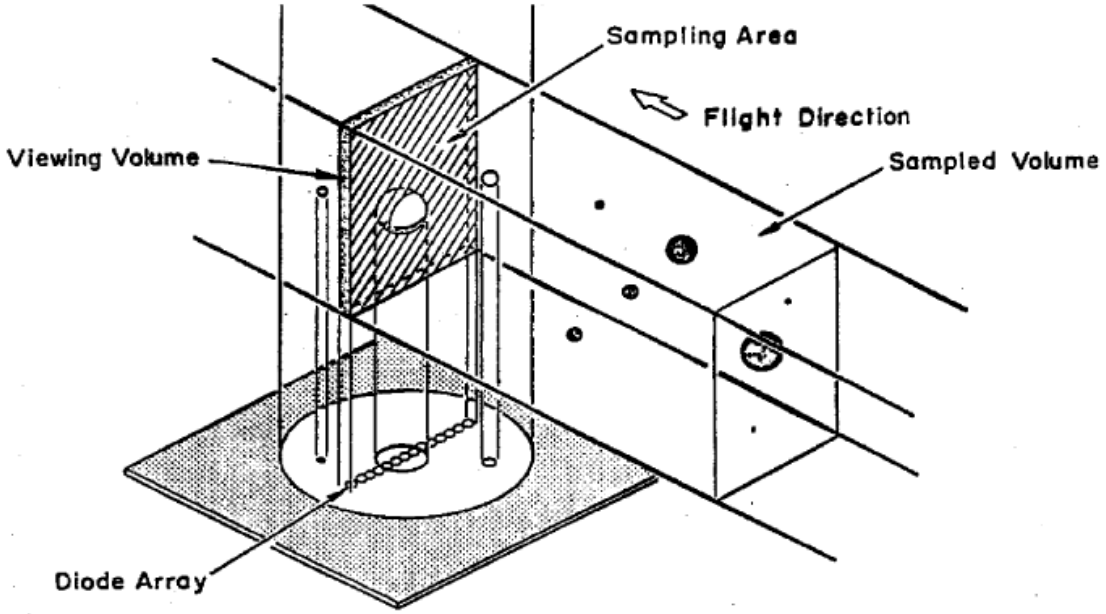

Figure 3.3: Baumgardner et al. (2001) Fig. 3: Schematic illustrating how the CIP probes function. Laser light is incident on the sampling area (from above in this schematic) at all times. When a particle enters the sampling area, it cases a shadow on the linear array of photodiodes below it, triggering the detector to record a particle event.

in Fig. 3.3. These OAPs also measure the shadows cast by particles on a photodiode array; however, in contrast to the 2DS, the CIPs only record one image per particle with a 1-D linear detector. The CIPs have 64-photodiode arrays as detectors (Baumgardner et al. 2001) and are often used to corroborate 2DS measurements. They are also useful for viewing particles with 3-level grey-scale imaging intensity (CIP15) or focusing on the subset of very large particles (CIP100). 3-level imaging intensity is achieved with the CIP15 by logging particle events when the shadow cast at the photodiode array reaches 25%, 50%, and 75% of the background level. The 2DS and CIP100 do not possess this feature and a threshold reduction of 50% is required for detection.

The 2DS, CIP15, and CIP100 have a high imaging cadence and a large sample volume, and provide measurements of size-resolved cloud particle number concentrations. Data processing was completed by H. Jones using in-house software; the Optical Array Shadow Imaging Software (OASIS). This software was developed by J. Crosier at the University of Manchester, and has been used in previous aircraft studies using the 2DS, CIP15, and CIP100 (e.g. Crosier et al. 2011, 2014; Taylor et al.

2016). OAP data were processed following the same methodology as Taylor et al. (2016) and the classification thresholds used are listed in Table 3.2. These processed data are used in the studies detailed herein.

The sample volume of the three OAPs varies with air velocity and sample area (particle size dependent) and was calculated using the 'Centre in' approach, following Heymsfield and Parrish (1978). The data processing software identifies each particle centre and traces the particle edge from this point through 360 °. This provides a quantitative measure of the asphericity, which can be subsequently used for particle phase discrimination.

The 2DS, CIP15, and CIP100 image with 10, 15, and 100 µm resolution respectively; resolution which allows for the segregation of cloud particles into small and low, medium, and high irregularity categories (see Table 3.2). Examples of these include cloud droplets, large drizzle drops, plate-like ice crystals, and dendrite ice crystals respectively. Division into such categories is based upon the particle circularity: circularities closer to 1 are less irregular (and more likely to be large droplets or drizzle) than larger values (likely ice crystals). This circularity parameter, C, is derived from the measured particle area, A, and perimeter, P (Crosier et al. 2011):

$$\mathrm{C} = \frac{\mathrm{P}^2}{4\pi\mathrm{A}} \tag{3.1}$$

Segregation is more efficient with the high resolution 2DS and CIP15 data than the lower resolution CIP100 data. Particle categorisation using the 2DS and CIP15 data is also dependent on size, as phase discrimination is not possible with small particles (<80 µm) due to the instruments' low resolution in this limit. Similarly, particles imaged at the edges of the array are segregated into separate categories (Edge, Table 3.2). The number concentration of these particles can be distinguished; however, these particles cannot be included in any size-resolved figures, such as number size distributions, as they are only partially imaged and therefore their full size and shape is not known. In Chapters 5 and 6, ice number concentrations were represented by the sum of the MI and HI categories (see Table 3.2). Additionally, number concentrations of large edge (EL, Table 3.2) particles were added to the total ice number. These data were constructed on a case-by-case basis, and particle images in each category were consulted to ascertain whether the particles were, by

Table 3.2: *Adapted from* Taylor et al. (2016) Table A1: Optical array probe data processing thresholds for classification using the Optical Array Shadow Imaging Software. 50 pixels corresponds to approximately 80 µm. Edge rejection removes particles touching the edge of the imaging array, as size data of these particles are not accurately known.

Category	Abbreviation	Area (pixels)	Circularity	Edge rejection
Small	S	< 50	All	On
Low irregularity	LI	≥ 50	< 1.2	On
Medium irregularity	MI	≥ 50	< 1.2-1.4	On
High irregularity	HI	≥ 50	> 1.4	On
Edge small	ES	< 50	All	Only edge
Edge large	EL	≥ 50	All	Only edge

majority, ice crystals.

The wing-mounted CDP, 2DS, CIP15, and CIP100 were modified to include anti-shatter tips during the ACCACIA campaign. Large cloud particles may break easily on the probe housing whilst travelling at aircraft velocities, producing artificially enhanced particle number concentrations at smaller sizes from the detection of these shattered artefacts. Anti-shatter tips were utilised (Fig. 3.4, Korolev et al. 2013) to minimise this effect. Additionally, inter-arrival time (IAT) analyses were carried out with the 2DS, CIP15, and CIP100 data: three 20 second intervals of high particle number concentrations were chosen, and figures of counts detected versus IAT were constructed (Crosier et al. 2011) similar to Field et al. (2006). Artefacts manifest as a mode at small IATs, where numerous particles have arrived at the detector in quick succession. Informed by these data, IAT thresholds were imposed to exclude these artefacts from the processed data. The applied thresholds were 2×10^{-6}, 1×10^{-6}, and 1×10^{-4} seconds respectively for the 2DS, CIP 15, and CIP 100 data. The latter threshold is greater due to an increased likelihood of the large particles imaged by the CIP100 colliding with the probe and breaking.

Data obtained using the Cloud Particle Imager (CPI, SPEC Inc., Lawson et al. 2001) are not used quantitatively in Chapter 5; however, the 2.3 µm spatial resolution, 8-bit images of cloud particles are used. This instrument measures cloud particles from 15 µm to 2500 µm. The high resolution of the CPI allows for phase

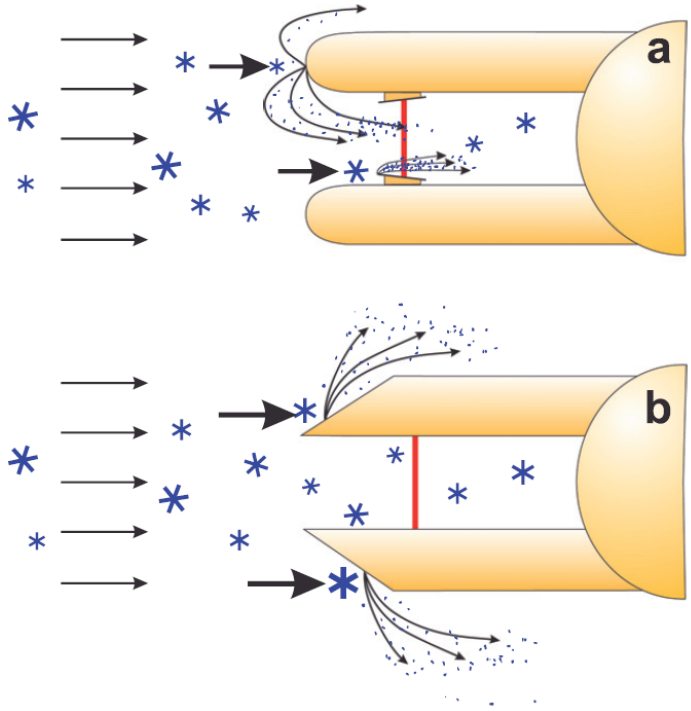

Figure 3.4: Korolev et al. (2013) Fig. 1: Schematic representation of anti-shatter Korolev tips. Arrows indicate the direction of air flow. **(a):** Large ice crystals (for example, dendrites) can impact the instrument housing when sampled and shatter into numerous pieces. Each of these small pieces could be counted as a cloud particle in this scenario, yet they would arrive at the detector in quick succession. **(b):** With the use of Korolev tips, the likelihood for measured crystal shattering is reduced, as artefacts are directed away from the detection system.

discrimination between liquid and ice, and the habit classification of ice crystals. Some error in phase identification can present at small sizes, where astigmatism in the imaging system can cause a spherical cloud droplet to appear slightly irregular, thus resulting in its categorisation as ice. Quantitative number concentrations are not used as the CPI has a small sample volume, causing artificially-high particle number concentrations in regions of low ambient concentrations (Lawson et al. 2001). For comparison, the maximum sample volume of the CPI is $0.006\,\mathrm{L\,s^{-1}}$ (Lawson et al. 2001), whereas the 2DS sample volume is $16\,\mathrm{L\,s^{-1}}$ at $100\,\mathrm{m\,s^{-1}}$ (Lawson et al. 2006). The larger sample volume of the 2DS therefore produces better particle counting statistics. As a result, the low ice number concentrations measured by the 2DS, CIP15, and CIP100 discussed in Chapters 5 and 6 were artificially enhanced by the CPI; therefore, these data are not used quantitatively in the studies detailed herein.

Aerosol

Data from the Passive-Cavity Aerosol Spectrometer Probe (PCASP 100-X, DMT, Rosenberg et al. 2012) are used in Chapters 4, 5, and 6. This optical particle counter (OPC) measures the size distribution of accumulation-mode aerosol particles of sizes 0.1 µm to 3 µm. The PCASP functions in a similar way to the CDP by optically detecting particles using scattered laser light.

Also mounted on the aircraft's wing, the PCASP samples air through an inlet. Aerosol particles are dried through heating in the internal cavity and then passed through to the imaging chamber (Collins et al. 2011). Light scattered by the interaction between the sampled particles and the imaging laser is then measured. Light scattered through 35°–120° is collected for detection (Rosenberg et al. 2012), where the intensity and direction of light scattered is influenced by particle size, shape, and refractive index (Collins et al. 2011). Corrections for these issues require compositional knowledge of the particles sampled; information that is often not available. These dependencies introduce uncertainty into the measured aerosol particle size distributions (Rosenberg et al. 2012); therefore, size calibrations using synthetic polystyrene latex (PSL) beads are conducted.

The Cloud Aerosol Spectrometer with Depolarisation (CAS-DPOL[1], DMT, Baumgardner et al. 2001; Glen and Brooks 2013) is also used in Chapters 4 and 5 to provide number concentrations and size distributions of aerosol and cloud particles from 0.6 µm to 50 µm.

The CAS-DPOL functions differently to the OAPs (2DS, CIPs) and the OPCs (PCASP, CDP): particle information is derived from linearly-polarised laser light scattered in both forward (4° to 12°) and backward (168° to 176°) directions. Four detectors – two forward-facing and two backward-facing – are used, as shown in Fig. 3.5. One forward-facing detector has a qualifier mask – like the CDP – to only count those particles within the specified depth of field, whilst the other measures total intensity. One of the backward-facing detectors measures linearly polarised light, whilst the other, again, measures total intensity.

Particle-by-particle data is recorded alongside the bulk concentration and sizing

[1]Studies often refer to this instrument using various names; for example, it is also often called the Cloud Aerosol Spectrometer with Polarisation (CASPOL).

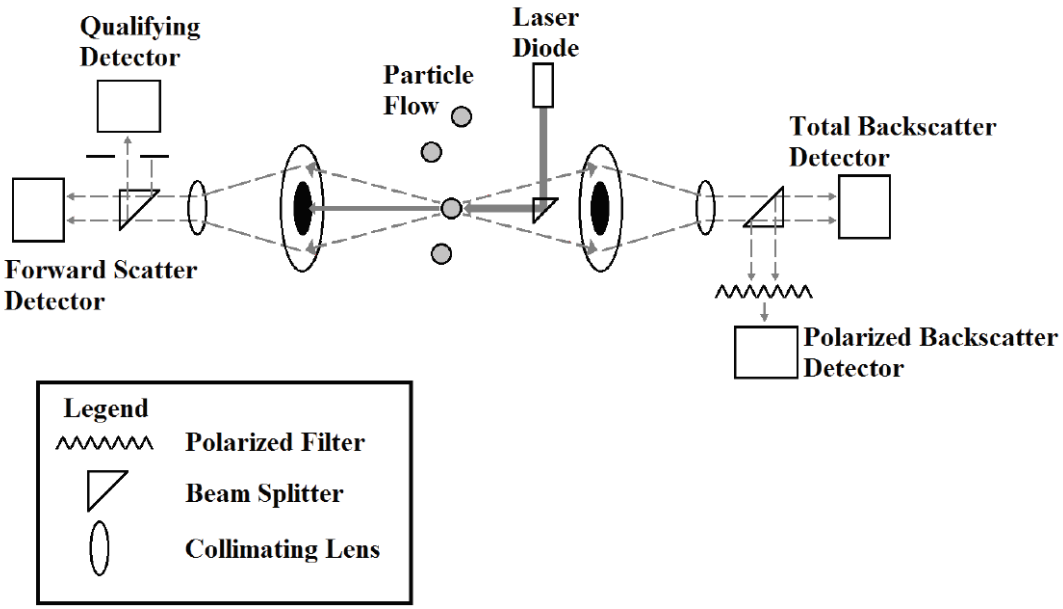

Figure 3.5: Glen and Brooks (2013) Fig. 1: Schematic of the Cloud and Aerosol Spectrometer with Depolarisation (CAS-DPOL). Dotted lines indicate the direction of light scattered during a particle detection event: light, in both forward and backward directions, is focused through collecting and collimating lenses on to four separate detectors.

information, allowing both the large- and small-scale properties of the aerosol population to be deduced (Glen and Brooks 2013). By also measuring the backward-scattered (168° to 176°) light, one can infer particle asphericity via the ratio of polarised to total backscattered intensities (Glen and Brooks 2013; Nichman et al. 2016). These polarisation data are not used here; however, there is evidence that they may be used to make distinctions between spherical liquid droplets and irregular ice crystals (e.g. Nichman et al. 2016).

3.2 Scanning Electron Microscopy (SEM)

Scanning electron microscopy (SEM) was used to analyse polycarbonate filters exposed from the FAAM BAe-146 aircraft in Chapter 4. The filtration system on the aircraft has been used in previous campaigns (e.g. Chou et al. 2008; Formenti et al. 2008), and follows the same design as the system used previously on the UK Met Office C-130 aircraft (Andreae et al. 2000).

Air is sampled through a specially-modified inlet which splits into a curved

tube, leading towards the cabin and filter system, and a straight bypass tube. This system was designed to remove large particles (including large aerosol particles and cloud droplets) from the air stream by inertial separation (Chou et al. 2008). Sub-isokinetic conditions, where the airspeed within the inlet is less than that outside, are maintained throughout sampling. These conditions are thought to lead to a coarse-mode particle enhancement: when air slows within the inlet, fast-travelling large particles from behind the air stream may pass into the sampled volume, artificially enhancing the large particle number concentration (Chou et al. 2008).

Seven filter pairs exposed during the springtime ACCACIA campaign were analysed with scanning electron microscopy. Chapter 4 details the SEM analysis of these aircraft filters. This off-line analysis technique allows for the elemental composition of collected aerosol particles to be established. Each polycarbonate filter was cut into segments and analysed with a Philips FEI XL30 Environmental Scanning Electron Microscope with Field-Emission Gun (ESEM-FEG), coupled with energy-dispersive X-ray spectroscopy (EDS). Further details of this technique are included in Chapter 4.

Electron microscopy bombards each sample with a beam of high energy electrons, thus dissipating energy through the sample. Figure 3.6 illustrates the two main modes of detection – secondary electron (SE) or back-scattered electron (BSE) – which are based on two of the fundamental interactions which can occur. SEs result from the direct interaction between the electron beam and a low energy (usually K-shell) electron in an atom within the sample. The K-shell electron is liberated through the transfer of kinetic energy from the incident electron beam (Fig. 3.6**A**). The vacant hole in the K-shell is subsequently filled by an electron from a higher energy shell, and this de-excitation releases an X-ray (Fig. 3.6**B**). SEs can provide high resolution, topographical information due to their interaction with electrons near the sample surface; SEs cannot be detected from deep within the sample.

BSEs occur when electrons within the high energy beam are elastically-scattered through interaction with positive atomic nuclei within the sample (Fig. 3.6**C**). The direction of these electrons is almost completely reversed, sending them back towards the electron gun. BSEs travel further within the sample than SEs, and can provide compositional information due to the atomic interactions which occur. The

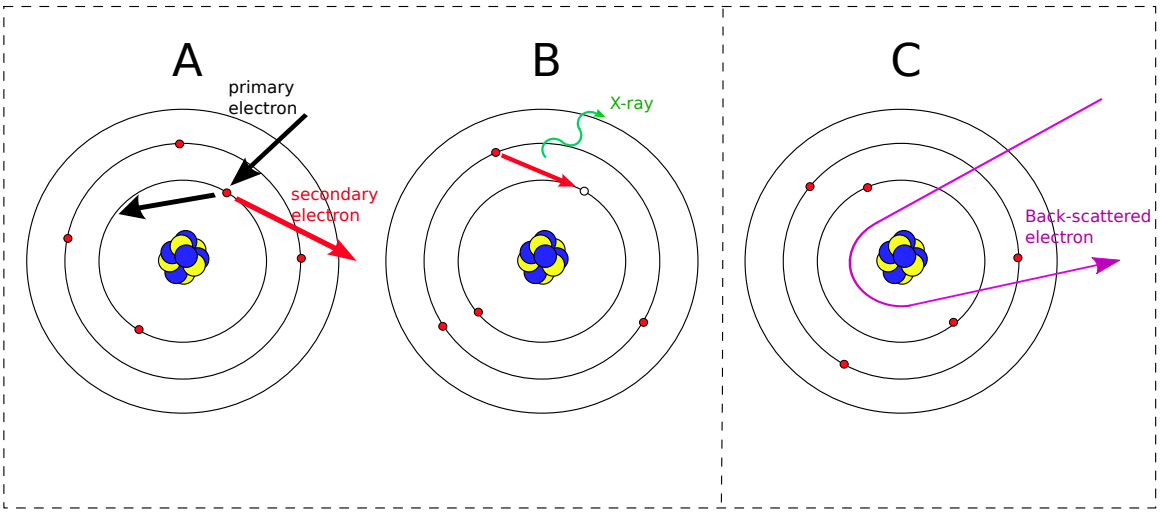

Figure 3.6: Schematic summarising the main processes which occur during SEM analysis. **A-B:** Incident primary electron transfers kinetic energy to K-shell (low energy) electron, liberating it from the atom. Electron from higher energy shell (L-shell in this case) de-excites to fill the hole left by the freed electron. De-excitation releases energy in the form of an X-ray, whose energy is related to the atom in question. **C:** primary electron elastically-scattered backwards by positive atomic nuclei. Electrons are represented by red circles, whilst protons and neutrons are shown by blue and yellow circles.

energy of BSEs is proportional to the atomic number of the elements measured, making the BSE mode a good option for the study of metallic elements (e.g. Fe, Cu). However, BSE mode produces a diminished resolution with comparison to SE mode as the electrons involved travel further within the sample.

A combination of SEs and BSEs are used to conduct elemental analysis alongside EDS. BSE detection mode provides good contrast between the particles and the background filter, allowing sound detection thresholds to be defined. The BSEs are used to define what is and is not a particle, then the electron beam bombards the identified particles with high-energy electrons. Sample electrons are then liberated and characteristic X-rays are released through the de-excitation of electrons from higher energy shells, through the pathway detailed in Fig. 3.6**A–B**. These X-rays are related to the atomic number of the element in question, and are measured using an EDS (Silicon) detector, producing an X-ray spectrum.

With EDS, two modes of particle coverage are available; core mode and centroid mode. Core mode analyses 70% of the identified particle area and computes a

mean spectrum, whilst centroid mode finds the particle centre and measures the X-ray spectrum from that point only. Core mode is a better option for heterogeneous, atmospheric aerosol particles and was therefore applied in the analyses detailed in Chapter 4. Automated particle analysis was carried out by moving the electron beam of the SEM through a pre-set grid. The beam was rastered over each particle, using the applied grey-scale BSE thresholds to distinguish particles from the filter substrate. Using BSE mode for threshold definition is preferred to SE mode as the thresholds can be better defined (through improved contrast in BSE mode). Analyses were conducted using two different magnifications: 1000× magnification, with 0.25 µm pixel size and 0.5 µm minimum particle size, and 4000× magnification, with 0.063 µm pixel size and 0.13 µm minimum particle size. This combination was chosen to give good sample coverage (>50 % at 1000× magnification) in addition to some data coverage of small particles (>0.13 µm at 4000× magnification).

The analyses detailed in Chapter 4 were conducted in hi-vacuum mode to minimise some known issues with this technique. Beam attenuation can occur if the chamber is at atmospheric pressure due to interaction with air molecules; therefore, a decreased chamber pressure is required when using a SEM. Lo-vacuum mode pumps water vapour into the sample chamber to promote interactions between the electron beam and the sample under a lower pressure, whilst hi-vacuum mode uses near-vacuum conditions and requires conductive samples. Sample charging can occur with SEM, and particles can be viewed to move and/or degrade if the sample becomes charged under electron bombardment. This artefact can occur more frequently with lo-vacuum mode; therefore, hi-vacuum mode was applied. The filter samples are not naturally conductive as they are made from a polycarbonate material; therefore, a carbon(graphite)-coating was applied and a copper ribbon was attached to each sample to allow for electrical conduction. This sample preparation ensured that electric charge did not accumulate on the sample surface, helping to minimise sample charging effects. Under such hi-vacuum conditions, the ESEM acts as a conventional SEM. Additionally, BSE mode is less prone to charging artefacts than SE mode, making it the more applicable choice for long analyses. Samples detailed in Chapter 4 were analysed overnight for ≥8 h.

In addition to charging and particle drifting, this technique is also prone to issues arising from particle topography and geometry. These are difficult to account for as particles with significant depth/height can cast shadows over the substrate if they are large enough. This may cause detection issues of any other particles falling within the shadow. Geometry corrections – the standardless ZAF corrections mentioned in Chapter 4 – assume the particles are homogeneous, smooth, and infinitely thick to the electron beam. These assumptions are typically not wholly accurate for atmospheric aerosol particles; therefore, some error is introduced to the morphological and compositional measurements made by the SEM-EDS system. This error contributes to the uncertainties attached to the compositional measurements; however, these complications are generally overcome by grouping particles into classifications, thus gaining statistical confidence.

The primary morphological properties computed by the EDS analysis include average diameter, shape, and aspect ratio. These are derived from the particle area measured by the EDAX^{TM} Genesis software, which itself is determined from the number of pixels illuminated per particle analysed. Particle diameter is calculated from this illuminated area: the number of pixels within the visible 2-D surface of each particle are summed and the average diameter is then deduced as the diameter of a circle with the equivalent area. As aerosol particles are seldom circular and are often irregularly-shaped, this approximation also carries some degree of error.

3.3 Large Eddy Model (LEM)

Large eddy simulations are used in Chapter 6 to investigate the performance of two established ice nucleation parameterisations, by comparing with in situ observations of Arctic mixed-phase clouds. Process models provide a detailed framework for the investigation of microphysical interactions, and such studies can be used to inform parameterisation development and testing strategies for larger-scale numerical weather prediction (NWP) models. Version 2.4 of the Large Eddy Model (LEM, UK Met Office, Gray et al. 2001) was used in Chapter 6 to achieve this. The LEM was operated on a multi-core computer system and was set up similarly to Connolly et al. (2013).

The LEM is an Eulerian, anelastic, non-hydrostatic 3-D model (Gray et al. 2001). Mass and momentum are conserved (Hill et al. 2014) following the Navier-Stokes equations; however, energy can be dissipated through diabatic processes, such as friction. Fluid density is stratified and decreases with increasing altitude. Cloud and boundary layer structure are simulated in isolation from large-scale meteorological features. Sub-grid atmospheric processes such as cloud microphysics, unresolved turbulence, and radiation are represented by parameterisations (Gray and Petch 2001). Prognostic variables – variables directly predicted by the model – include 3-D wind components (U, V, and W) and potential temperature perturbations, Θ'. The average wind speed from each case was imposed as the geostrophic wind forcing to maintain these wind components throughout each simulation (Connolly et al. 2013).

The LEM was initialised with the Θ, water vapour mixing ratio, and U and V wind components measured by dropsondes released during each case study. Cloud liquid water was initialised in the model with an adiabatic liquid water profile between the altitudes of the observed clouds in each case, as in Connolly et al. (2013). A damping layer was imposed at the top of the model domain to prevent vertically-propagating gravity waves from reflecting back off the model lid. This method of Newtonian damping reverts the prognostic variables, e.g. wind velocities or Θ perturbations, back to their respective horizontal mean values in this region (Gray and Petch 2001). Cyclical lateral boundary conditions were imposed in all simulations, producing pseudo-Lagrangian movement of the domain under the imposed wind fields. Every 150 seconds, the Edwards and Slingo (1996) long- and shortwave radiation scheme was called in the model. A sub-Arctic McClatchy profile was included to ensure the optical properties of the simulated atmosphere were representative of the region modelled: this profile is based on measurements of the emission and attenuation of radiation along a path in the atmosphere, and accounts for atmospheric temperature, pressure, and contributions from absorbing gases, such as water vapour and ozone (McClatchey et al. 1972).

A horizontal resolution of 120 m was applied in all LEM simulations, with a 16 km $\times$ 16 km grid size. The domain height was set to 3000 m, with a vertical resolution of 20 m between 0 m and 1500 m, and 50 m between 1500 m and 3000 m. This

domain structure was chosen as the temperature inversion in each case was below 1500 m; therefore, the cloud microphysics was likely to form in the high resolution region of the domain. This high resolution was not maintained for the full domain height due to computational cost. The chosen 3-D domain was split into slices and spread over multiple cores to quicken the processing time of the model.

In Chapter 6, model time steps were of the order of 0.3 seconds in each of the simulations presented. Three different surfaces were considered; namely, sea ice, marginal ice, and ocean. For the marginal ice and ocean cases, prescribed values of surface sensible and latent heat fluxes were imposed alongside a saturated surface to represent the ocean. The model converts the energy input by these initial conditions into temperature and moisture fluxes from the surface. These fluxes were absent from the sea ice case to restrict turbulent exchange from the surface and represent the influence of the frozen surface.

3.3.1 Microphysics

A bulk microphysical scheme is imposed in the LEM. These represent microphysical interactions as a function of a simulated parameter in the model. Each underlying particle size distribution is assumed to follow a given functional form, which can then be integrated analytically to calculate changes in bulk quantities (such as mass mixing ratio and number concentration). In contrast to spectral bin microphysics schemes, the particle size distribution is not prescribed and individual droplet activation and ice nucleation events are not tracked; instead, a bulk quantity is predicted based on the simulated thermodynamic properties.

Double-moment (both mass mixing ratios and number concentrations) ice crystals, snow, graupel, and rain are simulated in the LEM using the Morrison et al. (2005) microphysics scheme. Only single-moment (mass mixing ratios) water vapour and cloud droplets are represented. Prescribed droplet number concentrations of 100 cm^{-3} are simulated, such that any liquid mass that forms is evenly distributed amongst this concentration. Hydrometeors are quantified as scalar fields, with each hydrometeor class represented by a Gamma distribution:

$$f(D) = N_0 D^{p_c} e^{-\lambda D} \tag{3.2}$$

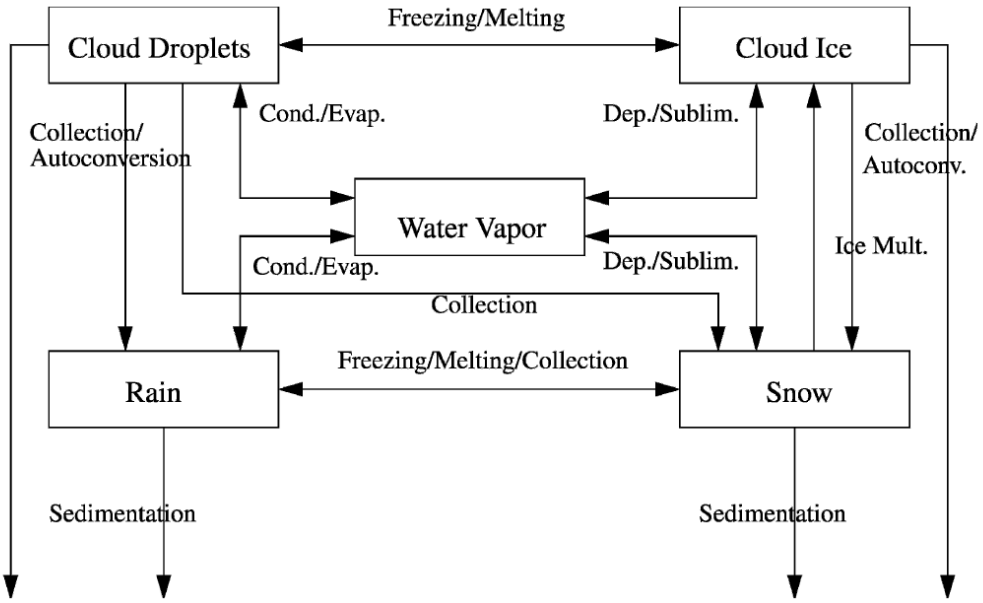

Figure 3.7: Morrison et al. (2005) Fig. 1: Flow diagram illustrating the different microphysical pathways of evolution represented by the Morrison bulk microphysics scheme.

where N_0 is the distribution intercept, D is the particle diameter, p_c is the spectral index (or, shape parameter) and λ is the slope of the distribution. The spectral index is a function of cloud and thermodynamic properties for droplets. This index is set to zero for cloud ice, rain, and snow; therefore, D^{p_c} simplifies to 1 (Morrison et al. 2005). Both N_0 and λ are calculated from the combination of these indices and the number concentration and mass mixing ratio of each hydrometeor.

Figure 3.7 summarises the physical interactions included in the Morrison bulk microphysics scheme. All hydrometeors are assumed to be spherical (Morrison et al. 2005). Microphysical processes such as primary production, auto-conversion between hydrometeors, and ice multiplication are represented (Morrison et al. 2005). Primary production relates to ice or droplet nucleation. In Chapter 6, the Cooper (1986) and DeMott et al. (2010) primary ice nucleation parameterisations are considered.

Coalescence between the droplet and rain classes is represented (Beheng 1994). The parameterisation scheme by Beheng (1994) partitions the total cloud liquid into droplet and rain categories, and applies the stochastic collection equation to simulate the evolution of the droplet spectrum. Coagulation of droplets to form rain (auto-conversion) or larger droplets (self-collection) and the growth of raindrops

through droplet collection (accretion) are considered by the scheme.

Auto-conversion also acts between the ice and snow classes via growth by diffusion (Harrington et al. 1995). The threshold diameter at which cloud ice transfers to the snow category is 125 µm (Harrington et al. 1995), and is limited to conditions which favour ice growth, i.e. ice supersaturation. Aggregation of ice and snow crystals (self-collection) is also represented, and follow Murakami (1990) for ice and Passarelli Jr (1978) for snow. Ice aggregation rates are modelled to be dependent on the number and mass of ice crystals present, their collection efficiencies, and their distribution of fall speeds (Murakami 1990). Snow aggregation is based upon an analytical model of stratiform clouds (Passarelli Jr 1978). Cloud droplets can also be depleted through collection by snow. Riming of frozen particles – either ice, snow, or graupel – is restricted to large sizes ($>$100 µm) only. Secondary ice multiplication is represented by the Hallett and Mossop (1974) rime-splintering relationship. For further information on the LEM or microphysics scheme, the reader is referred to Gray et al. (2001) and Morrison et al. (2005) respectively.

4 Size-segregated compositional analysis of aerosol particles collected in the European Arctic during the ACCACIA campaign

Young, G., Jones, H. M., Darbyshire, E., Baustian, K. J., McQuaid, J. B., Bower, K. N., Connolly, P. J., Gallagher, M.W., and Choularton, T.W.: Size-segregated compositional analysis of aerosol particles collected in the European Arctic during the ACCACIA campaign, Atmospheric Chemistry and Physics, 16, 4063–4079, doi:10.5194/acp-16-4063-2016, 2016.

This journal article was written by G. Young under guidance from H. M. Jones, P. J. Connolly, M. W. Gallagher, and T. W. Choularton. K. N. Bower, H. M. Jones, M. W. Gallagher, and T. W. Choularton were involved in the analysis planning. SEM analysis, subsequent data analysis, and research into both the technique and classification scheme were carried out by G. Young. Back trajectory analyses were carried out by E. Darbyshire. K. J. Baustian and J. B. McQuaid operated the filter sampling mechanism on the aircraft.

Atmos. Chem. Phys., 16, 4063–4079, 2016
www.atmos-chem-phys.net/16/4063/2016/
doi:10.5194/acp-16-4063-2016

Atmospheric Chemistry and Physics Open Access EGU

Size-segregated compositional analysis of aerosol particles collected in the European Arctic during the ACCACIA campaign

G. Young[1,*], H. M. Jones[1], E. Darbyshire[1], K. J. Baustian[2], J. B. McQuaid[2], K. N. Bower[1], P. J. Connolly[1], M. W. Gallagher[1], and T. W. Choularton[1]

[1]Centre for Atmospheric Science, University of Manchester, Manchester, UK
[2]School of Earth and Environment, University of Leeds, Leeds, UK
[*] *Invited contribution by G. Young, recipient of the EGU Outstanding Student Poster (OSP) Award 2015.*

Correspondence to: G. Young (gillian.young@manchester.ac.uk)

Received: 9 October 2015 – Published in Atmos. Chem. Phys. Discuss.: 29 October 2015
Revised: 10 February 2016 – Accepted: 8 March 2016 – Published: 29 March 2016

Abstract. Single-particle compositional analysis of filter samples collected on board the Facility for Airborne Atmospheric Measurements (FAAM) BAe-146 aircraft is presented for six flights during the springtime Aerosol–Cloud Coupling and Climate Interactions in the Arctic (ACCACIA) campaign (March–April 2013). Scanning electron microscopy was utilised to derive size-segregated particle compositions and size distributions, and these were compared to corresponding data from wing-mounted optical particle counters. Reasonable agreement between the calculated number size distributions was found. Significant variability in composition was observed, with differing external and internal mixing identified, between air mass trajectory cases based on HYbrid Single-Particle Lagrangian Integrated Trajectory (HYSPLIT) analyses. Dominant particle classes were silicate-based dusts and sea salts, with particles notably rich in K and Ca detected in one case. Source regions varied from the Arctic Ocean and Greenland through to northern Russia and the European continent. Good agreement between the back trajectories was mirrored by comparable compositional trends between samples. Silicate dusts were identified in all cases, and the elemental composition of the dust was consistent for all samples except one. It is hypothesised that long-range, high-altitude transport was primarily responsible for this dust, with likely sources including the Asian arid regions.

1 Introduction

The response of the Arctic environment to climate change has received increased interest in recent years due to the visible loss in sea-ice volume over the past 3 decades (e.g. Serreze et al., 2007; Perovich et al., 2008). The polar regions of our planet have a unique response to a warming atmosphere due to environmental characteristics vastly different to the mid-latitudes, including high surface albedo and strong variability in annual solar radiation. These factors cause the Arctic to respond to climatic changes at a heightened pace (Curry et al., 1996). The complexity of the Arctic environment requires detailed observations to further our understanding of the feedbacks and underlying processes involved; however, the ability to carry out such studies is hampered by the remote location, which is difficult for in situ investigation.

Existing numerical models do not effectively reproduce the changing Arctic environment. Discrepancies in forecasted sea-ice coverage, and predicted dates for 100 % loss, are due to a variety of uncertainties within the models themselves (e.g. de Boer et al., 2014). A key uncertainty in our ability to model how these changes will progress is in our representation of atmospheric aerosol–cloud interactions (Boucher et al., 2013). Aerosols play an important role in the Arctic radiative balance and their influence is thought to be amplified by the unique environmental conditions of this region (Quinn et al., 2007). The annual cycle of aerosol concentration in the Arctic varies significantly by season – with highs in spring of approximately 4–5 times that observed in late summer (Heintzenberg et al., 1986) – and such variabil-

ity impacts the microphysics of the mixed-phase clouds commonly observed (Verlinde et al., 2007).

The interaction of aerosol particles with clouds as ice nucleating particles (INPs) or cloud condensation nuclei (CCN) is dependent upon properties such as their size, hygroscopicity and composition (Pruppacher and Klett, 1997). Aerosol particles can therefore influence ice crystal or cloud droplet number, thus affecting properties such as droplet effective radius or cloud optical depth (Zhao et al., 2012); properties which significantly affect the net radiative impact of the cloud (Curry et al., 1996). The study of INPs has developed significantly in recent years via laboratory and field studies (DeMott et al., 2010; Hoose and Möhler, 2012). It is still not clear which properties of aerosol particles promote them to act as INPs in the atmosphere. They are generally thought to be insoluble, super-micron in size, have a similar molecular structure to ice (Pruppacher and Klett, 1997) and have the potential to produce chemical bonds with ice molecules at their surface (Murray et al., 2012). For example, mineral dusts are known INPs and are used regularly in laboratory studies of ice nucleation (e.g. Zimmermann et al., 2008; Connolly et al., 2009; Kanji et al., 2013; Yakobi-Hancock et al., 2013). Sources of these particles are not ubiquitous across the globe. Internally mixed particles can also act as INPs or (giant) CCN. A complex particle is difficult to clearly categorise as an INP or CCN as its nucleation will be heavily dependent on the environmental conditions. The presence of coatings on particles can also have a significant impact on their role in aerosol–cloud interactions. Coatings of soluble material could enhance CCN ability and promote secondary ice production via the formation of large cloud drops (Levin et al., 1996), whilst organic coatings could suppress the nucleating ability of an efficient INP (Möhler et al., 2008). It is not well understood which particles, in which mixing state and from which sources facilitate ice nucleation in the Arctic atmosphere.

Previous studies of Arctic aerosol have indicated that the population is primarily composed of organic material, continental pollutants (e.g. as sulfate or nitrate gases), crustal minerals and locally sourced species such as sea salt (Barrie, 1986; Hara et al., 2003; Behrenfeldt et al., 2008; Geng et al., 2010; Weinbruch et al., 2012). A wide range of sources contribute to this population and it is difficult to quantify the impact of different regions. Extended studies of Arctic aerosol have been conducted, which consider the differences in particle properties between seasons, showing that the annual cycle of aerosol particle composition (Ström et al., 2003; Weinbruch et al., 2012) and concentration (Ström et al., 2003; Tunved et al., 2013) is dominated by the influence of the Arctic haze (Barrie, 1986; Shaw, 1995). Between February and April, an influx of aerosol from anthropogenic sources becomes trapped in the stable Arctic atmosphere and persists for long periods of time (up to several weeks) before being removed by precipitation processes (Shaw, 1995). Spring in the European Arctic is routinely characterised by these high particle number concentrations, dominated by the accumulation mode, and low precipitation rates with comparison to summer, autumn and winter (Tunved et al., 2013). During this time, aerosol particles have the potential to interact with other species, grow and develop with a low chance of being removed from the atmosphere. This promotes an enhanced state of mixing (e.g. Hara et al., 2003), which compounds the difficulty in understanding how these particles interact with the clouds in the region. It is thought that the European continent is the primary source of this aerosol, with only small contributions from North America and Asia (Rahn, 1981); however, long-range transport from the Asian continent has been found to sporadically contribute to this phenomenon (Liu et al., 2015). Improving our understanding of the properties of these aerosol particles will help us to comprehend how they influence the clouds of the Arctic, and a strong method of achieving this is by identifying their chemical composition (Andreae and Rosenfeld, 2008).

By improving our knowledge of aerosol and cloud properties via in situ observational studies in the Arctic, it is possible to reduce the uncertainty associated with aerosol–cloud interactions (Vihma et al., 2014). To this end, the Aerosol–Cloud Coupling and Climate Interactions in the Arctic (ACCACIA) campaign was carried out in the European Arctic in 2013, utilising airborne- and ship-based measurements to collect a detailed data set of the Arctic atmosphere. The campaign was split into spring and summer segments, completed in March–April and July of 2013 respectively. During the spring section of the campaign, the Facility for Airborne Atmospheric Measurements (FAAM) BAe-146 atmospheric research aircraft was flown in the vicinity of Svalbard, Norway, with the capability of collecting in situ samples of aerosol particles on filters. This study presents the analysis of filter samples collected during this campaign, with a focus placed upon identifying the compositional properties and sources of the non-volatile, coarse-mode aerosol particles present in the atmosphere during the Arctic spring and inferring how these might interact with the cloud microphysics in the region.

Campaign overview

The springtime ACCACIA campaign flights were mainly conducted to the south-east of Svalbard, with the exception of flight B768, which was carried out to the north-west near the boundary with Greenland. Figure 1 details the science sections of each of the flights of interest, with direction from Svalbard to Kiruna, Sweden in all cases except B765. Corresponding dates are listed in Table 1.

As part of the springtime campaign, 47 mm diameter Nuclepore polycarbonate filters were exposed to ambient air from the FAAM BAe-146 aircraft to collect in situ samples of accumulation- and coarse-mode aerosol particles (sizes ~ 0.1 to $\sim 10\,\mu m$). Such particle sizes are approximately applicable to the study of CCN and INPs (Pruppacher and Klett, 1997). Analysis of one below-cloud

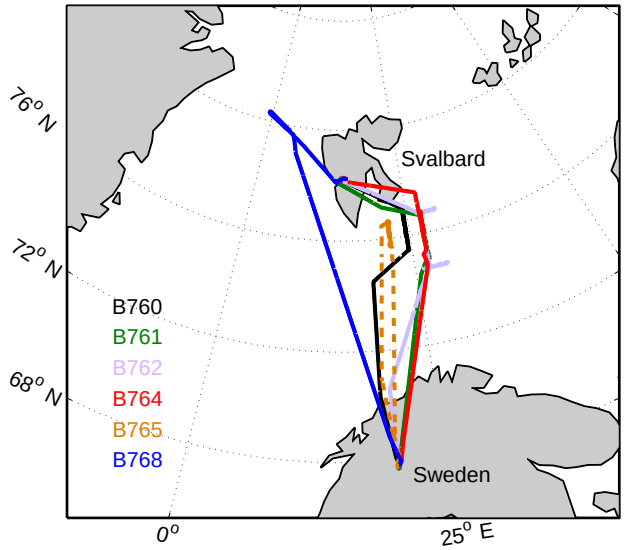

Figure 1. ACCACIA flight tracks of the main science periods undertaken for each flight where aerosol composition analysis was conducted.

set of filters from each case is shown, followed by a comparison between a below- and above-cloud pair from a single case study.

2 Methodology

2.1 Aircraft instrumentation and trajectory analysis

A range of cloud microphysics and aerosol instrumentation were used on board the FAAM BAe-146 aircraft to produce a detailed record of the observed Arctic atmosphere (as described by Liu et al., 2015; Lloyd et al., 2015). In this study, data from the Cloud Droplet Probe (CDP-100 Version 2, Droplet Measurement Technologies (DMT), Lance et al., 2010), the Cloud–Aerosol Spectrometer with Depolarisation (CAS-DPOL, DMT, Glen and Brooks, 2013) and the Passive Cavity Aerosol Spectrometer Probe (PCASP 100-X, DMT, Rosenberg et al., 2012) are used to provide context for and a comparison to the filter measurements. Throughout this article, the prefix *s* is imposed to represent number concentration measurements computed at standard temperature and pressure.

The accumulation-mode aerosol distribution was monitored by the PCASP. The CAS-DPOL measured both coarse-mode aerosol and, along with the CDP, cloud droplet number concentration. These externally mounted aircraft probes size and count their relative species via forward-scattering of the incident laser light through angles 35–120 and ∼ 4–12° (for both the CDP and CAS-DPOL), respectively. The PCASP measures particle concentrations and sizes in the range of 0.1 to 3 µm, the CAS-DPOL provides similar measurements from 0.6 to 50 µm (Glen and Brooks, 2013), and the CDP measures cloud droplets from 3 to 50 µm (Rosenberg et al., 2012).

Out of cloud, the CDP was used to provide an indication of the wet-mode diameter of coarse-mode ambient aerosol particles. The CAS-DPOL also measures coarse-mode aerosol concentrations when out of cloud. Within cloud, the liquid-water content (LWC) was derived from the observations of cloud droplet size. In this study, a LWC threshold of $\leq 0.01\,\mathrm{g\,m^{-3}}$, derived from CDP measurements, was employed to distinguish between out-of-cloud and in-cloud measurements. This threshold was applied to the CAS-DPOL, CDP and PCASP data to obtain an estimate of the ambient aerosol size distributions. These out-of-cloud observations are used in this study to validate the collection efficiency of the filter inlet system.

In addition to the in situ data gained from the instrumentation aboard the aircraft, back trajectory analyses were carried out to further contextualise the filter exposures. This was achieved using the National Oceanic and Atmospheric Administration HYbrid Single-Particle Lagrangian Integrated Trajectory (NOAA HYSPLIT 4.0) model (Draxler and Hess, 1998), in a similar manner to Liu et al. (2015). Horizontal and vertical wind fields were derived from GDAS reanalysis meteorology (Global Data Assimilation System; NOAA Air Resources Laboratory, Boulder, CO, USA) and used to calculate trajectories at 30 s intervals along the FAAM BAe-146 flight path. This analysis allows for the direction of the air mass to be inferred; however, it does not explicitly account for turbulent motions along the derived path and therefore carries a degree of uncertainty (Fleming et al., 2012). Trajectories dating back 6 days are presented to provide an indication of the source regions of the particles collected during the ACCACIA filter exposures.

Table 1. Details of FAAM flights undertaken during the spring segment of the ACCACIA campaign which had viable filter exposures. Corresponding filter case studies per flight are listed for reference.

Flight number	Date (2013)	Flight region*	Case studies
B760	21 Mar	South-east	1
B761	22 Mar	South-east	2
B762	23 Mar	South-east	3
B764	29 Mar	South-east	4,7
B765	30 Mar	South	5
B768	3 Apr	North-west	6

* With respect to Svalbard.

2.2 Filter collection

The filter collection mechanism on the FAAM BAe-146 aircraft comprises a stacked-filter unit (SFU), which allows for two filters (Whatman Nuclepore track etch membranes) to be exposed simultaneously to the air stream, allowing aerosol

particles to be collected on both. In the ACCACIA campaign, a combination of two filters with different nominal pore sizes was used in each exposure – a 10 µm pore filter was stacked in front of a 1 µm pore filter – allowing sub-micron aerosol particles that may pass through the pores of the first to be collected by the second.

The design of the inlet follows the same specifications as the UK Met Office C-130 aircraft filtration system described extensively by Andreae et al. (2000). Sub-isokinetic sampling conditions were maintained, potentially leading to a coarse-mode enhancement artefact (Chou et al., 2008). The design of the mechanism removes large cloud droplets from the sampled air using a bypass tube; therefore, contamination from droplets or rain is minimised (Chou et al., 2008; Johnson et al., 2012). Consequently, large particles (> 10 µm) are also thought to be removed from the collected sample, though the collection efficiency of the entire system is not known to have been formally quantified (Formenti et al., 2008; Johnson et al., 2012). Andreae et al. (2000) estimated the sampling efficiency of the inlet to be 35 % by mass for the coarse mode, with a 50 % cut-off threshold of ~ 3 µm (Formenti et al., 2003) and no losses identified for the accumulation mode. Chou et al. (2008) demonstrated that data collected via this inlet deviated from externally mounted particle counters above ~ 0.5 µm, after which the coarse-mode enhancement on the filter samples became evident. Additionally, the efficiencies of the filters themselves can be estimated: the 50 % cut-off diameter of the 10 µm Nuclepore filter is approximately 0.8–1 µm at the mean face velocity encountered during this study ($\sim 100\,\mathrm{cm\,s^{-1}}$) (John et al., 1983; Crosier et al., 2007), whilst the 1 µm filter has a 50 % collection efficiency at approximately 0.2 µm (Liu and Lee, 1976).

The filters were exposed on straight, level runs for approximately 10–30 min to obtain a sufficient sample for chemically speciated mass loadings. Although the filter system was designed to remove cloud droplets, the filters were primarily exposed out of cloud to further minimise the potential for contamination. Chosen filters were all exposed within the boundary layer (< 1000 m, see Table 2). Samples from below cloud were preferentially studied in this investigation (cases 1–6) as they likely included the main contributions of CCN and INPs at this time of year; however, one exposure from above cloud (case 7) is considered in Sect. 3.4.

2.3 Scanning electron microscopy

Using a Phillips FEI XL30 Environmental Scanning Electron Microscope with Field-Emission Gun (ESEM-FEG) in partnership with an energy-dispersive X-ray spectroscopy (EDS) system, automated single-particle analysis of the ACCACIA filter samples was undertaken at the University of Manchester's Williamson Research Centre (Hand et al., 2010; Johnson et al., 2012).

The coupled EDS system moves the sample stage through a pre-set grid to produce automated particle analysis of each sample. Particles are detected via the intensity of the backscattered electron signal. Grey-scale thresholds were set to identify particles under contrast with the background filter. The electron beam was then rastered over 70 % of the detected particle surface to produce an X-ray spectrum: relative elemental weight percentages of elements from C to Zn were recorded from the spectrum, measured and fitted with the EDAX™ Genesis software. For each measurement, standardless ZAF corrections were applied; corrections relating to atomic number, absorption and fluorescence. Parameters chosen for this analysis are listed in Table 3. A carbon-coating was applied to each sample to allow high vacuum mode to be used. The minimum particle sizes detectable by each scan correspond to 4 pixels in the given image and are listed in Table 3. The total number of particles scanned by the seven cases presented in this study is also listed in Table 3.

To act as a calibration, a blank filter pair was also analysed as Nuclepore filters have been shown to carry contaminants (Behrenfeldt et al., 2008). These were taken aboard the aircraft and treated similarly to the exposed filters. A small number of particles were identified: these appeared almost transparent under contrast and the majority produced a spectrum similar to the background filter. There was also a notable metallic influence and some particles were found to have moderate Cr or Fe fractions. These particles were found to be few in number and so should not greatly affect the outcome of this analysis.

Previous studies (e.g. Kandler et al., 2007; Hand et al., 2010; Formenti et al., 2011; Weinbruch et al., 2012) have shown that there are limitations to consider with this technique. The polycarbonate filters used during ACCACIA contaminate measurements of C and O in each particle detected. Studies using these filters have excluded C and O from their analysis to combat this issue (e.g. Krejci et al., 2005; Behrenfeldt et al., 2008; Hand et al., 2010). In this study, approximate thresholds of C and O are used to identify carbonaceous and biogenic species. However, only elements with $Z > 11$ (sodium) are used precisely within the classification scheme for the compositional analysis presented.

The electron beam produced by the scanning electron microscope (SEM) can negatively interact with some particle species, causing them to deform (Behrenfeldt et al., 2008). This is caused by the evaporation of the volatile components of the particles, either under the electron beam or as a result of the high vacuum (Li et al., 2003; Krejci et al., 2005). Little can be done to prevent this and it is difficult to manage when applying automated particle analysis. Behrenfeldt et al. (2008) found that this phenomenon only had a small impact on their results and could be disregarded. As a result, it can be assumed that the particles analysed by this method are dry and that any volatile components will have evaporated (Li et al., 2003).

Table 2. Summary of sampling conditions during each filter exposure. The geographic positions are also listed. Values quoted are arithmetic means, with 1σ in brackets where appropriate. In situ temperature data were collected with a Rosemount de-iced temperature sensor and the relative humidity (RH) data were derived from Buck CR2 hygrometer measurements.

Case	Conditions sampled	Exposure length (s)	Volume of air ($s\,dm^{-3}$)	Latitude (° N)	Longitude (° E)	Altitude (m)	Temperature (°C)	RH (%)
1	Clear	600	2312.3[b]	76.2	24.5	102 (5)	−11	91.9
2	Clear[a]	1700	2608.4	76.4	26.5	238 (107)	−8	96.8
3	Cloud haze	660	826.4	76.8	28.0	375 (5)	−18	108.4[c]
4	Clear[a]	540	754.8	76.6	27.2	91 (86)	−9	97.4
5	Clear	961	1249.3	76.2	22.0	71 (18)	−9	96.5
6	Clear	240	272.7	79.9	2.8	98 (44)	−8	95.3
7	Clear	720	1080.2	76.4	27.1	833 (59)	−13	86.9

[a] Filter was collected mostly under clear conditions, although some in-cloud sampling was encountered at the end of the exposure. [b] The total volume of air sampled during case 1 is high given its exposure length due to higher-than-average flow rates applied during that flight.
[c] Contaminated measurement, likely due to condensation on detection surface.

Table 3. Main parameters applied with SEM and EDAX™ Genesis software to carry out analysis of the ACCACIA aircraft filters.

SEM/EDAX™ Genesis analysis parameters		
Beam voltage (kV)	15	
Working distance (mm)	10	
Operating current (µA)	∼ 200	
Beam spot size	4	
Image resolution (px)	1024 × 800	
Total number of particles	139 630	
Magnifications applied	4000×	1000×
Filters analysed	1 and 10 µm	10 µm
Min. particle size (µm)	0.13	0.52
Field sizes (mm)	0.059 × 0.046	0.237 × 0.185

There are also several implicit factors, which may contribute some degree of uncertainty to the quantitative composition measurements gained. For example, errors can be introduced by uncertainties in the spectral fitting of the EDAX™ software (Krejci et al., 2005) or from the differing geometries of the individual particles measured (Kandler et al., 2007). Also, compositional data for particles less than 0.5 µm suffer from increased uncertainty (Kandler et al., 2011). The sample sizes considered here were too large to consider individual corrections; therefore, the measurements from the EDS analysis were taken as approximate values. Similarly, manual inspection of the images and spectra was not feasible due to the sample size and so an algorithm was imposed to remove any filter artefacts. These were typically a result of the software misclassifying the filter background as a particle itself and therefore displayed only the distinctive background signature. This background spectrum presented different characteristics than those considered to be carbon based; the artefacts were noisy, with very low detections in all but a few of the elements, whereas the particles thought to be carbonaceous displayed zero counts in some elements as expected. The fraction of detected particles removed by this algorithm was typically low (∼ 4–5 %), yet it is not possible to conclude if any real particles were removed. Krejci et al. (2005) placed an estimate of the total error involved with this technique to be around 10 % and found this value to be dependent on the sample and elements analysed.

2.4 Classifications

Elemental information gained from EDS analysis was taken further to identify particle species relevant to the atmosphere. The classification scheme applied in this investigation was derived from a variety of sources (e.g. Krejci et al., 2005; Geng et al., 2010; Hand et al., 2010); however, it is most prominently based upon the detailed scheme presented by Kandler et al. (2011). This scheme is detailed in Table S1.

2.4.1 Carbonaceous and biogenic

Approximate thresholds of C and O were utilised to distinguish carbonaceous and biological particles (Mamane and Noll, 1985). This approach has been adopted by other studies that applied a polycarbonate substrate (e.g. Kandler et al., 2007; Behrenfeldt et al., 2008; Hand et al., 2010). For example, particles included in this category could be soot particles or pollen grains (Behrenfeldt et al., 2008). Soot has been previously identified by introducing other properties into the classification process; for example, Hara et al. (2003) and Hand et al. (2010) categorised it via its characteristic chain-aggregate morphology. Due to the sample size, inspection of particle morphologies was not feasible in this study; therefore, carbonaceous particles were not specifically categorised.

Carbonaceous and biogenic particles have been segregated using compositional information in previous studies. Mamane and Noll (1985) measured distinctive small peaks in P, S, K and/or Ca with a dominating C influence in pollen grains. Similarly, Geng et al. (2010) utilised a comparable

threshold, also considering small amounts of Cl, S, K, N and/or P as indicators for biogenic species as these elements are important nutrients for plant life (Steinnes et al., 2000).

The carbonaceous and biogenic classifications likely include particles that may have some volatile component, which cannot be measured by this technique (see Sect. 2.3). The partial or complete evaporation of these particles therefore renders the presented fraction a lower limit; i.e. only the non-volatile cases could be measured. Coupled with the difficulty of distinguishing these particles from the filter background, it is important to note that the fractions of carbonaceous and biogenic classes presented by this study are approximations which are likely underestimating the true organic loading on these filters.

2.4.2 Sulfates, fresh and mixed chlorides

Sodium chloride (NaCl) from sea salt can enter the atmosphere as a consequence of sea-surface winds and these particles remain predominantly Na- and Cl-based for a short period of time. The lifetime of Cl is hindered by the tendency of these particles to accumulate sulfate in the atmosphere, thus producing particles primarily composed of Na–S (Hand et al., 2010). Due to this short lifetime, its presence is often used to indicate a fresh contribution from the sea surface (Hand et al., 2010). It is a common conclusion that a lack of Cl-containing particles and/or a significant fraction of S in a particulate sample is suggestive of aged aerosol (Behrenfeldt et al., 2008; Hand et al., 2010).

Aerosol containing S can infer an anthropogenic influence in a sample, as they are thought to have undergone a reaction with sulfur oxides (Geng et al., 2010). However, the Arctic Ocean is a natural source of dimethylsulfide (DMS), a gas which can also interact in the atmosphere to form sulfur dioxide. The contribution of this source is greater during the summer months due to decreased sea ice (Quinn et al., 2007), and is thought to have little influence during the dates of this study. The gas source cannot be concluded here but it can be stated that Na–S particles will have been present in the atmosphere for a sufficient length of time to allow for the interaction to take place.

The mixed chlorides category requires that particles must still be predominantly Na- and Cl- based, with a notable S contribution. This category also accounts for metallic contributions to the base NaCl species. The sulfates and fresh chloride categories are limited to the extremes of this distribution, with only S- and Cl-dominated signatures allowed respectively.

2.4.3 Silicates, mixed silicates, Ca-rich and gypsum

Complex internal mixing in particles is often indicative of a natural origin (e.g. Conny and Norris, 2011; Hoose and Möhler, 2012); however, coagulated particles can also be produced by high-temperature anthropogenic activities. A strong method of sourcing internally mixed particles involves the identification of Si: particles consisting of this element and various mixed metals are likely to be naturally occurring mineral dusts, and industrial by-products may lack this element in high quantities (Conny and Norris, 2011). Mineral dusts are typically composed of a variety of elements and tend to include significant fractions of Si and Al, with more minor contributions from Na, Mg, K, Ca and/or Fe amongst others.

Dusts are crucial constituents of the aerosol population as they are proven INPs (Zimmermann et al., 2008; Murray et al., 2012; Yakobi-Hancock et al., 2013). However, they can also act as CCN; for example, Ca-based dusts have been shown to form hygroscopic particles after reaction with nitrates in the atmosphere (Krueger et al., 2003). The springtime concentrations of nitrates in the Arctic (measured at the Alert sampling station in Canada) followed an increasing trend over 1990–2003 (Quinn et al., 2007), suggesting it is probable that this interaction could take place in this environment. Alternatively, internally mixed particles consisting of dusts, sulfates and sea salt can act as giant CCN (Andreae and Rosenfeld, 2008). In this study, the presence of such particles may be inferred by the detection of S or Cl with the typical dust-like signatures. This can occur if the dust in question has been transported over long distances and thus undergone cloud processing or acidification reactions (Mamane and Noll, 1985; Behrenfeldt et al., 2008). Or, more simply, these could be the result of a sea salt or sulfate coating on a mineral dust particle, and such mixtures have been modelled to have significant effects on warm clouds by augmenting the CCN population (Levin et al., 2005). Complex internal mixtures containing Si, S and/or Cl are therefore indicated in this study under the classification mixed silicates.

The mineral phase of aluminosilicates cannot be identified using the EDS method as these particles are closely related compositionally. The specific phases of dusts observed in SEM studies are often not quantified for this reason (Kandler et al., 2007; Hand et al., 2010). Instead, the individual X-ray counts and ratios between the elements measured were considered to classify their sampled particles into approximate groups such as silicates and carbonates. It has often been considered that Al, Ca and K are indicative of aluminosilicates (such as kaolinite), carbonate minerals such as calcite ($CaCO_3$) and dolomite ($CaMg(CO_3)_2$) – and clays/feldspars respectively (Formenti et al., 2011). Due to the lack of a quantitative C measurement, carbonate minerals were inferred from their Ca and Mg abundances in this study. Some mineral classes have a distinct elemental relationship and these can be classified; for example, gypsum ($CaSO_4 \cdot 2H_2O$) samples typically do not deviate from their base chemical formulae (Kandler et al., 2007). By this reasoning, gypsum was included as its own classification, whereas the vast majority of mineral dusts observed were grouped into the silicates, mixed silicates and Ca-rich categories, dependent on the relative quantities of Si, S and Ca they contained.

2.4.4 Phosphates and metallics

These groups include particles with significant influences from P and transition metals. Particles classified as phosphates in this study may include those composed of apatite – a Ca- and P-based mineral group – as factories which process these minerals are common in the nearby Kola Peninsula, Russia (Reimann et al., 2000).

The presence of transition metals can be viewed as an indicator for an industrial origin (Weinbruch et al., 2012). Potential local anthropogenic sources for the metallic particles include the coal burning facilities on Svalbard (in Longyearbyen and Barentsburg) or various metal smelters in the Kola Peninsula, Russia (Weinbruch et al., 2012). The metals included in the EDS analysis were Ti, Cr, Fe, Ni, Cu and Zn. Contributions from these may be attributable to anthropogenic and/or natural sources and could be in the form of metal oxides or constituents of complex minerals (Hand et al., 2010). Of those measured in this study, Fe and Al are the most likely to originate from a variety of sources as they are processed widely (Steinnes et al., 2000) and are common constituents in silicate-based dusts. Similarly, Zn may also be associated with biological material in addition to smelting emissions (Steinnes et al., 2000).

2.4.5 Biomass tracers

This group was introduced out of necessity given the results obtained. The other classifications were expected from hypothesised local sources; however, this group was introduced to account for the high quantity of K-based particles observed in one of the flights. These particles have negligible measurements of Si and are not thought to be mineralogical in nature. This category has been dubbed "biomass tracers" as several studies (e.g. Andreae, 1983; Chou et al., 2008; Hand et al., 2010; Quennehen et al., 2012) have identified particles sourced from biomass burning events to be rich in this element. These K-rich particles have been found to be prominent in forest fire and anthropogenic combustion emissions. It is unlikely that such particles could be sourced in the Arctic; therefore, their presence may infer transport from elsewhere (Quennehen et al., 2012). Biomass burning produces particles known as bottom ashes, which differ from the fly ash particles that are typically emitted during fossil fuel incomplete combustion processes (Umo et al., 2015). Activities which may produce these constituents could include firewood or agricultural burning (Andreae, 1983), or wildfires in warmer climates (Seiler and Crutzen, 1980).

2.4.6 Other

Particles which are not classified by the applied scheme are classed as other. The implication is that these particles are mixed. Figure 2 illustrates the difficulty with mixed particles; though local sites on the particle may be dominated by certain elements, the SEM analysis does not provide a spatial map of the elemental distribution across each particle surface.

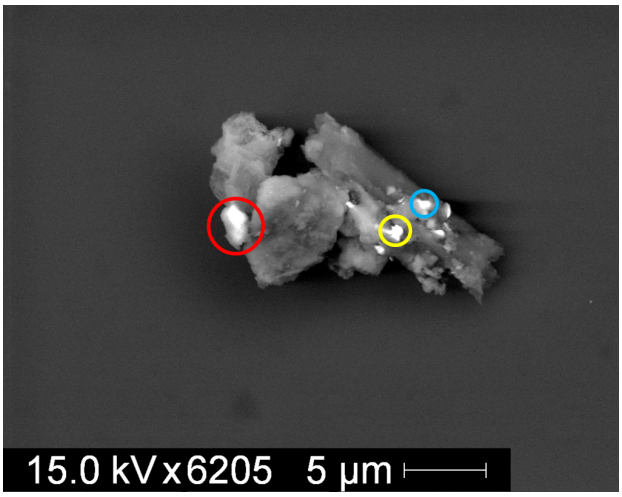

Figure 2. Mixed particle from case 5. The circles denote the spots scanned to give the following dominating elements: Red – Fe, Si and Al; Yellow – Fe, Cr, Ni, Si and Al; Blue – Fe, Cr, Ca, Cl, S, Si and Al. Scan of full particle indicates Si dominance.

Mixed particles are typically either unclassified or classified by their most abundant elements. The particle illustrated in Fig. 2 would be classified as a silicate dust as it is mixed but has a dominating Si influence. The size of the samples prevent manual inspection of every unclassified particle; therefore, the abundance of mixed particles within a data set must be inferred from the quantity quoted as "Other".

3 Results

3.1 HYSPLIT back trajectories

Air mass histories were calculated using HYSPLIT for each of the filter exposures to provide context with the environmental conditions in which they were sampled. Figure 3 shows the spatial extent of these trajectories in the top two panels and the mean altitudes covered are displayed in the bottom panel.

The mean altitude of the trajectories remains within the lower 1.5 km of the atmosphere. The modelled altitude typically increases with increased time backwards. Case 5 is the exception to this trend, as consistent low-altitude trajectories are modelled for the full duration shown. Also, the majority of these trajectories are reasonably smooth; however, a significant descent in height is modelled in case 4 at approximately −2 days.

A north-easterly wind was observed for cases 1 to 3, bringing air from over the dense Arctic sea ice to the region of interest to the south-east of Svalbard. When extended back

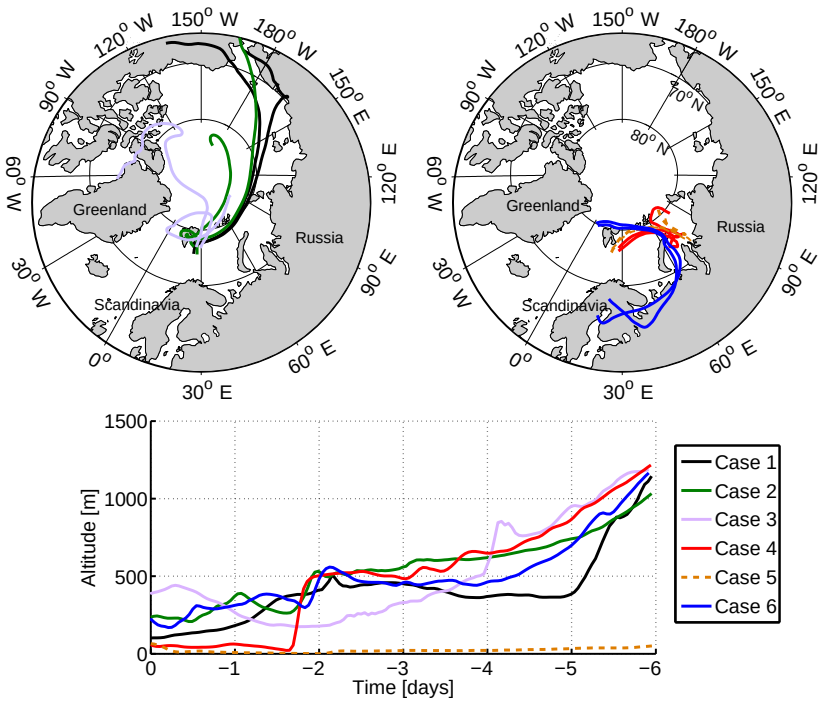

Figure 3. HYSPLIT air mass back trajectories for cases 1–6, initialised at the aircraft's position and calculated 6 days backwards. Trajectories at the beginning and end of each exposure are shown. Top left panel: cases 1 (black), 2 (green) and 3 (purple); top right panel: cases 4 (red), 5 (orange) and 6 (blue). The mean altitude covered by each of these trajectory groups is shown in the bottom panel.

by 6 days, differences between the air mass histories can be seen. From Fig. 3, cases 1 and 2 show some similarities, with the latter displaying more curvature anticlockwise than the former. Trajectories from case 3 are distinct from these two, with cyclonic curvature around the immediate vicinity of Svalbard and Greenland.

There is a clear partition in the direction of the trajectories as the spring campaign progressed. The first three exposures had source regions to the north and west of the exposure locations, whilst the latter three primarily sampled from the east. These latter trajectories are also more compact than the first three cases (Fig. 3). The air from cases 4 and 5 is traced back across the northern coast of Russia, whilst case 6 covers both the northern coast of Russia and Scandinavia. A large portion of these trajectories are clustered towards the continent, suggesting a strong influence from this region.

These two trajectory groups can be dissected further; two specific pairs can be identified (cases 1 and 2; 4 and 5), which display similar paths, and cases 3 and 6 appear unique in comparison. Overall, there appears to be a clear shift in the source region of these boundary layer exposures as the campaign progresses; from over the dense Arctic sea ice, through Greenland and northern Russia to the European continent.

3.2 Aerosol size

To investigate any issues with inlet collection efficiency (see Sect. 2.2), size distributions from the filter data were constructed and compared with arithmetic means of the wing-mounted probe data over each exposure period. Number size distributions were computed similarly to Chou et al. (2008); namely, the total number of particles detected in each scan was normalised by the area covered and total volume of air sampled, then scaled to the full filter area. Figure 4 illustrates these comparisons for each below-cloud filter pair analysed. Data from the PCASP, CAS-DPOL and CDP instruments are shown for comparison. These data use the standard scattering cross sections for the aircraft probes and no refractive index corrections were applied due to the expected mixed aerosol population.

Agreement between the filter-derived and the probe data appears dependent on the conditions sampled. For example, case 3 was exposed during a section where cloud haze was encountered, whereas cases 1, 5 and 6 were cleanly exposed out of cloud. Cases 2 and 4 sampled small amounts of cloud at the end of their exposures – at which point the probes measured some amount of cloud droplets and/or swollen aerosol particles – therefore, the probe distributions differ somewhat from the filter-derived particle distributions. Mean relative humidity (RH) values (Table 2) from each exposure were high (> 90 %) and the disagreement between filter and probe

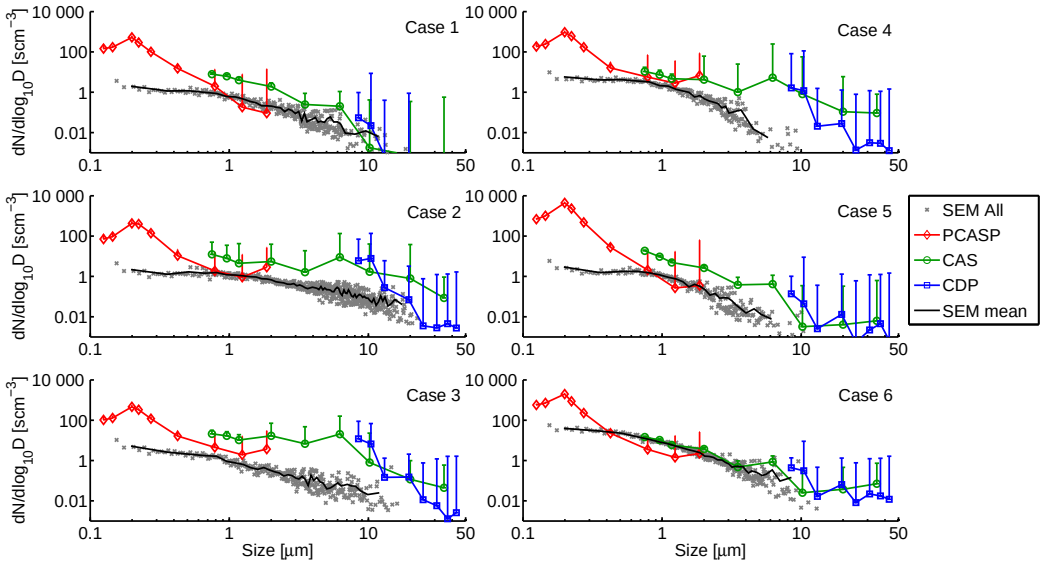

Figure 4. Size distributions ($dN/dlog_{10}D$) of particle data obtained via SEM analysis compared with averaged distributions from the optical particle counters at the relevant filter exposure times. Number concentrations are quoted with standard temperature and pressure corrections ($s\,cm^{-3}$). PCASP, CAS and CDP data are shown in red (diamonds), green (circles) and blue (squares) respectively. Only upwards error bars are shown for clarity. SEM data are shown as scatter points (grey, crosses) and the arithmetic mean of these data is shown in black.

data in Fig. 4 appears to correlate with these values. Case 1 displays good agreement under lower RH conditions, whilst cases 2, 3, 4 and 5 display poorer agreement under higher RH conditions. However, case 6 displays good agreement under relatively high RH. The derived RH values are similar; therefore, these trends could be circumstantial. The RH measure for case 3 is not trusted and is likely a consequence of condensation on the detection surface.

Qualitatively, there is reasonable agreement between the probe and SEM-derived number size distributions – providing confidence in the analysis presented – but this similarly highlights the limitations of the sample inlets on the aircraft for coarse aerosol as described by Trembath (2013). The discrepancies between these distributions, with relation to the inlet efficiency issues, are addressed further in Sect. 4.1.

3.3 Aerosol composition

The particle classifications detailed in Table S1 in the Supplement were applied to the compositional data obtained for each analysed filter pair. The dependence of composition on size is shown in Fig. 5, where only sizes which display good agreement with the wing-mounted probes have been included ($\sim$ 0.5–$\sim$10 µm). Data out with this range was viewed as being unrepresentative of the population, given the discrepancies at small and large sizes in Fig. 4.

Clear trends become apparent when implementing this size-segregated approach. Silicate dusts are identified in all samples, with greater concentrations found at larger sizes in all cases except the last. These dusts are especially abundant in the first three cases. Cases 4 and 5 are dominated by fresh chlorides at all sizes except the largest bins, and cases 3 and 6 also contained significant fractions of this species. Case 6 differs from the others, displaying increased Ca-rich, mixed chloride and other fractions. Similarly, the high sulfate loading in case 1 is unique, yet the composition trends of this case can be associated with the subsequent flight via the abundance of silicates; a link that is not so clear between cases 5 and 6.

Although the mineral phase cannot be identified, elemental ratios can be used to identify trends in the dust samples. For example, feldspars can be rich in Ca, K or Na, whilst clays may have significant fractions of Mg and/or Fe. The elemental ratios displayed in Fig. 6 are variable across the campaign. This variability is heightened in some ratios with respect to others; from Fig. 6, the K / Al and Ca / Al ratios are changeable but the Mg / Si ratio is low for all cases. The mean and median values of the Si / Al ratio do not differ substantially between the flights, whilst the K / Al, Fe / Si and Ca / Al ratios are heightened in case 6.

3.4 Comparison between below- and above-cloud samples

The samples detailed previously were all exposed below cloud and were chosen as the particles collected likely influenced the microphysics of clouds that formed above these collection altitudes. Most of these cases appear to be influenced by local sources; cases 4 and 5 in particular are predominantly composed of fresh chlorides. However, these

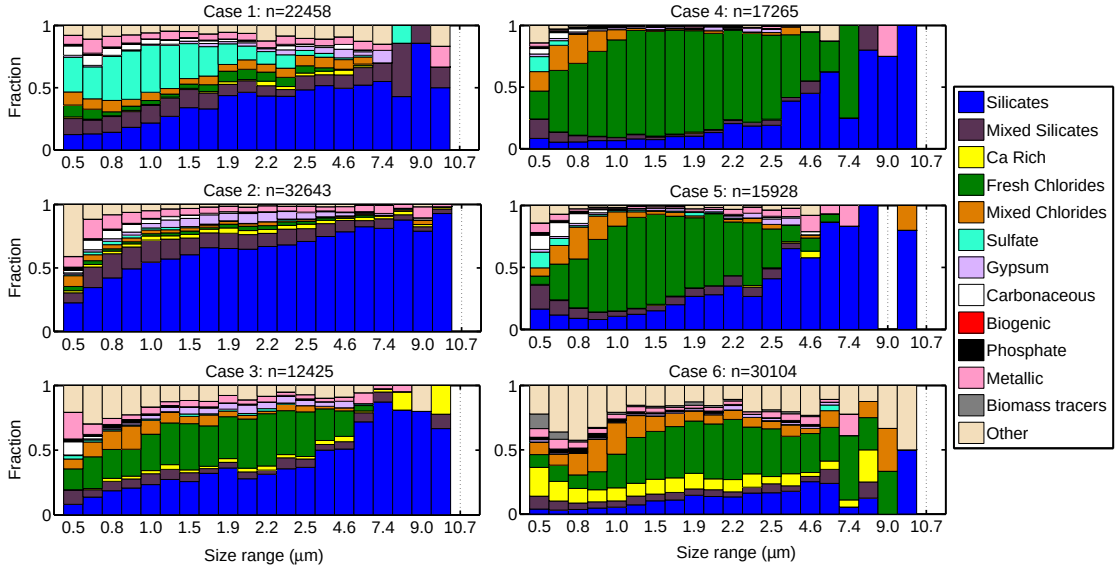

Figure 5. Size-segregated particle classifications applied to each below-cloud case, with each size bin normalised to show the fraction (by number) occupied by each classification. The sizes indicated are the bin centres. The number of particles scanned in each case is listed at the top of each panel.

cases do not obviously address the involvement of aerosol particles from distant sources.

As a test case, a filter pair exposed above cloud was analysed to compare the particle compositions. A comparison study was chosen: flight B764 provided consecutive filter exposures below and above (cases 4 and 7) a stratus cloud deck, approximately 1 h apart, allowing for a comparison between the respective compositional characteristics. The cloud located between the exposures was mixed-phase, with a measured sub-adiabatic CDP liquid-water content profile. This suggests that entrainment of aerosol from above may have been an important source contributing to changes in the cloud microphysical properties (Jackson et al., 2012), or that the liquid-water in the cloud had been depleted via precipitation processes. Air mass back trajectories varied little between the exposures, with both cases influenced by air from over the Barents Sea and the coast of northern Russia (see Fig. 3). The conditions sampled during each of these exposures are summarised in Table 2.

Figure 7 displays the compositional differences between the below- and above-cloud samples. The fraction of unclassified particles is greater in the above-cloud example for sizes $> 0.5\,\mu m$ (panel b), whilst a similar fraction was observed in both cases for sizes $\leq 0.5\,\mu m$ (panel a). Similarly, a comparable fraction of silicates is identified on both filter pairs. Greater fractions of fresh chlorides are found in case 4; however, a moderate loading of sea salt – and aged sea salt – is still identified in case 7. Case 7 also has a greater sulfate loading and the absolute number of particles detected was lower than in the below-cloud case. The size-segregated classifications, shown in panel c of Fig. 7, display significant unclassified fractions across most sizes, with increased contributions at < 1 and $> 3\,\mu m$. The dominating species changes from unclassified to fresh chlorides to silicates as particle size increases and significant mixed chloride fractions are also observed at small sizes.

4 Discussion

4.1 Size distributions

The filter-derived and probe-averaged size distributions from Sect. 3.2 compare reasonably well. The disagreement at the size limits ($\lesssim 0.5$ and $\gtrsim 10\,\mu m$) of these distributions implies that the inlet collection and filter efficiency issues discussed in Sect. 2.2 were influencing these samples. These collection issues have been found to have the greatest impact on the coarse mode (Andreae et al., 2000; Formenti et al., 2003). The results shown in Fig. 4 reflect this, where the agreement between the filter- and probe-distributions decreases with increasing size ($\gtrsim 1$–$2\,\mu m$). Coarse-mode enhancement relative to the probe data is not observed to the same extent as Chou et al. (2008). Reasonable agreement between these data is observed up to approximately $10\,\mu m$, as also concluded by Johnson et al. (2012) – whose samples were analysed using the same facilities in the Williamson Research Centre – and Chou et al. (2008).

Disagreement $< 0.5\,\mu m$ could be due to particles either passing through the filter pores at the time of exposure or being left undetected by the EDS analysis due to a decreasing signal-to-noise ratio and increasing interaction volume in this size limit (Kandler et al., 2011). Chou et al. (2008)

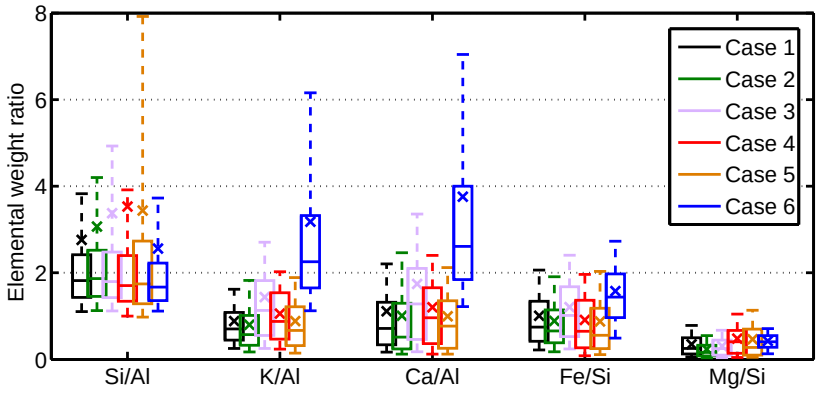

Figure 6. Mean elemental ratios from each case. Data from the silicates and mixed silicates categories only are included to provide an indication of the mineral phases measured. Box edges indicate the 25th and 75th percentiles, and the cross and the horizontal line dissecting the boxes represent the mean and median values respectively. The outliers extend to the 10 and 90 % thresholds of the data.

found that their accumulation-mode filter size distributions derived from transmission electron microscopy (TEM) correlated better with observational data obtained from a cabin-based PCASP variation sampling from a Counterflow Virtual Impactor inlet (CVI-PCASP) than their SEM-derived distributions. Given the similarity between the filtration techniques applied, this may suggest that the disagreement between the accumulation-mode distributions observed here could be a result of the limitations of the SEM technique rather than an issue with the filter sampling on the aircraft. However, Chou et al. (2008) also identified differences between the performance of their CVI-PCASP and externally mounted PCASP – with the former consistently overcounting compared to the latter – suggesting that possible inlet losses could be similarly affecting the wing-mounted PCASP used in this study. In summary, the SEM technique, filter mechanism collection efficiency, and possible inlet losses could all be introducing some magnitude of error to the comparisons shown in Fig. 4, and it is not trivial to identify which source of error is the most influential in these cases.

4.1.1 Cases 1 to 5

The compositional trends observed in Fig. 5 are typically different between each case. Compositional dominance varies from sulfates to silicates to fresh chlorides through the first five cases. Some particle classes, e.g. carbonaceous or sulfates, are mostly observed at sizes < 1 µm (excluding case 1), whilst others (e.g. silicates) are more common at larger particle sizes.

The influence of sulfates, silicates and fresh chlorides varies substantially in the first five cases; variability which could be inferred from the differences in the respective back trajectories. There are distinct similarities between the trends derived for cases 4 and 5, with dominant fresh chloride and silicate signatures observed (Fig. 5). Both cases display a similar mixed chloride loading between sizes 0.5 and 1 µm; particles which are likely sea salts mixed with sulfates.

The chloride classifications are not ubiquitously observed in the first five cases, with particularly low measurements of these species in cases 1 and 2. This suggests that the ocean was not a strong source of particles in these cases, whereas the significance of this source is clear in cases 3, 4 and 5. This hypothesis is strengthened by the back trajectories calculated for these exposures (Fig. 3); the air mass source for cases 1 and 2 was the frozen Arctic Ocean, whilst cases 4 and 5 both had low-altitude trajectories across the sea surface. During the transition over the ocean, sea salts could have been lifted into the air stream. Case 1 displays a high sulfate signature – a characteristic unique from the other cases – suggesting that these particles had sufficient time to interact with sulfate gases (from either anthropogenic or marine sources, see Sect. 2.4.2) during transit over the sea ice. There is a common link between the first three cases in their respective silicate loadings; the measured amount of silicate-based dusts is high in these cases, with a maximum reached during case 2. Potential sources of these dusts are discussed further in Sect. 4.2.

4.1.2 Case 6

Case 6 was exposed in a different location – to the north-west of Svalbard instead of the south-east – than the first five cases (see Table 1). The particle loading was much greater for this case, as indicated by the large number of particles collected (Fig. 5) and the very short sampling time (Table 2). The comparatively greater number concentration measured agrees with the aerosol climatology presented by Tunved et al. (2013) and results from the Arctic Study of Tropospheric Aerosol and Radiation (ASTAR) 2000 campaign (Hara et al., 2003), where trajectories from northern Russia and Europe coincided with noted "haze" events with increased particle loadings. Additionally, there are distinct

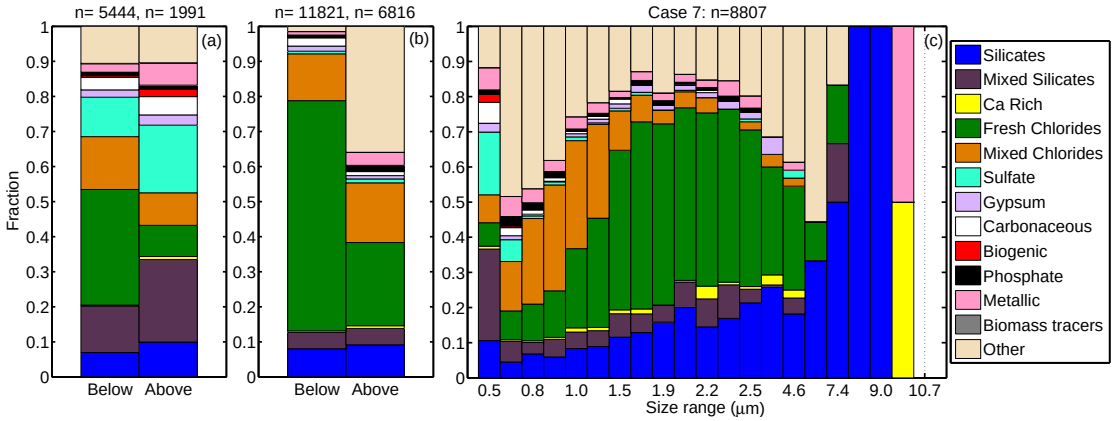

Figure 7. Compositional comparison between the below- and above-cloud samples (cases 4 and 7) from flight B764. **(a)** Averaged particle classifications $\leq 0.5\,\mu m$; **(b)** averaged particle classifications $> 0.5\,\mu m$; **(c)** size-segregated classifications from the above-cloud exposure. Each bin is normalised to show the fraction (by number) occupied by each classification and the number of particles analysed are listed above each panel. The sizes indicated in **(c)** are the bin centres.

compositional differences between cases 1–5 and case 6. This case is the only one not to be dominated by silicates at super-micron sizes and has the greatest proportion of Ca-rich particles, biomass tracers and unclassified particles across the sizes considered. Case 6 is unique in its dominant particle categories, their respective size evolution, and air mass back trajectory, emphasising its contrast to the other cases.

The magnitude of the biomass tracer fraction is only sufficient enough to be observed in case 6. These particles are mostly small in size, as shown in Fig. 5. Andreae (1983) have previously shown that there is a strong relationship between biomass particle species and particle size below 2 µm. The K measurements in these particles mirror the quantities measured by Umo et al. (2015) for bottom ashes, adding confidence to their identification as biomass products. Modelled back trajectories for case 6 hail from northern Russia and the European continent. Potential sources of these particles could include similar boreal forest fire events as those sampled by Quennehen et al. (2012), which were also observed at approximately the same time of year, or from European biomass activities.

The Ca-rich particles observed strongly in case 6 are distinct and not observed to the same magnitude in the other flights, implying a unique source. It is possible that these are naturally occurring carbonate dusts; however, Umo et al. (2015) also measured several species of Ca-based dusts in their wood and bottom ash samples, suggesting that these could also be from biomass burning activities. The strong detection of Ca-rich particles alongside the K-dominant biomass particles supports this conclusion here. The relative prevalence of K-rich and Ca-rich particles found in the sub- and super-micron ranges mirrors the relationship observed in the biomass burning study by Andreae (1983). The large Ca signature is also observed in the silicate and mixed silicate spectra for this case (Fig. S2 in the Supplement), and consequently affects the K / Al and Ca / Al ratios (shown in Fig. 6). It is unclear whether these enhanced values are a result of internal mixing of silicates with the Ca- or K-rich biomass particles or if they are real feldspar signatures (as K-feldspar or plagioclase). The Fe / Si ratio is also elevated for this case and this could be due to increased detection of clay-like dusts or hematite, and/or internal mixing with anthropogenic smelting emissions.

4.2 Sourcing the dust

Unexpectedly, large fractions of silicate dusts are observed in every case. These filters were collected in March when the majority of the surrounding surface was snow covered; therefore, there is no obvious local source of mineral dust. Weinbruch et al. (2012) also identified large dust fractions in their samples collected at Ny-Ålesund in April 2008, and these dusts would likely act as a source of ice nucleating particles for clouds in this region. The presence of dust in such quantities could either be due to some local source, long-range transport or a combination of these two avenues. To better understand the characteristics of these dusts, the elemental ratios in Fig. 6 can be considered. In general, the consistency in the median Si / Al ratio between each case suggests that the typical composition of the aluminosilicates has low variability, with each distribution skewed differently to account for the differences in the mean and variance values.

Elemental ratios can be used to infer a source of the mineral dusts. Several studies have investigated characteristic ratios of dusts from a variety of arid regions. For example, the African dust study by Formenti et al. (2008) calculated these ratios from airborne filter data and derived Si / Al, K / Al and Ca / Al ratios of approximately 3, 0.25 and 0.5 respectively. These values are within the limits of those calculated in this study (Fig. 6); however, a lack of good agreement suggests

that these sources may not be related to the dusts analysed here. Zhang et al. (2001) presented these ratios for dusts collected at various Asian sites, and their Tibetan and Loess Plateau samples were found to have Si / Al ratios of 4.6 and 2.5 respectively. The Loess values are consistent with the mean values obtained in all cases, whereas the Tibetan values lie within the upper bounds of samples 3 and 5. The Loess samples also had a Ca / Al ratio of 2.7, lying between the median and mean values obtained for case 6 and within the upper bound of case 3; however, it is much greater than the average ratio derived for the majority of these cases. Their K / Al ratio was found to be 0.95, consistent with the first five cases but not case 6. This could be due to the heightened K influence from biomass sources in case 6, but could also be coincidental and care must be taken when attributing a transported dust sample to a given source via this method. The dust collected here does appear to have more in common with the Asian samples than the African samples; however, the composition of dusts originating from the same source region is not always consistent and can vary between close geographical locations (Glen and Brooks, 2013). It is also unclear how these ratios would be affected by transportation, as atmospheric processing would likely alter the composition of ageing dust with respect to the freshly emitted dust characteristics reported in these studies. Despite this, it is worth noting that Liu et al. (2015) identified high-altitude plumes during the springtime ACCACIA campaign, which hailed from the Asian continent. It could be possible that dusts from these sources were advected over large distances in addition to the black carbon explicitly measured and modelled by Liu et al. (2015). The increase in mean trajectory altitude with time, as shown in Fig. 3, supports this theory as the descent of air from > 1000 m could be drawing dusts down to the low-altitudes considered. The theory that Asian dust contributes to the Arctic haze phenomenon is not new, and observations have indicated that this is the case (e.g. Rahn et al., 1977). However, models have not been able to produce conclusive evidence (Quinn et al., 2007). A key question in this hypothesis is theorising how the dust is lofted up to high altitudes in the atmosphere, and subsequently undergoes this long-range transportation, without experiencing cloud processing. It is possible that frontal uplifts at the source are responsible, with weakly scavenging mixed-phase clouds along the trajectories allowing the dust loading to remain so high.

4.3 Mixed aerosol particles

The degree of mixing in each case is different – as displayed by the variability in mean fractions shown in Fig. S2 in the Supplement – thus tying in with the differences between the air mass histories. Particles that have undergone long-range transport likely would have enhanced internal mixing and may not be adequately classified by the scheme employed here. Unclassified particles are prevalent in cases 3, 6 and 7 (Fig. 5). Variability within the categories (as seen in Fig. S2 in the Supplement) highlights the importance of treating the classifications with caution: they provide a good representation of the particle species collected, yet the ability of the criteria to account for mixed species is not always efficient.

The influence of unclassified particles on the population is most evident in the higher-altitude case: case 7 (Fig. 7) is distinctly different from its below-cloud counterpart (case 4, Fig. 5). In addition to the enhanced other fraction, large mixed chloride, sulfate and mixed silicate loadings are also identified above cloud (Fig. 7); classifications which could be attributed to anthropogenic influences. In this case, it is likely that these particles had undergone mixing over long-range transport. The contrast between the below- and above-cloud cases emphasises the segregation of the Arctic aerosol sources: whilst being influenced by local surface sources, the Arctic atmosphere is also affected by this influx of long-range transported aerosol particles – the Arctic haze – during the spring months (Barrie, 1986; Shaw, 1995; Liu et al., 2015). Both of these aerosol pathways will affect the cloud microphysics, and further investigation is required to better understand the importance of each. The particle classes detected in cases 4 and 7 could have interacted with the cloud layer as CCN or INPs, whilst the differences between them can be explained by the cloud restricting any direct mixing between the two populations.

The extent of internal and external mixing observed indicates that some INP predictions may be fraught with inaccuracy in this region; for example, DeMott et al. (2010) related INP concentration to the total aerosol concentration > 0.5 µm under the assumption that most of these aerosol particles are INPs. However, efficient INPs (e.g. mineral dusts) were not found to be consistently dominant in this limit. As suggested by DeMott et al. (2010), this relation may not be applicable in cases heavily influenced by marine sources, and the high loadings of super-micron sea salt identified in some of the ACCACIA cases would qualify these as such. The use of dust-based parameterisations such as Niemand et al. (2012) or DeMott et al. (2015) may provide a more accurate prediction of the INP concentration in these cases.

Whilst it is likely that the dusts observed in this study would act as INPs, it cannot be determined how the unclassified and mixed particle categories would interact with the clouds in this region. In particular, the lack of sound quantitative C and O measurements prevents organic coatings from being identified; coatings which are important in interpreting aerosol–cloud interactions. The mixed particles identified here could likely act as CCN as they would possess a soluble component provided by the Cl or S signatures. However, it is also likely that they could influence the INP population; whilst soluble coatings may suppress ice nucleating ability, the presence of IN-active coatings and/or complex internal mixing could act to enhance it. Examples of IN-active coatings could include biological material, as some strains of bacteria have been observed to be efficient INPs in laboratory studies (Möhler et al., 2007; Hoose and Möhler, 2012).

Some studies have identified cases where bacteria has survived long-range atmospheric transport by piggybacking dust particles (Yamaguchi et al., 2012). It is possible that such bacteria could influence the Arctic atmosphere via a similar transportation mechanism. Fundamentally, comprehending how these mixed particles interact and impact the cloud microphysics is a significant step to take towards improving our understanding of aerosol–cloud interactions in the Arctic springtime.

5 Conclusions

During the Aerosol–Cloud Coupling and Climate Interactions (ACCACIA) springtime campaign, in situ samples of Arctic aerosol particles were collected on polycarbonate filters. Analysis of these samples has been detailed, with a focus placed upon identifying the composition of the collected particles and investigating their potential sources. In total, six below-cloud exposures were analysed to infer how the local sources may influence the cloud microphysics of the region (Fig. 1) and one above-cloud case was considered to investigate the composition of transported particles (Fig. 7). The main findings of this study are as follows:

- Single-particle analysis of the filters produced number size distributions which were comparable (from approximately 0.5–10 µm) to those derived from the wing-mounted optical particle counters (Fig. 4). Better agreement between these distributions was achieved in lower RH sampling conditions. The composition of the particles collected was strongly dependent upon size across all samples, with crustal minerals and sea salts dominating the super-micron range. Carbon- and sulfur-based particles were mostly observed in the < 1 µm limit (Fig. 5). Large fractions of mixed particles – as shown by the other, mixed silicate and mixed chloride categories in Figs. 5 and 7 – were identified in each case. The impact of these particles on cloud microphysics as potential INPs and/or CCN is not quantifiable by this study.

- Distinct size-dependent compositional trends were observed in each sample, with stark differences between cases (Fig. 5). These differences were attributed to variations in the air mass histories; cases 1 and 2 presented a silicate dust dominance, whilst cases 4 and 5 had similar chloride and silicate loadings. These similarities were mirrored by their closely related source regions (Fig. 3). The relationship between composition and trajectory was strengthened by the unique attributes of case 6; both the trends and trajectory were distinct in this case and the particle classifications identified can be explained by hypothesised sources along the trajectory presented.

- Crustal minerals were identified in all cases, despite the seasonal local snow cover. The HYSPLIT back trajectories (Fig. 3) were variable in direction, yet typically increased in mean altitude over time. These dusts were therefore hypothesised to have undergone long-range, high-altitude transport from distant sources, through regions containing weakly scavenging mixed-phase clouds. Some elemental characteristics (Fig. 6) were found to be consistent with Asian dust sources; however, it is not known how long-range transport may affect the composition of these dusts and so this theory cannot be proven with these data.

The non-volatile, coarse-mode Arctic aerosol particles analysed by this study showed great variation between subsequent days and different meteorological conditions; therefore, it would be difficult to incorporate these findings into models. However, the measurements from the springtime ACCACIA campaign provide a good opportunity to simultaneously investigate both the properties of aerosol particles in the region and the microphysical characteristics of the clouds observed. Further study of the cloud microphysics of these cases, with reference to these aerosol observations, will allow us to improve both our understanding and the representation of aerosol–cloud interactions in climate models and act to reduce the uncertainty in forecasting the Arctic atmosphere in the future.

The Supplement related to this article is available online at doi:10.5194/acp-16-4063-2016-supplement.

Acknowledgements. This work was funded by the National Environment Research Council (NERC), under grant NE/I028696/1, as part of the ACCACIA campaign. G. Young was supported by a NERC PhD studentship. We would like to thank the ACCACIA project team for their efforts, and J. Crosier and N. Marsden for their helpful comments and advice. Airborne data were obtained using the BAe-146-301 Atmospheric Research Aircraft (ARA) flown by Directflight Ltd and managed by the Facility for Airborne Atmospheric Measurements (FAAM), which is a joint entity of the Natural Environment Research Council (NERC) and the Met Office. G. Young would also like to thank J. Fellowes and J. Waters at the Williamson Research Centre for their guidance with the ESEM instrument and the European Geosciences Union for funding the publication this article as part of an OSP 2015 award.

Edited by: W. T. Sturges

References

Andreae, M. O.: Soot Carbon and Excess Fine Potassium: Long-Range Transport of Combustion-Derived Aerosols, Science, 220, 1148–1151, doi:10.1126/science.220.4602.1148, 1983.

Andreae, M. O. and Rosenfeld, D.: Aerosol cloud precipitation interactions. Part 1. The nature and sources of cloud-active aerosols, Earth Sci. Rev., 89, 13–41, doi:10.1016/j.earscirev.2008.03.001, 2008.

Andreae, M. O., Elbert, W., Gabriel, R., Johnson, D. W., Osborne, S., and Wood, R.: Soluble ion chemistry of the atmospheric aerosol and SO_2 concentrations over the eastern North Atlantic during ACE-2, Tellus B, 52, 1066–1087, doi:10.1034/j.1600-0889.2000.00105.x, 2000.

Barrie, L. A.: Arctic Air Chemistry: An Overview, in: Arctic Air Pollution, edited by: Stonehouse, B., Cambridge University Press, Cambridge, UK, 1986.

Behrenfeldt, U., Krejci, R., Ström, J., and Stohl, A.: Chemical properties of Arctic aerosol particles collected at the Zeppelin station during the aerosol transition period in May and June of 2004, Tellus B, 60, 405–415, doi:10.1111/j.1600-0889.2008.00349.x, 2008.

Boucher, O., Randall, D., Artaxo, P., Bretherton, C., Feingold, G., Forster, P., Kerminen, V. M., Kondo, Y., Liao, H., Lohmann, U., Rasch, P., Satheesh, S. K., Sherwood, S., Stevens, B., and Zhang, X. Y.: Clouds and Aerosols, in: Climate Change 2013: The Physical Science Basis. Contribution of Working Group I to the Fifth Assessment Report of the Intergovernmental Panel on Climate Change, edited by: Stocker, T. F., Qin, D., Plattner, G. K., Tignor, M., Allen, S. K., Boschung, J., Nauels, A., Xia, Y., Bex, V., and Midgley, P. M., Cambridge University Press, Cambridge, United Kingdom, New York, NY, USA, 2013.

Chou, C., Formenti, P., Maille, M., Ausset, P., Helas, G., Harrison, M., and Osborne, S.: Size distribution, shape, and composition of mineral dust aerosols collected during the African Monsoon Multidisciplinary Analysis Special Observation Period 0: Dust and Biomass-Burning Experiment field campaign in Niger, January 2006, J. Geophys. Res., 113, D00C10, doi:10.1029/2008JD009897, 2008.

Connolly, P. J., Möhler, O., Field, P. R., Saathoff, H., Burgess, R., Choularton, T., and Gallagher, M.: Studies of heterogeneous freezing by three different desert dust samples, Atmos. Chem. Phys., 9, 2805–2824, doi:10.5194/acp-9-2805-2009, 2009.

Conny, J. M. and Norris, G. A.: Scanning Electron Microanalysis and Analytical Challenges of Mapping Elements in Urban Atmospheric Particles, Environ. Sci. Technol., 45, 7380–7386, doi:10.1021/es2009049, 2011.

Crosier, J., Allan, J. D., Coe, H., Bower, K. N., Formenti, P., and Williams, P. I.: Chemical composition of summertime aerosol in the Po Valley (Italy), northern Adriatic and Black Sea, Q. J. Roy. Meteor. Soc., 133, 61–75, doi:10.1002/qj.88, 2007.

Curry, J. A., Rossow, W. B., Randall, D., and Schramm, J. L.: Overview of Arctic Cloud and Radiation Characteristics, J. Climate, 9, 1731–1764, doi:10.1175/1520-0442(1996)009<1731:OOACAR>2.0.CO;2, 1996.

de Boer, G., Shupe, M. D., Caldwell, P. M., Bauer, S. E., Persson, O., Boyle, J. S., Kelley, M., Klein, S. A., and Tjernström, M.: Near-surface meteorology during the Arctic Summer Cloud Ocean Study (ASCOS): evaluation of reanalyses and global climate models, Atmos. Chem. Phys., 14, 427–445, doi:10.5194/acp-14-427-2014, 2014.

DeMott, P. J., Prenni, A. J., Liu, X., Kreidenweis, S. M., Petters, M. D., Twohy, C. H., Richardson, M. S., Eidhammer, T., and Rogers, D. C.: Predicting global atmospheric ice nuclei distributions and their impacts on climate, P. Natl. Acad. Sci. USA, 107, 11217–11222, doi:10.1073/pnas.0910818107, 2010.

DeMott, P. J., Prenni, A. J., McMeeking, G. R., Sullivan, R. C., Petters, M. D., Tobo, Y., Niemand, M., Möhler, O., Snider, J. R., Wang, Z., and Kreidenweis, S. M.: Integrating laboratory and field data to quantify the immersion freezing ice nucleation activity of mineral dust particles, Atmos. Chem. Phys., 15, 393–409, doi:10.5194/acp-15-393-2015, 2015.

Draxler, R. R. and Hess, G. D.: An Overview of the HYSPLIT_4 Modelling System for Trajectories, Dispersion, and Deposition, Aust. Meteorol. Mag., 47, 295–308, 1998.

Fleming, Z. L., Monks, P. S., and Manning, A. J.: Review: Untangling the influence of air-mass history in interpreting observed atmospheric composition, Atmos. Res., 104, 1–39, doi:10.1016/j.atmosres.2011.09.009, 2012.

Formenti, P., Elbert, W., Maenhaut, W., Haywood, J., Osborne, S., and Andreae, M. O.: Inorganic and carbonaceous aerosols during the Southern African Regional Science Initiative (SAFARI 2000) experiment: Chemical characteristics, physical properties, and emission data for smoke from African biomass burning, J. Geophys. Res., 108, 8488, doi:10.1029/2002JD002408, 2003.

Formenti, P., Rajot, J. L., Desboeufs, K., Caquineau, S., Chevaillier, S., Nava, S., Gaudichet, A., Journet, E., Triquet, S., Alfaro, S., Chiari, M., Haywood, J., Coe, H., and Highwood, E.: Regional variability of the composition of mineral dust from western Africa: Results from the AMMA SOP0/DABEX and DODO field campaigns, J. Geophys. Res., 113, D00C13, doi:10.1029/2008JD009903, 2008.

Formenti, P., Schütz, L., Balkanski, Y., Desboeufs, K., Ebert, M., Kandler, K., Petzold, A., Scheuvens, D., Weinbruch, S., and Zhang, D.: Recent progress in understanding physical and chemical properties of African and Asian mineral dust, Atmos. Chem. Phys., 11, 8231–8256, doi:10.5194/acp-11-8231-2011, 2011.

Geng, H., Ryu, J., Jung, H.-J., Chung, H., Ahn, K.-H., and Ro, C.-U.: Single-Particle Characterization of Summertime Arctic Aerosols Collected at Ny-Ålesund, Svalbard, Environ. Sci. Technol., 44, 2348–2353, doi:10.1021/es903268j, 2010.

Glen, A. and Brooks, S. D.: A new method for measuring optical scattering properties of atmospherically relevant dusts using the Cloud and Aerosol Spectrometer with Polarization (CASPOL), Atmos. Chem. Phys., 13, 1345–1356, doi:10.5194/acp-13-1345-2013, 2013.

Hand, V. L., Capes, G., Vaughan, D. J., Formenti, P., Haywood, J. M., and Coe, H.: Evidence of internal mixing of African dust and biomass burning particles by individual particle analysis using electron beam techniques, J. Geophys. Res., 115, D13301, doi:10.1029/2009JD012938, 2010.

Hara, K., Yamagata, S., Yamanouchi, T., Sato, K., Herber, A., Iwasaka, Y., Nagatani, M., and Nakata, H.: Mixing states of individual aerosol particles in spring Arctic troposphere during ASTAR 2000 campaign, J. Geophys. Res., 108, 4209, doi:10.1029/2002JD002513, 2003.

Heintzenberg, J., Hansson, H.-C., Ogren, J. A., Covert, D. S., and Blanchet, J.-P.: Physical and Chemical Properties of Arctic Aerosols and Clouds, in: Arctic Air Pollution, edited by: Stonehouse, B., Cambridge University Press, Cambridge, UK, 1986.

Hoose, C. and Möhler, O.: Heterogeneous ice nucleation on atmospheric aerosols: a review of results from laboratory experiments,

Atmos. Chem. Phys., 12, 9817–9854, doi:10.5194/acp-12-9817-2012, 2012.

Jackson, R. C., McFarquhar, G. M., Korolev, A. V., Earle, M. E., Liu, P. S. K., Lawson, R. P., Brooks, S., Wolde, M., Laskin, A., and Freer, M.: The dependence of ice microphysics on aerosol concentration in arctic mixed-phase stratus clouds during ISDAC and M-PACE, J. Geophys. Res., 117, D15207, doi:10.1029/2012JD017668, 2012.

John, W., Hering, S., Reischl, G., Sasaki, G., and Goren, S.: Characteristics of Nuclepore filters with large pore size – II. Filtration properties, Atmos. Environ., 17, 373–382, doi:10.1016/0004-6981(83)90054-9, 1983.

Johnson, B., Turnbull, K., Brown, P., Burgess, R., Dorsey, J., Baran, A. J., Webster, H., Haywood, J., Cotton, R., Ulanowski, Z., Hesse, E., Woolley, A., and Rosenberg, P.: In situ observations of volcanic ash clouds from the FAAM aircraft during the eruption of Eyjafjallajökull in 2010, J. Geophys. Res., 117, D00U24, doi:10.1029/2011JD016760, 2012.

Kandler, K., Benker, N., Bundke, U., Cuevas, E., Ebert, M., Knippertz, P., Rodríguez, S., Schütz, L., and Weinbruch, S.: Chemical composition and complex refractive index of Saharan Mineral Dust at Izaña, Tenerife (Spain) derived by electron microscopy, Atmos. Environ., 41, 8058–8074, doi:10.1016/j.atmosenv.2007.06.047, 2007.

Kandler, K., Lieke, K., Benker, N., Emmel, C., Küpper, M., Müller-Ebert, D., Ebert, M., Scheuvens, D., Schladitz, A., Schütz, L., and Weinbruch, S.: Electron microscopy of particles collected at Praia, Cape Verde, during the Saharan Mineral Dust Experiment: particle chemistry, shape, mixing state and complex refractive index, Tellus B, 63, 475–496, doi:10.1111/j.1600-0889.2011.00550.x, 2011.

Kanji, Z. A., Welti, A., Chou, C., Stetzer, O., and Lohmann, U.: Laboratory studies of immersion and deposition mode ice nucleation of ozone aged mineral dust particles, Atmos. Chem. Phys., 13, 9097–9118, doi:10.5194/acp-13-9097-2013, 2013.

Krejci, R., Ström, J., de Reus, M., and Sahle, W.: Single particle analysis of the accumulation mode aerosol over the northeast Amazonian tropical rain forest, Surinam, South America, Atmos. Chem. Phys., 5, 3331–3344, doi:10.5194/acp-5-3331-2005, 2005.

Krueger, B. J., Grassian, V. H., Laskin, A., and Cowin, J. P.: The transformation of solid atmospheric particles into liquid droplets through heterogeneous chemistry: Laboratory insights into the processing of calcium containing mineral dust aerosol in the troposphere, Geophys. Res. Lett., 30, 1148, doi:10.1029/2002GL016563, 2003.

Lance, S., Brock, C. A., Rogers, D., and Gordon, J. A.: Water droplet calibration of the Cloud Droplet Probe (CDP) and in-flight performance in liquid, ice and mixed-phase clouds during ARCPAC, Atmos. Meas. Tech., 3, 1683–1706, doi:10.5194/amt-3-1683-2010, 2010.

Levin, Z., Ganor, E., and Gladstein, V.: The Effects of Desert Particles Coated with Sulfate on Rain Formation in the Eastern Mediterranean, J. Appl. Meteorol., 35, 1511–1523, doi:10.1175/1520-0450(1996)035<1511:TEODPC>2.0.CO;2, 1996.

Levin, Z., Teller, A., Ganor, E., and Yin, Y.: On the interactions of mineral dust, sea-salt particles, and clouds: A measurement and modeling study from the Mediterranean Israeli Dust Experiment campaign, J. Geophys. Res., 110, D20202, doi:10.1029/2005JD005810, 2005.

Li, J., Pósfai, M., Hobbs, P. V., and Buseck, P. R.: Individual aerosol particles from biomass burning in southern Africa: 2. Compositions and aging of inorganic particles, J. Geophys. Res., 108, 8484, doi:10.1029/2002JD002310, 2003.

Liu, B. Y. H. and Lee, K. W.: Efficiency of membrane and nuclepore filters for submicrometer aerosols, Environ. Sci. Technol., 10, 345–350, doi:10.1021/es60115a002, 1976.

Liu, D., Quennehen, B., Darbyshire, E., Allan, J. D., Williams, P. I., Taylor, J. W., Bauguitte, S. J.-B., Flynn, M. J., Lowe, D., Gallagher, M. W., Bower, K. N., Choularton, T. W., and Coe, H.: The importance of Asia as a source of black carbon to the European Arctic during springtime 2013, Atmos. Chem. Phys., 15, 11537–11555, doi:10.5194/acp-15-11537-2015, 2015.

Lloyd, G., Choularton, T. W., Bower, K. N., Crosier, J., Jones, H., Dorsey, J. R., Gallagher, M. W., Connolly, P., Kirchgaessner, A. C. R., and Lachlan-Cope, T.: Observations and comparisons of cloud microphysical properties in spring and summertime Arctic stratocumulus clouds during the ACCACIA campaign, Atmos. Chem. Phys., 15, 3719–3737, doi:10.5194/acp-15-3719-2015, 2015.

Mamane, Y. and Noll, K. E.: Characterization of large particles at a rural site in the eastern United States: Mass distribution and individual particle analysis, Atmos. Environ., 19, 611–622, doi:10.1016/0004-6981(85)90040-X, 1985.

Möhler, O., DeMott, P. J., Vali, G., and Levin, Z.: Microbiology and atmospheric processes: the role of biological particles in cloud physics, Biogeosciences, 4, 1059–1071, doi:10.5194/bg-4-1059-2007, 2007.

Möhler, O., Benz, S., Saathoff, H., Schnaiter, M., Wagner, R., Schneider, J., Walter, S., Ebert, V., and Wagner, S.: The effect of organic coating on the heterogeneous ice nucleation efficiency of mineral dust aerosols, Environ. Res. Lett., 3, 025007, doi:10.1088/1748-9326/3/2/025007, 2008.

Murray, B. J., O'Sullivan, D., Atkinson, J. D., and Webb, M. E.: Ice nucleation by particles immersed in supercooled cloud droplets, Chem. Soc. Rev., 41, 6519–6554, doi:10.1039/c2cs35200a, 2012.

Niemand, M., Möhler, O., Vogel, B., Vogel, H., Hoose, C., Connolly, P., Klein, H., Bingemer, H., DeMott, P., Skrotzki, J., and Leisner, T.: A Particle-Surface-Area-Based Parameterization of Immersion Freezing on Desert Dust Particles, J. Atmos. Sci., 69, 3077–3092, doi:10.1175/JAS-D-11-0249.1, 2012.

Perovich, D. K., Richter-Menge, J. A., Jones, K. F., and Light, B.: Sunlight, water, and ice: Extreme Arctic sea ice melt during the summer of 2007, Geophys. Res. Lett., 35, L11501, doi:10.1029/2008GL034007, 2008.

Pruppacher, H. R. and Klett, J. D.: Microphysics of Clouds and Precipitation, 2nd Edn., Kluwer Academic Publishers, Dordrecht, the Netherlands, 1997.

Quennehen, B., Schwarzenboeck, A., Matsuki, A., Burkhart, J. F., Stohl, A., Ancellet, G., and Law, K. S.: Anthropogenic and forest fire pollution aerosol transported to the Arctic: observations from the POLARCAT-France spring campaign, Atmos. Chem. Phys., 12, 6437–6454, doi:10.5194/acp-12-6437-2012, 2012.

Quinn, P. K., Shaw, G., Andrews, E., Dutton, E. G., Ruoho-Airola, T., and Gong, S. L.: Arctic haze: current trends and

knowledge gaps, Tellus B, 59, 99–114, doi:10.1111/j.1600-0889.2006.00238.x, 2007.

Rahn, K. A.: Relative importances of North America and Eurasia as sources of Arctic aerosol, Atmos. Environ., 15, 1447–1455, doi:10.1016/0004-6981(81)90351-6, 1981.

Rahn, K. A., Borys, R. D., and Shaw, G. E.: The Asian source of Arctic haze bands, Nature, 268, 713–715, doi:10.1038/268713a0, 1977.

Reimann, C., Banks, D., and Caritat, P. de: Impacts of Airborne Contamination on Regional Soil and Water Quality: The Kola Peninsula, Russia, Environ. Sci. Technol., 34, 2727–2732, doi:10.1021/es9912933, 2000.

Rosenberg, P. D., Dean, A. R., Williams, P. I., Dorsey, J. R., Minikin, A., Pickering, M. A., and Petzold, A.: Particle sizing calibration with refractive index correction for light scattering optical particle counters and impacts upon PCASP and CDP data collected during the Fennec campaign, Atmos. Meas. Tech., 5, 1147–1163, doi:10.5194/amt-5-1147-2012, 2012.

Seiler, W. and Crutzen, P.: Estimates of gross and net fluxes of carbon between the biosphere and the atmosphere from biomass burning, Climatic Change, 2, 207–247, doi:10.1007/BF00137988, 1980.

Serreze, M. C., Holland, M. M., and Stroeve, J.: Perspectives on the Arctic's Shrinking Sea-Ice Cover, Science, 315, 1533–1536, doi:10.1126/science.1139426, 2007.

Shaw, G. E.: The Arctic Haze Phenomenon, B. Am. Meteorol. Soc., 76, 2403–2414, doi:10.1175/1520-0477(1995)076<2403:TAHP>2.0.CO;2, 1995.

Steinnes, E., Lukina, N., Nikonov, V., Aamlid, D., and Røyset, O.: A Gradient Study of 34 Elements in the Vicinity of a Copper-Nickel Smelter in the Kola Peninsula, Environ. Monit. Assess., 60, 71–88, doi:10.1023/A:1006165031985, 2000.

Ström, J., Umegård, J., Tørseth, K., Tunved, P., Hansson, H.-C., Holmén, K., Wismann, V., Herber, A., and König-Langlo, G.: One year of particle size distribution and aerosol chemical composition measurements at the Zeppelin Station, Svalbard, March 2000–March 2001, Phys. Chem. Earth, 28, 1181–1190, doi:10.1016/j.pce.2003.08.058, 2003.

Trembath, J. A.: Airborne CCN Measurements, PhD thesis, University of Manchester, Manchester, 2013.

Tunved, P., Ström, J., and Krejci, R.: Arctic aerosol life cycle: linking aerosol size distributions observed between 2000 and 2010 with air mass transport and precipitation at Zeppelin station, Ny-Ålesund, Svalbard, Atmos. Chem. Phys., 13, 3643–3660, doi:10.5194/acp-13-3643-2013, 2013.

Umo, N. S., Murray, B. J., Baeza-Romero, M. T., Jones, J. M., Lea-Langton, A. R., Malkin, T. L., O'Sullivan, D., Neve, L., Plane, J. M. C., and Williams, A.: Ice nucleation by combustion ash particles at conditions relevant to mixed-phase clouds, Atmos. Chem. Phys., 15, 5195–5210, doi:10.5194/acp-15-5195-2015, 2015.

Verlinde, J. Y., Harrington, J. Y., McFarquhar, G. M., Yannuzzi, V. T., Avramov, A., Greenberg, S., Johnson, N., Zhang, G., Poellot, M. R., Mather, J. H., Turner, D. D., Eloranta, E. W., Zak, B. D., Prenni, A. J., Daniel, J. S., Kok, G. L., Tobin, D. C., Holz, R., Sassen, K., Spangenberg, D., Minnis, P., Tooman, T. P., Ivey, M. D., Richardson, S. J., Bahrmann, C. P., Shupe, M., Demott, P. J., Heymsfield, A. J., and Schofield, R.: The Mixed-Phase Arctic Cloud Experiment, B. Am. Meteorol. Soc., 88, 205–221, doi:10.1175/BAMS-88-2-205, 2007.

Vihma, T., Pirazzini, R., Fer, I., Renfrew, I. A., Sedlar, J., Tjernström, M., Lüpkes, C., Nygård, T., Notz, D., Weiss, J., Marsan, D., Cheng, B., Birnbaum, G., Gerland, S., Chechin, D., and Gascard, J. C.: Advances in understanding and parameterization of small-scale physical processes in the marine Arctic climate system: a review, Atmos. Chem. Phys., 14, 9403–9450, doi:10.5194/acp-14-9403-2014, 2014.

Weinbruch, S., Wiesemann, D., Ebert, M., Schütze, K., Kallenborn, R., and Ström, J.: Chemical composition and sources of aerosol particles at Zeppelin Mountain (Ny Ålesund, Svalbard): An electron microscopy study, Atmos. Environ., 49, 142–150, doi:10.1016/j.atmosenv.2011.12.008, 2012.

Yakobi-Hancock, J. D., Ladino, L. A., and Abbatt, J. P. D.: Feldspar minerals as efficient deposition ice nuclei, Atmos. Chem. Phys., 13, 11175–11185, doi:10.5194/acp-13-11175-2013, 2013.

Yamaguchi, N., Ichijo, T., Sakotani, A., Baba, T., and Nasu, M.: Global dispersion of bacterial cells on Asian dust, Scientific Reports, 2, 525, doi:10.1038/srep00525, 2012.

Zhang, X. Y., Arimoto, R., Cao, J. J., An, Z. S., and Wang, D.: Atmospheric dust aerosol over the Tibetan Plateau, J. Geophys. Res., 106, 18471–18476, doi:10.1029/2000JD900672, 2001.

Zhao, C., Klein, S. A., Xie, S., Liu, X., Boyle, J. S., and Zhang, Y.: Aerosol first indirect effects on non-precipitating low-level liquid cloud properties as simulated by CAM5 at ARM sites, Geophys. Res. Lett., 39, L08806, doi:10.1029/2012GL051213, 2012.

Zimmermann, F., Weinbruch, S., Schütz, L., Hofmann, H., Ebert, M., Kandler, K., and Worringen, A.: Ice nucleation properties of the most abundant mineral dust phases, J. Geophys. Res., 113, D23204, doi:10.1029/2008JD010655, 2008.

5 Observed microphysical changes in Arctic mixed-phase clouds when transitioning from sea ice to open ocean

Young, G., Jones, H. M., Choularton, T. W., Crosier, J., Bower, K. N., Gallagher, M. W., Davies, R. S., Renfrew, I. A., Elvidge, A. D., Darbyshire, E., Marenco, F., Brown, P. R. A., Ricketts, H. M. A., Connolly, P. J., Lloyd, G., Williams, P. I., Allan, J. D., Taylor, J. W., Liu, D., and Flynn, M. J.: Observed microphysical changes in Arctic mixed-phase clouds when transitioning from sea ice to open ocean, Atmospheric Chemistry and Physics, 16, 13 945–13 967, doi:10.5194/acp-16-13945-2016, 2016.

This study was a collaboration between the University of Manchester, the University of East Anglia and the Met Office. The article was written by G. Young, under guidance from H. M. Jones and T. W. Choularton. Processing of cloud data and initial analysis was carried out by H. M. Jones. In depth cloud microphysics and aerosol analysis was carried out by G. Young. T. W. Choularton, J. Crosier, K. N. Bower, and M. W. Gallagher were involved in analysis planning and data interpretation. R. S. Davies, A. D. Elvidge, and I. A. Renfrew provided Figures 3 and 16, and were involved in the interpretation of these data. AVHRR visible image (Fig. 4**A**) was supplied by I. A. Renfrew. H. M. A. Ricketts helped to interpret dropsonde and synoptic data. CPIview (P J. Connolly) and OASIS (J. Crosier) data processing software were used for the CPI and for the wing-mounted OAPs (2DS, CIP15, and CIP100) respectively. Lidar and AIMMS data were processed by F. Marenco and

P. R. A. Brown respectively. P. R. A. Brown was involved with data quality management of the AIMMS and turbulence probe data. AMS data were provided by J. D. Allan and P. I. Williams. CPC and SP2 data were supplied by J. W. Taylor and D. Liu respectively. G. Lloyd and M. J. Flynn operated the cloud and aerosol instrumentation on board the aircraft. I. A. Renfrew was Mission Scientist for flight B762 and was involved in flight planning.

Atmos. Chem. Phys., 16, 13945–13967, 2016
www.atmos-chem-phys.net/16/13945/2016/
doi:10.5194/acp-16-13945-2016

Atmospheric Chemistry and Physics
Open Access
EGU

Observed microphysical changes in Arctic mixed-phase clouds when transitioning from sea ice to open ocean

Gillian Young[1], Hazel M. Jones[1], Thomas W. Choularton[1], Jonathan Crosier[2,1], Keith N. Bower[1], Martin W. Gallagher[1], Rhiannon S. Davies[3], Ian A. Renfrew[3], Andrew D. Elvidge[4], Eoghan Darbyshire[1], Franco Marenco[4], Philip R. A. Brown[4], Hugo M. A. Ricketts[2,1], Paul J. Connolly[1], Gary Lloyd[2,1], Paul I. Williams[2,1], James D. Allan[2,1], Jonathan W. Taylor[1], Dantong Liu[1], and Michael J. Flynn[1]

[1]Centre for Atmospheric Science, School of Earth and Environmental Sciences, University of Manchester, Manchester, UK
[2]National Centre for Atmospheric Science, University of Manchester, Manchester, UK
[3]School of Environmental Sciences, University of East Anglia, Norwich, UK
[4]Met Office, Exeter, UK

Correspondence to: Gillian Young (gillian.young@manchester.ac.uk)

Received: 13 May 2016 – Published in Atmos. Chem. Phys. Discuss.: 26 May 2016
Revised: 2 September 2016 – Accepted: 21 September 2016 – Published: 11 November 2016

Abstract. In situ airborne observations of cloud microphysics, aerosol properties, and thermodynamic structure over the transition from sea ice to ocean are presented from the Aerosol-Cloud Coupling And Climate Interactions in the Arctic (ACCACIA) campaign. A case study from 23 March 2013 provides a unique view of the cloud microphysical changes over this transition under cold-air outbreak conditions.

Cloud base lifted and cloud depth increased over the transition from sea ice to ocean. Mean droplet number concentrations, N_{drop}, also increased from $110 \pm 36\,cm^{-3}$ over the sea ice to $145 \pm 54\,cm^{-3}$ over the marginal ice zone (MIZ). Downstream over the ocean, N_{drop} decreased to $63 \pm 30\,cm^{-3}$. This reduction was attributed to enhanced collision-coalescence of droplets within the deep ocean cloud layer. The liquid water content increased almost four fold over the transition and this, in conjunction with the deeper cloud layer, allowed rimed snowflakes to develop and precipitate out of cloud base downstream over the ocean.

The ice properties of the cloud remained approximately constant over the transition. Observed ice crystal number concentrations averaged approximately 0.5–1.5 L^{-1}, suggesting only primary ice nucleation was active; however, there was evidence of crystal fragmentation at cloud base over the ocean. Little variation in aerosol particle number concentrations was observed between the different surface conditions; however, some variability with altitude was observed, with notably greater concentrations measured at higher altitudes (> 800 m) over the sea ice. Near-surface boundary layer temperatures increased by 13 °C from sea ice to ocean, with corresponding increases in surface heat fluxes and turbulent kinetic energy. These significant thermodynamic changes were concluded to be the primary driver of the microphysical evolution of the cloud. This study represents the first investigation, using in situ airborne observations, of cloud microphysical changes with changing sea ice cover and addresses the question of how the microphysics of Arctic stratiform clouds may change as the region warms and sea ice extent reduces.

1 Introduction

Projected increases in mean temperature due to climate change are greater in the Arctic than the midlatitudes (ACIA, 2005). Arctic surface temperatures are predicted to rise by up to 7 °C by the end of the 21st century (ACIA, 2005). As a consequence of recent warming, observations have shown a prominent decline in sea ice volume over the last 30 years (Serreze et al., 2007), with record-breaking seasonal melts becoming more frequent (e.g. 2004, 2007, and 2012, Stroeve et al., 2005; Perovich et al., 2008; Parkinson and Comiso,

2013). Observed surface air temperatures have displayed larger increases in the winter and spring seasons over the past 100 years (Serreze and Barry, 2011); seasonality which greatly affects the associated sea ice formation and melting processes (e.g. ACIA, 2005; Serreze and Barry, 2011).

It is important to better understand cloud microphysics in the Arctic as clouds contribute significantly towards the Arctic radiative budget (e.g. Intrieri et al., 2002; Shupe and Intrieri, 2004). Arctic clouds often differ from those seen at lower latitudes due to differences in aerosol properties and a unique boundary layer structure (Vihma et al., 2014). Additionally, the sea ice is coupled to the Arctic atmosphere and years of decreased summer sea ice extent have coincided with periods of increased cloudiness and humidity during the spring (Kapsch et al., 2013). The relationship between cloud and sea ice fraction adds complexity to Arctic radiative interactions, as increased cloud cover over a low-albedo ocean would typically act to cool the atmosphere through increased reflectivity of incident solar radiation (Curry et al., 1996; Shupe and Intrieri, 2004). However, in the Arctic this incoming shortwave (SW) solar radiation is minimal from autumn through to spring (Curry et al., 1996), allowing the upward longwave (LW) heat fluxes from the surface to dominate (Intrieri et al., 2002; Palm et al., 2010). The small cloud droplets common in Arctic clouds trap upwelling infrared radiation efficiently, leading to almost twice the amount of total LW than SW radiation at the surface per annum (Curry et al., 1996). Increased springtime cloudiness can therefore lead to increased trapped LW radiation and surface warming, thus potentially affecting the sea ice melt processes.

Single-layer mixed-phase stratocumulus (MPS) clouds are particularly common in the Arctic (e.g. Pinto, 1998; Shupe et al., 2006; Verlinde et al., 2007). Such clouds are sustained by small vertical motions and are characteristically topped with a liquid layer which facilitates ice formation below (Shupe et al., 2006; Vihma et al., 2014). Single-layer MPS are particularly prevalent in the transition seasons (Shupe et al., 2006; Morrison et al., 2012), whereas multi-layered MPS are more common during the summer (Curry et al., 1988, 1996). It is uncertain how Arctic cloud fractions will evolve with increased global temperatures (Curry et al., 1996) and comprehending their relationship with sea ice extent is key to improving the representation of radiative interactions in numerical models. Palm et al. (2010) used remote sensing techniques to show that cloudiness typically increases over the marginal ice zone (MIZ) and ocean in comparison to over the sea ice, forming deeper cloud layers with greater optical depth over the ocean. This study also identified increased cloud fractions in years with decreased sea ice cover, implying an important feedback for Arctic warming. Further investigation of cloud properties in the context of surface ice cover could therefore improve both our understanding of the microphysics of high-latitude clouds and their dependency on and sensitivity to the surface conditions.

Within global climate models (GCMs), one of the largest sources of uncertainty is our poor understanding of cloud and aerosol processes, and this is particularly an issue in the polar regions (Boucher et al., 2013). The paucity of observations in the Arctic leads to an inadequate understanding of aerosol–cloud interactions, which in turn impacts our ability to accurately model the cloud microphysics, boundary layer structure, and radiative interactions in this region (Curry et al., 1996). There has been a drive to collect more in situ observations of Arctic MPS over recent decades. Studies such as the Mixed-Phase Arctic Cloud Experiment (M-PACE, Verlinde et al., 2007) and the Indirect and Semi-Direct Aerosol Campaign (ISDAC, McFarquhar et al., 2011) collected in situ aircraft observations over the Beaufort Sea near Barrow, Alaska during the transition seasons (autumn 2004 and spring 2008 respectively). These studies have substantially improved our knowledge of transition season Arctic clouds; however, key questions remain. For example, how does cloud microphysics change with a changing surface? Do Arctic clouds differ with geographical location? Jackson et al. (2012) found a greater mean liquid water content in clouds over the ocean (during M-PACE) compared with those over the sea ice (during ISDAC), and substantial microphysical differences have been previously identified between cloud observations at three permanent measurement stations in the Canadian Arctic, based on meteorological differences (Shupe, 2011). Given such heterogeneity, studies of other Arctic regions are necessary.

The Aerosol-Cloud Coupling And Climate Interactions in the Arctic (ACCACIA) campaign was carried out to address these questions amongst others. Conducted in the European Arctic in 2013, the ACCACIA project was split into two campaign periods: one in spring (March–April), the other in summer (July). During the springtime campaign, the Facility for Airborne Atmospheric Measurements (FAAM) BAe-146 atmospheric research aircraft was used to collect high-resolution data of cloud and aerosol properties, along with meteorological parameters such as air temperature, humidity, and turbulence, in the Svalbard archipelago off the northern coast of Norway. A primary objective of the ACCACIA campaign was to investigate both the microphysical properties of MPS in the European Arctic and their relationship with sea ice cover. In this study, detailed observations from one case study are presented to illustrate the changing microphysical structure of clouds with sea ice extent.

2 Instrumentation and data analysis

2.1 FAAM aircraft

The FAAM modified BAe 146-301 Atmospheric Research Aircraft (ARA) is fitted with a suite of aerosol, cloud microphysics, and remote sensing instrumentation, detailed by Crosier et al. (2011), Liu et al. (2015), and Lloyd et al. (2015)

amongst others. Measurements from these instruments are used here to investigate microphysical properties of clouds in the context of their environment. In this article, all data are expressed as ambient measurements, and number and mass concentrations are not corrected to standard temperature and pressure conditions.

2.1.1 Meteorological instrumentation

The FAAM Core instrument set was active during this campaign (see Renfrew et al., 2008). The GPS-aided inertial navigation system and Rosemount temperature sensor are utilised in this study to provide a measure of the aircraft's geographical position and the ambient atmospheric temperature respectively. 3-D wind components were measured using both a 5-hole turbulence probe and an AIMMS20AQ turbulence probe (Beswick et al., 2008). Dropsondes were released during the campaign to retrieve vertical profiles of the atmospheric temperature and relative humidity (RH), amongst other properties. Additionally, a downward-facing Leosphere ALS450 lidar provided measurements of cloud top height below the aircraft.

2.1.2 Aerosol instrumentation

Sub-micron non-refractory aerosol composition was measured by a Compact Time-of-Flight Aerosol Mass Spectrometer (C-ToF-AMS, Aerodyne Research Inc., Canagaratna et al., 2007). This instrument has been used extensively in previous aircraft campaigns to characterise such aerosol (e.g. Morgan et al., 2010). Black carbon loadings were monitored with a Single Particle Soot Photometer (SP2, Droplet Measurement Technologies, DMT) and its usage during the ACCACIA campaign is discussed by Liu et al. (2015).

Fine-mode aerosol particle concentrations (spanning particle diameters, D_P, 3 nm–3 µm) were measured using a TSI 3786-LP ultrafine Condensation Particle Counter (CPC). A Passive Cavity Aerosol Spectrometer Probe (PCASP 100-X, DMT, Rosenberg et al., 2012) was used to count and size accumulation-mode aerosol particles of sizes 0.1 to 3 µm. Particle samples (of sizes $\sim$0.1–10 µm) were collected on Nuclepore polycarbonate filters exposed from the aircraft for compositional analysis (Young et al., 2016). Additionally, number concentrations and size distributions of aerosol particles and cloud droplets (of sizes 0.6 to 50 µm) were measured using a Cloud Aerosol Spectrometer with depolarisation (CAS-DPOL, DMT, Baumgardner et al., 2001; Glen and Brooks, 2013).

2.1.3 Cloud microphysical instrumentation

Size-resolved cloud droplet concentrations ($3\,\mu m < D_P < 50\,\mu m$) were measured with a Cloud Droplet Probe (CDP-100 Version 2, DMT, Lance et al., 2010). These measurements are used to derive the liquid water content (LWC) of the observed clouds in this study, and this measure is used to distinguish between in-cloud and out-of-cloud observations (using a threshold of $\leq 0.01\,g\,m^{-3}$ for the latter). Bulk liquid water measurements were also made using a hot-wire (Johnson-Williams) probe: these data compared well, yet there were signal lag issues when exiting cloud with the hot-wire probe. Therefore, the CDP measurement is solely used for the analysis detailed herein. Additionally, these CDP data are used to compute the mean cloud droplet effective radius within the cloud layers.

The 2-Dimensional Stereo particle imaging probe (2DS, SPEC Inc., Lawson et al., 2006) and Cloud Imaging Probes (CIP15, Baumgardner et al., 2001, and CIP100, DMT) are wing-mounted optical array shadow probes (OAPs) used here to investigate the ice phase of the clouds observed. The 2DS images with 10 µm resolution over a size range of 10 to 1280 µm, whilst the CIP15 and CIP100 provide 15 and 100 µm resolution from 15 to 930 and 100 to 6200 µm respectively. The CIP15 also provides additional information with 3-level grey-scale image intensity data, used to improve the correction of oversizing due to depth of field errors.

Processing and analysis of these OAP data has been discussed previously (Crosier et al., 2011, 2014; Taylor et al., 2016). Here, we follow the same data processing methodology as Taylor et al. (2016). Particle phase was established by segregating imaged particles into categories based on their circularity (Crosier et al., 2011); highly irregular particles were classified as ice crystals, whilst circular images were classified as cloud or drizzle drops, dependent on size. Image reconstruction was not used to extend the size ranges of the optical array probes. Phase identification of small particles (< 80 µm) could not be conducted due to the low resolution of the 2DS and CIP15 in this limit. Small particles measured by the OAPs are not considered in detail due to this phase uncertainty; therefore, CDP measurements are solely used to investigate small cloud particles. These are assumed to be liquid cloud droplets, and the potential contribution of small ice particles (< 80 µm) is not examined.

Finally, 8-bit images of cloud particles were taken with 2.3 µm spatial resolution using a Cloud Particle Imager (CPI, SPEC Inc. Lawson et al., 2001). However, the CPI is not used quantitatively in this study: the small sample volume introduces error into the measurements, manifesting as high local particle concentrations in regions of low ambient number concentrations (Lawson et al., 2001).

2.2 Additional data

Derived cloud top temperature from MODIS satellite retrievals and AVHRR visible satellite imagery are used to illustrate cloud spatial structure and distribution. Additionally, sea ice fraction from NASA's National Snow and Ice Data Center (NSIDC), derived from passive microwave brightness temperatures (Peng et al., 2013), and the approximate ice fraction from the Met Office Unified Model (MetUM) are used to contextualise the in situ observations.

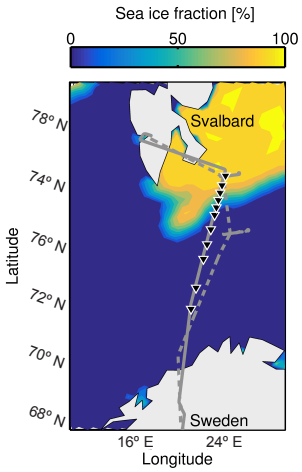

Figure 1. Flight track for B762 on 23 March 2013 over sea ice fraction (shading). Section 1 of the flight (grey, solid) was conducted at a high altitude, where 11 dropsondes (black triangles) were released. Section 2 of the flight (grey, dashed) conducted straight, level runs over the sea ice and open water, with a sawtooth profile over the transition region.

3 B762: Case study

Flight B762 took place on 23 March 2013. It was a two-part flight starting and ending in Kiruna, Sweden, and refuelling in Longyearbyen, Svalbard, Norway. Section 1 of the flight was a continuous high-altitude straight, level run (SLR) at approximately 8000 m, where the lidar was used to sample the cloud structure below. A number of dropsondes were released during this section and the release locations (shown in Fig. 1) allowed for measurements of the atmospheric structure over the varying surface conditions, i.e. open ocean, MIZ, and sea ice. The MIZ occurred between approximately 75 and 76.5° N, north of which a continuous sea ice pack was present. In this study, the MIZ is approximated by NSIDC ice fractions between 10 and 90 %, as indicated in Fig. 1. Other springtime ACCACIA flights were also designed to investigate changes in atmospheric properties over the transition between sea ice and the ocean; however, flight B762 was the only case which made detailed observations of cloud microphysics over both the sea ice and ocean as well as over the transition in between.

Section 2 was split into three parts: a series of SLRs at various altitudes over the sea ice, a sawtooth profile transitioning from sea ice to ocean, and a second set of SLRs over the ocean. The flight was designed to investigate the variation in cloud and boundary layer structure over the sea ice and the ocean. Low visibility prevented the second set of runs being completed as planned; however, good data coverage of the cloud over the ocean was still achieved.

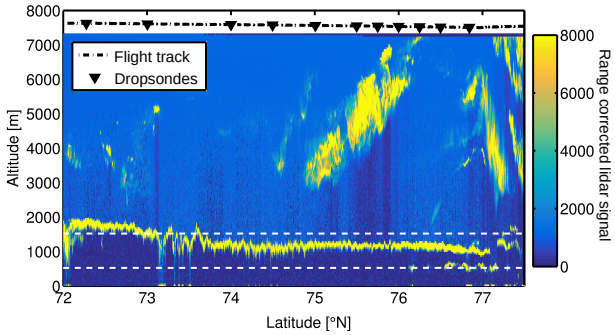

Figure 2. Lidar signal from section 1 of the flight. Aircraft altitude is indicated (black) and each dropsonde release point is marked (downward-facing triangles). White dotted lines are shown at 500 and 1500 m to ease comparison with the in situ observations.

Local atmospheric conditions

Cloud layers were observed with the lidar during section 1 of flight B762 (Fig. 2). A continuous layer was observed where cloud top descended from approximately 1900 to 1100 m with increasing latitude. Evidence of a second, lower-altitude cloud layer can be seen at high latitudes (500 m at 76.5° N) through breaks in the continuous layer. The 500 m cloud was not observed at lower latitudes along the flight path sampled (between approximately 73 and 73.5° N), as indicated by the surface echo measured during breaks in the cloud above. An intermittent, high-altitude cirrus layer (with optical depth ~ 0.5) was seen at various levels from 3000 to 8000 m at higher latitudes on the approach to Longyearbyen. However, these data cannot be used to indicate the spatial extent of these structures as measurements were only made along the flight path.

The structure of the lower troposphere was sampled extensively in section 1 by the 11 dropsondes marked in Fig. 1. A summary of key information from each dropsonde is listed in Table 1. These measurements were collected approximately 2 h before and to the west of the in situ cloud observations of section 2; however, the dropsonde and lidar measurements provide a good indication of the structure of the atmosphere during this study.

Figure 3 indicates that the boundary layer structure varied with latitude. Figure 3b and d show vertical profiles of Θ and RH data obtained from dropsondes nos. 5 and 11, collected at latitudes comparable to the in situ aircraft runs of section 2. A double potential temperature inversion can be seen over the sea ice (no. 11), whereas the temperature profile over the ocean indicates that the boundary layer was well-mixed and coupled to the surface (no. 5). The double temperature inversion over the sea ice is mirrored by twin RH peaks measured at the corresponding altitudes (~ 84 %, 500 and 1100 m, no. 11, Fig. 3d), suggesting the presence of two cloud layers <1500 m below a dry region above the bound-

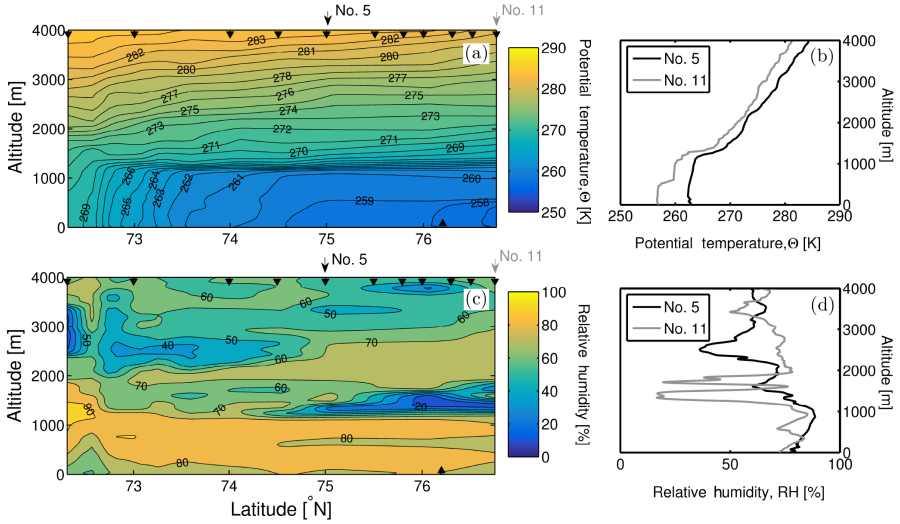

Figure 3. Contour figures of potential temperature (Θ, **a**) and relative humidity (RH, **c**) using data from the 11 dropsondes released on approach to Longyearbyen, Svalbard. Dropsonde release locations (downward-facing triangles) and the approximate sea ice edge (upward-facing triangle) are marked. Profiles of Θ **(b)** and RH **(d)** from dropsondes nos. 5 and 11 are also shown due to their comparable latitudes to the in situ observations (see Table 1). The positions of these dropsondes relative to the others are indicated above panels **(a, c)**.

Table 1. Key dropsonde information.

Sonde	Latitude [° N]	Longitude [° E]	Temperature[a] [°C]	Surface condition[b]
1	72.2	21.6	−3.4	Ocean
2	72.9	22.2	−4.4	Ocean
3	73.9	23.3	−7.3	Ocean
4	74.4	23.9	−9.3	Ocean
5	75.0	24.5	−10.5	Ocean
6	75.4	25.2	−12.3	Ocean
7	75.7	25.5	−13.3	MIZ
8	75.9	25.9	−14.2	MIZ
9	76.2	26.2	−14.7	Sea ice
10	76.4	26.6	−15.0	Sea ice
11	76.8	27.3	−16.4	Sea ice

MIZ: marginal ice zone. [a] Near-surface ambient atmospheric temperature. [b] Based on NSIDC daily average sea ice fraction.

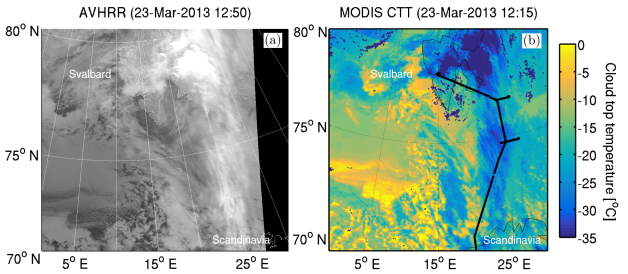

Figure 4. AVHRR visible satellite image **(a)** and cloud top temperature (CTT) derived from MODIS retrievals **(b)** at times close to the start of section 2 of B762. Section 2 of the flight track is indicated (black) in **(b)**.

ary layer (∼ 1500–2000 m). At lower latitudes over the ocean (74 °N), a single, moist layer was observed between approximately 300 and 1200 m. A single temperature inversion was measured by the dropsondes at approximately 1300 m at this latitude. These cloud layers measured by the dropsondes are in accordance with the lidar data (Fig. 2). However, these data are affected by a dry bias of approximately 15–20 %, where in-cloud RHs of 84 % in dropsonde no. 11 and 88 % in dropsonde no. 5 were measured. Dry biases have been observed in dropsonde data in previous studies (e.g. Ralph et al., 2005), and have been attributed to a slow response time at low temperatures (Poberaj et al., 2002; Miloshevich et al., 2004). Sondes are particularly prone to these response issues when descending from a dry region into a cloudy region (Wang, 2005), which was the case for both of our considered dropsondes.

Near-surface temperatures sampled by the dropsondes were approximately 13 °C colder to the north over the sea ice (−16.4 °C at 76.8° N) than over the ocean to the south (−3.4 °C at 72.2° N, see Table 1). Between the latitudes of the in situ measurements (dropsondes nos. 5 and 11), the difference in near surface temperature is approximately 6 °C.

Satellite imagery was examined to provide lateral context for the dropsonde and lidar measurements. Figure 4 displays AVHRR visible satellite imagery in panel a and the derived cloud top temperature from MODIS satellite data in panel b. The flight track of section 2 is overlaid to indicate the regions sampled with the aircraft. The high-altitude cirrus layer indicated by Fig. 2 can be seen with both of these data. This cirrus cloud was to the north-west of the main science region

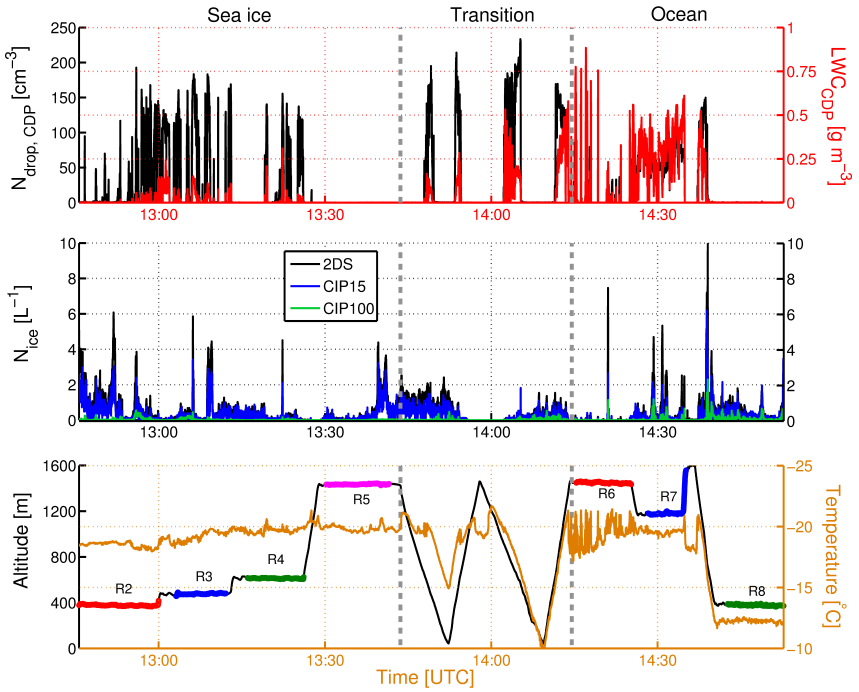

Figure 5. Time series of data collected during the science period of ACCACIA flight B762. Top: CDP droplet number concentration (black) and derived liquid water content (red). Middle: 2DS (black), CIP15 (blue), and CIP100 (green) ice number concentration. Bottom: GPS altitude (black), with individual SLRs noted in colour, and temperature measured by the Rosemount de-iced temperature sensor (orange). SLR colours relate to data shown in Figs. 6 and 9. Sea ice, transition, and ocean regions are indicated above the top row.

investigated, closer to Spitsbergen. At the locations sampled during the aircraft runs (Fig. 4b), there is no clear indication of a higher cirrus cloud layer, and the cloud top temperature is approximately −18 and −23 °C over the sea ice and ocean regions respectively.

A weak low pressure system was present to the east during the sampling period; however, conditions were dominated by high pressure to the west, causing a northerly flow of air from over the sea ice. Cold-air outbreak conditions, with wind speeds of $\sim 10\,\mathrm{ms}^{-1}$ measured within the boundary layer, were maintained for the duration of the science period. Aircraft measurements were made through a band of cloud orientated in the N–S direction, influenced by this northerly flow. Back trajectory analyses (shown in the Supplement, Fig. S1) also show that the sampled air came from the north, having travelled from northern Canada and/or Greenland, depending on the period of interest.

4 In situ observations

4.1 Cloud microphysics

4.1.1 Sea ice

Section 2 of the flight began in Longyearbyen, Svalbard and ended in Kiruna, Sweden. A series of SLRs were performed on an easterly or westerly heading, at an approximately constant latitude. Details of each run are listed in Table 2. Run 7 finished early due to instrument icing as a result of flying in the supercooled mixed-phase cloud layer. No additional runs after run 8 were possible as visibility was severely reduced due to below-cloud haze. A time series of the microphysical observations is shown in Fig. 5.

Figure 6 shows the droplet and ice crystal number concentrations (N_{drop}, N_{ice}) measured over the sea ice by the CDP and 2DS. These measurements indicate the presence of a mixed-phase cloud between 300 and 700 m, with mean droplet and ice number concentrations of approximately $90\,\mathrm{cm}^{-3}$ and $1\,\mathrm{L}^{-1}$ respectively at ~ 400 m. Mean droplet number concentrations varied with altitude in cloud, with an overall average (and standard deviation) of $110 \pm 36\,\mathrm{cm}^{-3}$. 2DS ice concentrations agree well with the CIP15 (shown in Fig. 5). Derived mean CDP LWC peaks at $\sim 0.05\,\mathrm{g\,m}^{-3}$ at 400 m, where the mean temperature is −19 °C. For the majority of the sea ice cloud layer sampled, rimed crystals dominated. Other habits such as columns and dendrites were also prevalent. The double temperature inversion suggested by the sea ice dropsondes in Fig. 3 can also be seen here at 600 and 1100 m, though not as clearly. The secondary cloud layer at ~ 1000 m, indicated by the dual RH peaks in Fig. 3c and d, is observed; however, it is not as extensive as the main layer. This layer likely dissipated somewhat from the time of the

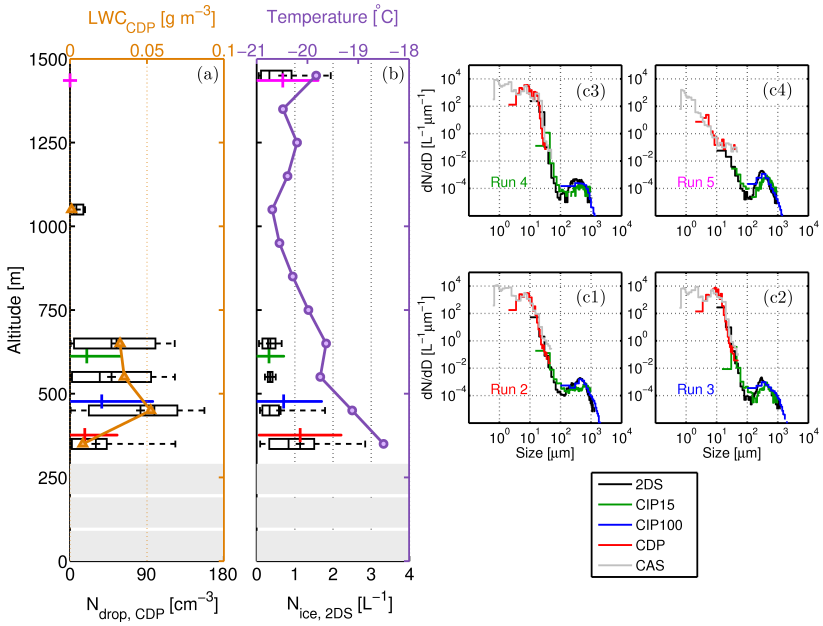

Figure 6. Microphysics summary of averaged observations over the sea ice. **(a)** CDP droplet number concentration (boxes, black) with derived liquid water content overlaid (orange). **(b)** 2DS ice crystal number concentration (boxes, black) with mean temperature measured overlaid (purple). Only CDP and 2DS data $> 0.5\,\mathrm{cm}^{-3}$ and $> 0.05\,\mathrm{L}^{-1}$ respectively have been included. Box edges represent the 25th and 75th percentiles, and the median and mean values are denoted by | and + respectively. Altitudes not sampled are blocked out (≤ 300 m). **(a, b)** Number concentrations from each SLR are shown in colour at each corresponding altitude (run 2: red, run 3: blue, run 4: green, run 5: magenta). Arithmetic means are indicated (|) with each horizontal bar extending to $\pm 1\sigma$. **(c1–4)** Number size distributions ($\mathrm{d}N/\mathrm{d}D$) from each SLR over the sea ice (runs 2–5). Legend refers to **(c)** only.

Table 2. Straight and level run information. Values quoted are arithmetic mean quantities, with 1σ listed in brackets.

Run	Start time [UTC]	End time [UTC]	Direction	Altitude[a] [m]	Temperature[b] [°C]	% in cloud[c]	Latitude [° N]	Surface condition
2	12:45:39	13:00:00	W to E	377 (6)	−18.5 (0.2)	11.7	76.8	Sea ice
3	13:03:07	13:12:06	E to W	477 (5)	−19.2 (0.4)	27.0	76.8	Sea ice
4	13:16:03	13:26:10	W to E	612 (3)	−19.7 (0.2)	17.8	76.8	Sea ice
5	13:30:15	13:41:33	E to W	1435 (4)	−19.9 (0.3)	0	76.8	Sea ice
6	14:15:20	14:25:16	W to E	1449 (6)	−19.4 (0.9)	14.7	74.8	Ocean
7	14:28:19	14:35:09	E to W	1190 (56)	−19.6 (0.3)	92.0	74.8	Ocean
8	14:42:39	14:52:46	W to E	378 (5)	−12.3 (0.1)	0	74.8	Ocean

[a] Derived from GPS measurements. [b] Ambient temperature measured with the Rosemount de-iced temperature sensor. [c] In cloud defined as when CDP LWC $\geq 0.01\,\mathrm{g\,m}^{-3}$.

dropsonde measurements. For the purpose of this study, this sea ice cloud (300–700 m) is treated as a single-layer MPS.

During these sea ice SLRs, the aim was to measure below, in, and above the cloud layer. The lowest altitude case (run 2) was carried out in a haze layer present between cloud base and the surface. This haze was only measured over the sea ice region. As described by Young et al. (2016), aircraft filters were exposed during this run, and a silicate dust concentration of $\sim 0.4\,\mathrm{cm}^{-3}$ was measured. No vertical profiles of mineral dust were obtained, and these data are only valid below cloud, at approximately 380 m, over the sea ice. The size distribution of this mineral dust, in conjunction with the cloud top temperature (−19.7 °C), was used to evaluate the Niemand et al. (2012, hereafter N12) primary ice nucleation parameterisation. Due to turbulent motions within the cloud, ambient temperatures could not be used as an indicator of ice-nucleating particles (INPs) or ice crystals at specific altitudes; therefore, the coldest in-cloud temperature was used to provide an upper limit of predicted ice concentrations within the cloud. Predicted ice number concentrations were approximately $0.7\,\mathrm{L}^{-1}$. Dust concentrations of double and triple that measured were also used to evaluate N12 to test sensi-

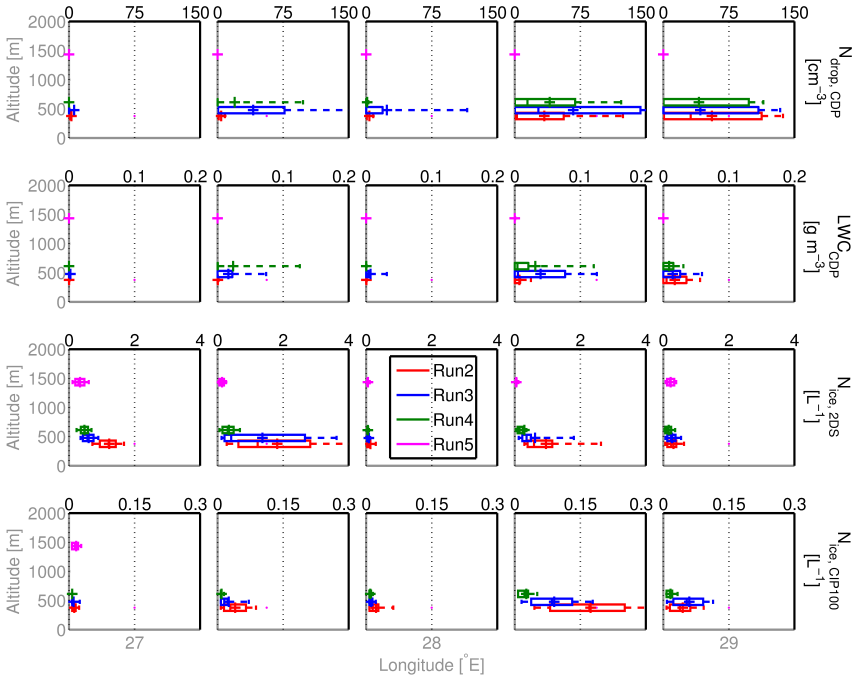

Figure 7. Percentile plots of CDP droplet number concentration (first row), CDP liquid water content (second row), 2DS ice number concentration (third row) and CIP100 ice number concentration (fourth row) measured over the sea ice. Each column represents a different longitude bin, moving from west (left) to east (right). Data are plotted against altitude (grey axis) and are coloured differently dependent on the SLR at which the data were measured, as indicated in the legend. Data correspond to the scale on the top x axis of each segment.

tivity to this input. The shape of the dust surface area distribution was maintained and the number concentration in each bin was scaled accordingly. Dust number concentrations $> 0.5\,\mu m$ were also used to evaluate the DeMott et al. (2015, hereafter D15) parameterisation, predicting $0.02\,L^{-1}$. Additionally, number concentrations of all measured aerosol particles $> 0.5\,\mu m$ from the aircraft filters, PCASP, and CAS-DPOL were used to evaluate the DeMott et al. (2010, hereafter D10) and Tobo et al. (2013, hereafter T13) parameterisations. Predicted ice number concentrations were 1.90 and $1.10\,L^{-1}$, respectively, using PCASP data. Inputs and outputs of these four parameterisations are detailed in Table 3.

Longitudinally separated data from runs 2, 3, and 4 are displayed in Fig. 7. The cloud was observed to be spatially inhomogeneous. Cloud particle concentrations increase at similar geographical locations indicating that the same cloud layer was sampled at the different altitudes. Run 5 was conducted above the cloud layer to characterise aerosol size distributions and composition. However, ice crystals were observed, and images collected by the CPI towards the end of this run are shown in Fig. 8. Pristine bullet rosettes were observed, indicating that these crystals had fallen from a greater height without interaction with liquid cloud. Bullet rosettes were observed at the western fringes of the sea ice cloud with the 2DS and CIP15 ($\sim 27°$ E, Fig. 7); however, some crystal aggregates were also observed with the CPI in the main cloud, though these were very few in number. Due to the dominance of large rimed ice crystals, it is difficult to conclusively state if appreciable concentrations of these bullet rosettes precipitated into and interacted with the main cloud layer considered.

Figure 6c1–4 show the number size distributions measured along each SLR carried out over the sea ice. A droplet mode at $\sim 10\,\mu m$ can be seen in Fig. 6c1–3 – corresponding to the in-cloud runs (runs 2–4) – with the CAS-DPOL and CDP measurements. This mode is distinctly missing from the run 5 data; negligible droplet concentrations were observed at this altitude, with ice crystals dominating overall particle concentrations.

4.1.2 Ocean

Figure 9 shows the droplet and ice crystal number concentrations for the ocean section of the flight. Over the ocean, the cloud layer extends from 700 to 1500 m. CDP LWC displays a more consistent profile in this section, with a mean value of $\sim 0.3\,g\,m^{-3}$ measured between approximately 1100 and 1400 m. Mean droplet number concentrations were again variable with altitude, with an overall average (and standard deviation) of $63 \pm 30\,cm^{-3}$. 2DS ice crystal data do not follow the same trend as the droplet data, with variable concentrations measured at each altitude bin.

Table 3. Summary of inputs to and evaluations of the N12 (Niemand et al., 2012), D15 (DeMott et al., 2015), D10 (DeMott et al., 2010), and T13 (Tobo et al., 2013) parameterisations. Silicate dust concentrations derived from filter analysis presented by Young et al. (2016) are used to evaluate N12 and D15. No filter data are available over the ocean.

Surface	Temperature [°C]	Aerosol input	$N_{aerosol}$ [cm^{-3}]	N_{ice} [L^{-1}]			
				N12	D15	D10	T13
Sea ice	−19.7	Filter[a]	0.4	0.7[b]	–	–	–
		Filter[a,c]	0.2	–	0.02	–	–
		2 × Filter[a]	0.7	1.4[b]	–	–	–
		3 × Filter[a]	1.1	2.1[b]	–	–	–
		Filter[c]	0.6	–	–	0.9	0.07
		PCASP[c]	2.00	–	–	1.90	1.10
		CAS-DPOL[c]	6.85	–	–	3.31	19.7
Ocean	−20.1	PCASP[c]	2.72	–	–	2.23	2.66
		CAS-DPOL[c]	1.11	–	–	1.28	0.34

[a] Silicate dust concentration. [b] Derived frozen fraction applied to dust distribution. [c] Particle concentration > 0.5 µm.

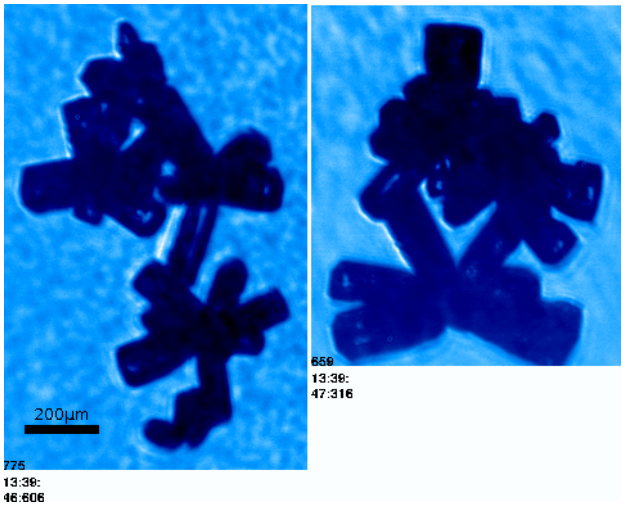

Figure 8. CPI ice crystal images from run 5. Time stamps are indicated below each image.

Run 7 was conducted within the cloud layer and probe icing was noted. The ice number concentrations from this run are not substantially greater than any of the others, suggesting this icing problem may not have greatly affected the measurements; however, there is an increased CIP100 mode within the number size distributions (at sizes > 100 µm, Fig. 9c2) which is not mirrored by the CIP15.

This cloud is more homogeneous in the liquid phase than the layer measured over the sea ice (Fig. 10), with consistent droplet concentrations and LWC values (∼ 70 cm^{-3} and 0.3 g m^{-3} respectively) measured with changing longitude during each run. As with the sea ice SLRs, a clear droplet mode is visible at approximately 10 µm in runs 6 and 7 (Fig. 9c1, 2). This mode is not clear in run 8. This run was carried out at low altitude below cloud to collect aerosol data. However, as with run 5, some ice was measured by the 2DS, CIP100, and CIP15 (Figs. 9 and 10). Images from the CIP100 during run 8 are shown in Fig. 11. Large dendritic crystals are present, with notable riming, of sizes ∼ 1–1.6 mm. Their size and structure suggests interaction with cloud droplets within cloud, subsequent growth, and eventual precipitation as snow.

High ice number concentrations were measured between 700 and 900 m at cloud base. Size distributions from the microphysics probes during this period are shown in Fig. 9c4: an enhanced secondary mode of ice crystals ≥ 100 µm is observed, in addition to a broadened CDP distribution. The mean temperature measured was approximately −16 °C and numerous large dendrites were observed; large, fragile crystals which may fragment easily upon collision. CIP100 images of these crystals are shown in Fig. S2. 2DS ice crystal concentrations increase to a mean value of approximately 5 L^{-1}, much greater than the mean concentration observed within the mixed cloud layer (∼ 1 L^{-1}).

Below-cloud aerosol measurements were again used to evaluate the D10 and T13 parameterisations in conjunction with the cloud top temperature (−20.1 °C). Using PCASP data as input, predicted INP concentrations were 2.23 and 2.66 L^{-1} respectively (see Table 3). No filter data are available over the ocean; therefore, N12 and D15 could not be evaluated.

4.1.3 Transition region

Several profiles were flown in a sawtooth over the transition region between the sea ice and open ocean. Profile 5 was conducted over sea ice, profiles 6 and 7 were over the MIZ, and profile 8 was over the ocean (see Table 4).

Figure 12 shows the CDP droplet number concentrations and derived LWC from each profile, with altitude and mean droplet effective radius, R_{eff}, overlaid in the top and bot-

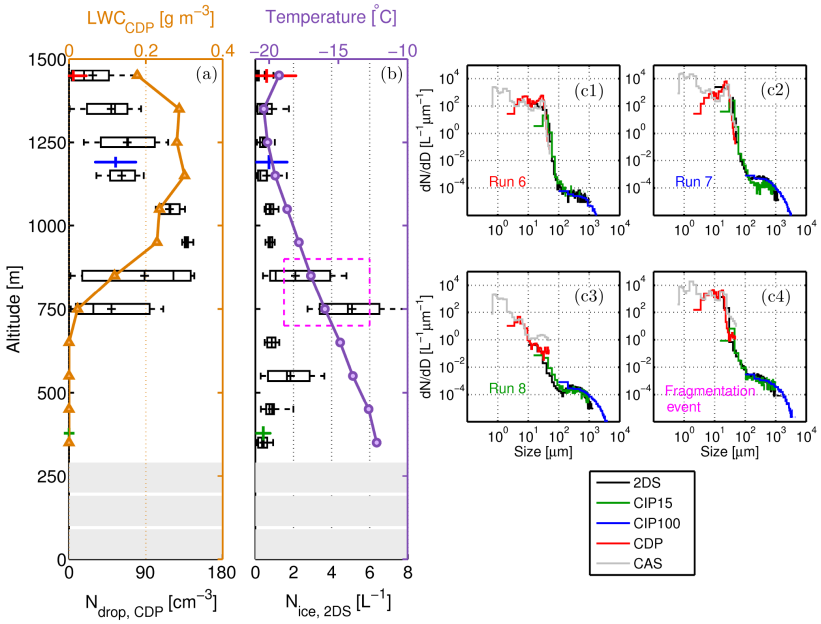

Figure 9. Microphysics summary of averaged observations over the ocean. Data are displayed similarly to Fig. 6. In **(a, b)**, data from each SLR are again shown in colour at each corresponding altitude (run 6: red, run 7: blue, run 8: green) as before. **(c1–4)** Number size distributions (dN/dD) from each SLR over the ocean (runs 6–8). Legend refers to **(c)** only. High ice number concentrations at cloud base are labelled as a fragmentation event (see Sects. 4.1.2 and 5.3).

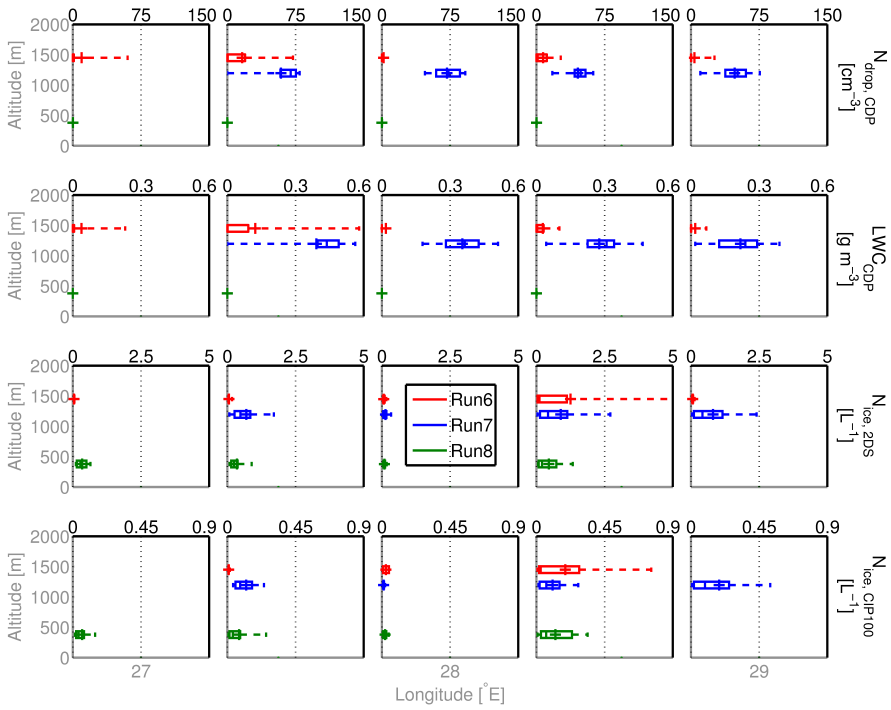

Figure 10. Percentile plots of CDP droplet number concentration (first row), CDP liquid water content (second row), 2DS ice number concentration (third row), and CIP100 ice number concentration (fourth row) measured over the ocean. As in Fig. 7, columns represent different longitude bins and data are coloured by SLR (as shown in the legend).

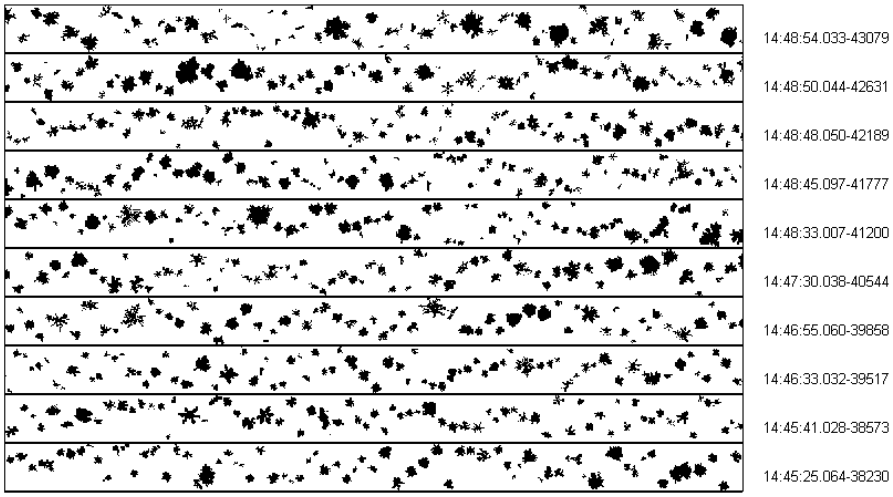

Figure 11. Example CIP100 data from run 8. Vertical width of image strip represents a size range of 6.4 mm.

Table 4. Sawtooth profile information.

Profile	Time [UTC]		Altitude [m]		Latitude [° N]		Temperature [°C]	
	Start	End	Start	End	Start	End	Min	Max
5	13:43:37	13:52:15	1423	47	76.6	76.1	−21.2	−15.0
6	13:52:15	13:57:50	43	1450	76.1	75.8	−20.7	−14.9
7	13:57:50	14:09:27	1459	42	75.8	75.1	−21.7	−9.4
8	14:09:28	14:14:32	43	1469	75.1	74.8	−21.3	−9.3

tom rows respectively. These data show a clear lifting and deepening of the cloud layer when transiting from sea ice to open ocean. Mean in-cloud droplet number concentrations increase through the transition, peaking at $145 \pm 54\,\mathrm{cm}^{-3}$ during profile 7. N_{drop} then begins to decrease in profile 8 ($120 \pm 33\,\mathrm{cm}^{-3}$). The corresponding mean LWC and droplet effective radii increase from 0.1 to $0.4\,\mathrm{g\,m}^{-3}$ and 5 to 8–10 µm respectively over the transition from sea ice to ocean.

Figure 13 shows the 2DS and CIP100 ice concentrations measured over the transition region. Ice number concentrations measured by each instrument remain consistent over the transition, with a mean number concentration of approximately $0.1\,\mathrm{L}^{-1}$ measured by the CIP100 over the sea ice and ocean. A slight decrease in the mean 2DS ice concentration can be seen from sea ice to ocean, from approximately 1.5 to $0.5\,\mathrm{L}^{-1}$. The lifting and deepening of the liquid cloud layer seen in Fig. 12 is not apparent with these ice data. The CIP100 in particular shows a contrasting trend; increasing concentrations below cloud toward the surface suggests precipitation as snow from the cloud layers above. The measured concentrations marginally increase over the ocean, and this precipitation is observed over a greater altitude range due to the lifting of cloud base.

The double temperature inversion indicated in the dropsonde data (Fig. 3) can be viewed in the first two profiles. The lower inversion is eroded to produce a clear, single inversion at ∼1400 m during the last profile over the ocean. The gradient of the temperature profile decreases over the ocean due to surface warming, whilst the cloud top temperature remains approximately −20 °C with the changing surface.

4.2 Aerosol

Aerosol number concentrations measured by the various probes on board the aircraft are reported in Table 5. CPC particle number concentrations are greater at high altitudes (> 800 m) over both surfaces, as is the total concentration recorded by the PCASP over sea ice. The gradient in CPC concentration is greatest over the ocean, with a high-altitude measurement of over 4 times that measured at low altitude. These number concentrations are not observed to the same extent in the PCASP data.

Over the ocean, the number concentrations measured by the PCASP (both total and > 0.5 µm) and CAS-DPOL are approximately constant with altitude. Concentrations of large aerosol (which may act as ice-nucleating particles, $D_{\mathrm{P}} > 0.5$ µm) are approximately uniform with altitude over the ocean. Over the sea ice, a greater loading of coarse-mode aerosol is measured nearer the surface and this consistency with altitude is not observed.

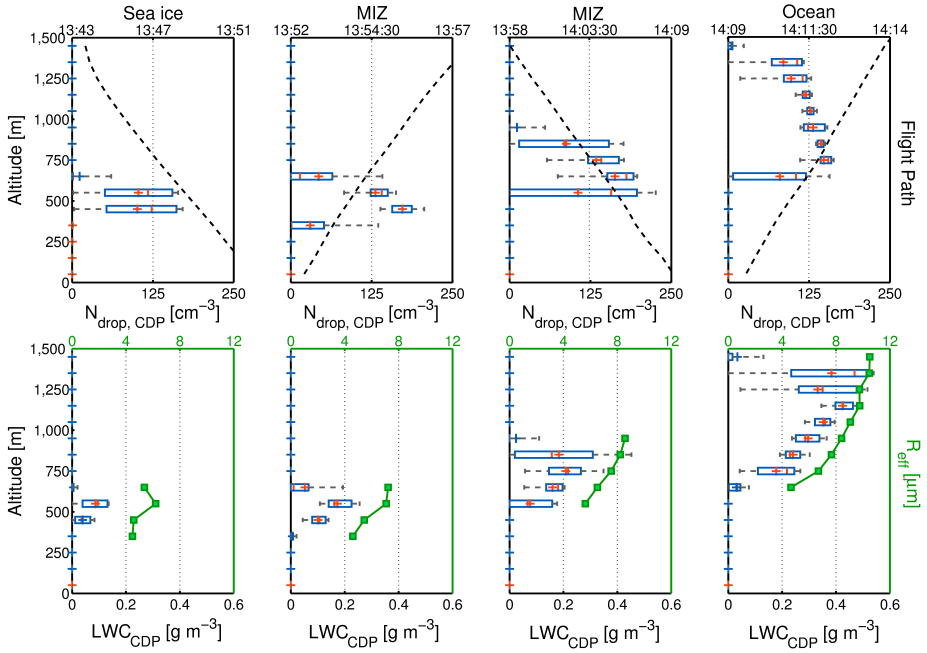

Figure 12. CDP data from the sawtooth profiles. Cloud droplet number concentration (cm^{-3}, top row) and derived LWC ($g\,m^{-3}$, bottom row) are shown. Box edges again indicate the 25 and 75 % thresholds of the data, mean values are shown as a red cross and outliers extend to the 10 and 90 % thresholds of the data. The altitude of the aircraft is indicated (black, dashed) in the top row and mean droplet effective radius – in µm, derived from CDP measurements – is shown (green) in the bottom row. Columns indicate the different profiles, transitioning from sea ice to ocean from left to right.

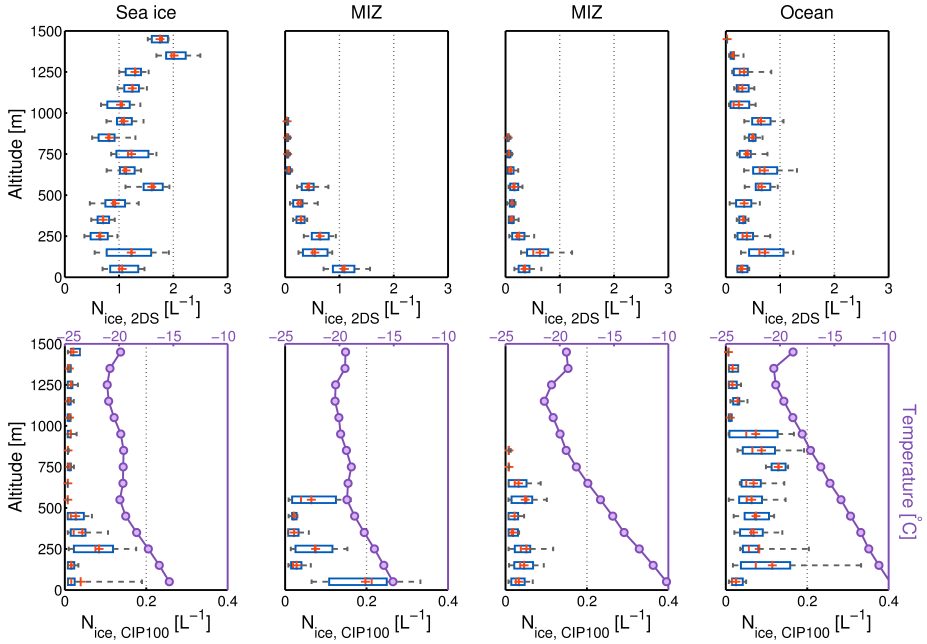

Figure 13. Ice number concentrations (L^{-1}) from the 2DS and CIP100 over the transition region. Data are displayed similarly to Fig. 12. Temperature is overlaid (purple) in the bottom row.

In general, the number concentrations measured over the ocean are lower than over the sea ice. Figure 14 displays the size distributions from the PCASP and CAS-DPOL split into high- and low-altitude data. Small particles measured by the PCASP ($0.1\,\mu m < D_P < 0.5\,\mu m$) reach a greater number concentration over the sea ice than over the ocean. Low-altitude CAS-DPOL concentrations over the sea ice are heightened with comparison to the high-altitude data. It is possible that swollen aerosol particles associated with the haze layer were being measured, enhancing the number concentration. Such particles may not be removed from these data using the CDP LWC $\leq 0.01\,g\,m^{-3}$ out-of-cloud threshold applied here. Over the ocean, data from both instruments are more comparable; however, the low-altitude PCASP data show a greater loading across most sizes.

Non-refractory sub-micron aerosol composition measured by the AMS is shown in Fig. 15. Technical issues prevented continuous measurement over the ocean, with problems occurring during run 7. The measured nitrate mass loading remains low and consistent throughout. The sulfate loading is variable with altitude, especially over the transition region between ice and ocean. Higher mass loadings are measured at higher altitudes ($\sim 1\,\mu g\,m^{-3}$ at 1400 m). Increasing during the last SLR over the sea ice (run 5), the signal becomes highly variable over the sawtooth profile. Such variability is also observed in the organic and ammonium traces. PCASP particle number and SP2 black carbon (BC) mass observations follow the same trends throughout the science period, both mirroring the same sinusoidal pattern over the MIZ. Both signals are variable, with increases observed at high altitudes, but no distinct differences are observed between sea ice and ocean measurements.

4.3 Boundary layer dynamics

Turbulent kinetic energy (TKE) and sensible and latent heat fluxes measured along the flight path are shown in Fig. 16. Approximate MetUM ice fraction is shown in the left-hand and middle columns. Over the sea ice, the sensible and latent heat fluxes and the TKE remain relatively constant at about $0\,W\,m^{-2}$ and $0.5\,m^2\,s^{-2}$ respectively. More variability is observed in these three parameters over the ocean. Sensible heat fluxes range from -20 to $0\,W\,m^{-2}$ at low altitude over the sea ice, whilst substantially greater values of $> 30\,W\,m^{-2}$ are observed over the ocean, with $> 100\,W\,m^{-2}$ measured in some instances. A similar difference is observed with the latent heat fluxes with variable measurements of approximately $> 50\,W\,m^{-2}$ over the ocean, contrasting observations of $\sim 0\,W\,m^{-2}$ over the sea ice. Low-altitude (~ 350 m) TKE increases from approximately 0–0.5 to $1.5\,m^2\,s^{-2}$ over the transition. TKE, sensible heat fluxes, and latent heat fluxes all increase and become more variable over the MIZ and ocean compared to the sea ice, with the greatest values typically observed at low altitude over the ocean.

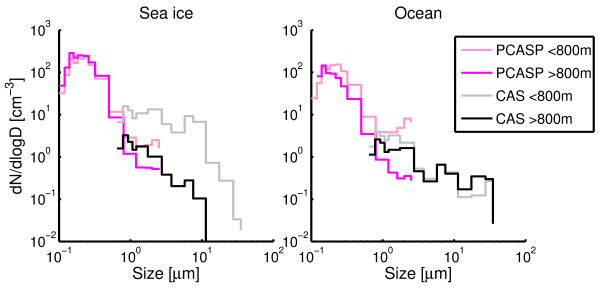

Figure 14. PCASP and CAS-DPOL particle size distributions over sea ice and ocean. Data are split into lower and higher than 800 m to reflect altitude influences. Only out-of-cloud (CDP LWC $\leq 0.01\,g\,m^{-3}$) data are included.

The turbulence and AIMMS probes recorded vertical velocity throughout the science period. The turbulence probe suffered some icing effects during runs 7 and 8, whilst the AIMMS probe collected no data for run 8 due to a technical issue. Averaged PDFs from over the sea ice and ocean are shown in Fig. 17. The turbulence probe and AIMMS PDFs compare well. The sea ice PDF displays little variation, with the majority of measurements lying close to the mean value. Maxima and minima of the distribution are approximately $\pm 1\,m\,s^{-1}$. In comparison, the ocean PDFs are significantly broader, with more variability from the mean observed. Maxima and minima of the ocean PDF extend to $\pm 2\,m\,s^{-1}$ and the distribution is skewed toward updraughts.

5 Discussion

5.1 Sea ice

The averaged data over sea ice point toward a low-altitude cloud with a low liquid water content (Fig. 6). Ice crystal number concentrations are spatially variable within the cloud (Fig. 7) yet they are consistent, suggesting only primary ice nucleation was active. The temperature within the cloud was between -18 and $-20\,°C$ (Fig. 6b), far below the range required for secondary ice production (e.g. Hallett and Mossop, 1974).

Data from runs 2, 3, and 4 depict the typical structure of a single-layer Arctic mixed-phase cloud (e.g. Verlinde et al., 2007; Morrison et al., 2012; Vihma et al., 2014): a liquid layer at cloud top, with ice formation and aggregation below. Such processes are inferred from the relative quantities of ice crystals measured by the 2DS and CIP100 instruments (Fig. 7), as the latter can measure much larger ice crystals than the former. In Fig. 6c, the ice mode is smaller at cloud top (Fig. 6c3, run 4) than cloud base (Fig. 6c1, run 2), indicating that ice nucleation may be occurring towards cloud top; however, this cannot be verified with these data and vertical mixing likely has an influence.

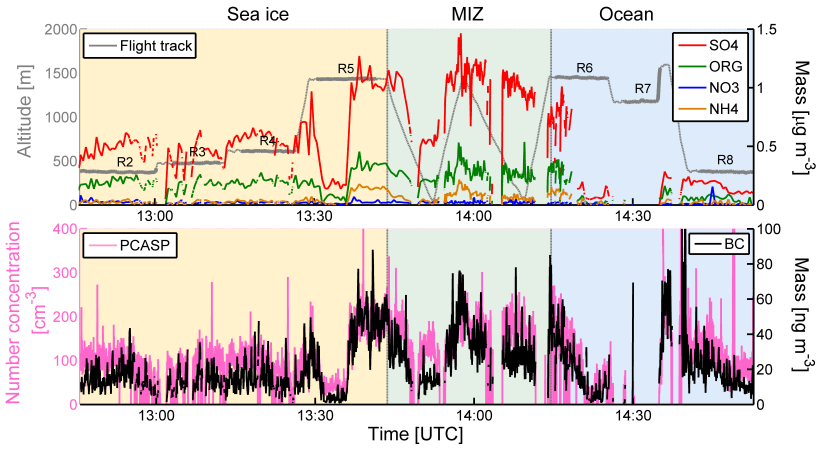

Figure 15. Time series of AMS and SP2 mass loading and PCASP number concentration. Top: flight track is shown in grey (with SLRs indicated in bold) with AMS species indicated by the legend in the top right. Bottom: aerosol number concentration and black carbon mass loading from the PCASP (pink) and SP2 (black) respectively. Only out of cloud (CDP LWC $\leq 0.01\,\mathrm{g\,m^{-3}}$) data are included.

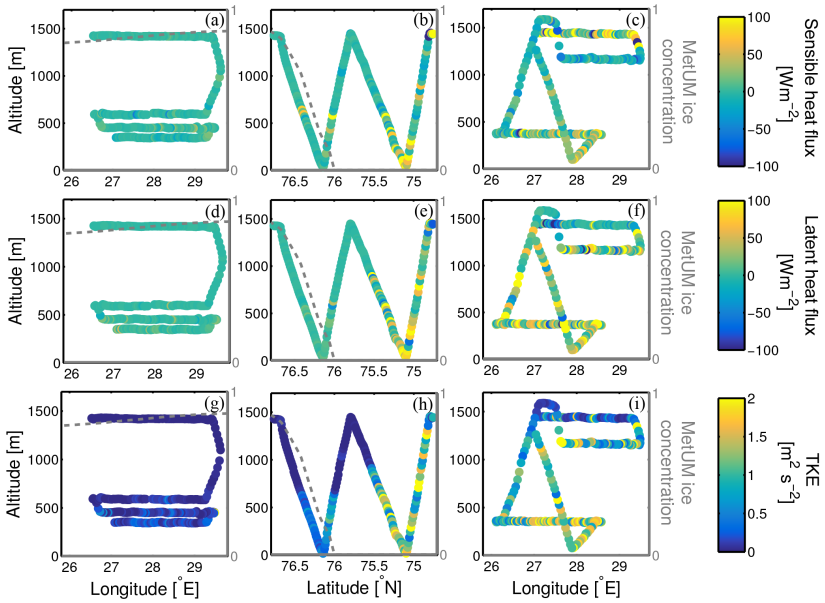

Figure 16. Sensible **(a–c)** and latent **(d–f)** heat fluxes and turbulent kinetic energy (TKE, **g–i**) calculated at 10 s intervals along the flight path. The path of the aircraft with respect to latitude (middle column) or longitude (left- and right-hand columns) is shown, with the measurements indicated in colour. The left column displays data from over the sea ice, whilst the middle and right columns show MIZ and ocean data respectively. Approximate MetUM sea ice fraction is shown (grey, dashed) over the sea ice and MIZ (left and middle columns), and is absent over the ocean (right column).

Run 5 was planned to be an above-cloud aerosol run; however, the 2DS and CIP100 instruments detect notable ice number concentrations to the western end of the run (Fig. 7). This suggests that precipitation from above was being sampled, which could possibly be from the high-altitude cirrus layer observed closer to Spitsbergen (Figs. 2 and 4). Additionally, RH data from the high-latitude dropsondes (Fig. 3c) indicate the possibility of a higher cloud layer (∼2000–3000 m) in this region. CPI ice crystal images during run 5 (Fig. 8) also point towards the sampling of another cloud, as the imaged bullet rosettes typically form at higher, colder altitudes and aggregate as they descend. This ice precipitation was observed predominantly to the west of and was separate from the main cloud layer sampled over the sea ice, and thus was excluded from comparison with the ocean cloud layer.

Observed aerosol concentrations varied substantially with altitude over the sea ice. Results show elevated sulfate, PCASP, CPC, and BC measurements during run 5 (Table 5

Table 5. Background aerosol information, split into high- (> 800 m) and low-altitude (< 800 m) data over the respective surfaces. Arithmetic mean values of number concentration (cm^{-3}) are reported, with 1 standard deviation in brackets.

Instrument	High altitude over ice	Low altitude over ice	High altitude over sea	Low altitude over sea
CPC	351.0 (410.2)	133.4 (34.0)	595.0 (836.8)	129.0 (68.2)
PCASP	109.4 (57.2)	86.2 (21.1)	41.2 (31.4)	48.3 (22.0)
PCASP (> 0.5 µm)	0.95 (4.76)	1.94 (4.97)	0.17 (1.62)	0.54 (3.85)
CAS-DPOL	1.27 (3.72)	11.2 (19.7)	2.48 (7.82)	2.27 (7.29)

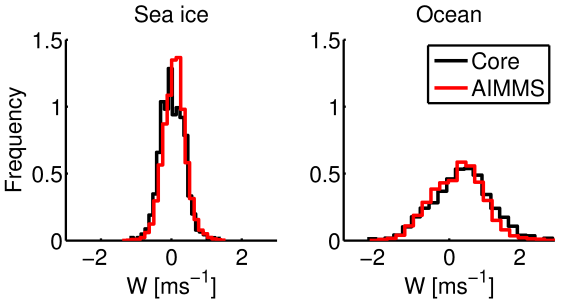

Figure 17. Probability density function (PDF) of updraught velocity from the core turbulence (black) and AIMMS (red) probes. Data from runs 2, 3, and 4 are used for the sea ice, and data from runs 6 and 7 for the ocean. Data from each SLR are normalised such that the mean value is zero.

and Fig. 15), the latter of which is consistent with the Asian BC plumes identified during the ACCACIA campaign (Liu et al., 2015). These plumes contained an average BC mass loading of $\sim 27\,ng\,s\,m^{-3}$ during flight B762, consistent with the low-altitude measurements here (Fig. 15). Similarly, this mass loading is also equivalent to the annual median BC concentration measured at Zeppelin, Svalbard over the period 1998–2007 (Eleftheriadis et al., 2009). PCASP data do not increase as much as the CPC data at high altitudes, suggesting either a pollution layer characterised by small particle sizes ($3\,nm < D_P < 0.1\,\mu m$) or new particle formation at these heights.

More large particles are measured close to the sea ice surface, as shown by the $> 0.5\,\mu m$ PCASP and CAS-DPOL measurements (Table 5). This suggests contributions of primary particle emissions from the surface. A large fraction of these low-altitude particles were sea salt (Young et al., 2016), which could have been transported from the nearby ocean or lofted into the atmosphere by near-surface winds over polynyas or leads in the sea ice. Additionally, frost flowers could be a surface source of modified sea-salt aerosol (Xu et al., 2013); however, their characteristic signature would not be detectable by the analysis presented by Young et al. (2016).

Observed ice crystal number concentrations vary little over the sea ice, with slight increases toward cloud base attributable to aggregation and precipitation out of the cloud. Using the D10 parameterisation, predicted INP concentrations were 0.9, 1.90, and $3.31\,L^{-1}$ for aerosol particle number concentrations measured by the aircraft filters (Young et al., 2016), PCASP, and CAS-DPOL respectively (listed in Table 3). When using D10, the filter data produce the best agreement with the mean 2DS ice concentration in the mixed cloud layer. D10 predictions using the probe data overestimate with comparison to the mean observed in the cloud; an overestimation which can be explained by incorrectly assuming that all predicted INPs nucleate to form ice crystals. The large fraction of coarse-mode sea salt particles identified over the sea ice (Young et al., 2016) is unlikely to contribute to the INP population as these are inefficient INPs. Despite this, given the uncertainties in the parameterisation itself, these predictions do well to replicate the ice observed in the cloud. T13 was derived from forest ecosystem data and, therefore, represents an environment with plentiful biological aerosol particles that may act as INPs. T13 predictions are highly variable with these data, giving $0.07\,L^{-1}$ with the filter data and $19.7\,L^{-1}$ with the CAS-DPOL. This variability is not surprising, as small increases in an INP-active aerosol population – such as that used to derive T13 – would cause significant changes in the ice crystal number concentrations in the clouds. Despite this, the T13 parameterisation agrees well with the observed ice number concentrations when PCASP data are used for its evaluation ($1.10\,L^{-1}$).

For comparison, parameterisations based on mineral dust data were considered. N12 and D15 were evaluated with the dust size distribution and number concentration of dust particles $> 0.5\,\mu m$, derived from the aircraft filters (Table 3). As discussed by Young et al. (2016), this dust loading is likely under-represented as a result of the analysis technique and collection efficiency issues. Evaluations of N12 with measured, double, and triple dust loadings all compare well with the run 2 ice data, illustrating a lack of sensitivity to this input. However, N12 agrees best with observations when the measured dust concentrations from the filters are used. Agreement with observations is poor when applying the D15 parameterisation. This parameterisation was developed to simulate the high nucleating efficiencies of mineral dusts at temperatures $< -20\,°C$; therefore, our data are at the upper limit of its applicability. Given the good agreement of

N12 with our observations, at temperatures well within the range represented by the parameterisation, it can be speculated that the ice number concentrations observed over the sea ice may be explained by the dust loadings present.

Over the sea ice, the liquid water content is low ($\sim 0.03\,\mathrm{g\,m^{-3}}$, Fig. 6a) and the mean droplet radius is small ($\sim$ 4–5 µm, Fig. 12), with mean droplet number concentrations of $110 \pm 36\,\mathrm{cm^{-3}}$. It is possible that the cloud layer interacted with aerosol from above via entrainment processes, as suggested by the presence of numerous small cloud droplets; with more CCN available, more cloud droplets can form (Jackson et al., 2012). Mean droplet number concentrations from the CDP (Fig. 6) are consistent with both the high- and low-altitude PCASP number concentrations measured (Table 5), further suggesting that the ambient aerosol mixed with the cloud layer from above and below.

The vertical velocity PDFs (Fig. 17) and TKE (Fig. 16) suggest that the boundary layer over the sea ice is stable with relatively little mixing compared to downstream. Little variability and low values are observed in the measured TKE, sensible heat flux, and latent heat flux (Fig. 16). The potential temperature profiles from the dropsondes (Fig. 3a, b) also indicate weakly stable stratification with very strong temperature inversions, emphasising that boundary layer mixing was inhibited over the sea ice. A lack of substantial vertical air motions may explain the low LWC; by the WBF mechanism, the ice crystals act as a sink for vapour in the cold temperatures observed ($\sim -20\,^{\circ}\mathrm{C}$). This causes the suppression of the liquid phase via a suppressed supersaturation and cloud droplets remain small.

5.2 Marginal ice zone

When transitioning from sea ice to ocean, both cloud depth and cloud base height increase (Fig. 12). The most significant change in cloud microphysics over the transition is in the liquid phase, where the liquid water content and mean droplet size increase from 0.1 to $0.4\,\mathrm{g\,m^{-3}}$ and 5 to 10 µm respectively. Mean N_{drop} peaks at $145 \pm 54\,\mathrm{cm^{-3}}$ during profile 7, and falls to $120 \pm 33\,\mathrm{cm^{-3}}$ during profile 8. This decrease in N_{drop} is accompanied by an increase in R_{eff} towards cloud top, from 8 to 10 µm, indicating enhanced collision coalescence within the deeper, ocean-based cloud layer (Fig. 12).

A cloud with high N_{drop} over the sea ice would reflect incident solar radiation efficiently (Twomey, 1974); however, as the sea ice surface itself is highly reflective, the net impact of the cloud on the sea ice radiative interactions is difficult to interpret. As the sea ice gives way to the MIZ, the increased droplet number concentration, mean droplet effective radius, liquid water content, and cloud depth suggest that the cloud optical thickness and albedo also increase (Twomey, 1974). With increased optical and geometrical thickness, upwelling LW radiation from the surface can be trapped and incident solar radiation can be scattered more efficiently. Radiative predictions are hindered by the weak solar heating experienced during the Arctic spring; however, it is likely that these properties would cause a net warming at the surface due to the increasing LW influence from the ocean, and could potentially enhance the melting processes of the nearby sea ice (Palm et al., 2010). Over the ocean, droplet number concentrations decrease throughout the cloud, whilst the mean droplet effective radii increase. With fewer, larger, cloud droplets, the cloud over the ocean may not be as efficient as scattering solar radiation as the sea ice cloud, if their microphysical properties are compared irrespective of their environments. However, the thick cloud over the ocean would act to significantly increase the net albedo of the ocean regime, whilst the net impact of the sea ice cloud is unclear.

The ambient temperatures experienced within the cloud layers (Fig. 13) remain colder than required for secondary ice production and warmer than the homogeneous freezing threshold throughout. The observed 2DS ice crystal concentrations are consistently low – approximately $0.5\text{–}1.5\,\mathrm{L^{-1}}$ – throughout the transition, again indicating that only primary ice nucleation was active. Higher ice concentrations are observed at high altitudes (up to $2\,\mathrm{L^{-1}}$ at ~ 1350 m) over the sea ice, suggesting that some precipitation was again measured from a higher cloud layer. This agrees with the conclusion from run 5, as both this profile and run 5 were conducted close together (1400 m) and to the west ($\sim$ 26.5–27 °E) of the main science region. Though some seeding from above is probable in both run and profile 5, the ice concentrations measured during the SLRs over sea ice and ocean – and the remaining profiles over the MIZ – suggest that this is not the case for the majority of these data.

The sulfate, organic, ammonium, and BC loadings vary almost sinusoidally with altitude over the transition region, with maxima reached at the peaks of the sawtooth profile (Fig. 15). These peaks occur above the cloud layer, as indicated in Fig. 12. These species commonly act as CCN in the atmosphere and could be acting to increase the cloud droplet number concentration across the MIZ. There is no evidence that the organic species influences the ice phase, as the former varies significantly whereas the latter remains approximately constant. The observed increases in mass loading are small, as are the increases in number concentration measured by the PCASP (Fig. 15); therefore it is unlikely that they are the cause of the significant microphysical changes observed.

Measured surface heat fluxes – both sensible and latent – become more variable and increase over the transition to ocean, with greatest values measured at low altitudes (< 1000 m). The approximate MetUM ice fraction indicated in Fig. 16 mirrors the transition of this variability, with little deviation from $0\,\mathrm{W\,m^{-2}}$ measured when sea ice is present and significant variability developing over the transition to open water. Similar changes are observed in the TKE data, where increased turbulence is induced as the air mass moves over the broken sea ice and comparatively warm ocean.

5.3 Ocean

Between sea ice and ocean, the most prominent microphysical difference is in the liquid phase. The observed cloud is deeper, with a mean LWC and droplet number concentration of $\sim 0.3\,\mathrm{g\,m^{-3}}$ and $63 \pm 30\,\mathrm{cm^{-3}}$ respectively (Fig. 9).

Observed ice crystal number concentrations within the oceanic cloud are similar to those measured over the sea ice (0.5–$1\,\mathrm{L^{-1}}$) and the D10 INP predictions are in reasonable agreement (~ 1–$2\,\mathrm{L^{-1}}$, Table 3). T13 predictions are more variable with the input data, resulting in 2.66 and $0.34\,\mathrm{L^{-1}}$ using PCASP and CAS-DPOL data respectively. As discussed previously, T13 is particularly sensitive to the number concentration of aerosol particles used as input, with little difference in N_{aerosol} causing significantly different predictions (Table 3). The CAS-DPOL prediction is in better agreement with the ice number concentrations observed in this case than the PCASP prediction. The ice phase measurements are consistent with altitude; however, there is an increase at the base of the mixed cloud layer (~ 700–$900\,\mathrm{m}$). This increase could be due to sedimentation of ice crystals or low sampling statistics at these altitudes. However, the presence of dendritic ice crystals (Fig. S2) combined with an ice concentration of $\sim 5\,\mathrm{L^{-1}}$, a mean temperature of approximately $-16\,^{\circ}\mathrm{C}$, and an enhanced ice crystal mode in the size distributed data (Fig. 9c4) suggests that ice-ice collisions may have taken place at cloud base (Rangno and Hobbs, 2001). Dendritic crystals are susceptible to break up, and have been shown to fragment due to air velocity alone (Griggs and Choularton, 1986). The ambient temperatures were too low to suggest secondary ice formation via the Hallett–Mossop pathway (Hallett and Mossop, 1974), but it is possible that some crystal fragmentation due to collisions enhanced the observed primary ice concentration at these altitudes.

Probe icing was an issue during run 7 and this effect can be seen in the sharp increase in the CIP100 and corresponding decrease in the 2DS ice number concentrations in Fig. 9c2. Run 8 was intended to be a low-altitude, below-cloud run; however, precipitation particles were again observed. Contrasting run 5, this precipitation is related to the observed ocean cloud layer sampled above during runs 6 and 7: images from the CIP100 (Fig. 11) indicate that these particles are large and rimed, inferring an interaction with liquid droplets within the mixed layer above.

Aerosol data were not available for a significant fraction of the ocean component of the flight. Despite this, it can still be seen that the mass loadings of all AMS-measured species are low in this region (Fig. 15). The measured BC loading is more variable over the ocean than the sea ice or MIZ, varying from approximately 10 to $100\,\mathrm{ng\,m^{-3}}$. This variability is mirrored by the particle number concentration measured by the PCASP. The heightened BC loadings are consistent with the monthly average reported by Eleftheriadis et al. (2009) for Feb/Mar at Zeppelin station, Svalbard ($\sim 80\,\mathrm{ng\,m^{-3}}$). There is also consistency between the high- and low-altitude measurements from the CAS-DPOL and PCASP ($> 0.5\,\mu\mathrm{m}$) over the ocean, suggesting a constant vertical profile of large aerosol in this region. Aerosol number concentrations were found to be lower in general over the ocean than over the sea ice. No aircraft filters were exposed over the ocean; therefore, the composition of the coarse-mode aerosol could not be established.

From Fig. 3, the atmosphere is notably warmer over the ocean than over the sea ice. There is a steady increase in the boundary layer potential temperature measured by the dropsondes from north to south. The changes in the Θ profiles are most prominent in the boundary layer, with less variability observed $> 1500\,\mathrm{m}$. The near-surface temperature inferred by the dropsondes increases by $13\,^{\circ}\mathrm{C}$ between the most northerly and southerly latitudes sampled. Over the transition from sea ice to ocean, the inferred temperature difference at the surface was approximately $6\,^{\circ}\mathrm{C}$. The ocean surface was, therefore, significantly warmer than the sea ice, and this sharp temperature gradient affected the both structure of the boundary layer and any clouds that formed within it.

The broader vertical wind PDFs over the ocean (Fig. 17) suggest increased turbulence levels and mixing within the boundary layer. This is in agreement with Figs. 3 and 16: the surface temperature increased with transition from the frozen sea ice to the warm ocean, thus increasing sensible heat and latent heat fluxes from the surface. At low altitude over the ocean, both of these measures routinely exceeded $20\,\mathrm{W\,m^{-2}}$, whilst they remained consistent at approximately $0\,\mathrm{W\,m^{-2}}$ over the sea ice. Measured TKE was significantly higher at low altitude over the ocean than over the sea ice, suggesting a much more turbulent boundary layer over the open water. The contrast between the observed cloud microphysics over sea ice and ocean is most likely due to these increased fluxes and induced turbulent motions. The warmer, more turbulent boundary layer promotes the efficient collision-coalescence (and subsequent growth via sustained supersaturations) of cloud droplets, promoting a higher mean droplet effective radius and lower number concentration (Fig. 12). A consistent source of heat and moisture to the BL, enhanced turbulence (Fig. 16), a deeper cloud layer, and a greater liquid water content (Fig. 9) allowed rimed snowflakes to form which precipitated from the cloud. This precipitation will act to deplete the liquid in the cloud, potentially leading to cloud break up further downstream.

5.4 Study comparison

The sea ice cloud has little in common with the single-layer stratocumulus case observed during M-PACE (Verlinde et al., 2007). Conversely, the microphysics observed here agrees better with observations made during the M-PACE cirrus case study: the high-altitude, predominantly liquid, cloud layer observed below the cirrus cloud had a similar LWC

to that measured here. Low ice number concentrations were identified in this layer, as they were found to be connected to the cirrus cloud above it through precipitating snow. In addition, this cloud layer was at a similar temperature (approximately −20 °C) to the sea ice cloud observed here. The close proximity to the cold sea ice surface could be causing this cloud to behave like a high-altitude, decoupled cloud: with little-to-no surface sensible and latent heat fluxes affecting the cloud (with little variability from $0\,W\,m^{-2}$ observed, Fig. 16), the resultant microphysics may evolve as it would higher up in the troposphere. During ISDAC, the springtime single-layer MPS observed over the sea ice had a similar mean LWC to our sea ice cloud ($0.1 \pm 0.13\,g\,m^{-3}$, Jackson et al., 2012), further suggesting this is a common observation of MPS over sea ice.

Our measurements show that the cloud downstream over the ocean was deeper than the sea ice cloud, agreeing with the observations of Palm et al. (2010). In contrast to the sea ice case, our ocean observations compare well with the ocean-based, single-layer stratocumulus observed during M-PACE (Verlinde et al., 2007; Jackson et al., 2012). Low droplet concentrations ($46 \pm 30\,cm^{-3}$) and a comparable mean LWC ($0.19 \pm 0.12\,g\,m^{-3}$) were measured during M-PACE (Jackson et al., 2012) and, coupled with our observations, this suggests that such properties are common amongst ocean-based single-layer MPS. Through a comparison between M-PACE and ISDAC data, Jackson et al. (2012) also concluded that this larger mean LWC during M-PACE was caused by moisture fluxes from the ocean below.

Mean droplet number concentrations varied from $110 \pm 36\,cm^{-3}$ over the sea ice, to $145 \pm 54\,cm^{-3}$ over the MIZ, to $63 \pm 30\,cm^{-3}$ over the ocean. These concentrations were variable with altitude (Figs. 6, 9, 12) and also varied substantially with longitude over the sea ice (Fig. 7) and ocean (Fig. 10) where such data were available. These values are consistent with the first ACCACIA spring case reported by Lloyd et al. (2015) but not the second: as also concluded by the authors, their second spring case was subjected to a higher aerosol loading which enhanced the droplet number concentration of the cloud. Consistency between the liquid phase in this study, the spring case 1 from Lloyd et al. (2015), and the MPS observations reported by other Arctic studies (e.g. Verlinde et al., 2007; McFarquhar et al., 2011; Jackson et al., 2012) suggest that droplet number concentrations of $\sim 150\,cm^{-3}$ or below are common amongst Arctic mixed-phase single-layer stratocumulus in the transition seasons. Mean droplet effective radii over the sea ice are comparable to previous springtime Arctic studies (e.g. 5.7 µm, Earle et al., 2011), whilst the larger effective radii measured over the ocean agree better with observations of autumnal Arctic single- and multilayer clouds (e.g. approximately 10 and 8–13 µm respectively, Klein et al., 2009; Morrison et al., 2009). These observations again suggest that larger droplet sizes may be a common occurrence in ocean-based clouds, whilst small droplets are common in clouds over sea ice, regardless of season.

The ice phase is approximately constant across the transition from sea ice to ocean. Again, these measurements agree well with the springtime ACCACIA cases presented by Lloyd et al. (2015): the ice concentrations are variable and can reach up to $\sim 10\,L^{-1}$ (thought to be due to crystal fragmentation here), yet they are low on average (0.5–$1.5\,L^{-1}$) throughout the mixed cloud layer. The sea ice cloud observed here would fall into the Type IV category established by Rangno and Hobbs (2001), as it was characterised by droplet concentrations of $> 100\,cm^{-3}$, small droplet effective radii, and only a few ice crystals per litre of air (Figs. 6, 12, and 13). These findings are consistent with the classification of clouds observed during ISDAC, as discussed by Jackson et al. (2012). The ocean cloud borders on the Type V category, with larger droplet sizes, mean droplet number concentrations $< 100\,cm^{-3}$, and precipitation developing; however, the observed ice number concentrations are still in better agreement with the Type IV criteria. One could postulate that the continued development of the ocean cloud over the warm surface, with further growth of even larger cloud droplets that might subsequently freeze, could allow the cloud layer to evolve into a Type V cloud, with more ice and less liquid. The microphysical characteristics of these clouds may be more susceptible to cloud glaciation and break up via the WBF mechanism. The M-PACE clouds were categorised as Type V (e.g. McFarquhar et al., 2007; Jackson et al., 2012), with higher ice crystal (mean of $2.8 \pm 6.9\,L^{-1}$ for mixed-phase single-layer stratus, McFarquhar et al., 2007) and lower droplet number concentrations than reported here. From these differences, one might infer that the M-PACE clouds were simply further developed than those observed in this study, or that there may be some influence from either different geographical aerosol sources, minor secondary ice production (as suggested by Jackson et al., 2012), or seasonal dependencies. Results from ISDAC may address the geographical hypothesis, as ice crystal and cloud droplet concentrations of approximately 0.5–$1.5\,L^{-1}$ and $\sim 150\,cm^{-3}$ were observed over broken sea ice during the early spring at Barrow, Alaska (April 2008, McFarquhar et al., 2011; Jackson et al., 2012). These concentrations are comparable to our sea ice observations; however, the ISDAC clouds were much warmer, with cloud top temperatures ranging from −15 to −12 °C. The microphysical consistency between these clouds observed in different locations may suggest that a similar source of INPs is influencing these clouds, or that the ice phase is not highly sensitive to variability in aerosol properties between different locations. Variability in droplet number between different measurement locations can be more easily explained via pollution events, for example, such as that observed by Lloyd et al. (2015).

The Arctic Study of Tropospheric Aerosol and Radiation (ASTAR-2004) campaign also made cloud observations in the vicinity of Svalbard; however, much higher ice crystal

concentrations (up to $50\,L^{-1}$) were observed (May 2004, Gayet et al., 2009). This phenomenon was explained by Hallett–Mossop secondary ice production. Ice enhancement due to crystal collisions was inferred at cloud base over the ocean here, but the temperature was consistently too cold to allow for secondary ice via the Hallett–Mossop pathway. The lack of dominating secondary ice in the Arctic clouds studied here is again consistent with McFarquhar et al. (2011), Jackson et al. (2012), and Lloyd et al. (2015), leading to the conclusion that the single-layer MPS present in the Arctic during early spring are typically too cold for this phenomenon, irrespective of their geographical location. Primary ice nucleation was found to be solely responsible for the ice in the clouds examined here, whilst secondary ice formation has been found to play a greater role in the late spring and summer (Gayet et al., 2009; Lloyd et al., 2015).

6 Conclusions

In situ aircraft observations of cloud microphysics, aerosol properties, and boundary layer structure have been presented from the Aerosol-Cloud Coupling And Climate Interactions in the Arctic (ACCACIA) campaign. Using data from one case study (flight B762, 23 March 2013, Fig. 1), we have shown how the microphysics of single-layer mixed-phase stratiform clouds can significantly change over the transition from sea ice to ocean. This study represents the first investigation of in situ, measured cloud microphysical changes over this transition, and offers insight into how the microphysics of Arctic stratiform clouds may change with decreasing sea ice extent in the future.

The conclusions of this study are as follows.

– Systematic changes in microphysical properties were observed between the sea ice and ocean, which are summarised in Fig. 18. Cloud base lifted and cloud depth increased over the transition (Figs. 6, 9, 12). Both cloud droplet number and mean size increased over the marginal ice zone (MIZ), from 110 ± 36 to $145 \pm 54\,cm^{-3}$ and 5 to 8 µm respectively. Further downstream over the ocean, mean droplet number concentrations decreased ($63 \pm 30\,cm^{-3}$) and droplet effective radii increased (up to 10 µm) due to collision-coalescence within the deepening cloud layer. Consequently, the liquid water content increased almost fourfold over the full transition from sea ice to ocean. Considering the clouds alone, the clouds over the sea ice and MIZ – with relatively high numbers of small cloud droplets – would likely reflect incoming SW radiation more efficiently than the ocean cloud, promoting a cooling effect; however, as upwelling LW radiation dominates during the Arctic spring, it is more likely that each of these clouds would contribute towards a net warming at the surface by trapping upwelling LW radiation.

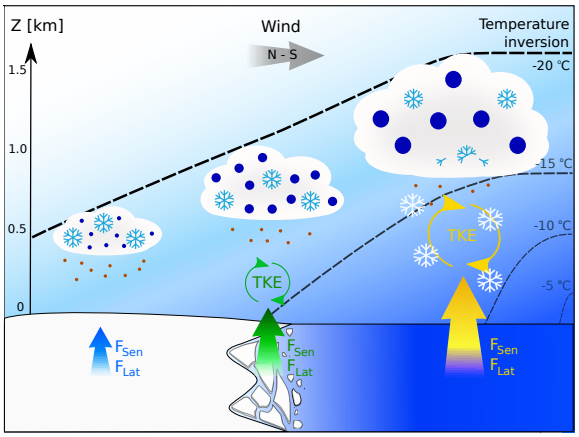

Figure 18. Schematic summarising the development of cloud microphysical, aerosol, and thermodynamic properties across the transition from sea ice to ocean. Aerosol particles, taken to represent the PCASP measurements, are illustrated as brown circles, and cloud droplets are similarly shown in blue. Cloud ice and snowflakes are shown as blue and white crystals respectively. The number of aerosol, droplet, and ice crystal symbols in each regime represents their number concentration in each case. Vertical arrows depict sensible and latent heat fluxes (F_{sen}, F_{lat}) from the surface, and increase in strength with size and from blue, through green, to yellow. Curled arrows represent the development of turbulent kinetic energy (TKE) below the clouds and their colour and size again represent the quantities measured. Temperature isotherms illustrate the changing BL structure over the transition from the cold sea ice to the warm ocean.

– The boundary layer warmed significantly from sea ice to ocean, with a near-surface temperature difference of 13 °C observed between the most northerly and southerly latitudes sampled (Table 1). Increased surface fluxes, vertical motion, and turbulent activity (Figs. 16 and 17) infer substantially more mixing in the boundary layer over both the MIZ and ocean than over the sea ice. This is concluded to be the cause of the microphysical changes observed during this case study, as the increased heat and turbulence likely promoted the formation of more cloud droplets over the MIZ and increased the probability of efficient collision-coalescence within the deepening cloud layer over the ocean.

– The predominant change in cloud microphysics was in the liquid phase, suggesting a similar source of INPs in both regimes. Observed ice number concentrations were low and remained low over the transition (Fig. 13), suggesting only primary ice formation was active. However, evidence of crystal fragmentation was observed at cloud base over the ocean (Fig. 9), leading to minor contributions of secondary ice. The ice crystals were typically found to be larger over the ocean than over the sea ice. Such crystals were observed below cloud over the ocean as rimed snowflakes, precipitating out of the

cloud (Fig. 11). Predicted ice crystal number concentrations using the DeMott et al. (2010), Niemand et al. (2012), Tobo et al. (2013), and DeMott et al. (2015) parameterisations compared reasonably well, to within the uncertainty attributed to the parameterisations themselves (approximately an order of magnitude), with the ice observations over the sea ice and ocean (Figs. 6 and 9). Poorer agreement, when using the D15 parameterisation, for example, could be attributed to extrapolation of the relationship to the limits of its applicability.

– Good agreement was identified between the ice crystal number concentrations measured in this study and those reported from ISDAC; both campaigns observed mean ice concentrations of approximately 0.5–1.5 L^{-1} during the early spring at different locations within the Arctic Circle. This consistency suggests that geographically dependent aerosol sources may not have a prominent influence on the ice phase of these clouds. In contrast, substantial microphysical differences were identified between this study and previous late spring (ASTAR-2004), summer (ACCACIA), and autumnal (M-PACE) studies, emphasising that seasonality remains a crucial factor in the study of Arctic cloud microphysics.

These in situ observations offer a good test case for cloud-resolving and weather prediction model validation in the Arctic. Investigating the influence of the surface on cloud microphysics in such models, and studying how sensitive the simulated clouds are to changes in both surface and aerosol properties, could allow us to improve our understanding of how the microphysics of Arctic single-layer stratiform clouds may adapt and respond to our warming climate.

7 Data availability

Processed data from the ACCACIA campaign are archived on the NCAS British Atmospheric Data Centre (http://catalogue.ceda.ac.uk/uuid/88f95b1d52804b27882fbb798b116d3a). Satellite data are available from NEODAAS NERC Satellite Receiving Station, Dundee University, UK (http://www.sat.dundee.ac.uk). Raw cloud and aerosol data are archived at the University of Manchester and are available on request. Lidar data are available from F. Marenco (franco.marenco@metoffice.gov.uk) on request.

The Supplement related to this article is available online at doi:10.5194/acp-16-13945-2016-supplement.

Acknowledgements. This work was funded by the National Environment Research Council (NERC), under grant NE/I028696/1, as part of the ACCACIA campaign. Gillian Young was supported by a NERC PhD studentship. We would like to thank everyone involved in the ACCACIA project. Gillian Young would also like to thank E. Simpson for her helpful advice on schematic design. Airborne data were obtained using the BAe-146-301 Atmospheric Research Aircraft (ARA) flown by Directflight Ltd and managed by the Facility for Airborne Atmospheric Measurements (FAAM), which is a joint entity of the Natural Environment Research Council (NERC) and the Met Office. MODIS data were accessed via the NASA LAADS Web Archive. AVHRR data were produced by the NEODAAS NERC Satellite Receiving Station, Dundee University, UK (http://www.sat.dundee.ac.uk). Sea ice data were obtained from the National Snow and Ice Data Center (NSIDC).

Edited by: M. Krämer
Reviewed by: three anonymous referees

References

ACIA: Arctic Climate Impact Assessment,990–1020, Cambridge University Press, Cambridge, UK, 2005.

Baumgardner, D., Jonsson, H., Dawson, W., O'Connor, D., and Newton, R.: The cloud, aerosol and precipitation spectrometer: a new instrument for cloud investigations, Atmos. Res., 59–60, 251–264, doi:10.1016/S0169-8095(01)00119-3, 2001.

Beswick, K. M., Gallagher, M. W., Webb, A. R., Norton, E. G., and Perry, F.: Application of the Aventech AIMMS20AQ airborne probe for turbulence measurements during the Convective Storm Initiation Project, Atmos. Chem. Phys., 8, 5449–5463, doi:10.5194/acp-8-5449-2008, 2008.

Boucher, O., Randall, D., Artaxo, P., Bretherton, C., Feingold, G., Forster, P., Kerminen, V. M., Kondo, Y., Liao, H., Lohmann, U., Rasch, P., Satheesh, S. K., Sherwood, S., Stevens, B., and Zhang, X. Y.: Clouds and Aerosols, in: Climate Change 2013: The Physical Science Basis. Contribution of Working Group I to the Fifth Assessment Report of the Intergovernmental Panel on Climate Change, edited by: Stocker, T. F., Qin, D., Plattner, G. K., Tignor, M., Allen, S. K., Boschung, J., Nauels, A., Xia, Y., Bex, V., and Midgley, P. M., Cambridge University Press, Cambridge, United Kingdom and New York, NY, USA, doi:10.1017/CBO9781107415324.016, 2013.

Canagaratna, M., Jayne, J., Jimenez, J., Allan, J., Alfarra, M., Zhang, Q., Onasch, T., Drewnick, F., Coe, H., Middlebrook, A., Delia, A., Williams, L., Trimborn, A., Northway, M., DeCarlo, P., Kolb, C., Davidovits, P., and Worsnop, D.: Chemical and microphysical characterization of ambient aerosols with the aerodyne aerosol mass spectrometer, Mass Spectrom. Rev., 26, 185–222, doi:10.1002/mas.20115, 2007.

Crosier, J., Bower, K. N., Choularton, T. W., Westbrook, C. D., Connolly, P. J., Cui, Z. Q., Crawford, I. P., Capes, G. L., Coe, H., Dorsey, J. R., Williams, P. I., Illingworth, A. J., Gallagher, M. W., and Blyth, A. M.: Observations of ice multiplication in a weakly convective cell embedded in supercooled mid-level stratus, Atmos. Chem. Phys., 11, 257–273, doi:10.5194/acp-11-257-2011, 2011.

Crosier, J., Choularton, T. W., Westbrook, C. D., Blyth, A. M., Bower, K. N., Connolly, P. J., Dearden, C., Gallagher, M. W., Cui, Z., and Nicol, J. C.: Microphysical properties of cold frontal rainbands, Q. J. Roy. Meteor. Soc., 140, 1257–1268, doi:10.1002/qj.2206, 2014.

Curry, J. A., Ebert, E. E., and Herman, G. F.: Mean and turbulence structure of the summertime Arctic cloudy boundary layer, Q. J. Roy. Meteor. Soc., 114, 715–746, doi:10.1002/qj.49711448109, 1988.

Curry, J. A., Rossow, W. B., Randall, D., and Schramm, J. L.: Overview of Arctic Cloud and Radiation Characteristics, J. Climate, 9, 1731–1764, doi:10.1175/1520-0442(1996)009<1731:OOACAR>2.0.CO;2, 1996.

DeMott, P. J., Prenni, A. J., Liu, X., Kreidenweis, S. M., Petters, M. D., Twohy, C. H., Richardson, M. S., Eidhammer, T., and Rogers, D. C.: Predicting global atmospheric ice nuclei distributions and their impacts on climate, P. Natl. Acad. Sci., 107, 11217–11222, doi:10.1073/pnas.0910818107, 2010.

DeMott, P. J., Prenni, A. J., McMeeking, G. R., Sullivan, R. C., Petters, M. D., Tobo, Y., Niemand, M., Möhler, O., Snider, J. R., Wang, Z., and Kreidenweis, S. M.: Integrating laboratory and field data to quantify the immersion freezing ice nucleation activity of mineral dust particles, Atmos. Chem. Phys., 15, 393–409, doi:10.5194/acp-15-393-2015, 2015.

Earle, M. E., Liu, P. S. K., Strapp, J. W., Zelenyuk, A., Imre, D., McFarquhar, G. M., Shantz, N. C., and Leaitch, W. R.: Factors influencing the microphysics and radiative properties of liquid-dominated Arctic clouds: Insight from observations of aerosol and clouds during ISDAC, J. Geophys. Res.-Atmos., 116, D00T09, doi:10.1029/2011JD015887, 2011.

Eleftheriadis, K., Vratolis, S., and Nyeki, S.: Aerosol black carbon in the European Arctic: Measurements at Zeppelin station, Ny-Ålesund, Svalbard from 1998-2007, Geophys. Res. Lett., 36, L02809, doi:10.1029/2008GL035741, 2009.

Gayet, J.-F., Treffeisen, R., Helbig, A., Bareiss, J., Matsuki, A., Herber, A., and Schwarzenboeck, A.: On the onset of the ice phase in boundary layer Arctic clouds, J. Geophys. Res.-Atmos., 114, D19201, doi:10.1029/2008JD011348, 2009.

Glen, A. and Brooks, S. D.: A new method for measuring optical scattering properties of atmospherically relevant dusts using the Cloud and Aerosol Spectrometer with Polarization (CASPOL), Atmos. Chem. Phys., 13, 1345–1356, doi:10.5194/acp-13-1345-2013, 2013.

Griggs, D. J. and Choularton, T. W.: A laboratory study of secondary ice particle production by the fragmentation of rime and vapour-grown ice crystals, Q. J. Roy. Meteor. Soc., 112, 149–163, doi:10.1002/qj.49711247109, 1986.

Hallett, J. and Mossop, S. C.: Production of Secondary Ice Particles during the Riming Process, Nature, 249, 26–28, doi:10.1038/249026a0, 1974.

Intrieri, J. M., Fairall, C. W., Shupe, M. D., Persson, P. O. G., Andreas, E. L., Guest, P. S., and Moritz, R. E.: An annual cycle of Arctic surface cloud forcing at SHEBA, J. Geophys. Res.-Oceans, 107, 8039, doi:10.1029/2000JC000439, 2002.

Jackson, R. C., McFarquhar, G. M., Korolev, A. V., Earle, M. E., Liu, P. S. K., Lawson, R. P., Brooks, S., Wolde, M., Laskin, A., and Freer, M.: The dependence of ice microphysics on aerosol concentration in arctic mixed-phase stratus clouds during ISDAC and M-PACE, J. Geophys. Res.-Atmos., 117, D15207, doi:10.1029/2012JD017668, 2012.

Kapsch, M.-L., Graversen, R. G., and Tjernström, M.: Springtime atmospheric energy transport and the control of Arctic summer sea-ice extent, Nat. Clim. Change, 3, 744–748, doi:10.1038/nclimate1884, 2013.

Klein, S. A., McCoy, R. B., Morrison, H., Ackerman, A. S., Avramov, A., Boer, G. d., Chen, M., Cole, J. N. S., Del Genio, A. D., Falk, M., Foster, M. J., Fridlind, A., Golaz, J.-C., Hashino, T., Harrington, J. Y., Hoose, C., Khairoutdinov, M. F., Larson, V. E., Liu, X., Luo, Y., McFarquhar, G. M., Menon, S., Neggers, R. A. J., Park, S., Poellot, M. R., Schmidt, J. M., Sednev, I., Shipway, B. J., Shupe, M. D., Spangenberg, D. A., Sud, Y. C., Turner, D. D., Veron, D. E., Salzen, K. v., Walker, G. K., Wang, Z., Wolf, A. B., Xie, S., Xu, K.-M., Yang, F., and Zhang, G.: Intercomparison of model simulations of mixed-phase clouds observed during the ARM Mixed-Phase Arctic Cloud Experiment. I: Single-layer cloud, Q. J. Roy. Meteor. Soc., 135, 979–1002, doi:10.1002/qj.416, 2009.

Lance, S., Brock, C. A., Rogers, D., and Gordon, J. A.: Water droplet calibration of the Cloud Droplet Probe (CDP) and in-flight performance in liquid, ice and mixed-phase clouds during ARCPAC, Atmos. Meas. Tech., 3, 1683–1706, doi:10.5194/amt-3-1683-2010, 2010.

Lawson, R. P., Baker, B. A., Schmitt, C. G., and Jensen, T. L.: An overview of microphysical properties of Arctic clouds observed in May and July 1998 during FIRE ACE, J. Geophys. Res., 106, 14989, doi:10.1029/2000JD900789, 2001.

Lawson, R. P., O'Connor, D., Zmarzly, P., Weaver, K., Baker, B., Mo, Q., and Jonsson, H.: The 2D-S (Stereo) Probe: Design and Preliminary Tests of a New Airborne, High-Speed, High-Resolution Particle Imaging Probe, J. Atmos. Ocean. Tech., 23, 1462, doi:10.1175/JTECH1927.1, 2006.

Liu, D., Quennehen, B., Darbyshire, E., Allan, J. D., Williams, P. I., Taylor, J. W., Bauguitte, S. J.-B., Flynn, M. J., Lowe, D., Gallagher, M. W., Bower, K. N., Choularton, T. W., and Coe, H.: The importance of Asia as a source of black carbon to the European Arctic during springtime 2013, Atmos. Chem. Phys., 15, 11537–11555, doi:10.5194/acp-15-11537-2015, 2015.

Lloyd, G., Choularton, T. W., Bower, K. N., Crosier, J., Jones, H., Dorsey, J. R., Gallagher, M. W., Connolly, P., Kirchgaessner, A. C. R., and Lachlan-Cope, T.: Observations and comparisons of cloud microphysical properties in spring and summertime Arctic stratocumulus clouds during the ACCACIA campaign, Atmos. Chem. Phys., 15, 3719–3737, doi:10.5194/acp-15-3719-2015, 2015.

McFarquhar, G. M., Zhang, G., Poellot, M. R., Kok, G. L., McCoy, R., Tooman, T., Fridlind, A., and Heymsfield, A. J.: Ice properties of single-layer stratocumulus during the Mixed-Phase Arctic Cloud Experiment: 1. Observations, J. Geophys. Res.-Atmos., 112, D24201, doi:10.1029/2007JD008633, 2007.

McFarquhar, G. M., Ghan, S., Verlinde, J., Korolev, A., Strapp, J. W., Schmid, B., Tomlinson, J. M., Wolde, M., Brooks, S. D., Cziczo, D., Dubey, M. K., Fan, J., Flynn, C., Gultepe, I., Hubbe, J., Gilles, M. K., Laskin, A., Lawson, P., Leaitch, W. R., Liu, P., Liu, X., Lubin, D., Mazzoleni, C., MacDonald, A.-M., Moffet, R. C., Morrison, H., Ovchinnikov, M., Shupe, M. D., Turner, D. D., Xie, S., Zelenyuk, A., Bae, K., Freer, M., and Glen, A.: Indirect and Semi-direct Aerosol Campaign: The Impact of Arc-

tic Aerosols on Clouds, B. Am. Meteorol. Soc., 92, 183–201, doi:10.1175/2010BAMS2935.1, 2011.

Miloshevich, L. M., Paukkunen, A., Vömel, H., and Oltmans, S. J.: Development and Validation of a Time-Lag Correction for Vaisala Radiosonde Humidity Measurements, J. Atmos. Ocean. Tech., 21, 1305–1327, doi:10.1175/1520-0426(2004)021<1305:DAVOAT>2.0.CO;2, 2004.

Morgan, W. T., Allan, J. D., Bower, K. N., Highwood, E. J., Liu, D., McMeeking, G. R., Northway, M. J., Williams, P. I., Krejci, R., and Coe, H.: Airborne measurements of the spatial distribution of aerosol chemical composition across Europe and evolution of the organic fraction, Atmos. Chem. Phys., 10, 4065–4083, doi:10.5194/acp-10-4065-2010, 2010.

Morrison, H., McCoy, R. B., Klein, S. A., Xie, S., Luo, Y., Avramov, A., Chen, M., Cole, J. N. S., Falk, M., Foster, M. J., Del Genio, A. D., Harrington, J. Y., Hoose, C., Khairoutdinov, M. F., Larson, V. E., Liu, X., McFarquhar, G. M., Poellot, M. R., von Salzen, K., Shipway, B. J., Shupe, M. D., Sud, Y. C., Turner, D. D., Veron, D. E., Walker, G. K., Wang, Z., Wolf, A. B., Xu, K.-M., Yang, F., and Zhang, G.: Intercomparison of model simulations of mixed-phase clouds observed during the ARM Mixed-Phase Arctic Cloud Experiment. II: Multilayer cloud, Q. J. Roy. Meteor. Soc., 135, 1003–1019, doi:10.1002/qj.415, 2009.

Morrison, H., de Boer, G., Feingold, G., Harrington, J., Shupe, M. D., and Sulia, K.: Resilience of persistent Arctic mixed-phase clouds, Nat. Geosci., 5, 11–17, doi:10.1038/ngeo1332, 2012.

Niemand, M., Möhler, O., Vogel, B., Vogel, H., Hoose, C., Connolly, P., Klein, H., Bingemer, H., DeMott, P., Skrotzki, J., and Leisner, T.: A Particle-Surface-Area-Based Parameterization of Immersion Freezing on Desert Dust Particles, J. Atmos. Sci., 69, 3077–3092, doi:10.1175/JAS-D-11-0249.1, 2012.

Palm, S. P., Strey, S. T., Spinhirne, J., and Markus, T.: Influence of Arctic sea ice extent on polar cloud fraction and vertical structure and implications for regional climate, J. Geophys. Res.-Atmos., 115, D21209, doi:10.1029/2010JD013900, 2010.

Parkinson, C. L. and Comiso, J. C.: On the 2012 record low Arctic sea ice cover: Combined impact of preconditioning and an August storm, Geophys. Res. Lett., 40, 1356–1361, doi:10.1002/grl.50349, 2013.

Peng, G., Meier, W. N., Scott, D. J., and Savoie, M. H.: A long-term and reproducible passive microwave sea ice concentration data record for climate studies and monitoring, Earth Syst. Sci. Data, 5, 311–318, doi:10.5194/essd-5-311-2013, 2013.

Perovich, D. K., Richter-Menge, J. A., Jones, K. F., and Light, B.: Sunlight, water, and ice: Extreme Arctic sea ice melt during the summer of 2007, Geophys. Res. Lett., 35, L11501, doi:10.1029/2008GL034007, 2008.

Pinto, J. O.: Autumnal Mixed-Phase Cloudy Boundary Layers in the Arctic., J. Atmos. Sci., 55, 2016–2038, doi:10.1175/1520-0469(1998)055<2016:AMPCBL>2.0.CO;2, 1998.

Poberaj, G., Fix, A., Assion, A., Wirth, M., Kiemle, C., and Ehret, G.: Airborne all-solid-state DIAL for water vapour measurements in the tropopause region: system description and assessment of accuracy, Appl. Phys. B, 75, 165–172, doi:10.1007/s00340-002-0965-x, 2002.

Ralph, F. M., Neiman, P. J., and Rotunno, R.: Dropsonde Observations in Low-Level Jets over the Northeastern Pacific Ocean from CALJET-1998 and PACJET-2001: Mean Vertical-Profile and Atmospheric-River Characteristics, Mon. Weather Rev., 133, 889–910, doi:10.1175/MWR2896.1, 2005.

Rangno, A. L. and Hobbs, P. V.: Ice particles in stratiform clouds in the Arctic and possible mechanisms for the production of high ice concentrations, J. Geophys. Res.-Atmos., 106, 15065–15075, doi:10.1029/2000JD900286, 2001.

Renfrew, I. A., Moore, G. W. K., Kristjánsson, J. E., Ólafsson, H., Gray, S. L., Petersen, G. N., Bovis, K., Brown, P. R. A., Føre, I., Haine, T., Hay, C., Irvine, E. A., Lawrence, A., Ohigashi, T., Outten, S., Pickart, R. S., Shapiro, M., Sproson, D., Swinbank, R., Woolley, A., and Zhang, S.: The Greenland Flow Distortion experiment, B. Am. Meteorol. Soc., 89, 1307–1324, doi:10.1175/2008BAMS2508.1, 2008.

Rosenberg, P. D., Dean, A. R., Williams, P. I., Dorsey, J. R., Minikin, A., Pickering, M. A., and Petzold, A.: Particle sizing calibration with refractive index correction for light scattering optical particle counters and impacts upon PCASP and CDP data collected during the Fennec campaign, Atmos. Meas. Tech., 5, 1147–1163, doi:10.5194/amt-5-1147-2012, 2012.

Serreze, M. C. and Barry, R. G.: Processes and impacts of Arctic amplification: A research synthesis, Global Planet. Change, 77, 85–96, doi:10.1016/j.gloplacha.2011.03.004, 2011.

Serreze, M. C., Holland, M. M., and Stroeve, J.: Perspectives on the Arctic's Shrinking Sea-Ice Cover, Science, 315, 1533–1536, doi:10.1126/science.1139426, 2007.

Shupe, M. D.: Clouds at Arctic Atmospheric Observatories. Part II: Thermodynamic Phase Characteristics, J. Appl. Meteorol. Clim., 50, 645–661, doi:10.1175/2010JAMC2468.1, 2011.

Shupe, M. D. and Intrieri, J. M.: Cloud Radiative Forcing of the Arctic Surface: The Influence of Cloud Properties, Surface Albedo, and Solar Zenith Angle, J. Climate, 17, 616–628, doi:10.1175/1520-0442(2004)017<0616:CRFOTA>2.0.CO;2, 2004.

Shupe, M. D., Matrosov, S. Y., and Uttal, T.: Arctic Mixed-Phase Cloud Properties Derived from Surface-Based Sensors at SHEBA, J. Atmos. Sci., 63, 697–711, doi:10.1175/JAS3659.1, 2006.

Stroeve, J. C., Serreze, M. C., Fetterer, F., Arbetter, T., Meier, W., Maslanik, J., and Knowles, K.: Tracking the Arctic's shrinking ice cover: Another extreme September minimum in 2004, Geophys. Res. Lett., 32, L04501, doi:10.1029/2004GL021810, 2005.

Taylor, J. W., Choularton, T. W., Blyth, A. M., Liu, Z., Bower, K. N., Crosier, J., Gallagher, M. W., Williams, P. I., Dorsey, J. R., Flynn, M. J., Bennett, L. J., Huang, Y., French, J., Korolev, A., and Brown, P. R. A.: Observations of cloud microphysics and ice formation during COPE, Atmos. Chem. Phys., 16, 799–826, doi:10.5194/acp-16-799-2016, 2016.

Tobo, Y., Prenni, A. J., DeMott, P. J., Huffman, J. A., McCluskey, C. S., Tian, G., Pöhlker, C., Pöschl, U., and Kreidenweis, S. M.: Biological aerosol particles as a key determinant of ice nuclei populations in a forest ecosystem, J. Geophys. Res.-Atmos., 118, 10100–10110, doi:10.1002/jgrd.50801, 2013.

Twomey, S.: Pollution and the planetary albedo, Atmos. Environ., 8, 1251–1256, doi:10.1016/0004-6981(74)90004-3, 1974.

Verlinde, J., Harrington, J. Y., McFarquhar, G. M., Yannuzzi, V. T., Avramov, A., Greenberg, S., Johnson, N., Zhang, G., Poellot, M. R., Mather, J. H., Turner, D. D., Eloranta, E. W., Zak, B. D., Prenni, A. J., Daniel, J. S., Kok, G. L., Tobin, D. C., Holz, R., Sassen, K., Spangenberg, D., Minnis, P., Tooman, T. P., Ivey,

M. D., Richardson, S. J., Bahrmann, C. P., Shupe, M., Demott, P. J., Heymsfield, A. J., and Schofield, R.: The Mixed-Phase Arctic Cloud Experiment, B. Am. Meteorol. Soc., 88, 205–221, doi:10.1175/BAMS-88-2-205, 2007.

Vihma, T., Pirazzini, R., Fer, I., Renfrew, I. A., Sedlar, J., Tjernström, M., Lüpkes, C., Nygård, T., Notz, D., Weiss, J., Marsan, D., Cheng, B., Birnbaum, G., Gerland, S., Chechin, D., and Gascard, J. C.: Advances in understanding and parameterization of small-scale physical processes in the marine Arctic climate system: a review, Atmos. Chem. Phys., 14, 9403–9450, doi:10.5194/acp-14-9403-2014, 2014.

Wang, J.: Evaluation of the Dropsonde Humidity Sensor Using Data from DYCOMS-II and IHOP_2002, J. Atmos. Ocean. Tech., 22, 247–257, doi:10.1175/JTECH1698.1, 2005.

Xu, L., Russell, L. M., Somerville, R. C. J., and Quinn, P. K.: Frost flower aerosol effects on Arctic wintertime longwave cloud radiative forcing, J. Geophys. Res., 118, 13282–13291, doi:10.1002/2013JD020554, 2013.

Young, G., Jones, H. M., Darbyshire, E., Baustian, K. J., McQuaid, J. B., Bower, K. N., Connolly, P. J., Gallagher, M. W., and Choularton, T. W.: Size-segregated compositional analysis of aerosol particles collected in the European Arctic during the ACCACIA campaign, Atmos. Chem. Phys., 16, 4063–4079, doi:10.5194/acp-16-4063-2016, 2016.

6 Microphysical sensitivity of coupled springtime Arctic stratocumulus to modelled primary ice over the ice pack, marginal ice, and ocean

Young, G., Connolly, P. J., Jones, H. M., and Choularton, T. W.: Microphysical sensitivity of coupled springtime Arctic stratocumulus to modelled primary ice over the ice pack, marginal ice, and ocean, Atmospheric Chemistry and Physics Discussions, doi:10.5194/acp-2016-898, **in review**, 2016.

This article was written by G. Young. Model runs were conducted by G. Young. Data analysis of model output and aircraft measurements was also carried out by G. Young. H. M. Jones processed the 2DS data used for comparison within the article. P. J. Connolly advised on model set up and experiment design. T. W. Choularton advised on pathways of analysis and the writing of the final article.

Microphysical sensitivity of coupled springtime Arctic stratocumulus to modelled primary ice over the ice pack, marginal ice, and ocean

Gillian Young[1], Paul J. Connolly[1], Hazel M. Jones[1], and Thomas W. Choularton[1]

[1]Centre for Atmospheric Science, School of Earth and Environmental Sciences, University of Manchester, Manchester, UK.

Correspondence to: Gillian Young (gillian.young@manchester.ac.uk)

Abstract.

This study uses large eddy simulations to test the sensitivity of single-layer mixed-phase stratocumulus to primary ice number concentrations in the European Arctic. Observations from the Aerosol-Cloud Coupling and Climate Interactions in the Arctic (ACCACIA) campaign are considered for comparison with cloud microphysics modelled using the Large Eddy Model (LEM, UK Met. Office). We find that cloud structure is very sensitive to ice number concentrations, N_{ice}, and small increases can cause persisting mixed-phase clouds to glaciate and break up.

Three key sensitivities are identified with comparison to in situ cloud observations over the sea ice pack, marginal ice zone (MIZ), and ocean. Over sea ice, we find deposition-condensation ice formation rates are overestimated, leading to cloud glaciation. When ice formation is limited to water-saturated conditions, we find microphysics comparable to the aircraft observations over all surfaces considered. We show that warm supercooled (-13 °C) mixed-phase clouds over the MIZ are simulated to reasonable accuracy when using both the DeMott et al. (2010) and Cooper (1986) parameterisations. Over the ocean, we find a strong sensitivity of Arctic stratus to ice number concentrations. Cooper (1986) performs poorly at the lower ambient temperatures, leading to comparatively higher ice number concentrations ($2.43\,L^{-1}$ at the cloud top temperature, approximately -20 °C) and cloud glaciation. A small decrease in the predicted N_{ice} ($2.07\,L^{-1}$ at -20°C), using the DeMott et al. (2010) parameterisation, causes mixed-phase conditions to persist for 24 h over the ocean. However, this representation leads to the formation of convective structures which reduce the cloud liquid water through snow precipitation, promoting cloud break up. Decreasing the ice crystal number concentration further ($0.54\,L^{-1}$, using a relationship derived from ACCACIA observations) allows mixed-phase conditions to be maintained for at least 24 h with more stability in the liquid and ice water paths. Sensitivity to N_{ice} is also evident at low number concentrations, where $0.1\times N_{ice}$ predicted by the DeMott et al. (2010) parameterisation results in the formation of rainbands within the model; rainbands which also act to deplete the liquid water in the cloud and promote break up.

1 Introduction

The significant uncertainties associated with global climate model (GCM) predictions may be largely attributed to the inadequate treatment of sub-grid scale, such as cloud microphysical, parameterisations (Boucher et al., 2013). These uncertainties

are predicted to enhance discrepancies in temperature forecasts at the polar regions of our planet (ACIA, 2005; Serreze and Barry, 2011; Stocker et al., 2013). The accuracy of these forecasts can be improved by developing the modelled representation of the physical processes involved through comparisons with in situ observations (Curry et al., 1996).

Various observational studies have shown that single-layer mixed-phase stratocumulus (MPS) clouds are common in the Arctic (e.g. Pinto, 1998; Shupe et al., 2006; Verlinde et al., 2007; Morrison et al., 2012). These clouds have been observed to persist for $\sim$12 h (Shupe et al., 2006) – with some lasting longer than 100 h (Shupe et al., 2011) – whilst maintaining cloud top temperatures as low as -30 °C (Verlinde et al., 2007). Single-layer Arctic MPS typically form at low altitudes and maintain a liquid layer at cloud top which facilitates ice formation and precipitation below (Rangno and Hobbs, 2001; Shupe et al., 2006; Verlinde et al., 2007; McFarquhar et al., 2011; Jackson et al., 2012; Morrison et al., 2012, amongst others). The Wegener-Bergeron-Findeisen (WBF) mechanism strongly influences MPS and initiates a continually-changing microphysical structure. Moderate vertical motions maintain these clouds, where mixing ensures that the proximity between ice crystals and cloud droplets is variable whilst sustaining supersaturated conditions (Korolev and Isaac, 2003).

Models do not reproduce the microphysical structure and radiative interactions of these persistent Arctic mixed-phase clouds well (e.g. Tjernström et al., 2008; Klein et al., 2009; Morrison et al., 2009; Morrison et al., 2012; de Boer et al., 2014). Detailed cloud resolving model (CRM) simulations have previously shown that commonly-used mid-latitude parameterisations, such as Cooper (1986) or Meyers et al. (1992), overestimate the cloud ice number concentration, N_{ice}, in Arctic MPS, causing the rapid depletion of liquid and cloud glaciation (Harrington et al., 1999; Prenni et al., 2007). Modelled MPS are particularly sensitive to N_{ice}, with small decreases in simulated ice number causing significant increases in modelled liquid water path (Harrington and Olsson, 2001).

Four ice nucleation modes are commonly represented in models, and three (immersion-, contact-, and condensation-freezing) require the presence of cloud droplets for initiation (Pruppacher and Klett, 1997). Immersion-freezing occurs when a cloud droplet is nucleated by an aerosol particle of mixed composition; mixing which likely incorporates both soluble and insoluble fractions. Solubility is a crucial property of an efficient cloud condensation nuclei (CCN) whilst efficient ice nucleating particles (INPs) are insoluble (Pruppacher and Klett, 1997; Murray et al., 2012). The inclusion of an insoluble fraction would allow a CCN to obtain some ability as an INP (de Boer et al., 2010). In the atmosphere, soluble coatings on previously CCN-inactive particles, like desert dusts, promote ice nucleation via this pathway (Bigg and Leck, 2001). For example, organic coatings can suppress the ability of an INP to nucleate via the deposition mode (Möhler et al., 2008; Primm et al., 2016). Deposition-freezing results from the direct deposition of water vapour onto an INP, and is often linked with condensation-freezing due to difficulties in distinguishing these mechanisms in measurements. Deposition-freezing may occur in both water- and ice-supersaturated conditions. The frequency of MPS in the Arctic suggests that ice formation in these clouds is tied to the liquid phase, as preferential nucleation via deposition-freezing may, in theory, result in a higher proportion of fully glaciated clouds than are observed (de Boer et al., 2011; Vihma et al., 2014). Consequently, recent studies (e.g. de Boer et al., 2011) suggest that liquid-dependent modes of nucleation are dominant in Arctic MPS at sub-zero temperatures greater than -25 °C.

Liquid-dependent freezing may be inferred by observations in the Arctic. Previous studies have found correlations between the number concentrations of ice crystals and large ($>$23 µm) cloud drops (and drizzle drops, Hobbs and Rangno, 1998; Rangno

and Hobbs, 2001). These large liquid particles have an increased likelihood of containing a partially-insoluble nucleus, or colliding with one, due to aerosol scavenging; therefore, they may nucleate via immersion- or contact-freezing respectively. Arctic aerosol particles are often well-mixed due to long-range transport (Young et al., 2016b); therefore, they can provide an efficient platform for immersion-freezing (Bigg and Leck, 2001; de Boer et al., 2010). Similarly, mixed particles can promote ice nucleation through collisions with cloud droplets; however, contact-freezing nuclei are generally thought to be predominantly insoluble and ice-active, with little CCN ability (Young, 1974).

Investigating the sensitivity of MPS to ice crystal number concentrations will help to improve our understanding of the microphysical limitations of these clouds. Here, we test if primary ice formation under water-saturation conditions improves the modelled microphysical structure with comparison to deposition-condensation freezing, with the hypothesis that ice number concentrations will be suppressed and liquid fractions will be enhanced under this restriction. Modelling studies which utilise immersion-freezing have successfully simulated the persistence of Arctic stratocumulus clouds, producing sustained liquid water in the presence of ice crystals for up to 12 h (de Boer et al., 2010).

Here, we use in situ cloud observations of Arctic MPS, from the Aerosol-Cloud Coupling and Climate Interactions in the Arctic (ACCACIA) campaign of 2013, as a guide to infer the microphysical sensitivity of modelled clouds to both ice number and surface conditions. We use the Large Eddy Model (LEM, UK Met Office, Gray et al., 2001) to simulate cloud microphysics observed over the sea ice, marginal ice zone (MIZ), and ocean. The UK's BAe-146-301 Atmospheric Research Aircraft was used during the springtime (Mar-Apr) campaign, collecting high-resolution in situ observations of the cloud microphysics encountered (Lloyd et al., 2015; Young et al., 2016a). Several dropsondes were launched from the aircraft during these cases to provide vertical profiles of the boundary layer (BL) structure. By combining dropsonde and in situ measurements, the sensitivity of modelled cloud microphysics to changes in predicted ice number concentrations is tested to infer the microphysical limitations of persistent springtime MPS in the European Arctic.

2 Methodology

2.1 Aircraft Instrumentation

Measurements from instruments on-board the Facility for Airborne Atmospheric Measurements' (FAAM) BAe-146 aircraft during three chosen case studies are presented to test the ability of the LEM to reproduce the Arctic mixed-phase clouds observed. Specifically, data from two wing-mounted instruments – the 2-Dimensional Stereo Particle imaging probe (2DS, Lawson et al., 2006) and Cloud Droplet Probe (CDP-100 Version 2, Droplet Measurement Technologies (DMT), Lance et al., 2010) – are used to investigate the mixed-phase clouds, as these probes can measure the sizes and number concentrations of ice crystals (80-1280 µm) and cloud droplets (3-50 µm) respectively. Details on the functioning of these probes, data analysis, and subsequent particle phase discrimination have been discussed previously by Crosier et al. (2011, 2014) and Taylor et al. (2016). The use of these instruments during ACCACIA is discussed by Lloyd et al. (2015) and Young et al. (2016a).

Aerosol particle data are used for the evaluation of the DeMott et al. (2010) ice nucleation parameterisation. Data from the Passive-Cavity Aerosol Spectrometer Probe (PCASP 100-X, Droplet Measurement Technologies, Rosenberg et al., 2012) are

used to size and count aerosol particles from sizes 0.1 µm to 3 µm. Additionally, dropsondes released during each case are used to provide representative vertical profiles of potential temperature, water vapour mixing ratio, and wind fields to initialise the model.

2.2 Large Eddy Model (LEM)

The LEM allows cloud microphysics to be studied in isolation from large scale meteorological features. Cloud microphysical interactions, wind velocities, and turbulent motions within the boundary layer are simulated to allow a detailed investigation of cloud formation and evolution over the domain (Boucher et al., 2013). Here, we consider three case studies of observations over the sea ice, marginal ice zone, and ocean; cases 1, 2, and 3 respectively.

A 16 km$\times$16 km domain was used, centred on the respective dropsonde release points in each case, with a spatial resolution of 120 m and a model height of 3 km applied. A vertical resolution of 20 m was imposed from the surface to above the altitude of the boundary layer temperature inversion (1500 m), above which it was reduced to 50 m. The LEM was run for 24 hours to simulate the respective observations. The first 3 hours of each simulation was not considered due to model spin-up. For all cases, cyclic lateral boundary conditions were imposed. A sponge layer was applied to the top 500 m of the domain, allowing the fields to revert back to their initial conditions in this region. Long- and shortwave radiation was modelled using the Edwards and Slingo (1996) scheme and was called every 150 seconds within the model. Dropsonde profiles of potential temperature, wind speed, and water vapour mixing ratio were used to initialise the model. An adiabatic liquid water profile was assumed up to the first temperature inversion (approximately 600 m, 350 m, and 1150 m for cases 1, 2, and 3 respectively).

Over the ocean and marginal ice zone (cases 2 and 3), surface fluxes were calculated by the model, which assumes a water-saturated, ocean surface. Small sensible heat fluxes (1 W m^{-2}) were imposed to simulate the sea ice surface (case 1), as studies have measured such values adjacent to the ice pack (e.g. Sotiropoulou et al., 2014). A sub-Arctic McClatchy profile was imposed in all simulations to ensure the initialised vertical profiles of tropospheric temperature, pressure, water vapour, and ozone were representative of the environment modelled.

No large-scale subsidence was imposed in these simulations to allow the microphysical effect of ice number and surface fluxes to be studied in isolation. Imposed subsidence would affect the microphysical structure of the modelled clouds, and the effect of including large-scale subsidence is discussed in Sect. 5.4.1.

2.2.1 Primary Ice Nucleation

The double-moment microphysics scheme by Morrison et al. (2005) is used within the LEM to test the sensitivity of the simulated mixed-phase Arctic clouds to ice number concentration. This scheme represents single-moment liquid, with a prescribed droplet number, and double-moment ice, snow, graupel, and rain. Quoted N_{ice} in this article represents the summed contributions of the ice crystal, graupel, and snow number concentrations simulated. 2DS measurements are not segregated into such categories; therefore, bulk, "total ice" number concentrations are compared. A mean droplet number of 100 cm^{-3}, approximated from the aircraft observations, is applied in all simulations. The sensitivity of the ice phase to this number is not considered here.

Deposition-condensation, immersion-, and contact-freezing are all represented within the Morrison microphysics scheme. The form of the deposition-condensation freezing parameterisation was varied in this study to test the cloud microphysical response. Immersion-freezing is included as the Bigg parameterisation (Bigg 1953 - hereafter, B53) and contact-freezing is represented by the Meyers parameterisation (Meyers et al. 1992 - hereafter, M92). The influence of these parameterisations on simulated ice number concentrations is detailed in the Supplement. To investigate the sensitivity of the modelled microphysics to predictable primary ice number concentrations, B53 immersion- and M92 contact-freezing were switched off within the microphysics scheme, and the sole contribution to N_{ice} from one implemented parameterisation was considered.

Three distinct ice nucleation parameterisations were imposed in this study (Fig. 1). Firstly, the deposition-condensation ice nucleation parameterisation proposed by Cooper 1986 (hereafter, C86) was tested against the ACCACIA observations. This relationship is commonly used within the Morrison microphysics scheme in the Weather Research and Forecasting (WRF) model, amongst others. In Eq. 1, N_{ice} represents the number concentration of pristine ice crystals, and $T_0 - T_K$ defines the sub-zero temperature. This parameterisation is used to simulate ice number concentrations below 265 K only.

$$N_{ice}[m^{-3}, T_K] = 5 \cdot \exp\left(0.304\left[T_0 - T_K\right]\right) \tag{1}$$

Secondly, an approximation of the DeMott et al. 2010 (hereafter, D10) parameterisation was applied. This study derived a detailed relationship between INP number, temperature, and aerosol number concentration based on an amalgamation of different INP field data. D10 was imposed at temperatures below 264 K and at water-saturation (in accordance with DeMott et al., 2010).

$$N_{INP}[m^{-3}, T_K] = 0.0594\left(273.16 - T_K\right)^{3.33}\left(n_{aer,0.5}\right)^{0.0264(273.16-T_K)+0.0033} \tag{2}$$

Equation 2 predicts the number concentration of INPs active at the given temperature, T_K. As input, it requires $n_{aer,0.5}$: the number concentration of aerosol particles with diameter, D_P, greater than 0.5 µm. These aerosol data were averaged using PCASP measurements in the close vicinity to the observed cloud, producing input concentrations of 1.13 cm^{-3}, 1.77 cm^{-3}, and 2.20 cm^{-3} over the sea ice, MIZ, and ocean respectively. Below-cloud data were solely used over the ocean, whereas above-cloud measurements were included in the sea ice and MIZ calculations as the observed clouds had sub-adiabatic liquid water profiles, making entrainment processes – from the lateral or top boundaries of the clouds – likely.

Additionally, a curve was fitted to the observed ice crystal number concentrations during ACCACIA and used within the model. Data from ACCACIA flights B761, B762, B764, B765, and B768 were included in the derivation of this curve. Microphysical data from B762, and B761/B768, have been previously detailed by Young et al. (2016a) and Lloyd et al. (2015)

Table 1. Predicted N_{ice} [L^{-1}] using each parameterisation considered in this study at the observed cloud top temperatures in each case.

Case Number	Temperature[a] [K (°C)]	C86	D10[b]	ACC	D10[b] ×0.1	D10[b] ×10
1	253.4 (-19.8)	2.03	1.31	0.51	0.13	13.1
2	260.5 (-12.7)	0.23	0.34	0.17	0.03	3.37
3	252.8 (-20.4)	2.43	2.07	0.54	0.21	20.7

[a]Cloud top temperature (CTT)

[b]$N_{INP,L^{-1}}$

respectively. Young et al. (2016b) illustrate the corresponding flight tracks of each of these cases. Bulk number concentrations from these flights were plotted against temperature and the following relationship was derived from these data:

$$N_{ice}[m^{-3}, T_K] = \frac{0.068\Big(273.5 - T_K\Big)^{3.3}}{\exp\Big(0.05\big(273.16 - T_K\big)\Big)} \tag{3}$$

This curve is valid below 265 K. Temperatures greater than this were subject to minor secondary ice production; therefore, the primary ice component could not be cleanly extracted from these data. These observed ice data spanned 252 K to 265 K. This curve somewhat mirrors the shape of D10 (Fig. 1); however, it is weighted by an exponential term to provide better agreement with the observations at low temperatures. In this article, this curve will be abbreviated to ACC. We expect this empirically-derived relationship to perform well with comparison to the observations; therefore, ACC is used to assess how well the two established parameterisations, C86 and D10, reproduce the cloud microphysics observed.

INPs are not depleted in this study; however, ice crystal number concentrations are prognostic within the Morrison et al. (2005) microphysics scheme. Aerosol particles are not strictly represented in the LEM and the microphysical representation is bulk, not binned. These simulations are only representative of a system with a replenishing source of INPs, and are therefore idealistic representations of the modelled clouds.

The primary objective of this study is to identify the sensitivity of cloud stability to ice crystal number concentration. DeMott et al. (2010) suggest that INP number concentrations need to be predicted to within a factor of 10 to avoid an unrealistic treatment of mixed-phase cloud microphysics. Therefore, D10×10 and D10×0.1 were considered – in addition to C86, D10, and ACC – to additionally test sensitivity of simulated mixed-phase cloud microphysics to large changes in ice crystal number concentration. Figure 1 illustrates the performance of each parameterisation considered: the C86 and ACC cases, dependent only on temperature, are valid across the three observational studies chosen, whilst the D10 parameterisation – and variations thereof – is variable between cases given its dependence on observed aerosol particle number concentrations.

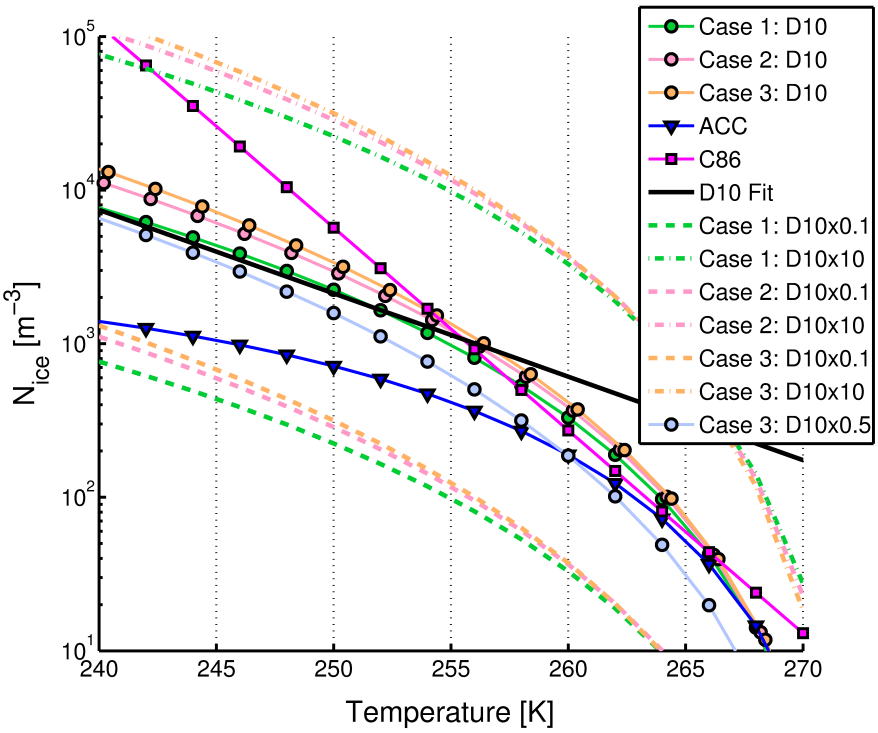

Figure 1. Evaluation of the five parameterisations used (C86, D10, ACC, D10×0.1, and D10×10) in the three cases considered with respect to temperature. **Case 1:** sea ice, **case 2:** marginal ice zone (MIZ), and **case 3:** ocean. The black line depicts the temperature-dependent fit of DeMott et al. (2010) for reference. The C86 parameterisation and ACC are valid for all cases, whereas the different aerosol particle loadings are accounted for with the D10 parameterisation. D10×0.5 is implemented with the ocean case in Sect. 5.4.2.

3 Aircraft observations

In situ observations of cloud microphysics over the sea ice and ocean during ACCACIA flight B762 (23 Mar 2013), and over the marginal ice zone (MIZ) during flight B764 (29 Mar 2013), are considered for model comparison. Microphysical observations from flight B762 have been detailed previously by Young et al. (2016a). The corresponding flight tracks are illustrated in Fig. 2. These case studies were chosen due to the availability of dropsondes for model initialisation and temporally-close in situ aircraft observations. Dropsondes from B762 distinctly sampled either the sea ice or ocean (as shown in Fig. 2**a**). The ocean dropsonde was far from the sea ice edge (∼140 km). The B764 dropsonde (Fig. 2**b**) was dropped over the MIZ. As in Young et al. (2016a), the MIZ is defined as sea ice fractions >10 % and <90 % based on NSIDC data (National Snow and Ice Data Centre, Fig. 2). These three cases were conducted over similar longitudes (∼27 °E) and approximately the same latitude range (∼75-77 °N).

Figure 3 shows the potential temperature, vapour, and wind speed profiles measured by each dropsonde used to initialise the LEM. In all cases, the net wind direction was north-easterly, bringing cold air from over the sea ice pack to the over the

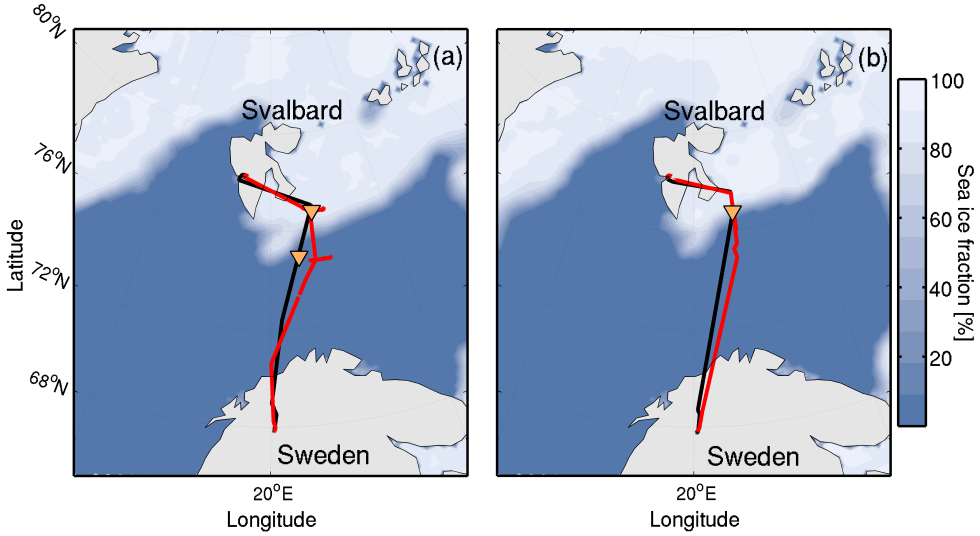

Figure 2. Flight track of **(a)** B762 and **(b)** B764, with section 1 (black) and section 2 (red) indicated. Dropsondes were released during section 1, whilst in situ observations were made during section 2. Dropsonde release locations are marked (orange triangles). Case 1 (sea ice, north) and case 3 (ocean, south) are from flight B762, whilst case 2 (MIZ) is from B764. Sea ice fraction is shown in shading.

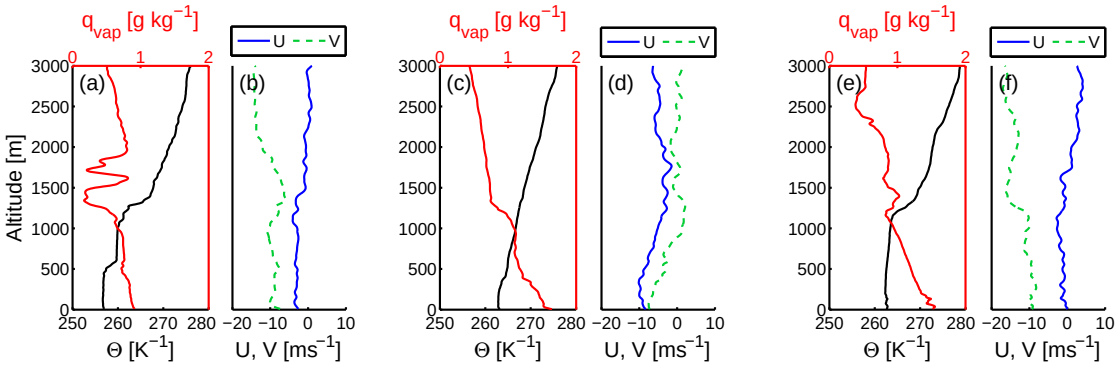

Figure 3. Potential temperature, vapour mixing ratio, and wind speed profiles measured by the three dropsondes used to initialise the LEM in this study. **(a-b):** dropsonde 1 released over the sea ice during flight B762. **(c-d):** dropsonde 2 released over the MIZ during flight B764. **(e-f):** dropsonde 3 released over the ocean during flight B762.

comparatively warm ocean. The potential temperature profile for the sea ice case (case 1) displays a double inversion; the first at ∼500 m and the second at ∼1200 m. The latter inversion is at approximately the same altitude as that measured in the ocean case (case 3). The MIZ case shows a subtle inversion at approximately 400 m; however, it is not as prominent as the other two cases.

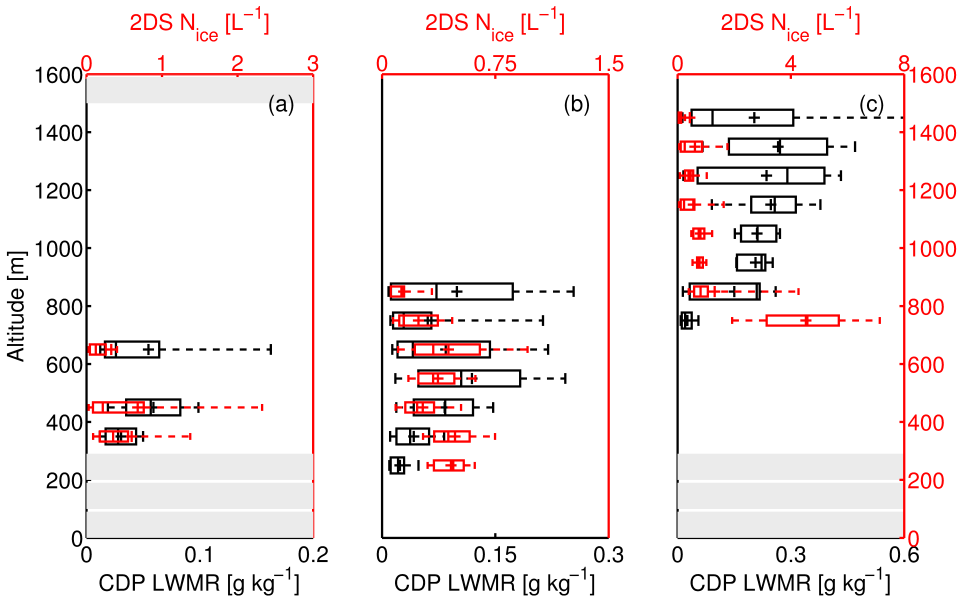

Figure 4. Observations of 2DS ice number concentration (red) and CDP liquid water mixing ratio (LWMR, black). **(a):** Sea ice, case 1. **(b):** MIZ, case 2. **(c):** Ocean, case 3. Only observations from mixed-phase cloud are included, with a derived CDP liquid water content threshold of $\geq$0.01 g m^{-3} distinguishing in-cloud measurements. Box edges: 25th and 75th percentiles, Median: | , and Mean: +. Altitudes not sampled by the aircraft are indicated with grey boxes.

Table 2. Summary of cloud observations for each of the three cases considered. Values quoted are averaged quantities, with 1σ in brackets.

Case Number	Flight	Date [2013]	Surface Conditions	Cloud Extent [m]	LWMR[a] [g kg^{-1}]	N$_{ice}^{b}$ [L^{-1}]
1	B762	23 Mar	Sea ice	300-700	0.05 (0.04)	0.47 (0.86)
2	B764	29 Mar	MIZ/Ocean	200-900	0.09 (0.07)	0.35 (0.20)
3	B762	23 Mar	Ocean	700-1500	0.24 (0.13)	0.55 (0.95)

[a] Liquid water mixing ratio

[b] Ice crystal number concentration

In situ measurements for all cases show a distinct, mixed-phase cloud from approximately 300 m to 700 m (case 1), 200 m to 900 m (case 2) and 700 m to 1500 m (case 3, Fig. 4). These measurements are summarised in Table 2. Liquid water mass mixing ratios (LWMRs), derived from CDP measurements, provide a direct comparison with the LEM: the liquid measurements in the sea ice case are low, of the order of $\sim$0.05 g kg^{-1}, whereas the MIZ and ocean cases have larger mixing ratios ($\sim$0.1-0.3 g kg^{-1}). 2DS ice number concentrations are consistently low within the cloud layer in all cases, on the order of approximately 0.2-1.5 L^{-1}. High ice number concentrations at cloud base in case 3 are thought to be minor contributions of

secondary ice due to crystal fragmentation (Young et al., 2016a). Cloud top temperatures (CTTs) were approximately -20°C, -13°C and -20°C respectively (Table 1). Such temperatures are too cold for efficient secondary ice production and too warm for homogeneous ice nucleation (Hallett and Mossop, 1974; Pruppacher and Klett, 1997). For this study, modelled microphysics below 1500 m is focused upon as this is directly comparable with these aircraft observations.

4 Results

4.1 Control simulations

Within the Morrison et al. (2005) bulk microphysics scheme, the C86 ice nucleation parameterisation is used to simulate the heterogeneous nucleation of ice. Onset conditions commonly used in the WRF model ($T < -8°C$ and $S_w > 0.999$, or $S_i > 1.08$) were applied as a control simulation for each case. Figure 5 shows the ice number concentrations, N_{ice}, and liquid water mixing ratios, Q_{liq}, modelled over the sea ice (case 1), MIZ (case 2), and ocean (case 3). In case 1, no liquid water is modelled (Fig. 5**a**). Ice number concentrations of $\sim 3\,L^{-1}$ are simulated at an altitude of approximately 1000 m for the first 10 h of the run, peaking at $3.4\,L^{-1}$. This ice then dissipates, after which N_{ice} $\sim 1\,L^{-1}$ is maintained at 500 m for the remainder of the simulation. This sustained number concentration is within the range observed ($0.47 \pm 0.86\,L^{-1}$, Table 2); however, mixed-phase conditions are not modelled. In contrast, co-existing regions of liquid and ice are simulated in cases 2 and 3. Modelled N_{ice} over the MIZ ($\sim 1.0\,L^{-1}$, Fig. 5**b**) is in reasonable agreement with the mean observed ($0.35 \pm 0.20\,L^{-1}$, Table 2). Persistent mixed-phase conditions are simulated in case 2 for approximately 16 h. Such conditions are also attained in case 3 (Fig. 5**c**), with modelled ice number concentrations much greater than observed; modelled N_{ice} peaks at $3.7\,L^{-1}$, compared with $0.55 \pm 0.95\,L^{-1}$ observed. This case glaciates after approximately 15 h. Therefore, under the conditions commonly used in the WRF model, C86 overpredicts N_{ice} and unsuccessfully reproduces the observed mixed-phase conditions over all three surfaces considered. To force the formation of persistent liquid in all cases, we restrict the formation of primary ice to water-saturated conditions in our subsequent model runs.

4.2 Ice nucleation at water-saturation

4.2.1 Case 1: Sea ice

Figure 6**(a, d, g)** shows modelled N_{ice} and liquid water mixing ratio, Q_{liq}, using the three main parameterisations – C86, D10, and ACC – over the sea ice. Vertical (Z-Y) slices of N_{ice}, Q_{liq}, and W at 21 h are included in the Supplement (Fig. S2). A mixed-phase cloud is simulated at ~500 m after 17 h, with a liquid layer at cloud top with ice formation and precipitation below. Peak Q_{liq} varies from C86 at the smallest ($0.09\,g\,kg^{-1}$), through D10 ($0.1\,g\,kg^{-1}$), to ACC at the largest ($0.14\,g\,kg^{-1}$, Table 3). N_{ice} and Q_{liq} increase with time as the cloud evolves. Modelled N_{ice} is of the same order of magnitude using each parameterisation, with maximum values of $2.32\,L^{-1}$, $1.29\,L^{-1}$, and $0.47\,L^{-1}$ attained by C86, D10, and ACC respectively.

Figure 7 shows a comparison between measured and modelled (total) N_{ice}, $N_{ice>100\mu m}$, and Q_{liq} for each case when using these three parameterisations. Comparisons including D10×10 and D10×0.1 are included in the Supplement (Fig. S5). Mean

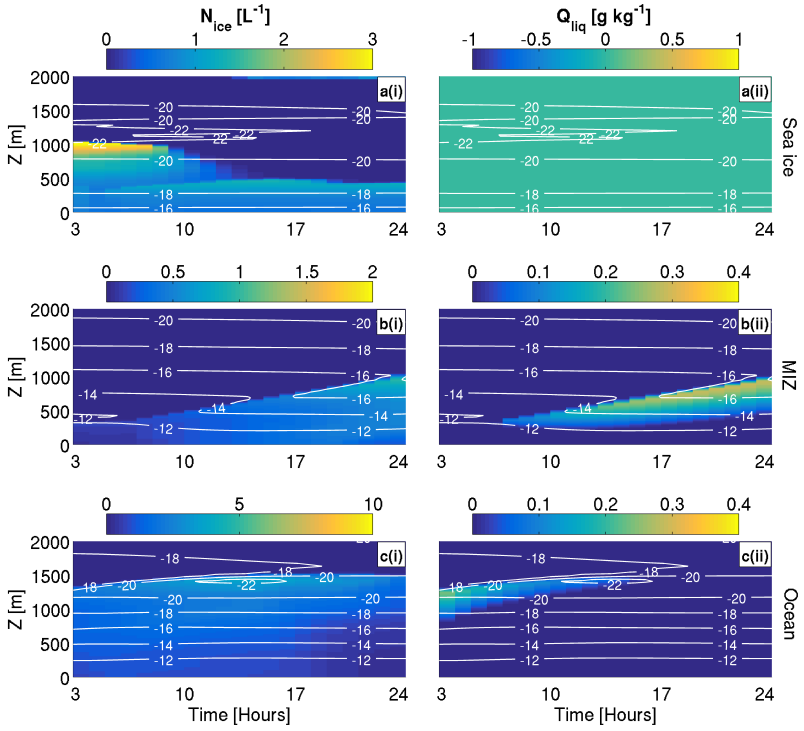

Figure 5. Simulated ice number concentrations (N_{ice}, **(i)**) and liquid water mixing ratios (Q_{liq}, **(ii)**) using the C86 parameterisation under default WRF conditions ($T < -8°C$, $S_w > 0.999$, or $S_i > 1.08$). **a:** Sea ice (case 1), **b:** MIZ (case 2), **c:** Ocean (case 3). Run length 24 hours. Temperature (°C) contours are overlaid in white. Note changing colour bar for each subfigure.

Table 3. Maximum modelled values during each case for each parameterisation implemented at water-saturation.

Case	Parameter	C86	D10	ACC	D10×10	D10×0.1
Sea ice (case 1)	N_{ice} [L^{-1}]	2.32	1.29	0.47	2.89	0.13
	Q_{liq} [g kg^{-1}]	0.09	0.10	0.14	0	0.16
MIZ (case 2)	N_{ice} [L^{-1}]	1.09	1.03	0.36	6.57	0.11
	Q_{liq} [g kg^{-1}]	0.29	0.28	0.34	0.12	0.39
Ocean (case 3)	N_{ice} [L^{-1}]	3.83	3.01	0.71	15.5	0.37
	Q_{liq} [g kg^{-1}]	0.32	0.32	0.36	0.10	0.38

parameters modelled at 21 h during case 1 are shown in Fig.7**(a, d, g)**. The method for choosing these time steps is detailed in the Supplement (Figs. S6). C86 produces the greatest ice number concentration, with D10 producing the second greatest and ACC producing the least (Fig. 7**a**). The empirically-derived ACC relationship provides the best agreement with the mean observed N_{ice} as expected, simulating approximately 0.4 L^{-1}.

Software for processing the 2DS data cannot distinguish between liquid and ice at small sizes (<80 µm); therefore, the number concentration of small ice crystals is not a reliable measure with this instrument. For this reason, the observed number concentration of ice crystals greater than 100 µm are also compared with those modelled in this size range. Figure 7**d** shows this comparison for case 1. Again, ACC performs well, with approximately 0.2 L^{-1} simulated. D10 and C86 produce a larger $N_{ice>100\mu m}$ than observed. Figure 7**g** shows the comparison of observed LWMR and modelled Q_{liq}. Modelled variability is not as clear as with the N_{ice} data, and most of the variability occurs at the same altitude (500 m). In contrast to N_{ice} and $N_{ice>100\mu m}$, ACC produces the greatest Q_{liq}, while C86 and D10 underestimate with respect to the observations.

Modelled N_{ice} and Q_{liq} for D10×10 and D10×0.1 are shown in Fig. 8**(a, g)**, and D10 is again included (Fig. 8**d**) for comparison. D10×0.1 produces N_{ice} values which are approximately a factor of 2 too low. As a consequence of these lower ice number concentrations, Q_{liq} is enhanced, with maximum of 0.16 g kg^{-1} modelled. In contrast, no liquid water is simulated when using D10×10, with peak ice number concentrations of 2.89 L^{-1} produced at approximately 400 m.

Liquid and ice water paths (LWP and IWP, respectively) are shown in Fig. 9**(a, d)**. Both increase with model time when using each of the parameterisations. D10×0.1 produces the highest LWP and lowest IWP. D10×10 produces no liquid – giving a LWP of zero – and the simulated IWP increases initially (between approximately 17 h and 20 h), but subsequently decreases. The D10 and C86 parameterisations produce similar trends in the LWP and IWP traces, resulting in approximately 15-20 g m^{-2} and 2-3 g m^{-2} respectively by 24 h.

4.2.2 Case 2: Marginal ice zone

Figure 6**(b, e, h)** shows that there is little variation between the simulations over the MIZ (case 2). C86 and D10 produce comparable peak N_{ice} and Q_{liq} values (Table 3). These parameterisations also produce a similar LWP ($\sim$100 g m^{-2}) and IWP ($\sim$7 g m^{-2}) by the end of each simulation (Fig. 9**b, e**). More liquid and less ice is simulated with ACC (Fig. 6**h**, Table 3).

D10×0.1 produces the lowest N_{ice} overall (0.11 L^{-1}, Fig. 8**h**). This allows Q_{liq} to be greater than in the other simulations (0.39 g kg^{-1}, Table 3) and the simulated LWP and IWP increase steadily with time (Fig. 9**b, e**). D10×0.1 produces the lowest IWP, whilst D10×10 produces the greatest. N_{ice} of up to 6.6 L^{-1} are simulated using D10×10, with a suppressed Q_{liq} (Fig. 8**b**).

At 17 h, N_{ice} modelled using ACC are lower (0.2 L^{-1}) in comparison to the mean observed at each altitude bin (Fig. 7**b**). However, ACC overpredicts $N_{ice>100\mu m}$ compared to observations (0.13 L^{-1} versus 0.03 L^{-1}, Fig. 7**e**). D10 produces the greatest N_{ice} in this case, yet C86 produces a similar concentration. Again, D10 and C86 both overpredict $N_{ice>100\mu m}$ and variability in Q_{liq} is limited to the same altitude (700 m, Fig. 7**h**).

4.2.3 Case 3: Ocean

Figure 6**(c, f, i)** shows that there is more variation between the parameterisations over the ocean (case 3). C86 causes cloud glaciation at approximately 17 h. Liquid water is simulated at cloud top until this point. D10 produces a mixed-phase cloud layer for the full 24 h duration of the run. Again, more liquid and less ice is modelled using ACC (Table 3). D10×0.1 produces peak N_{ice} values that are almost a factor of 2 lower than observed for case 3 ($0.37\,L^{-1}$), allowing the greatest peak Q_{liq} to form out of the five parameterisations considered ($0.38\,g\,kg^{-1}$, Fig. 8**i**, Table 3). Q_{liq} is high with comparison to the ACCACIA observations (Table 2); however, N_{ice} is in better agreement than the D10 simulations in this case. In contrast, D10×10 causes rapid glaciating events to occur (Fig. 8**c**). These repeat every ∼3 h of the model simulation. Little liquid water is produced throughout ($\sim 0.1\,g\,kg^{-1}$); however, small increases are modelled alongside the glaciating bursts.

Substantial differences can be identified between the three main parameterisations considered. At 7 h, C86 produces the highest N_{ice}, with D10 producing the second greatest and ACC producing the least (Fig. 7**c**). D10 and C86 overpredict $N_{ice>100\mu m}$, as with cases 1 and 2. Again, ACC provides good agreement with the mean N_{ice} observed as expected, simulating approximately $0.4\,L^{-1}$. ACC also produces a comparable $N_{ice>100\mu m}$ ($\sim 0.2\,L^{-1}$, Fig. 7**f**). A more complex picture occurs in Fig. 7**i**: Q_{liq} is at its greatest at the chosen time step (7 h, Fig. S8); therefore the ±4 h variability illustrated is always less than the mean modelled profile shown using each parameterisation. As with case 1, C86 and D10 underestimate Q_{liq}, and ACC performs well, with comparison to the observations.

The steady increase of IWP and LWP seen in cases 1 and 2 is not modelled in case 3: all simulations produce a decreasing LWP with time, whilst the majority also produce a decreasing IWP (Fig. 9**c, f**). A consistent IWP and steadily decreasing LWP are modelled with ACC. The rapid glaciating events modelled with D10×10 (shown in Fig. 8**c**) can again be seen in the IWP, with a maximum value of nearly $25\,g\,m^{-2}$ attained at approximately 14 h (Fig. 9**f**). The LWP is zero for the majority of this simulation; however, a small amount of liquid also forms at 14 h. As with case 2, D10 and C86 produce similar IWP and LWPs in case 3 for the majority of the simulations; however, these diverge at approximately 17 h when the C86 case glaciates (Fig. 9**c, f**).

During the D10 simulation, peculiar trends form in both the LWP and IWP traces at approximately 19 h. Peaks and troughs in the IWP trace correspond with peaks in the LWP at approximately 20 h and 22 h. To investigate these LWP and IWP trends further, Fig. 10 shows X-Y planar views of each simulated parameterisation at 21 h: LWP and IWP are total integrated values over the full height of the domain, and W is chosen at approximately cloud top (1500 m). Little variation can be seen in D10×10 (Fig. 10**a**) and C86 (Fig. 10**b**) at this time as N_{ice} and Q_{liq} have dissipated and not reformed yet. Co-located hot spots of IWP, LWP, and vertical velocity can be seen in the D10 simulation (Fig. 10**c**). Strong updraughts are modelled in close vicinity to enhanced downdraughts. Regions of high LWP or IWP are not seen in the ACC case (Fig. 10**d**); however, similar activity can be identified in the D10×0.1 (Fig. 10**e**) case. This structure is most visible in the LWP as little ice is simulated.

The parameterisations represented in Fig.10**(c, d, e)** were considered further: the D10 case produces the most ice and least liquid of the three, with D10×0.1 vice versa. Hot-spots of LWP, IWP, and W form with D10, but not with ACC. Defined structure can be seen in the LWP of D10×0.1, and this shape mirrors a region of isolated downdraughts (Fig.10**e**). These

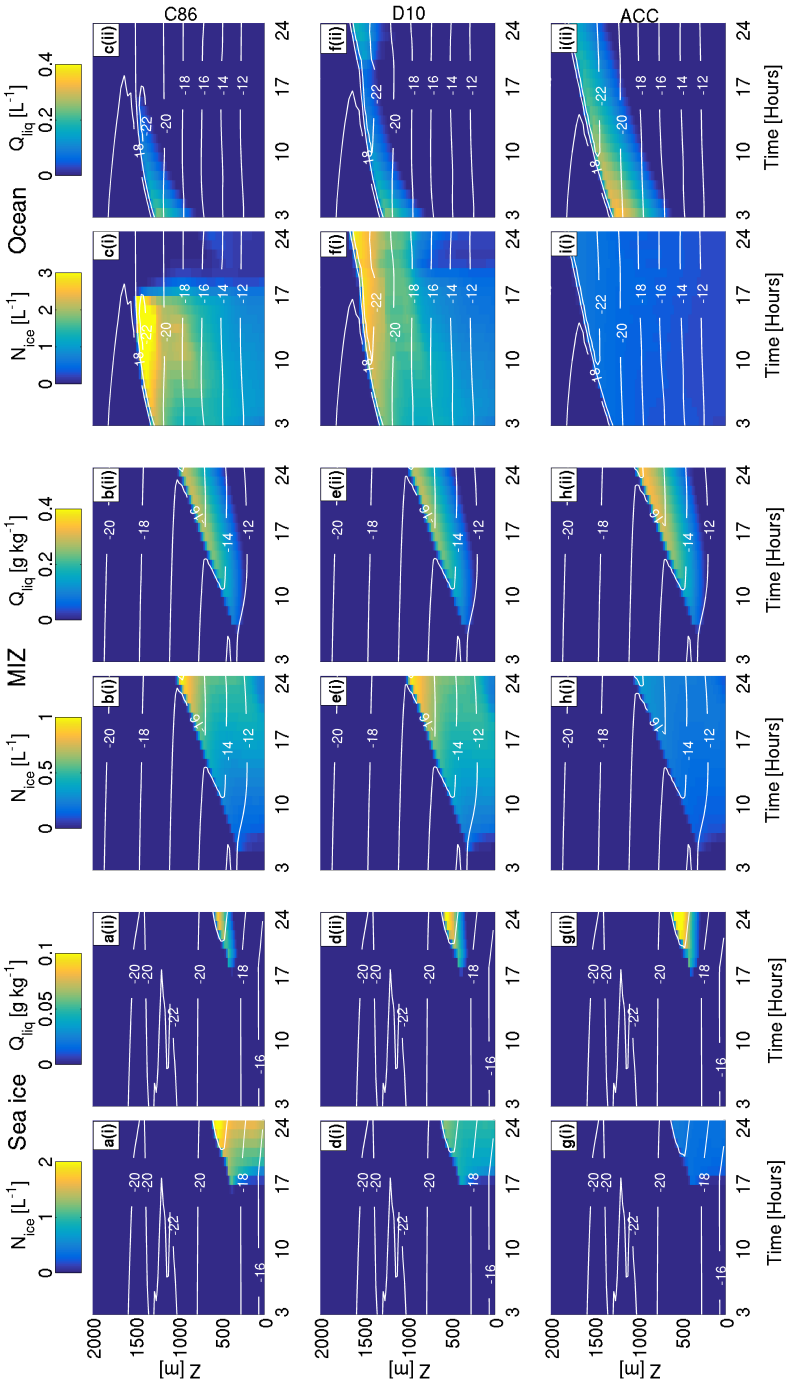

Figure 6. Simulated ice number concentrations (N_{ice}, **(i)**) and liquid water mixing ratios (Q_{liq}, **(ii)**) using the (**a-c**) C86, (**d-f**) D10, and (**g-i**) ACC parameterisations. All are restricted to water-saturation. **(a, d, g):** Sea ice (case 1), **(b, e, h):** MIZ (case 2), **(c, f, i):** Ocean (case 3). Run length 24 hours. Temperature (°C) contours are overlaid in white. Note changing colour bar at the top of each column, which corresponds to data in that column only.

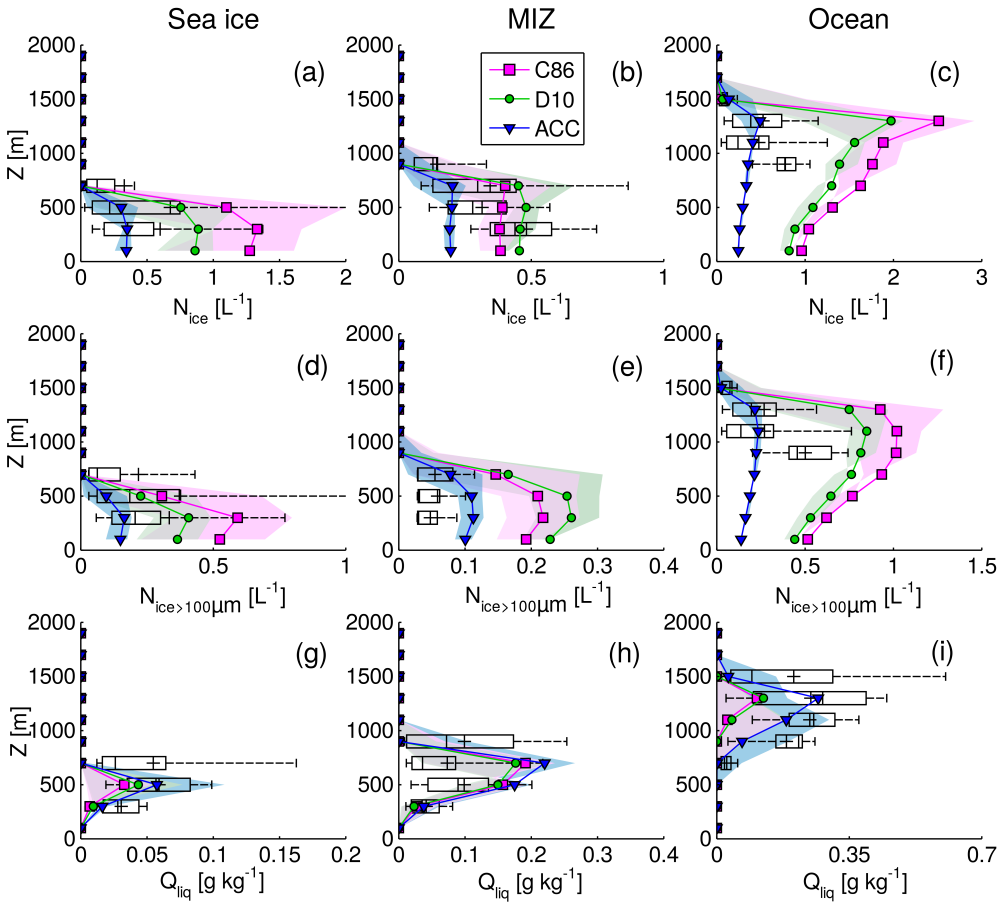

Figure 7. Observed N_{ice}, $N_{ice>100\mu m}$, and Q_{liq} for the sea ice (**column 1**), MIZ (**column 2**), and ocean (**column 3**) cases. Observations are shown as black boxes. Box edges represent the 25th and 75th percentiles, and the median and mean values are denoted by | and + respectively. Mean modelled values using the C86 (magenta), D10 (green), and ACC (blue) parameterisations are overlaid. Model time steps of 21 h, 17 h, and 7 h are used for the sea ice, MIZ, and ocean cases respectively, as these time steps offer the best comparison with the observations. Shading (in pink, green, or blue for C86, D10, and ACC respectively) indicates variability in the model parameters from $\pm$3 h in cases 1 and 2, and $\pm$4 h in case 3, where a larger interval is implemented in the latter case as the chosen parameters showed little variability over the shorter time step **(a-c):** N_{ice}; **(d-f):** $N_{ice>100\mu m}$; and **(g-i):** Q_{liq}. Observed N_{ice} data from noted shattering event (Young et al., 2016a) are excluded in panels **c** and **f**, so that only primary contributions of ice are considered.

features may be linked to precipitation from the simulated cloud, and Fig. 11 shows the solid (snow + graupel) and liquid (rain) precipitation modelled in the D10, ACC, and D10$\times$0.1 simulations for case 3.

With D10, a greater number concentration of solid precipitation (up to 1 L^{-1}) is modelled than in the ACC (0.29 L^{-1}) or D10$\times$0.1 (0.17 L^{-1}) simulations. Similarly, significantly more rain is modelled (up to 27 L^{-1}) in the D10$\times$0.1 simulation in

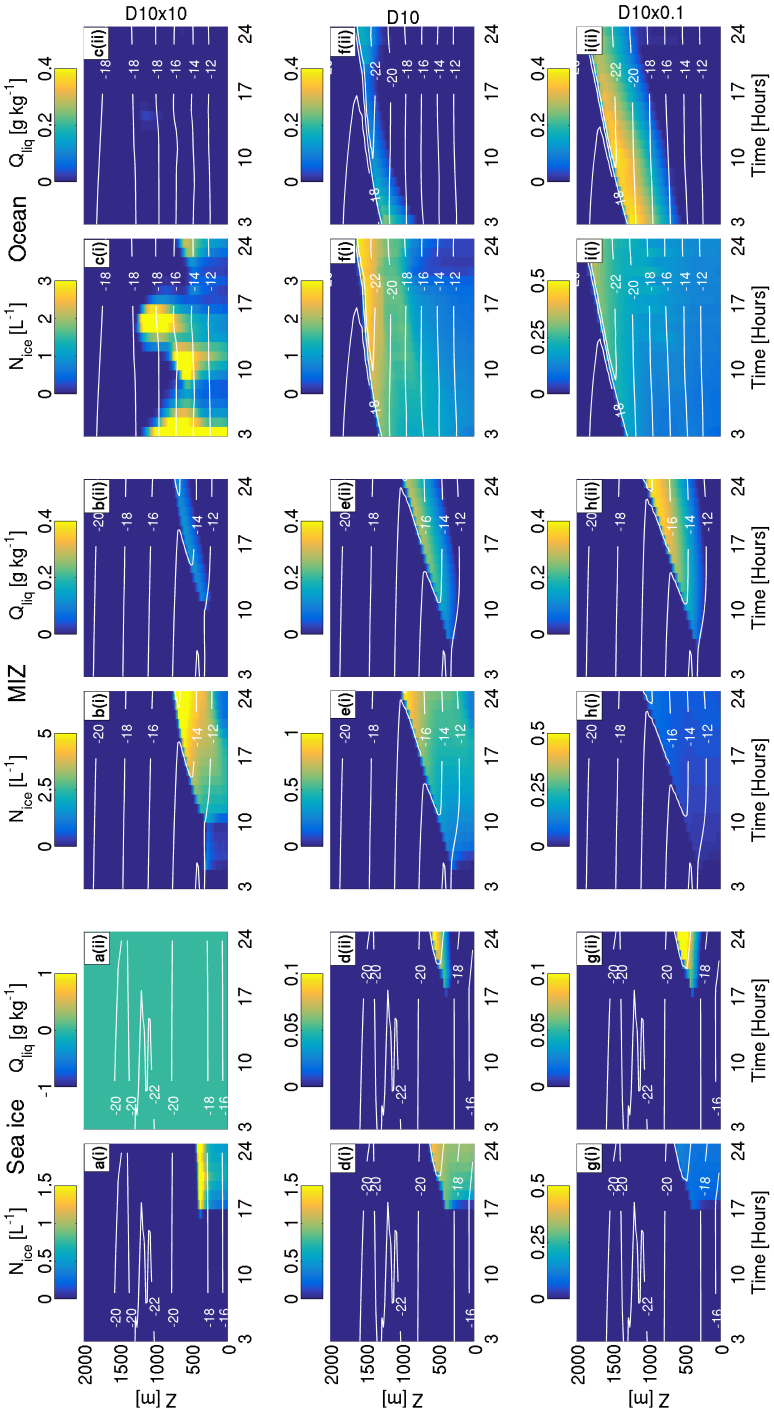

Figure 8. Sensitivity of cloud structure to ice crystal number. **(a-c):** D10×10, **(d-f):** D10, **(g-i):** D10×0.1. As previous, N_{ice} and Q_{liq} are shown, and columns indicate sea ice, MIZ, and ocean from left to right. Run length 24 hours. Temperature (°C) contours are overlaid in white. Note changing colour bars for each subfigure.

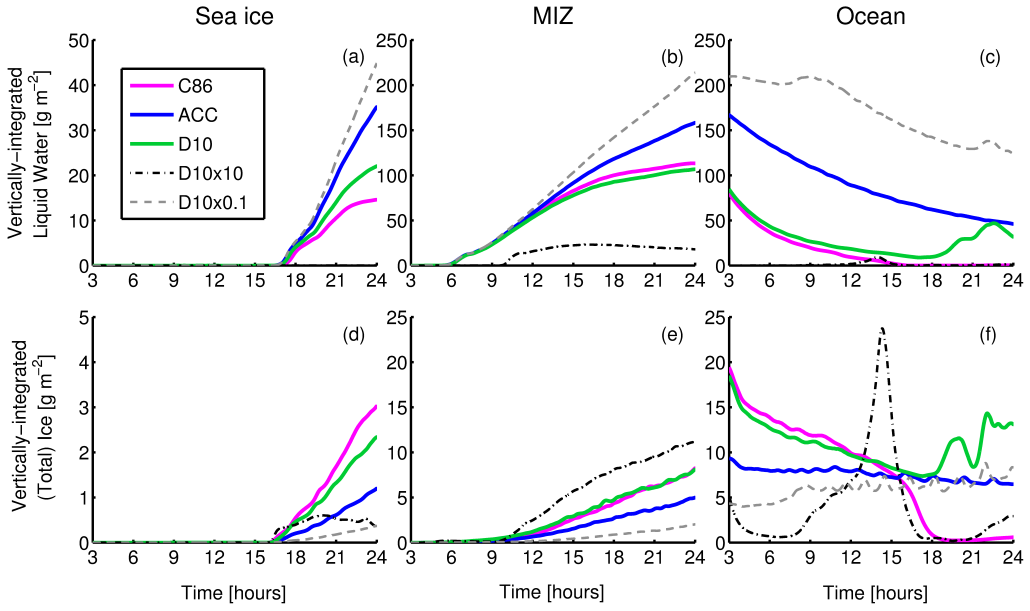

Figure 9. Vertically-integrated liquid (**a-c**) and ice water paths (**d-f**) for the sea ice, MIZ, and ocean cases when implementing each of the C86, ACC, D10, D10×10, and D10×0.1 parameterisations under water-saturated conditions.

comparison to ACC (17 L^{-1}) or D10 (12 L^{-1}). With comparison to D10 and D10×0.1, ACC produces less solid and less liquid precipitation respectively. Precipitation modelled during cases 1 and 2 are shown in the Supplement (Fig. S9).

5 Discussion

5.1 Ice nucleation at water-saturation: Cooper (1986)

Using in situ observations for reference, we have shown that ice nucleation under water-saturated conditions allows mixed-phase conditions to be modelled over the sea ice, marginal ice zone (MIZ), and ocean. Using C86 deposition-condensation freezing in the Morrison et al. (2005) microphysics scheme as a control for each case, the mixed-phase conditions observed over the MIZ (case 2) and the ocean (case 3) are captured by the model; however, no liquid is modelled over the sea ice (case 1). Cases 2 and 3 impose surface fluxes from the simulated ocean surface below; fluxes which induce turbulence in the modelled clouds. The lack of strong surface sensible and latent heat fluxes in case 1 restricts the formation of liquid water in the model as the second imposed criterion of ice supersaturation ($S_i > 1.08$) is attained first. This modelled microphysics is unrepresentative of the observations during case 1. It is unlikely that the nucleation mechanisms involved in these clouds would differ substantially between the sea ice, MIZ, and ocean. Therefore, we suggest that deposition-condensation freezing is ineffective at ubiquitously reproducing Arctic MPS over the range of surfaces possible.

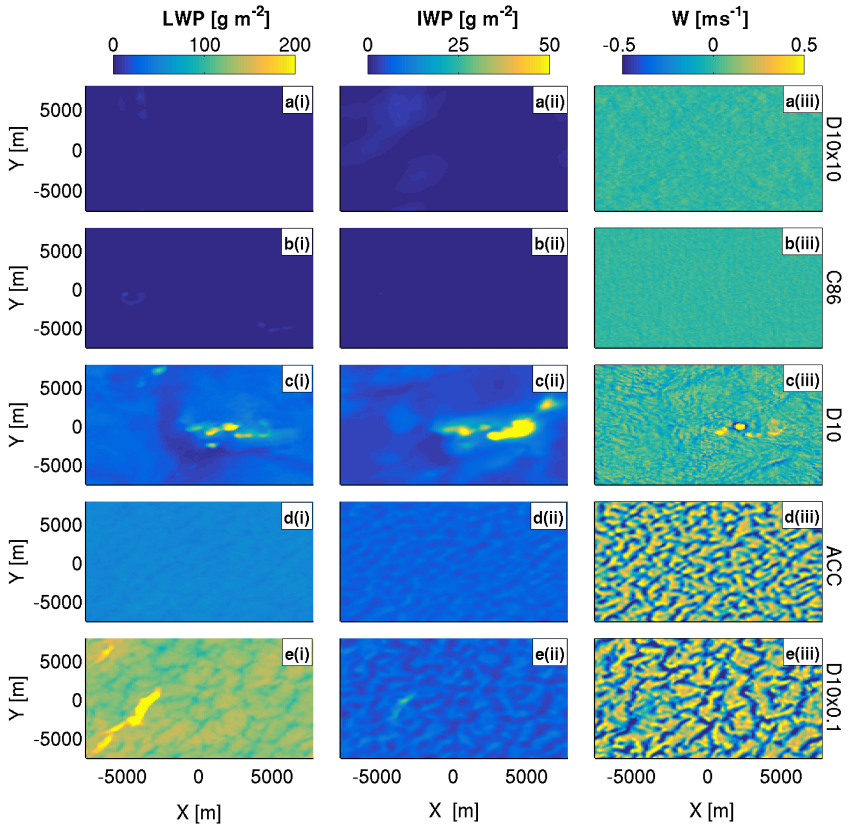

Figure 10. Liquid and ice water path (**first** (**i**) and **second** (**ii**) columns) and vertical velocity at approximately 1500 m (**third** (**iii**) column) for each of the five ice nucleation parameterisation scenarios in the ocean case. Planar X-Y slices are shown at 21 h. Runs are arranged such that the simulation which produced the most ice (D10×10, **a**) is on the top row, and that which produced the least ice (D10×0.1, **e**) is on the bottom row. Note changing colour bar at the top of each column, which corresponds to data in that column only.

5.2 Relationship with predicted INPs: DeMott et al. (2010)

Of the two established parameterisations considered (Cooper 1986 and DeMott et al. 2010), D10 produces the best agreement with the observed ice and liquid in all cases. In particular, it reproduces the low ice number concentrations observed during case 2.

D10 predicts the number of INPs – not ice crystals – active at a given temperature, T_K. Though reasonable agreement is found with observations, D10 still produces too many ice crystals in each case (Fig. 6**d, e, f**). D10 predicts approximately double and quadruple the number of ice crystals observed at the respective CTTs in cases 1 and 3 (Tables 1 and 2). Young et al. (2016b) found a large fraction of super-micron sea salt particles over the sea ice (case 1) and below the MIZ cloud (case 2). No filter data were available for the ocean case (case 3); however, it can be assumed that a similar fraction of these aerosol particles

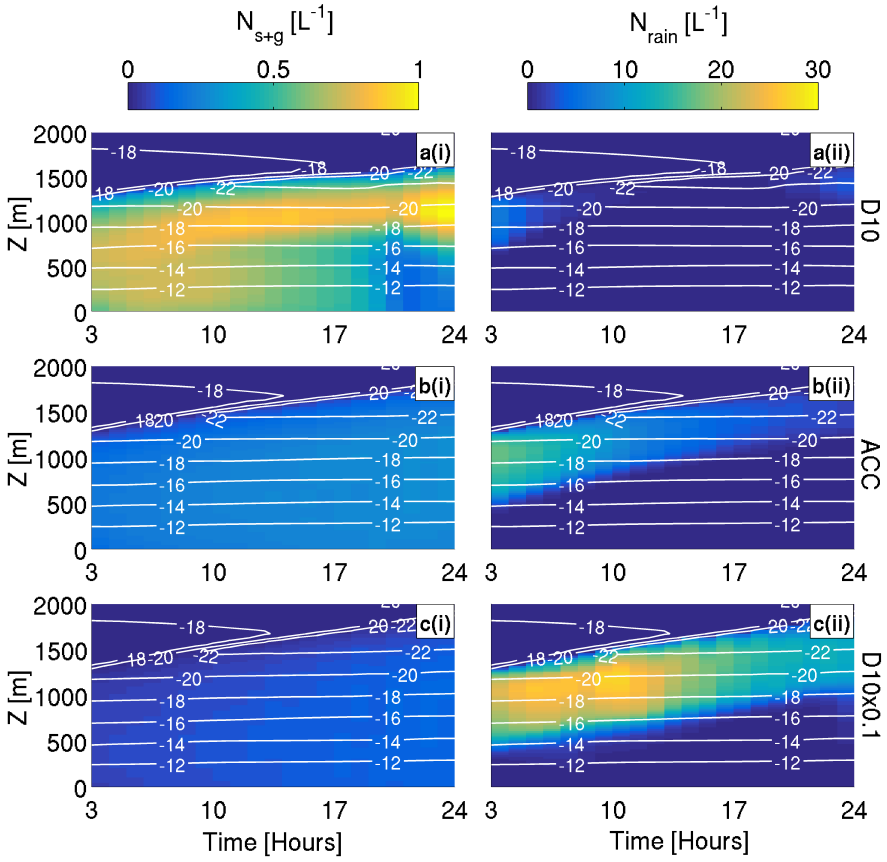

Figure 11. Summed snow and graupel number concentrations (N_{s+g}, (**i**)) and rain number concentration (N_{rain}, (**ii**)) using (**a**) D10 , (**b**) ACC, and (**c**) D10×0.1 during case 3. Run length 24 hours. Temperature (°C) contours are overlaid in white. Note changing colour bar at the top of each column, which corresponds to data in that column only.

may also be sea salt, given they were found upstream over the sea ice under the same meteorological conditions (Young et al., 2016a). Given these results, it is not surprising that D10 overestimates the quantity of super-micron INPs available to nucleate ice in these conditions, as sea salt is an inefficient INP and constitutes a large fraction of $n_{aer,0.5}$.

Additionally, an approximation of D10 was applied. The average aerosol number concentration ($0.5 < D_P \leq 1.6\,\mu m$, DeMott et al., 2010) in each case was used to evaluate Eq. 2 to give a temperature-dependent function. This idealised scenario would only be representative of a region where the aerosol particle number concentration was being replenished and INPs were not depleted. Such replenishment is likely unrepresentative of the Arctic, as there are few in situ sources of INP in this region. Additionally, a constant input of aerosol particle number concentration was used in Eq. 2, irrespective of altitude in the model; therefore, spatial variability of INPs in the boundary layer is not represented. Particle number concentrations typically decrease

with altitude away from local surface sources; therefore, this approximation of vertical homogeneity may also be positively influencing the number concentration of ice crystals predicted by D10.

5.3 ACCACIA observational fit: ACC

For the three case studies considered, predicted number concentrations of large ice crystals ($>100\,\mu m$) using the empirically-derived ACC relationship compare well with the observations as expected; however, it is interesting to note how the modelled cloud evolves in these simulations. ACC allows for persistent mixed-phase conditions to be simulated for the full 24 h duration in case 3, and for ≥ 8 h in cases 1 and 2. Cloud temperatures are colder and cloud top is higher than in the C86, D10, or D10×10 simulations, due to strong radiative cooling from the heightened Q_{liq}. The modelled liquid-dominated clouds display enhanced cloud-driven convection across the full domain (Figs. 10, S2-S4). Only the D10×0.1 simulations produce colder temperatures and a higher cloud top. As expected due to its empirical origin, ACC produces the best microphysical agreement with observations for cases 1 and 3 (Fig. 7**g, i**); however, too much Q_{liq} is modelled in case 2 (Fig. 7**h**). Too few ice crystals are modelled to sufficiently deplete the liquid phase via the WBF mechanism. Ice crystal habits are not explicitly resolved in the microphysics scheme, which could influence the modelled Q_{liq}. Habits which undergo efficient vapour growth (e.g. stellar dendrites or sector plates, Mason, 1993) would allow increased ice mass to be modelled, with a consistent N_{ice} and a suppressed Q_{liq}.

The ACC relationship was derived from 2DS ice number concentration data from five springtime ACCACIA flights. The small sample size restricted the range over which a relationship could be established. Ice observations between 252 K and 265 K were collected; therefore, the dependence of ice number concentration on temperatures outwith this range could not be tested. Further observations in this temperature range could allow this relationship to be validated and potentially extended further; however, based on these ACCACIA data, this curve is not applicable beyond $252\,K < T_k < 265\,K$. Temperatures colder than this limit are modelled in case 3 due to increasing cloud top height and strong radiative cooling; therefore, these results must be interpreted with caution.

5.4 Ice number sensitivity

5.4.1 Cloud microphysics

As shown by previous studies (Harrington and Olsson, 2001; Morrison et al., 2011; Ovchinnikov et al., 2011, amongst others), the microphysical structure of Arctic MPS is highly sensitive to ice crystal number. Greater ice number concentrations enhance the efficiency of the WBF process – leading to the depletion of liquid water within the cloud – whilst lower number concentrations allow liquid droplets to persist under moderate vertical motions. D10 sensitivity tests for cases 1 and 2 behave as would be expected: D10×0.1 produces significantly less ice, allowing liquid to dominate and cloud top height to increase, whilst D10×10 produces high ice number concentrations which glaciate case 1 and strongly suppress the liquid of case 2 (Fig. 8). Mixed-phase conditions are maintained in case 2; however, N_{ice} is much larger than observed using this parameterisation (Fig. 4, Table 2). Additionally, in case 3, D10×10 causes rapid glaciating events to occur.

To compare between our water-saturated simulations, we define two stages of cloud evolution: a formation phase, characterised by an increasing LWP, and a decaying phase, with a decreasing LWP. In cases 1 and 2, each parameterisation causes the simulated clouds to remain in the formation phase by the end of each run (Fig. 9**c, f**). Both the LWP and IWP typically increase during these simulations. The LWP of case 2 begins to plateau towards 24 h in these cases, indicating the possible start of the decaying phase. Case 3 attained this phase immediately, as shown by the decreasing LWPs modelled.

Modelled LWPs and IWPs are smaller in case 1 than in both cases 2 and 3. Case 1 imposed negligible surface fluxes; therefore, cloud dynamics was driven primarily by longwave radiative cooling (similar to Ovchinnikov et al., 2011). In the observations, a lack of strong turbulent motions within this cloud layer caused a suppressed LWMR in the vicinity of moderate ice number concentrations (Young et al., 2016a). The LEM reproduces these conditions well in the absence of strong surface fluxes (sensible heat fluxes of 1 W m^{-2} imposed). The ocean-surface cases (2 and 3) implement strong surface fluxes, allowing turbulent motions to sustain a greater Q_{liq} within the mixed-phase cloud layer (Morrison et al., 2008).

Cloud top height clearly increases with model time in cases 1 and 2, and more subtly in case 3. Large-scale subsidence, which would act to suppress cloud top ascent, was not imposed in these simulations. This increasing cloud top was observed by Young et al. (2016a) over the transition from sea ice to ocean; therefore, the modelled cloud structure is in good agreement with observations without large-scale subsidence imposed. However, the temperatures simulated in case 2 (Figs. 6, 8**b, e, h**) are colder than observed (Table 1). Despite this, N_{ice} modelled with the temperature-dependent parameterisations considered is in reasonable agreement with the observations (Fig. 7**b**). Case 2 occurred on a different day to cases 1 and 3; therefore, different synoptic conditions were influencing the sampled cloud systems. Increasing the modelled large-scale subsidence acts to increase the modelled temperatures (not shown, Fig. S10); however, a substantial subsidence would be required to match the observations. Given that imposing large-scale subsidence increases the temperature and suppresses Q_{liq}, without greatly affecting N_{ice}, we suggest that a greater imposed subsidence may improve the agreement with the observations in case 2.

Cloud top reaches higher altitudes in the ACC and D10×0.1 simulations – across all surfaces – compared to D10, C86, and D10×10, due to a greater liquid water content; as more liquid forms from the vapour field, more heat is released, pushing the cloud top higher. These liquid-dominated cases are also shown to experience enhanced convection across the full domain in case 3 (Fig. 10). With increased cloud top height, enhanced radiative and evaporative cooling enforce downdraughts whilst increased latent heat release from droplet formation and growth strengthens updraughts. In the C86, D10, and D10×10 simulations, a greater N_{ice} suppresses efficient droplet growth, latent heat release, cloud top ascent, and strong radiative cooling through the WBF mechanism. This finding is in agreement with Harrington and Olsson (2001), who showed that a high N_{ice} produces weaker BL convection and a shallower BL, whilst liquid-dominated mixed-phase clouds promote a higher cloud top and deeper BL.

5.4.2 Cloud glaciation or break up

Over the ocean (case 3), C86 leads to cloud glaciation when freezing is implemented under both deposition-condensation (Fig. 5**c**) and water-saturated (Fig. 6**c**) conditions. This cloud glaciation is tied to the number of ice crystals produced: over the temperature range shown in Fig. 1, D10×10 and C86 typically produce the most ice, and so rapid ice formation is simulated

once the onset thresholds are reached. This suppresses the liquid phase within the cloud layers, either immediately (D10×10) or after an accumulation period (C86). However, D10 produces a similar N_{ice} (2.07 L^{-1}) to C86 (2.42 L^{-1}, Table 1) at the CTTs considered. This subtle difference in predicted ice number allows the D10 cloud to persist, whilst the C86 cloud glaciates.

While D10 produces a persistent mixed-phase cloud for the full duration, peculiar trends appear at times >20 h. Figure 9 shows the development of peaks and troughs in the IWP, with corresponding peaks in the LWP, after this time. From Fig. 10**c**, localised hot spots of LWP, IWP, and vertical velocity can be seen. These localised regions of increased ice and/or liquid result from isolated convective cells within the cloud. The formation of these cells forces the cloud top higher (Fig. 6**f**), with renewed liquid and ice formation. Similar structures can be seen in the D10×0.1 simulations (Fig. 10**e**); however, these appear mostly in the LWP field and have an elongated, banded shape in comparison to the compact, almost circular, structures which evolve in D10. These localised regions of enhanced convection can be linked to increased precipitation (Fig. 11). Specifically, increased solid (snow + graupel) precipitation is modelled using D10, whilst increased liquid (rain) precipitation is modelled in D10×0.1.

The formation of convective cells in the ocean case mirrors cold air outbreak observations: as cold air moves from over the sea ice to the ocean, the boundary layer becomes thermodynamically unstable, allowing temperature perturbations to cause strong positive feedbacks on the cloud structure. Mixed-phase clouds are sustained by moderate vertical motions (e.g. Shupe et al., 2008a, b), driven by latent heating from hydrometeor growth within the cloud and radiative cooling at cloud top (Pinto, 1998; Harrington and Olsson, 2001). At the cold temperatures considered (approximately -20 °C), ice grows favourably by vapour growth in the vicinity of liquid droplets and, given a high enough N_{ice}, updraughts are enhanced through latent heat release. With enforced updraughts, water supersaturations are sustained, more cloud droplets form, and cloud top is forced to higher altitudes. With more liquid and a higher cloud top, enhanced radiative cooling strengthens downdraughts adjacent to the updraught columns. With a deeper cloud layer, precipitation can form by an increased likelihood of collision-coalescence of droplets, or ice crystal growth and aggregation, within the downdraughts. The formation of precipitation warms and dries the cloud, reinforcing the updraughts and recycling the process. In the D10 ocean case – with high ice number concentrations, but not high enough for glaciation – the accumulation of N_{ice} promotes this pathway, with the development of precipitation being the key factor in the localised, runaway convection that occurs.

With precipitation as snow or rain, Q_{liq} is depleted from the cloud layer. The D10 case produces high number concentrations of snow, which depletes Q_{liq} efficiently. Once the convective activity starts in this case, the cloud liquid is depleted; however, it is also partially restored through sustained supersaturations in the strong updraughts. In the D10×0.1 case, the Q_{liq} depletion is slower as rain is less efficient at removing droplets than snow. Both of these precipitation pathways would therefore likely lead to cloud break up if the simulation time was extended further.

Given the two pathways of precipitation identified by Fig. 11, a question arose: do these structures form as a result of the functional form of D10, or are they related simply to ice number? ACC produced an N_{ice} between D10 and D10×0.1, and no heterogeneous structures were observed. Therefore, to address this question, D10×0.5 was imposed in the LEM (see Fig. 1). For comparison with Table 1, D10×0.5 predicts 1.04 L^{-1} at the CTT. Figure 12 illustrates modelled N_{ice} and Q_{liq} for the D10, D10×0.5, and D10×0.1 simulations over the ocean. LWP and IWP modelled at 21 h are also shown. D10×0.5 produces less ice than D10 and less liquid than D10×0.1: this simulation behaves as expected to also give the microphysical mid-point

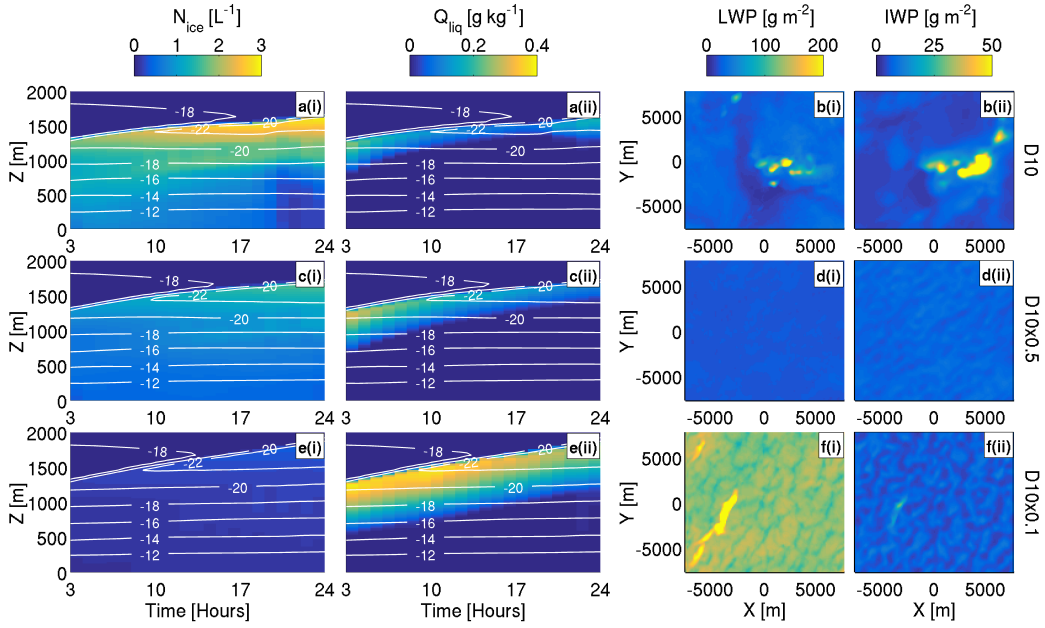

Figure 12. N_{ice}, Q_{liq}, LWP, and IWP modelled in the D10 (**a,b**), D10×0.5 (**c-d**), and D10×0.1 (**e-f**) simulations over the ocean (case 3). N_{ice} and Q_{liq} are shown in the **first** and **second** columns, plotted against time and altitude as previously. LWP and IWP (**third** and **fourth** columns) are X-Y planar views at 21 h, as also shown in Fig. 10. **(a, c, e):** Temperature (°C) contours overlaid in white. Note changing colour bar at the top of each column, which corresponds to data in that column only.

between the D10 and D10×0.1 scenarios. Therefore, the modelled cloud persistence and stability is not just a feature of ACC. A homogeneous cloud structure is modelled with D10×0.5 and the localised hot-spots of the D10 and D10×0.1 cases are not present. Such hot-spots do not form in the D10×0.5 simulation. Modelled precipitation (Fig. S11 in the Supplement) using this parameterisation is significantly less than D10 (snow + graupel) and D10×0.1 (rain), and the simulated cloud persists for the full 24 h duration with no break up.

Additionally, a larger domain size was imposed to test if these convective cells were related to the imposed cyclical boundary conditions: both similar structures and LWP / IWP trends formed (not shown, Figs. S12, S13), suggesting these convective cells are not simply a result of the domain configuration. Within the time scales imposed in this study (24 h), these cells are only observed over the ocean (case 3). Given more time (33 h), case 2 also develops convective cells and precipitation when D10 and D10×0.1 are imposed (not shown, Figs. S14– S17). Therefore, we conclude that – in two of the ACCACIA cases considered, which occurred on different days, under different synoptic conditions, with different air mass histories (Young et al., 2016b) – model simulations using the D10 ice nucleation parameterisation can produce localised cellular structure within the mixed-phase cloud layer, given enough time to do so.

Here, the development of appreciable precipitation is particularly sensitive to ice number. ACC and D10×0.5 maintain mixed-phase conditions for 24 h over the ocean, with no cell development (Fig. 12), suggesting there is a "sweet spot" for N_{ice}

in this case. Glaciation occurs with C86, persistence is achieved with D10×0.5 and ACC, and convective cells form in D10 and D10×0.1: it is unclear which representation is correct in this environment, as observations do show the development of roll convection in cold air outbreak scenarios as the cold air masses move over the warm ocean (e.g. Hartmann et al., 1997). Additionally, snow precipitation was observed by Young et al. (2016a) in this case. It cannot be stated whether the time scales of convection development modelled here are good representations of this phenomenon.

5.4.3 Cloud persistence

Mixed-phase conditions are sustained for at least 8 h in all three cases when imposing the three main parameterisations; ACC, D10, and C86. By additionally considering the sensitivity tests (D10×10, and D10×0.1), we can suggest limitations of N_{ice} which maximise cloud persistence in each case, based on the predictions at the cloud top temperature (Table 1). Over the sea ice (case 1), ACC performs well as expected (producing $0.51\,L^{-1}$ at the CTT) and produces a comparable Q_{liq} (Fig. 7**a, g**). D10 only marginally overpredicts N_{ice} ($1.31\,L^{-1}$, Table 1). D10×0.1 produces too few ice crystals and simulated Q_{liq} is too high with comparison to the observations (Table 3). C86 predicts too much ice ($2.03\,L^{-1}$, Table 1), peaking at $2.32\,L^{-1}$ when implemented in the model (Table 3). Given these results, optimal mixed-phase cloud persistence, and comparable microphysics, is modelled with $0.51\,L^{-1} < N_{ice(CTT)} < 1.31\,L^{-1}$ over the sea ice. With reference to the observed N_{ice} ($0.47 \pm 0.86\,L^{-1}$, Table 2), the upper limit proposed here is more than twice the mean value, but is still within one standard deviation.

Over the MIZ (case 2), all parameterisations produce a mixed-phase, sustained cloud layer. Without observations to compare to, it may not have been possible to identify which has a more realistic grounding. However, we have shown that C86 and D10 perform similarly and produce marginally higher ice number concentrations than are observed (Fig. 7**b**). These relationships predict ice/INP number concentrations of $0.23\,L^{-1}$ / $0.34\,L^{-1}$ respectively at the CTT of case 2. Q_{liq} also agrees well with observations when implementing these parameterisations. However, both C86 and D10 overpredict $N_{ice>100\mu m}$, suggesting the majority of modelled ice is growing too efficiently. This is likely representative of this case, as the warm, sub-zero cloud temperatures (-13 °C) would not promote efficient ice crystal growth. ACC also produces a sustained, mixed-phase cloud layer in case 2; however, a significantly greater Q_{liq} is modelled than is observed ($0.22\,g\,kg^{-1}$, compared with $0.07\,g\,kg^{-1}$, at 700 m in Fig. 7**h**). This suggests that the simulated ice number concentration is not sufficient enough to suppress the formation of liquid with this relationship. Optimal mixed-phase cloud persistence and comparable microphysical structure is modelled when $0.23\,L^{-1} < N_{ice(CTT)} < 0.34\,L^{-1}$ over the MIZ, where the upper limit is in good agreement with the mean observed and the lower limit is within one standard deviation (0.35±0.20, Table 2).

Over the ocean (case 3), strong sensitivities to N_{ice} emerge. D10×10 simulates a high N_{ice}; therefore rapid, repeating glaciating events occur. This is not representative of the persistent, mixed-phase MPS of interest. C86 allows a mixed-phase cloud layer to form for some time, approximately 17 h, after which it glaciates due to accumulated ice concentrations. This glaciating event does not occur with D10, even though only $\sim 0.4\,L^{-1}$ less ice is predicted at the CTT. Both C86 and D10 do not reproduce the observed cloud liquid well (Fig. 7**i**). D10×0.1 produces reasonable agreement with the N_{ice} and Q_{liq} observations at 7 h (Fig. S5); however, the rapidly increasing cloud top height and Q_{liq} with time are not also representative of the observations. As discussed in Sect. 5.4.1, large-scale subsidence may help to constrain these properties. The empirically-

derived ACC relationship compares well with both N_{ice} and Q_{liq} – when not considering the shattering event at cloud base (Fig. 4**c**) – where $0.54\,L^{-1}$ is predicted at the case 3 CTT. As expected, this is in very good agreement with the mean ice number concentration observed ($0.55\pm0.95\,L^{-1}$, Table 2). The N_{ice} values predicted in D10 and D10×0.1 produce a microphysical structure with enhanced precipitation, which may lead to cloud break up after time. Steady mixed-phase conditions were only simulated when implementing ACC and D10×0.5. Therefore, to simulate a consistent cloud layer over the ocean in case 3, $0.54\,^{-1} < N_{ice(CTT)} < 1.04\,L^{-1}$ is required.

From these three cases, it is clear that small differences in the predicted N_{ice} can produce significant microphysical impacts on the modelled clouds. The best prediction of N_{ice} for each case is different; however, they are of a similar order of magnitude and vary only a little between each case. Case 2 requires the least N_{ice} due to the comparatively warmer CTT (-12.7 °C), whereas cases 1 and 3 – with similar CTTs (approximately -20 °C) – require N_{ice} over a similar range (approximately $0.5\,L^{-1}$ to $1.3\,L^{-1}$) to produce a sustained, mixed-phase cloud layer with N_{ice} and Q_{liq} in approximate agreement with in situ observations. These limitations are based upon the parameterisations chosen in this study (C86, D10, ACC, D10×0.1, and D10×10); therefore, further work should be conducted to test other relationships and constrain the identified limitations in each case. These results are in accordance with Ovchinnikov et al. (2011), whose modelled springtime Arctic MPS glaciated when an ice number concentration of $2\,L^{-1}$ was imposed, whilst $0.5\,L^{-1}$ produced mixed-phase conditions with both consistent LWP and IWPs attained after ∼3.5 h. Given these are idealised simulations (with constant SW radiation and no INP depletion), the ability of the model to simulate realistic conditions should be inferred with caution: results from this study can simply conclude that small increases in the modelled ice crystal number concentration can cause persistent mixed-phase clouds to glaciate.

6 Conclusions

In this study, we have used large eddy simulations to investigate the microphysical sensitivity of Arctic mixed-phase clouds to primary ice number concentrations and surface conditions. The Large Eddy Model (LEM, UK Met Office, Gray et al., 2001) was used to simulate cloud structure and evolution over the sea ice, marginal ice zone (MIZ), and ocean. Aircraft observations of cloud microphysics from the Aerosol-Cloud Coupling and Climate Interactions in the Arctic (ACCACIA) campaign were used as a guide to indicate which simulations gave the most realistic microphysical representation. We used two primary ice nucleation parameterisations (Cooper, 1986; DeMott et al., 2010, abbreviated to C86 and D10 respectively), one derived from ACCACIA observations (ACC, Eq. 3), and an upper and lower sensitivity test (D10×10 and D10×0.1) to produce ice crystal number concentrations within the modelled clouds.

Three main sensitivities arise from the three considered cases.

- C86 cannot reproduce the sea ice cloud (case 1) under the conditions commonly used in the Weather Research and Forecasting (WRF) model with the Morrison et al. (2005) microphysics scheme (Fig. 5). However, these criteria do allow for a mixed-phase layer to form in cases 2 and 3, when the ocean provides strong sensible heat fluxes to the BL. This result demonstrates that deposition ice nucleation is not wholly representative of ice nucleation in the Arctic springtime

clouds observed during the ACCACIA campaign. Ice nucleation in water-saturated conditions must be implemented to create a mixed-phase cloud layer in our three considered cases (Fig. 6).

– Warm supercooled mixed-phase clouds over the MIZ can be modelled to reasonable accuracy by using the C86 and D10 parameterisations (Figs. 6, 7). At the cloud top temperature attained by case 2 (-12.7 °C), the difference between the C86 and D10 parameterisations is small (Fig. 1, Table 1). These parameterisations overpredict the ice number concentrations at the colder temperatures modelled in cases 1 and 3 (approximately -20 °C). ACC is modulated to have a weakened temperature-dependence; therefore, persistent, mixed-phase cloud layers are modelled in all three cases using this relationship.

– Results shown here illustrate that microphysical structure is particularly sensitive to the modelled ice crystal number concentration when simulating clouds over an ocean surface. With marginally too much ice (e.g. 2.43 L^{-1}, C86, Table 1), cloud glaciation occurs. Slightly less ice (2.07 L^{-1}, D10, Table 1) allows for persistent mixed-phase conditions for some time (approximately 24 h); however, convective cells form with heightened snow precipitation, which may promote cloud break up. Conversely, too much liquid and very few ice crystals (0.21 L^{-1}, D10×0.1, Table 1) may also promote cloud break up via precipitation as rain. Case 3 simulations show that there is a "sweet spot" for simulating ice in ocean-based single-layer Arctic MPS (attained by ACC and D10×0.5), where the number concentration of ice is low enough to sustain a reasonable Q_{liq} through vertical motions and high enough to suppress the liquid phase and restrict efficient collision-coalescence and rain formation. In this narrow limit, the influence of the WBF mechanism is depleted. The fact that this "sweet spot" can be attained by halving the D10 prediction of INP number concentration – yet it is overshot with D10×0.1 – illustrates just how sensitive the cloud structure is to the ice phase. Therefore, we suggest that the method of parameterising the ice number concentration in bulk microphysical models is very important, as small differences in the predicted ice concentration can have substantial effects on the microphysical structure and lifetime of Arctic MPS.

These idealised simulations assume an infinite source of INPs to the modelled clouds; here, INP are not depleted by activation or precipitation. An infinite source of INPs is likely unrepresentative of the Arctic environment (Pinto, 1998), as there are few in situ sources of INPs (e.g. mineral dusts, Murray et al., 2012). Although Young et al. (2016b) identified mineral dusts during all flights of the ACCACIA campaign, further work should include prognosing INPs in such simulations to investigate how their depletion could affect the microphysical structure of these clouds. Several studies have previously identified INP depletion as an important process to represent in modelling Arctic MPS (Harrington et al., 1999; Harrington and Olsson, 2001, amongst others). Additionally, the Morrison et al. (2005) microphysics scheme has been used for its detailed representation of microphysical interactions, such as ice aggregation and growth, but it can be utilised further to represent aerosol particle properties. Size distributions can be prescribed; therefore, the D10 parameterisation could be developed to give a spatially-dependent INP prediction based on aerosol particle observations, likely leading to a more comprehensive treatment of INP variability throughout the domain.

Acknowledgements. This work was funded as part of the ACCACIA campaign (grant NE/I028696/1) by the National Environment Research Council (NERC). G. Young was supported by a NERC PhD studentship. We would like to thank A. Hill and B. Shipway for advising on the microphysics scheme. Additionally, we would like to thank K. Bower, M. Gallagher, and J. Crosier for helpful discussions. Airborne data were obtained using the BAe-146-301 Atmospheric Research Aircraft [ARA] flown by Directflight Ltd and managed by the Facility for Airborne Atmospheric Measurements [FAAM], which is a joint entity of the Natural Environment Research Council [NERC] and the Met Office. Sea ice data were obtained from the National Snow and Ice Data Centre (NSIDC).

References

ACIA: Arctic Climate Impact Assessment, pp. 990–1020, Cambridge University Press, 2005.

Bigg, E. K.: The formation of atmospheric ice crystals by the freezing of droplets, Quarterly Journal of the Royal Meteorological Society, 79, 510–519, doi:10.1002/qj.49707934207, 1953.

Bigg, E. K. and Leck, C.: Cloud-active particles over the central Arctic Ocean, Journal of Geophysical Research, 106, 32 155, doi:10.1029/1999JD901152, 2001.

Boucher, O., Randall, D., Artaxo, P., Bretherton, C., Feingold, G., Forster, P., Kerminen, V. M., Kondo, Y., Liao, H., Lohmann, U., Rasch, P., Satheesh, S. K., Sherwood, S., Stevens, B., and Zhang, X. Y.: Clouds and Aerosols, in: Climate Change 2013: The Physical Science Basis. Contribution of Working Group I to the Fifth Assessment Report of the Intergovernmental Panel on Climate Change, edited by: Stocker, T. F., Qin, D., Plattner, G. K., Tignor, M., Allen, S. K., Boschung, J., Nauels, A., Xia, Y., Bex, V., and Midgley, P. M., Cambridge University Press, Cambridge, United Kingdom and New York, NY, USA, doi:10.1017/CBO9781107415324.016, 2013.

Cooper, W. A.: Ice Initiation in Natural Clouds, Meteorological Monographs, 21, 29–32, doi:10.1175/0065-9401-21.43.29, 1986.

Crosier, J., Bower, K. N., Choularton, T. W., Westbrook, C. D., Connolly, P. J., Cui, Z. Q., Crawford, I. P., Capes, G. L., Coe, H., Dorsey, J. R., Williams, P. I., Illingworth, A. J., Gallagher, M. W., and Blyth, A. M.: Observations of ice multiplication in a weakly convective cell embedded in supercooled mid-level stratus, Atmospheric Chemistry & Physics, 11, 257–273, doi:10.5194/acp-11-257-2011, 2011.

Crosier, J., Choularton, T. W., Westbrook, C. D., Blyth, A. M., Bower, K. N., Connolly, P. J., Dearden, C., Gallagher, M. W., Cui, Z., and Nicol, J. C.: Microphysical properties of cold frontal rainbands, Quarterly Journal of the Royal Meteorological Society, 140, 1257–1268, doi:10.1002/qj.2206, 2014.

Curry, J. A., Rossow, W. B., Randall, D., and Schramm, J. L.: Overview of Arctic Cloud and Radiation Characteristics., Journal of Climate, 9, 1731–1764, doi:10.1175/1520-0442(1996)009<1731:OOACAR>2.0.CO;2, 1996.

de Boer, G., Hashino, T., and Tripoli, G. J.: Ice nucleation through immersion freezing in mixed-phase stratiform clouds: Theory and numerical simulations, Atmospheric Research, 96, 315–324, doi:10.1016/j.atmosres.2009.09.012, 2010.

de Boer, G., Morrison, H., Shupe, M. D., and Hildner, R.: Evidence of liquid dependent ice nucleation in high-latitude stratiform clouds from surface remote sensors, Geophysics Research Letters, 38, L01803, doi:10.1029/2010GL046016, 2011.

de Boer, G., Shupe, M. D., Caldwell, P. M., Bauer, S. E., Persson, O., Boyle, J. S., Kelley, M., Klein, S. A., and Tjernström, M.: Near-surface meteorology during the Arctic Summer Cloud Ocean Study (ASCOS): evaluation of reanalyses and global climate models, Atmospheric Chemistry & Physics, 14, 427–445, doi:10.5194/acp-14-427-2014, 2014.

DeMott, P. J., Prenni, A. J., Liu, X., Kreidenweis, S. M., Petters, M. D., Twohy, C. H., Richardson, M. S., Eidhammer, T., and Rogers, D. C.: Predicting global atmospheric ice nuclei distributions and their impacts on climate, Proceedings of the National Academy of Sciences, doi:10.1073/pnas.0910818107, 2010.

Edwards, J. M. and Slingo, A.: Studies with a flexible new radiation code. I: Choosing a configuration for a large-scale model, Quarterly Journal of the Royal Meteorological Society, 122, 689–719, doi:10.1002/qj.49712253107, 1996.

Gray, M. E. B., Petch, J. C., Derbyshire, S. H., Brown, A. R., Lock, A. P., Swann, H. A., and Brown, P. R. A.: Version 2.3 of the Met Office Large Eddy Model: Part II. Scientific Documentation., Tech. rep., 2001.

Hallett, J. and Mossop, S. C.: Production of Secondary Ice Particles during the Riming Process, Nature, 249, 26–28, doi:10.1038/249026a0, 1974.

Harrington, J. Y. and Olsson, P. Q.: On the potential influence of ice nuclei on surface-forced marine stratocumulus cloud dynamics, Journal of Geophysical Research: Atmospheres, 106, 27 473–27 484, doi:10.1029/2000JD000236, 2001.

Harrington, J. Y., Reisin, T., Cotton, W. R., and Kreidenweis, S. M.: Cloud resolving simulations of Arctic stratus. Part II: Transition-season clouds, Atmospheric Research, 51, 45–75, doi:10.1016/S0169-8095(98)00098-2, 1999.

Hartmann, J., Kottmeier, C., and Raasch, S.: Roll Vortices and Boundary-Layer Development during a Cold Air Outbreak, Boundary-Layer Meteorology, 84, 45–65, doi:10.1023/A:1000392931768, 1997.

Hobbs, P. V. and Rangno, A. L.: Microstructures of low and middle-level clouds over the Beaufort Sea, Quarterly Journal of the Royal Meteorological Society, 124, 2035–2071, doi:10.1002/qj.49712455012, 1998.

Jackson, R. C., McFarquhar, G. M., Korolev, A. V., Earle, M. E., Liu, P. S. K., Lawson, R. P., Brooks, S., Wolde, M., Laskin, A., and Freer, M.: The dependence of ice microphysics on aerosol concentration in arctic mixed-phase stratus clouds during ISDAC and M-PACE, Journal of Geophysical Research (Atmospheres), 117, D15207, doi:10.1029/2012JD017668, 2012.

Klein, S. A., McCoy, R. B., Morrison, H., Ackerman, A. S., Avramov, A., Boer, G. d., Chen, M., Cole, J. N. S., Del Genio, A. D., Falk, M., Foster, M. J., Fridlind, A., Golaz, J.-C., Hashino, T., Harrington, J. Y., Hoose, C., Khairoutdinov, M. F., Larson, V. E., Liu, X., Luo, Y., McFarquhar, G. M., Menon, S., Neggers, R. A. J., Park, S., Poellot, M. R., Schmidt, J. M., Sednev, I., Shipway, B. J., Shupe, M. D., Spangenberg, D. A., Sud, Y. C., Turner, D. D., Veron, D. E., Salzen, K. v., Walker, G. K., Wang, Z., Wolf, A. B., Xie, S., Xu, K.-M., Yang, F., and Zhang, G.: Intercomparison of model simulations of mixed-phase clouds observed during the ARM Mixed-Phase Arctic Cloud Experiment. I: single-layer cloud, Quarterly Journal of the Royal Meteorological Society, 135, 979–1002, doi:10.1002/qj.416, 2009.

Korolev, A. and Isaac, G.: Phase transformation of mixed-phase clouds, Quarterly Journal of the Royal Meteorological Society, 129, 19–38, doi:10.1256/qj.01.203, 2003.

Lance, S., Brock, C. A., Rogers, D., and Gordon, J. A.: Water droplet calibration of the Cloud Droplet Probe (CDP) and in-flight performance in liquid, ice and mixed-phase clouds during ARCPAC, Atmospheric Measurement Techniques, 3, 1683–1706, doi:10.5194/amt-3-1683-2010, 2010.

Lawson, R. P., O'Connor, D., Zmarzly, P., Weaver, K., Baker, B., Mo, Q., and Jonsson, H.: The 2D-S (Stereo) Probe: Design and Preliminary Tests of a New Airborne, High-Speed, High-Resolution Particle Imaging Probe, Journal of Atmospheric and Oceanic Technology, 23, 1462, doi:10.1175/JTECH1927.1, 2006.

Lloyd, G., Choularton, T. W., Bower, K. N., Crosier, J., Jones, H., Dorsey, J. R., Gallagher, M. W., Connolly, P., Kirchgaessner, A. C. R., and Lachlan-Cope, T.: Observations and comparisons of cloud microphysical properties in spring and summertime Arctic stratocumulus during the ACCACIA campaign, Atmospheric Chemistry & Physics, 15, 3719–3737, doi:10.5194/acp-15-3719-2015, 2015.

Mason, B. J.: Growth Habits and Growth Rates of Snow Crystals, Proceedings of the Royal Society of London Series A, 441, 3–16, doi:10.1098/rspa.1993.0045, 1993.

McFarquhar, G. M., Ghan, S., Verlinde, J., Korolev, A., Strapp, J. W., Schmid, B., Tomlinson, J. M., Wolde, M., Brooks, S. D., Cziczo, D., Dubey, M. K., Fan, J., Flynn, C., Gultepe, I., Hubbe, J., Gilles, M. K., Laskin, A., Lawson, P., Leaitch, W. R., Liu, P., Liu, X., Lubin, D., Mazzoleni, C., MacDonald, A.-M., Moffet, R. C., Morrison, H., Ovchinnikov, M., Shupe, M. D., Turner, D. D., Xie, S., Zelenyuk, A., Bae, K., Freer, M., and Glen, A.: Indirect and Semi-direct Aerosol Campaign: The Impact of Arctic Aerosols on Clouds., Bull. Am. Meteorol. Soc., 92, 183–201, doi:10.1175/2010BAMS2935.1, 2011.

Meyers, M. P., Demott, P. J., and Cotton, W. R.: New Primary Ice-Nucleation Parameterizations in an Explicit Cloud Model., Journal of Applied Meteorology, 31, 708–721, doi:10.1175/1520-0450(1992)031<0708:NPINPI>2.0.CO;2, 1992.

Möhler, O., Benz, S., Saathoff, H., Schnaiter, M., Wagner, R., Schneider, J., Walter, S., Ebert, V., and Wagner, S.: The effect of organic coating on the heterogeneous ice nucleation efficiency of mineral dust aerosols, Environmental Research Letters, 3, 025007, doi:10.1088/1748-9326/3/2/025007, 2008.

Morrison, H., Curry, J. A., and Khvorostyanov, V. I.: A New Double-Moment Microphysics Parameterization for Application in Cloud and Climate Models. Part I: Description., Journal of Atmospheric Sciences, 62, 1665–1677, doi:10.1175/JAS3446.1, 2005.

Morrison, H., Pinto, J. O., Curry, J. A., and McFarquhar, G. M.: Sensitivity of modeled arctic mixed-phase stratocumulus to cloud condensation and ice nuclei over regionally varying surface conditions, Journal of Geophysical Research (Atmospheres), 113, D05203, doi:10.1029/2007JD008729, 2008.

Morrison, H., McCoy, R. B., Klein, S. A., Xie, S., Luo, Y., Avramov, A., Chen, M., Cole, J. N. S., Falk, M., Foster, M. J., Del Genio, A. D., Harrington, J. Y., Hoose, C., Khairoutdinov, M. F., Larson, V. E., Liu, X., McFarquhar, G. M., Poellot, M. R., von Salzen, K., Shipway, B. J., Shupe, M. D., Sud, Y. C., Turner, D. D., Veron, D. E., Walker, G. K., Wang, Z., Wolf, A. B., Xu, K.-M., Yang, F., and Zhang, G.: Intercomparison of model simulations of mixed-phase clouds observed during the ARM Mixed-Phase Arctic Cloud Experiment. II: Multilayer cloud, Quarterly Journal of the Royal Meteorological Society, 135, 1003–1019, doi:10.1002/qj.415, 2009.

Morrison, H., Zuidema, P., Ackerman, A. S., Avramov, A., de Boer, G., Fan, J., Fridlind, A. M., Hashino, T., Harrington, J. Y., Luo, Y., Ovchinnikov, M., and Shipway, B.: Intercomparison of cloud model simulations of Arctic mixed-phase boundary layer clouds observed during SHEBA/FIRE-ACE, Journal of Advances in Modeling Earth Systems, 3, M06003, doi:10.1029/2011MS000066, 2011.

Morrison, H., de Boer, G., Feingold, G., Harrington, J., Shupe, M. D., and Sulia, K.: Resilience of persistent Arctic mixed-phase clouds, Nature Geoscience, 5, 11–17, doi:10.1038/ngeo1332, 2012.

Murray, B. J., O'Sullivan, D., Atkinson, J. D., and Webb, M. E.: Ice nucleation by particles immersed in supercooled cloud droplets., Chem Soc Rev., 41, 6519–54, doi:10.1039/c2cs35200a, 2012.

Ovchinnikov, M., Korolev, A., and Fan, J.: Effects of ice number concentration on dynamics of a shallow mixed-phase stratiform cloud, Journal of Geophysical Research: Atmospheres, 116, doi:10.1029/2011JD015888, d00T06, 2011.

Pinto, J. O.: Autumnal Mixed-Phase Cloudy Boundary Layers in the Arctic., Journal of Atmospheric Sciences, 55, 2016–2038, doi:10.1175/1520-0469(1998)055<2016:AMPCBL>2.0.CO;2, 1998.

Prenni, A. J., Harrington, J. Y., Tjernström, M., Demott, P. J., Avramov, A., Long, C. N., Kreidenweis, S. M., Olsson, P. Q., and Verlinde, J.: Can Ice-Nucleating Aerosols Affect Arctic Seasonal Climate?, Bulletin of the American Meteorological Society, 88, 541, doi:10.1175/BAMS-88-4-541, 2007.

Primm, K. M., Schill, G. P., Veghte, D. P., Freedman, M. A., and Tolbert, M. A.: Depositional ice nucleation on NX illite and mixtures of NX illite with organic acids, Journal of Atmospheric Chemistry, pp. 1–15, doi:10.1007/s10874-016-9340-x, 2016.

Pruppacher, H. R. and Klett, J. D.: Microphysics of Clouds and Precipitation, Kluwer Academic Publishers, 1997.

Rangno, A. L. and Hobbs, P. V.: Ice particles in stratiform clouds in the Arctic and possible mechanisms for the production of high ice concentrations, Journal of Geophysical Research: Atmospheres, 106, 15 065–15 075, doi:10.1029/2000JD900286, 2001.

Rosenberg, P. D., Dean, A. R., Williams, P. I., Dorsey, J. R., Minikin, A., Pickering, M. A., and Petzold, A.: Particle sizing calibration with refractive index correction for light scattering optical particle counters and impacts upon PCASP and CDP data collected during the Fennec campaign, Atmospheric Measurement Techniques, 5, 1147–1163, doi:10.5194/amt-5-1147-2012, 2012.

Serreze, M. C. and Barry, R. G.: Processes and impacts of Arctic amplification: A research synthesis, Global and Planetary Change, 77, 85 – 96, doi:dx.doi.org/10.1016/j.gloplacha.2011.03.004, 2011.

Shupe, M. D., Matrosov, S. Y., and Uttal, T.: Arctic Mixed-Phase Cloud Properties Derived from Surface-Based Sensors at SHEBA., Journal of Atmospheric Sciences, 63, 697–711, doi:10.1175/JAS3659.1, 2006.

Shupe, M. D., Daniel, J. S., de Boer, G., Eloranta, E. W., Kollias, P., Long, C. N., Luke, E. P., Turner, D. D., and Verlinde, J.: A Focus On Mixed-Phase Clouds, Bulletin of the American Meteorological Society, 89, 1549, doi:10.1175/2008BAMS2378.1, 2008a.

Shupe, M. D., Kollias, P., Persson, P. O. G., and McFarquhar, G. M.: Vertical Motions in Arctic Mixed-Phase Stratiform Clouds, Journal of Atmospheric Sciences, 65, 1304, doi:10.1175/2007JAS2479.1, 2008b.

Shupe, M. D., Walden, V. P., Eloranta, E., Uttal, T., Campbell, J. R., Starkweather, S. M., and Shiobara, M.: Clouds at Arctic Atmospheric Observatories. Part I: Occurrence and Macrophysical Properties, Journal of Applied Meteorology and Climatology, 50, 626–644, doi:10.1175/2010JAMC2467.1, 2011.

Solomon, A., Feingold, G., and Shupe, M. D.: The role of ice nuclei recycling in the maintenance of cloud ice in Arctic mixed-phase stratocumulus, Atmospheric Chemistry and Physics, 15, 10 631–10 643, doi:10.5194/acp-15-10631-2015, 2015.

Sotiropoulou, G., Sedlar, J., Tjernström, M., Shupe, M. D., Brooks, I. M., and Persson, P. O. G.: The thermodynamic structure of summer Arctic stratocumulus and the dynamic coupling to the surface, Atmospheric Chemistry and Physics, 14, 12 573–12 592, doi:10.5194/acp-14-12573-2014, 2014.

Stocker, T., Qin, D., Plattner, G.-K., Alexander, L., Allen, S., Bindoff, N., Bréon, F.-M., Church, J., Cubasch, U., Emori, S., Forster, P., Friedlingstein, P., Gillett, N., Gregory, J., Hartmann, D., Jansen, E., Kirtman, B., Knutti, R., Krishna Kumar, K., Lemke, P., Marotzke, J., Masson-Delmotte, V., Meehl, G., Mokhov, I., Piao, S., Ramaswamy, V., Randall, D., Rhein, M., Rojas, M., Sabine, C., Shindell, D., Talley, L., Vaughan, D., and Xie, S.-P.: Technical Summary, in: Climate Change 2013: The Physical Science Basis. Contribution of Working Group I to the Fifth Assessment Report of the Intergovernmental Panel on Climate Change, edited by: Stocker, T.F., D. Qin, G.-K. Plattner, M. Tignor, S.K. Allen, J. Boschung, A. Nauels, Y. Xia, V. Bex and P.M. Midgley, Cambridge University Press, Cambridge, United Kingdom and New York, NY, USA, doi:10.1017/CBO9781107415324.005, 2013.

Taylor, J. W., Choularton, T. W., Blyth, A. M., Liu, Z., Bower, K. N., Crosier, J., Gallagher, M. W., Williams, P. I., Dorsey, J. R., Flynn, M. J., Bennett, L. J., Huang, Y., French, J., Korolev, A., and Brown, P. R. A.: Observations of cloud microphysics and ice formation during COPE, Atmospheric Chemistry and Physics, 16, 799–826, doi:10.5194/acp-16-799-2016, 2016.

Tjernström, M., Sedlar, J., and Shupe, M. D.: How Well Do Regional Climate Models Reproduce Radiation and Clouds in the Arctic? An Evaluation of ARCMIP Simulations, Journal of Applied Meteorology and Climatology, 47, 2405, doi:10.1175/2008JAMC1845.1, 2008.

Verlinde, J., Harrington, J. Y., McFarquhar, G. M., Yannuzzi, V. T., Avramov, A., Greenberg, S., Johnson, N., Zhang, G., Poellot, M. R., Mather, J. H., Turner, D. D., Eloranta, E. W., Zak, B. D., Prenni, A. J., Daniel, J. S., Kok, G. L., Tobin, D. C., Holz, R., Sassen, K., Spangenberg, D., Minnis, P., Tooman, T. P., Ivey, M. D., Richardson, S. J., Bahrmann, C. P., Shupe, M., Demott, P. J., Heymsfield, A. J., and Schofield, R.: The Mixed-Phase Arctic Cloud Experiment, Bulletin of the American Meteorological Society, 88, 205, doi:10.1175/BAMS-88-2-205, 2007.

Vihma, T., Pirazzini, R., Fer, I., Renfrew, I. A., Sedlar, J., Tjernström, M., Lüpkes, C., Nygård, T., Notz, D., Weiss, J., Marsan, D., Cheng, B., Birnbaum, G., Gerland, S., Chechin, D., and Gascard, J. C.: Advances in understanding and parameterization of small-scale physical processes in the marine Arctic climate system: a review, Atmospheric Chemistry & Physics, 14, 9403–9450, doi:10.5194/acp-14-9403-2014, 2014.

Young, G., Jones, H. M., Choularton, T. W., Crosier, J., Bower, K. N., Gallagher, M. W., Davies, R. S., Renfrew, I. A., Elvidge, A. D., Darbyshire, E., Marenco, F., Brown, P. R. A., Ricketts, H. M. A., Connolly, P. J., Lloyd, G., Williams, P. I., Allan, J. D., Taylor, J. W.,

Liu, D., and Flynn, M. J.: Observed microphysical changes in Arctic mixed-phase clouds when transitioning from sea ice to open ocean, Atmospheric Chemistry and Physics, 16, 13 945–13 967, doi:10.5194/acp-16-13945-2016, 2016a.

Young, G., Jones, H. M., Darbyshire, E., Baustian, K. J., McQuaid, J. B., Bower, K. N., Connolly, P. J., Gallagher, M. W., and Choularton, T. W.: Size-segregated compositional analysis of aerosol particles collected in the European Arctic during the ACCACIA campaign, Atmospheric Chemistry and Physics, 16, 4063–4079, doi:10.5194/acp-16-4063-2016, 2016b.

Young, K. C.: The Role of Contact Nucleation in Ice Phase Initiation in Clouds, Journal of the Atmospheric Sciences, 31, 768–776, doi:10.1175/1520-0469(1974)031<0768:TROCNI>2.0.CO;2, 1974.

7 Summary and conclusions

Aircraft observations of cloud, aerosol, and boundary layer properties from the ACCACIA campaign have been synthesised and presented to provide insight into the microphysics of springtime mixed-phase clouds. In Chapter 4, aerosol particles were analysed using scanning electron microscopy to identify their composition and infer ice nucleating potential. In Chapter 5, in situ measurements were scrutinised to investigate how cloud microphysical structure varies over the transition from sea ice to ocean. In Chapter 6, large eddy simulations were used to test the sensitivity of cloud structure, evolution, and persistence to the number of ice crystals within the modelled mixed-phase clouds. The following sections summarise the conclusions from these three studies.

7.1 Particle composition in the European Arctic

Chapter 4 describes the scanning electron microscopy (SEM) analysis of aircraft filters exposed during the springtime ACCACIA campaign. Size-segregated compositional data were derived from seven filter samples to identify which aerosol particle species were present in the Arctic boundary layer and infer their possible influence in aerosol-cloud interactions.

- Derived filter data compared reasonably well with aerosol particle size distributions measured by three aircraft instruments: the Cloud Droplet Probe (CDP), the Cloud Aerosol Spectrometer with Depolarisation (CAS-DPOL), and the Passive-Cavity Aerosol Spectrometer Probe (PCASP). Discrepancies between these data were identified at small (approximately $\leq 0.5\,\mu m$) and large (approximately $\geq 10\,\mu m$) sizes: uncertainties at small particle sizes were attributed to limitations of the SEM technique, whilst large size disagreement

was caused by particle collection efficiency issues. Improved agreement between filter- and probe-derived size distributions was identified in lower relative humidity (RH) sampling conditions, as less water was associated with the particles.

- Compositional variability was identified between the six below cloud filter samples. Dominant particle species varied from sulphates, to silicate dusts, to sea salts in the first five cases. Unique compositional trends were identified in case 6. These properties could be related to its distinct air mass history. Source regions varied from the Arctic sea ice, through to Greenland and Siberia in the first five cases, whilst case 6 was subject to a polluted air mass from the European continent. Dominant particle classes were unclassified mixed particles, Ca-rich dusts, and biomass tracers. These Ca- and K-rich particles were likely produced from biomass burning activities over the European continent, much like the boreal forest fires studied by Quennehen et al. (2012). These results suggest that particle composition can be related to air mass history in these cases.

- Carbon- and sulphur-based particles were predominantly observed in the sub-micron size range, whilst silicate dusts and sea salts dominated super-micron sizes. Large, coarse-mode particles are thought to typically act as ice nucleating particles (INPs). The super-micron mineral dusts identified in each case would likely act as INPs in this environment; however, sea salt is an inefficient INP and therefore would not efficiently nucleate ice in these conditions, unless it was internally-mixed with an insoluble particle.

- Mineral dust was identified in all cases and no distinct compositional differences could be identified, suggesting a consistent source. Si / Al and Mg / Si ratios of all cases compared well; however, case 6 was subject to high Ca and K influences from biomass burning activities. Consequently, the Ca / Al and K / Al ratios were amplified in case 6 with comparison to the first five cases. This compositional consistency suggests that these dust particles had likely undergone long-range high-altitude transport from lower latitudes.

- The long-range transport hypothesis was strengthened by comparing below

and above cloud samples. Heightened fractions of mixed mineral dusts and unclassified aerosol particles were identified above cloud. In particular, a greater fraction of large particles (>0.5 µm) were unclassified, and it is difficult to predict how these particles would participate in aerosol-cloud interactions.

Enhanced mixing makes the interpretation of aerosol-cloud interactions difficult. The ability of mixed particles to act as cloud condensation nuclei (CCN) or INPs is unknown, as their activation to form either cloud droplets or ice crystals respectively depends on the environmental conditions. Mixed particles also have an increased probability to nucleate ice particles via the immersion-freezing nucleation mode in water-saturated conditions.

7.2 Cloud microphysical changes with sea ice cover

Chapter 5 details how the microphysics of Arctic mixed-phase clouds responds to a changing surface by using in situ aircraft observations. High resolution measurements of cloud, aerosol, and thermodynamic properties from one case study were scrutinised to investigate the changing cloud microphysical structure over the transition from sea ice to ocean.

Key findings from this study are detailed as follows:

- Cloud microphysics over the sea ice during springtime is characterised by moderately high number concentrations (N_{drop}, $110 \pm 36\,cm^{-3}$) of small cloud droplets (effective radius, R_{eff}, 4–5 µm). Our observations agree well with previous measurements made close to Barrow, Alaska during the Indirect and Semi-Direct Aerosol Campaign (ISDAC, McFarquhar et al. 2011). Here, a cloud liquid water content (LWC) of approximately $0.1\,g\,m^{-3}$ was identified over the sea ice, whilst measurements during ISDAC averaged to $0.1 \pm 0.13\,g\,m^{-3}$ (Jackson et al. 2012). Additionally, the low liquid water content observed here agrees well with observations of high altitude clouds during the autumnal Mixed-Phase Arctic Cloud Experiment (M-PACE, Verlinde et al. 2007). Therefore, sea ice clouds likely behave similarly to high altitude clouds which are unaffected by surface fluxes, as the sea ice pack acts as a barrier between the ocean and the boundary layer.

- Over the transition from sea ice to ocean, the liquid properties of the mixed-phase cloud changed significantly. Near-surface temperatures increased, producing a more dynamic boundary layer. The induced turbulence from increased sensible and latent heat fluxes caused N_{drop} and mean R_{eff} to increase over the marginal ice zone (MIZ). N_{drop} increased from $110 \pm 36\,cm^{-3}$ over the sea ice to $145 \pm 54\,cm^{-3}$ over the MIZ, and the mean R_{eff} increased from approximately 5 µm to 8 µm. With increased number concentrations of small droplets, the MIZ-based cloud would have a greater albedo and optical thickness; therefore, it would be more efficient at reflecting incident shortwave (SW) solar radiation than the cloud over the sea ice. As the sea ice itself is also an efficient reflector of solar radiation, it is likely that the cloud in this location would have little influence on the amount of SW radiation reflected. Therefore, the sea ice cloud would likely contribute towards net radiative interactions by trapping any upwelling longwave radiation; however, this cannot be confirmed with these data.

- With a consistent source of heat and moisture from the warm ocean, the boundary layer warmed and became unstable. Both cloud base height and depth increased over the ocean, allowing for efficient collision-coalescence to occur within the deep cloud layer. N_{drop} decreased ($63 \pm 30\,cm^{-3}$), whilst the mean R_{eff} increased (up to 10 µm). The LWC increased to almost four times that measured over the sea ice. These properties are in agreement with observations of ocean-based single-layer Arctic stratocumulus during the autumn (during M-PACE, Jackson et al. 2012), where a mean LWC of $0.19 \pm 0.12\,g\,m^{-3}$ and a mean N_{drop} of $46 \pm 30\,cm^{-3}$ were found. Jackson et al. (2012) also concluded that this increased liquid water content and lower N_{drop} – with comparison to the ISDAC observations over broken sea ice – could be attributed to the heat and moisture fluxes from the ocean surface.

- Surprisingly, the ice crystal number concentration varied only a little over the changing surface. This may be due to the reasonable consistency in the large particle number concentrations over the transition. Consistently low ice number concentrations suggest that primary ice nucleation solely was active.

Good agreement in the ice phase was identified between the ACCACIA and ISDAC observations (approximately $0.5\,L^{-1}$). Even in the ocean-based cloud, ice crystal number concentrations were in better agreement with ISDAC observations than M-PACE observations over the open ocean. This suggests that the sampled springtime clouds were either insensitive to geographical sources of INPs, or that a similar source was influencing both cases, thousands of miles apart.

The surface conditions greatly affected cloud microphysics, influencing a clear development of the cloud liquid phase through a changing boundary layer structure. This may suggest that, as the Arctic sea ice retreats further, thicker ocean-based clouds may become more common in the high latitudes. These clouds would have a greater cloud top albedo than the ocean surface below; therefore, they would reflect incident solar radiation efficiently and promote atmospheric cooling. However, these thick clouds would also trap upwelling longwave radiation efficiently. With longwave radiation dominating radiative interactions in the Arctic spring, it is likely that a positive feedback loop between the melting sea ice surface, thicker liquid-dominated clouds, and a net warming effect at the surface would be enforced.

7.3 Sensitivity of modelled Arctic clouds

Chapter 6 investigates how modelled microphysical structure reacts to the number of primary ice crystals simulated within Arctic mixed-phase clouds. Using large eddy simulations, three case studies were modelled with reference to observations made over the sea ice, MIZ, and ocean during the springtime ACCACIA campaign. Two primary ice nucleation parameterisations (Cooper 1986; DeMott et al. 2010), and a relationship derived from ACCACIA observations, were imposed to study the sensitivity of cloud structure, evolution, and lifetime to both the number of ice crystals simulated within the cloud and the fluxes from the surface.

Key findings from this study are detailed as follows:

- Ice onset conditions commonly used in the Weather Research and Forecasting (WRF) model (T $<$ -8°C and $S_w > 0.999$, or $S_i > 1.08$, using the Cooper 1986

parameterisation), were unable to produce microphysics comparable to the observations over all surfaces considered. Over the sea ice, ice formed under deposition conditions, leading to overpredicted ice crystal number concentrations, N_{ice}, and no liquid water. Improved agreement with observations was attained when the deposition condition ($S_i > 1.08$) was removed and ice nucleation was forced to occur at water-saturation only. This limitation allowed mixed-phase clouds to form – with comparable microphysics to observations – over the sea ice, MIZ, and ocean, and persist for at least 8 h.

- Ice number concentrations predicted by the Cooper 1986 (hereafter, C86) parameterisation were typically too high in all cases; agreement was particularly poor in the sea ice and ocean cases, whilst C86 performed better in the warmer MIZ case. Modelled N_{ice} peaked at $2.32\,L^{-1}$, $1.09\,L^{-1}$, and $3.83\,L^{-1}$ over the sea ice, MIZ, and ocean, whilst averaged number concentrations from observations were $0.47 \pm 0.86\,L^{-1}$, $0.35 \pm 0.20\,L^{-1}$, and $0.55 \pm 0.95\,L^{-1}$ respectively.

- Predictions of INP number concentrations using the DeMott et al. 2010 (hereafter, D10) parameterisation – also applied under water-saturated conditions – were implemented under the assumption that all INPs nucleate to form ice crystals. N_{ice} decreased with comparison to the C86 simulations over the sea ice and ocean, peaking at $1.29\,L^{-1}$ and $3.01\,L^{-1}$ respectively. D10 and C86 perform similarly in the MIZ case, capturing the lower ice number concentrations observed. Given these results, both of these parameterisations (C86 and D10) are recommended for use in modelling the microphysics of warm supercooled MPS when appreciable surface fluxes, representative of the ocean, are applied.

- A fit to observed 2DS ice number concentrations during the springtime ACCACIA campaign (ACC) was also implemented in the model. This relationship produced a comparable microphysical structure in each case, with a peak N_{ice} of $0.47\,L^{-1}$, $0.36\,L^{-1}$, and $0.71\,L^{-1}$ modelled over the sea ice, MIZ, and ocean respectively. Additionally, good agreement with observed liquid water mixing ratios ($0.05 \pm 0.04\,g\,kg^{-1}$, $0.09 \pm 0.07\,g\,kg^{-1}$, and $0.24 \pm 0.13\,g\,kg^{-1}$) was found. However, N_{ice} was underpredicted and Q_{liq} was overpredicted in case 2, and the C86 and D10 simulations agree better with observations in this

case. It was appropriate to use the ACC relationship when modelling these springtime ACCACIA cases; however, the applicability of this parameterisation outwith these data could not be established.

- Modelled cloud microphysics was found to be highly sensitive to ice crystal number concentrations. In each case, D10×0.1 produced too few ice crystals, whereas D10×10 produced far too many. D10×10 caused cloud glaciation in cases 1 and 3, and produced an N_{ice} 10× greater than observations in case 2. To maximise cloud lifetime, $0.51\,L^{-1} < N_{ice(CTT)} < 1.31\,L^{-1}$, $0.23\,L^{-1} < N_{ice(CTT)} < 0.34\,L^{-1}$, and $0.54^{-1} < N_{ice(CTT)} < 1.04\,L^{-1}$ were required for the sea ice, MIZ, and ocean cases respectively.

- Over the ocean, peculiar trends formed in the liquid and ice water paths (LWP / IWP) when imposing the D10 parameterisation: circular, convective structures formed which pushed cloud top higher and reinvigorated the liquid water mixing ratio. Precipitation as snow was modelled, which depleted the liquid within the cloud. Similar trends formed when implementing D10×0.1; however, these were seen most clearly in the LWP field and were elongated in shape, instead of circular. In contrast to the D10 simulations, these convective bands corresponded with heightened rain precipitation, which acted to steadily deplete the cloud liquid water throughout the simulation.

Modelled cloud microphysics was highly sensitive to ice crystal number concentrations. Improved agreement with observations was found when restricting known primary ice parameterisations to water-saturated conditions; however, small increases in predicted ice number caused persistent mixed-phase conditions to glaciate. This was particularly clear in case 3, which was continually forced by a warm ocean surface. Results from this case may infer how cloud break up occurs in cold air outbreak scenarios as, dependent on the number concentration of ice crystals modelled, convective cells formed. Increased snow or rain precipitation was associated with these cells; precipitation which depleted the liquid content of the modelled cloud.

7.4 Aerosol-cloud interactions in the Arctic

The springtime Arctic aerosol population was found to be variable between subsequent days. Mixed particles were prevalent in every sample – from mixed silicates and chlorides to unclassifiable particles – making aerosol-cloud interactions difficult to interpret. Chapter 6 demonstrated that water-saturation was required to model persistent, mixed-phase clouds over the sea ice, MIZ, and ocean, and this threshold encapsulates all four ice nucleating mechanisms (deposition, condensation, immersion, and contact). Mixed aerosol particles likely have some soluble and insoluble fractions, allowing them to act as either CCN or INPs depending on the environmental conditions. Such aerosol particles could activate into a cloud droplet upon water-saturation, then subsequently freeze if air temperatures decrease sufficiently to activate the insoluble fraction of the particle. Conversely, if these mixed particles were highly insoluble, they may act as efficient contact-freezing INPs. Given the particle composition data detailed in Chapter 4 and modelling results shown in Chapter 6, implementing a water-saturation threshold on modelled primary ice nucleation parameterisations would be recommended to greatly improve agreement with the observed microphysics of springtime Arctic mixed-phase clouds.

Long-range transport was hypothesised to be responsible for the compositional consistency of the silicate dusts measured during every case. In Chapter 5, high number concentrations of small aerosol particles were identified at high altitudes over the sea ice, suggesting the presence of a pollution layer aloft. Liu et al. (2015) found that high altitude plumes of black carbon (BC) were influencing the European Arctic during the springtime ACCACIA campaign, having travelled from Asia. These findings are in agreement with previous studies who suggest that the Arctic haze is a result of long-range transported pollution from the mid-latitudes.

Microphysical observations during the springtime ACCACIA campaign show that the clouds contained low ice crystal number concentrations (approximately $0.5\,\mathrm{L}^{-1}$) which could be attributed to primary ice nucleation alone. Secondary ice production was not observed to any great extent in these clouds due to their cold temperatures. This allowed the relationship between aerosol particles and cloud

microphysics to be investigated by applying parameterisations. Given the compositional data obtained in Chapter 4, mineral dust number concentrations from flight B762 (case 3, Chapter 4) were tested with the Niemand et al. 2012 (hereafter, N12) and DeMott et al. 2015 (hereafter, D15) parameterisations, whilst aerosol particle number concentrations greater than 0.5 µm in size ($n_{aer,0.5}$) were used to evaluate the D10 and Tobo et al. 2013 (hereafter, T13) parameterisations. Ice number concentrations obtained using the N12 parameterisation were in good agreement with the in situ observations. Poorer agreement was found using D15; however, this was attributed to its use at the upper limit of its applicable temperature range (-20 °C). D10 marginally overestimates INP number concentrations, likely due to the large fraction of super-micron sea salt aerosol particles found during this case. Sea salt is an inefficient INP, yet it constitutes a sizeable fraction of the $n_{aer,0.5}$ input to the parameterisation. The good result of N12, and minor overprediction of D10, suggests that the dust loadings may be responsible for the observed ice number concentrations. Dusts were identified in all cases; therefore, it would be useful to test the ability of these parameterisations to predict N_{ice} in the other ACCACIA cases, under different meteorological conditions.

Predictions using the T13 parameterisation were highly variable. This is unsurprising as small changes in the number concentration of efficient biological INPs would likely have significant impacts on the ice number concentrations, and Twohy et al. (2016) showed that the number concentrations of such particles can be highly variable in the atmosphere with both time of day and season. Over a similar geographical location, Pratt et al. (2009) showed that biological particles nucleate cloud ice crystals by analysing ice crystal residuals. Biological particle concentrations are likely underestimated by numerical models, potentially due to missing sources and/or poorly represented transport pathways (Twohy et al. 2016). Biological particles are an important source of INPs which need to be better quantified and, in relation to the studies detailed here, it is unclear how these INPs would affect cloud microphysics in the Arctic as the SEM technique employed in Chapter 4 cannot adequately measure this particle species.

Aerosol-cloud interactions have been a focus of this thesis; however, Chapter 5

highlighted the importance of boundary layer structure and dynamics in understanding cloud microphysical evolution. The liquid phase of the observed cloud changed significantly over the transition from sea ice to ocean; most noticeably, the liquid water content increased almost four-fold and the mean cloud droplet effective radius doubled. The primary driver of these changes was the warming boundary layer, which was being positively forced by consistent heat and moisture fluxes from the ocean surface. This altered microphysical structure would cause these clouds to behave differently in cloud-radiation interactions, where the optically-thick MIZ cloud would scatter incident shortwave solar radiation and trap upwelling heat from the surface more efficiently than the sea ice cloud. The geometrical thickness of the ocean cloud would allow it to also act as an efficient insulator, trapping heat in the boundary layer. However, it would significantly increase the albedo of the ocean environment, promoting atmospheric cooling. Minimal solar radiation is present at this time of year; therefore, the radiative interactions of these clouds are dominated by longwave fluxes from the surface. It is therefore likely that these clouds, with the microphysical structure detailed in Chapter 5, would contribute a net warming effect at the surface and thus have the potential to have a detrimental effect on the nearby sea ice.

Chapter 5 showed that the cloud ice crystal number concentration remained consistent over the transition from sea ice to ocean, whilst the liquid phase and cloud macrophysical structure transformed. Observed consistency in the ice phase during the springtime ACCACIA campaign – as shown by comparison between Chapters 5 and 6, and data presented by Lloyd et al. (2015) – suggests that N_{ice} is not sensitive to the dynamical changes induced by the surface or highly variable aerosol particle compositional trends. However, modelled microphysics was found to be highly sensitive to N_{ice} in Chapter 6. This may suggest that Arctic cloud microphysical structure may be vulnerable to changes in the INP population. If the ice phase becomes more sensitive to variability in the aerosol particle population – changes which may occur due to increasing anthropogenic emissions and altered circulation patterns due to atmospheric warming – the typical microphysical structure of single-layer Arctic clouds would likely be affected.

7.5 Further work

Chapters 4, 5, and 6 improve our understanding of aerosol-cloud interactions in the Arctic; however, further work is required to constrain the large uncertainties associated with modelling the climatological changes which are under way.

The ACCACIA data provides a unique, high-resolution insight into the short-term variability of cloud microphysics over a two week window. These data have not been exhausted and further analysis could be carried out. For example, dust data derived from the filter analyses have only been compared to cloud data for one case (Chapter 5). This case was the coldest springtime case encountered; therefore, it is the most likely to produce good agreement with dust-based parameterisations given their increasing efficiency as INPs with decreasing temperature. Further investigation of the warmer cases (flights B764 and B765, cases 4 and 5 in Chapter 4) should be prioritised, given the uncertainty in the source of cloud ice at warm sub-zero temperatures. In particular, it would be beneficial to investigate if appreciable secondary ice production is ever seen in these early springtime clouds. Similarly, data from flights B764 and B765 could be used to investigate if the high sea salt fractions collected inversely influence the number of primary ice crystals in the nearby clouds. The sea salt loadings from the springtime ACCACIA campaign peaked during these cases; therefore, an investigation into the microphysical properties of the clouds observed on these days, with comparison to the particle composition measurements detailed in Chapter 4, would be beneficial for our holistic understanding of aerosol-cloud interactions in this region.

Further development of the modelling methodology of Chapter 6 should be conducted to represent the depletion of INPs. These updates would improve the treatment of modelled microphysics and could allow for a more realistic comparison with observations. Similarly, including a spatial distribution of INPs and modelling the cloud microphysical response to INP plumes could improve our understanding of the sensitivities and limitations of these mixed-phase clouds. In the meantime, the water-saturation restriction tested in Chapter 6 is not computationally expensive and could easily be implemented into the Weather Research and Forecasting (WRF) model as the same microphysical scheme is used (Morrison et al.

2005). Therefore, it would be advantageous to test if this restriction can also improve the ability of such a numerical weather prediction (NWP) model to simulate these persistent Arctic mixed-phase clouds.

The relationship between back trajectories and particle composition could cause issues with modelling these scenarios in large-scale models, as this variability may be difficult to capture. Despite this, the compositional and air mass history consistency between cases 4 and 5 in Chapter 4 suggests that regional fields could be constructed which introduce the dominant species observed when the air masses hail from that direction. However, these proposed model developments would likely be computationally expensive; therefore, it may not be practical to include such detailed geographically-dependent aerosol-cloud interactions in large-scale models. Instead, further investigation – and parameterisation – with bin microphysics and process models may provide an easier route to include these interactions in global climate models.

Aerosol particle composition varied strongly with air mass history. Back trajectories from over the northern coast of Russia and Siberia were found to be clean and dominated by fresh chlorides from the sea surface; however, trajectories moving further south over the European continent and Scandinavia were highly polluted and biomass burning tracers were identified. The cold early spring likely influences biomass burning activity in the densely-populated continent where, for example, fuel burning may be common for heating purposes. Only one of the springtime ACCACIA cases (case 6) displayed this behaviour. However, from this discussion, important questions arise: are all air masses from the east, towards northern Russia, clean? And are all European air masses polluted? It is not known if the ACCACIA data are unique in their notable dust fractions, or if one polluted air mass – out of six case studies – is a representative number for the season and region considered. Perhaps these pollution cases are uncommon and the ACCACIA campaign period encountered one by chance. To address this issue, more data are required to test how representative the ACCACIA observations are of the European Arctic during the spring.

More measurements of aerosol, cloud, and boundary layer properties in the springtime Arctic are required. In particular, particle compositional data – with

close proximity to cloud – should be an area of focus. More filter exposures below and above an observed cloud deck would be particularly beneficial: the comparison detailed in Chapter 4 was the only such pair obtained during ACCACIA, therefore it cannot be concluded whether the comparisons made and conclusions drawn are representative. To improve confidence in these data, the size-dependent collection issues of the filter inlet should be better quantified through characterisation with a wind tunnel. Filter exposures are a good method of studying aerosol particle composition off-line; however, compositional data with temporal resolution would provide a more detailed insight into the properties of aerosol particles during the Arctic haze. For example, single particle mass spectrometry techniques could be used to provide on-line compositional measurements on a particle-by-particle basis (e.g. Pratt and Prather 2010). Additionally, INPs were inferred in Chapter 4 via particle composition; however, direct measurements would provide an alternative view of which particles nucleate ice in this region. Future campaigns could employ ice nucleus detectors to directly measure ambient INPs and correlate these measurements with observed cloud microphysics. Alternatively, ice crystal residuals could be collected, like the study by Pratt et al. (2009), to identify which particle species are preferentially nucleating ice crystals in the Arctic boundary layer.

Conclusions drawn from Chapters 4, 5, and 6 have improved our understanding of aerosol-cloud interactions in the Arctic. With some questions answered, others emerge: for example, can we confirm that long-range transported dusts are nucleating ice in these clouds? If so, this may have substantial consequences for the Arctic in our warming climate. If low, consistent concentrations of transported dusts are nucleating ice in these mixed-phase stratocumulus clouds, any change to their mixing states or number concentrations may significantly affect the microphysics of these clouds. It is difficult to predict if dust properties would change appreciably in a warming climate due to the increasing atmospheric air temperature alone. However, with increasing anthropogenic emissions in the mid-latitudes, the probability of internal mixing with these natural dusts may also increase. Additionally, atmospheric circulation patterns will likely be affected, potentially influencing traditional transport pathways from the mid-latitudes. It is therefore difficult to predict how these clouds may microphysically change due to climate change. Dynamically,

Chapter 5 showed that the sea ice restricts turbulent motion in clouds and, with decreasing Arctic sea ice coverage, the thicker liquid-dominated mixed-phase clouds over the ocean may become more common. It is therefore likely that these single-layer mixed-phase stratocumulus will play a key role in the Arctic radiative balance in the future.

This thesis has improved our knowledge of springtime aerosol-cloud interactions and cloud microphysics in the European Arctic, and provides insight into potential areas of development for regional and global climate models. Links were made between air mass history and aerosol particle compositional trends, with the further suggestion that mineral dusts may be nucleating ice particles in the mixed-phase clouds observed. A changing boundary layer structure, over the transition from sea ice to ocean, was shown to have a significant impact on the liquid phase of these clouds, whilst the ice phase was insensitive to these changes. This microphysical development has implications for the role of these clouds in the radiative budget, with a greater liquid water content influencing both their albedo and their ability to trap upwelling LW radiation. However, modelled cloud evolution and lifetime was found to be highly sensitive to the ice phase, and mixed-phase conditions could only be maintained over all surfaces considered when ice nucleation was limited to liquid-dependent pathways. These results highlight that the method of parameterising ice number concentrations is important, whilst emphasising the need to better characterise and parameterise observations of Arctic MPS for use in numerical models.

Bibliography

Abe, M., Nozawa, T., Ogura, T., and Takata, K.: Effect of retreating sea ice on Arctic cloud cover in simulated recent global warming, Atmospheric Chemistry and Physics, 16, 14 343–14 356, doi:10.5194/acp-16-14343-2016, 2016.

ACIA: Arctic Climate Impact Assessment. ACIA Overview report., pp. 990–1020, Cambridge University Press, 2005.

Allan, J. D., Williams, P. I., Najera, J., Whitehead, J. D., Flynn, M. J., Taylor, J. W., Liu, D., Darbyshire, E., Carpenter, L. J., Chance, R., Andrews, S. J., Hackenberg, S. C., and McFiggans, G.: Iodine observed in new particle formation events in the Arctic atmosphere during ACCACIA, Atmospheric Chemistry and Physics, 15, 5599–5609, doi:10.5194/acp-15-5599-2015, 2015.

Andreae, M. O., Elbert, W., Gabriel, R., Johnson, D. W., Osborne, S., and Wood, R.: Soluble ion chemistry of the atmospheric aerosol and SO concentrations over the eastern North Atlantic during ACE-2, Tellus B, 52, 1066–1087, doi:10.1034/j.1600-0889.2000.00105.x, 2000.

Ariya, P. A., Sun, J., Eltouny, N. A., Hudson, E. D., Hayes, C. T., and Kos, G.: Physical and chemical characterization of bioaerosols - Implications for nucleation processes, International Reviews in Physical Chemistry, 28, 1–32, doi: 10.1080/01442350802597438, 2009.

Atkinson, J. D., Murray, B. J., Woodhouse, M. T., Whale, T. F., Baustian, K. J., Carslaw, K. S., Dobbie, S., O'Sullivan, D., and Malkin, T. L.: The Importance of Feldspar for Ice Nucleation by Mineral Dust in Mixed-Phase Clouds, Nature, 498, 355–358, doi:10.1038/nature12278, 2013.

Barrie, L. A.: Arctic Air Chemistry: An Overview, in: Arctic Air Pollution, Cambridge University Press, (Edited by Stonehouse, B.), 1986.

Barrie, L. A., Bottenheim, J. W., Schnell, R. C., Crutzen, P. J., and Rasmussen, R. A.: Ozone destruction and photochemical reactions at polar sunrise in the lower Arctic atmosphere, Nature, 334, 138–141, doi:10.1038/334138a0, 1988.

Baumgardner, D., Jonsson, H., Dawson, W., O'Connor, D., and Newton, R.: The cloud, aerosol and precipitation spectrometer: a new instrument for cloud investigations, Atmospheric Research, 59, 251–264, doi:10.1016/S0169-8095(01)00119-3, 2001.

Beard, K. V.: Ice initiation in warm-base convective clouds: An assessment of microphysical mechanisms, Atmospheric Research, 28, 125–152, doi:10.1016/0169-8095(92)90024-5, 1992.

Beheng, K. D.: A parameterization of warm cloud microphysical conversion processes, Atmospheric Research, 33, 193–206, doi:10.1016/0169-8095(94)90020-5, 1994.

Behrenfeldt, U., Krejci, R., Ström, J., and Stohl, A.: Chemical properties of Arctic aerosol particles collected at the Zeppelin station during the aerosol transition period in May and June of 2004, Tellus Series B, 60, 405–415, doi:10.1111/j.1600-0889.2008.00349.x, 2008.

Bergeron, T.: On the physics of clouds and precipitation, in: Proces Verbaux de l'Association de Météorologie, The International Union of Geodesy and Geophyics, Karlsruhe, Germany, pp. 156–178, 1935.

Bigg, E. K.: The formation of atmospheric ice crystals by the freezing of droplets, Quarterly Journal of the Royal Meteorological Society, 79, 510–519, doi:10.1002/qj.49707934207, 1953.

Bigg, E. K.: Ice forming nuclei in the high Arctic, Tellus Series B, 48, 223–233, doi:10.1034/j.1600-0889.1996.t01-1-00007.x, 1996.

Bigg, E. K. and Leck, C.: Cloud-active particles over the central Arctic Ocean, Journal of Geophysical Research (Atmospheres), 106, 32 155, doi: 10.1029/1999JD901152, 2001.

Birch, C. E., Brooks, I. M., Tjernström, M., Shupe, M. D., Mauritsen, T., Sedlar, J., Lock, A. P., Earnshaw, P., Persson, P. O. G., Milton, S. F., and Leck, C.: Modelling atmospheric structure, cloud and their response to CCN in the central Arctic: ASCOS case studies, Atmospheric Chemistry and Physics, 12, 3419–3435, doi: 10.5194/acp-12-3419-2012, 2012.

Boucher, O., Randall, D., Artaxo, P., Bretherton, C., Feingold, G., Forster, P., Kerminen, V. M., Kondo, Y., Liao, H., Lohmann, U., Rasch, P., Satheesh, S. K., Sherwood, S., Stevens, B., and Zhang, X. Y.: Clouds and Aerosols, in: Climate Change 2013 – The Physical Science Basis: Working Group I Contribution to the Fifth Assessment Report of the Intergovernmental Panel on Climate Change, edited by: Stocker, T. F., Qin, D., Plattner, G. K., Tignor, M., Allen, S. K., Boschung, J., Nauels, A., Xia, Y., Bex, V., and Midgley, P. M., p. 571–658, Cambridge University Press, Cambridge, United Kingdom and New York, NY, USA, doi:10.1017/CBO9781107415324.016, 2014.

Browse, J., Carslaw, K. S., Arnold, S. R., Pringle, K., and Boucher, O.: The scavenging processes controlling the seasonal cycle in Arctic sulphate and black carbon aerosol, Atmospheric Chemistry and Physics, 12, 6775–6798, doi:10.5194/acp-12-6775-2012, 2012.

Caquineau, S., Gaudichet, A., Gomes, L., and Legrand, M.: Mineralogy of Saharan dust transported over northwestern tropical Atlantic Ocean in relation to source regions, Journal of Geophysical Research (Atmospheres), 107, 4251, doi: 10.1029/2000JD000247, 2002.

Chou, C., Formenti, P., Maille, M., Ausset, P., Helas, G., Harrison, M., and Osborne, S.: Size distribution, shape, and composition of mineral dust aerosols collected during the African Monsoon Multidisciplinary Analysis Special Observation Period 0: Dust and Biomass-Burning Experiment field campaign in Niger,

January 2006, Journal of Geophysical Research (Atmospheres), 113, D00C10, doi: 10.1029/2008JD009897, 2008.

Collins, D. R., Jonsson, H. H., Seinfeld, J. H., Flagan, R. C., Gassó, S., Hegg, D. A., Russell, P. B., Schmid, B., Livingston, J. M., Öström, E., Noone, K. J., Russell, L. M., and Putaud, J. P.: In situ aerosol-size distributions and clear-column radiative closure during ACE-2, Tellus Series B, 52, 498–525, doi:10.3402/tellusb.v52i2.16175, 2011.

Connolly, P. J., Möhler, O., Field, P. R., Saathoff, H., Burgess, R., Choularton, T., and Gallagher, M.: Studies of heterogeneous freezing by three different desert dust samples, Atmospheric Chemistry and Physics, 9, 2805–2824, doi:10.5194/acp-9-2805-2009, 2009.

Connolly, P. J., Vaughan, G., Cook, P., Allen, G., Coe, H., Choularton, T. W., Dearden, C., and Hill, A.: Modelling the effects of gravity waves on stratocumulus clouds observed during VOCALS-UK, Atmospheric Chemistry and Physics, 13, 7133–7152, doi:10.5194/acp-13-7133-2013, 2013.

Cooper, W. A.: Ice Initiation in Natural Clouds, Meteorological Monographs, 21, 29–32, doi:10.1175/0065-9401-21.43.29, 1986.

Crosier, J., Bower, K. N., Choularton, T. W., Westbrook, C. D., Connolly, P. J., Cui, Z. Q., Crawford, I. P., Capes, G. L., Coe, H., Dorsey, J. R., Williams, P. I., Illingworth, A. J., Gallagher, M. W., and Blyth, A. M.: Observations of ice multiplication in a weakly convective cell embedded in supercooled mid-level stratus, Atmospheric Chemistry and Physics, 11, 257–273, doi:10.5194/acp-11-257-2011, 2011.

Crosier, J., Choularton, T. W., Westbrook, C. D., Blyth, A. M., Bower, K. N., Connolly, P. J., Dearden, C., Gallagher, M. W., Cui, Z., and Nicol, J. C.: Microphysical properties of cold frontal rainbands, Quarterly Journal of the Royal Meteorological Society, 140, 1257–1268, doi:10.1002/qj.2206, 2014.

Curry, J. A., Ebert, E. E., and Herman, G. F.: Mean and turbulence structure of

the summertime Arctic cloudy boundary layer, Quarterly Journal of the Royal Meteorological Society, 114, 715–746, doi:10.1002/qj.49711448109, 1988.

Curry, J. A., Rossow, W. B., Randall, D., and Schramm, J. L.: Overview of Arctic Cloud and Radiation Characteristics., Journal of Climate, 9, 1731–1764, doi:10.1175/1520-0442(1996)009<1731:OOACAR>2.0.CO;2, 1996.

Curry, J. A., Hobbs, P. V., King, M. D., Randall, D. A., Minnis, P., Isaac, G. A., Pinto, J. O., Uttal, T., Bucholtz, A., Cripe, D. G., Gerber, H., Fairall, C. W., Garrett, T. J., Hudson, J., Intrieri, J. M., Jakob, C., Jensen, T., Lawson, P., Marcotte, D., Nguyen, L., Pilewskie, P., Rangno, A., Rogers, D. C., Strawbridge, K. B., Valero, F. P. J., Williams, A. G., and Wylie, D.: FIRE Arctic Clouds Experiment., Bulletin of the American Meteorological Society, 81, 5–29, doi:10.1175/1520-0477(2000)081<0005:FACE>2.3.CO;2, 2000.

de Boer, G., Eloranta, E. W., and Shupe, M. D.: Arctic Mixed-Phase Stratiform Cloud Properties from Multiple Years of Surface-Based Measurements at Two High-Latitude Locations, Journal of Atmospheric Sciences, 66, 2874–2887, doi:10.1175/2009JAS3029.1, 2009.

de Boer, G., Morrison, H., Shupe, M. D., and Hildner, R.: Evidence of liquid dependent ice nucleation in high-latitude stratiform clouds from surface remote sensors, Geophysics Research Letters, 38, L01803, doi:10.1029/2010GL046016, 2011.

de Boer, G., Shupe, M. D., Caldwell, P. M., Bauer, S. E., Persson, O., Boyle, J. S., Kelley, M., Klein, S. A., and Tjernström, M.: Near-surface meteorology during the Arctic Summer Cloud Ocean Study (ASCOS): evaluation of reanalyses and global climate models, Atmospheric Chemistry and Physics, 14, 427–445, doi:10.5194/acp-14-427-2014, 2014.

DeMott, P. J., Prenni, A. J., Liu, X., Kreidenweis, S. M., Petters, M. D., Twohy, C. H., Richardson, M. S., Eidhammer, T., and Rogers, D. C.: Predicting global atmospheric ice nuclei distributions and their impacts on climate, Proceedings of the National Academy of Sciences, doi:10.1073/pnas.0910818107, 2010.

DeMott, P. J., Möhler, O., Stetzer, O., Vali, G., Levin, Z., Petters, M. D., Murakami, M., Leisner, T., Bundke, U., Klein, H., Kanji, Z. A., Cotton, R., Jones, H., Benz, S., Brinkmann, M., Rzesanke, D., Saathoff, H., Nicolet, M., Saito, A., Nillius, B., Bingemer, H., Abbatt, J., Ardon, K., Ganor, E., Georgakopoulos, D. G., and Saunders, C.: Resurgence in Ice Nuclei Measurement Research, Bulletin of the American Meteorological Society, 92, 1623–1635, doi:10.1175/2011BAMS3119.1, 2011.

DeMott, P. J., Prenni, A. J., McMeeking, G. R., Sullivan, R. C., Petters, M. D., Tobo, Y., Niemand, M., Möhler, O., Snider, J. R., Wang, Z., and Kreidenweis, S. M.: Integrating laboratory and field data to quantify the immersion freezing ice nucleation activity of mineral dust particles, Atmospheric Chemistry and Physics, 15, 393–409, doi:10.5194/acp-15-393-2015, 2015.

Diehl, K. and Wurzler, S.: Heterogeneous Drop Freezing in the Immersion Mode: Model Calculations Considering Soluble and Insoluble Particles in the Drops, Journal of the Atmospheric Sciences, 61, 2063–2072, doi:10.1175/1520-0469(2004)061<2063:HDFITI>2.0.CO;2, 2004.

Dusek, U., Frank, G. P., Hildebrandt, L., Curtius, J., Schneider, J., Walter, S., Chand, D., Drewnick, F., Hings, S., Jung, D., Borrmann, S., and Andreae, M. O.: Size Matters More Than Chemistry for Cloud-Nucleating Ability of Aerosol Particles, Science, 312, 1375–1378, doi:10.1126/science.1125261, 2006.

Earle, M. E., Liu, P. S. K., Strapp, J. W., Zelenyuk, A., Imre, D., McFarquhar, G. M., Shantz, N. C., and Leaitch, W. R.: Factors influencing the microphysics and radiative properties of liquid-dominated Arctic clouds: Insight from observations of aerosol and clouds during ISDAC, Journal of Geophysical Research (Atmospheres), 116, D00T09, doi:10.1029/2011JD015887, 2011.

Edwards, J. M. and Slingo, A.: Studies with a flexible new radiation code. I: Choosing a configuration for a large-scale model, Quarterly Journal of the Royal Meteorological Society, 122, 689–719, doi:10.1002/qj.49712253107, 1996.

Eleftheriadis, K., Vratolis, S., and Nyeki, S.: Aerosol black carbon in the European Arctic: Measurements at Zeppelin station, Ny-Ålesund, Svalbard from 1998-2007, Geophysics Research Letters, 36, L02809, doi:10.1029/2008GL035741, 2009.

Elvidge, A. D., Renfrew, I. A., Weiss, A. I., Brooks, I. M., Lachlan-Cope, T. A., and King, J. C.: Observations of surface momentum exchange over the marginal ice zone and recommendations for its parametrisation, Atmospheric Chemistry and Physics, 16, 1545–1563, doi:10.5194/acp-16-1545-2016, 2016.

Engvall, A.-C., Krejci, R., Ström, J., Treffeisen, R., Scheele, R., Hermansen, O., and Paatero, J.: Changes in aerosol properties during spring-summer period in the Arctic troposphere, Atmospheric Chemistry and Physics, 8, 445–462, doi:10.5194/acp-8-445-2008, 2008.

Fan, J., Ovtchinnikov, M., Comstock, J. M., McFarlane, S. A., and Khain, A.: Ice formation in Arctic mixed-phase clouds: Insights from a 3-D cloud-resolving model with size-resolved aerosol and cloud microphysics, Journal of Geophysical Research (Atmospheres), 114, D04205, doi:10.1029/2008JD010782, 2009.

Field, P. R., Heymsfield, A. J., and Bansemer, A.: Shattering and Particle Interarrival Times Measured by Optical Array Probes in Ice Clouds, Journal of Atmospheric and Oceanic Technology, 23, 1357–1371, doi:10.1175/JTECH1922.1, 2006.

Findeisen, W.: Kolloid-meteorologische Vorgänge bei Niederschlagsbildung, Meteorologische Zeitschrift, 55, 121–133, 1938.

Fletcher, N. H.: The Physics of Rain Clouds, Cambridge University Press, Cambridge, United Kingdom, 1962.

Formenti, P., Rajot, J. L., Desboeufs, K., Caquineau, S., Chevaillier, S., Nava, S., Gaudichet, A., Journet, E., Triquet, S., Alfaro, S., Chiari, M., Haywood, J., Coe, H., and Highwood, E.: Regional variability of the composition of mineral dust from western Africa: Results from the AMMA SOP0/DABEX and DODO field campaigns, Journal of Geophysical Research (Atmospheres), 113, D00C13, doi:10.1029/2008JD009903, 2008.

Formenti, P., Schütz, L., Balkanski, Y., Desboeufs, K., Ebert, M., Kandler, K., Petzold, A., Scheuvens, D., Weinbruch, S., and Zhang, D.: Recent progress in understanding physical and chemical properties of African and Asian mineral dust, Atmospheric Chemistry and Physics, 11, 8231–8256, doi:10.5194/acp-11-8231-2011, 2011.

Gayet, J.-F., Treffeisen, R., Helbig, A., Bareiss, J., Matsuki, A., Herber, A., and Schwarzenboeck, A.: On the onset of the ice phase in boundary layer Arctic clouds, Journal of Geophysical Research (Atmospheres), 114, D19 201, doi:10.1029/2008JD011348, 2009.

Geng, H., Ryu, J., Jung, H.-J., Chung, H., Ahn, K.-H., and Ro, C.-U.: Single-Particle Characterization of Summertime Arctic Aerosols Collected at Ny-Ålesund, Svalbard, Environmental Science Technology, 44, 2348–2353, doi:10.1021/es903268j, 2010.

Glen, A. and Brooks, S. D.: A new method for measuring optical scattering properties of atmospherically relevant dusts using the Cloud and Aerosol Spectrometer with Polarization (CASPOL), Atmospheric Chemistry and Physics, 13, 1345–1356, doi:10.5194/acp-13-1345-2013, 2013.

Gray, M. E. B. and Petch, J.: Version 2.3 of the Met Office Large Eddy Model: Part I. User Documentation., Tech. rep., 2001.

Gray, M. E. B., Petch, J. C., Derbyshire, S. H., Brown, A. R., Lock, A. P., Swann, H. A., and Brown, P. R. A.: Version 2.3 of the Met Office Large Eddy Model: Part II. Scientific Documentation., Tech. rep., 2001.

Grossman, R. L.: An analysis of vertical velocity spectra obtained in the bomex fair-weather, trade-wind boundary layer, Boundary-Layer Meteorology, 23, 323–357, doi:10.1007/BF00121120, 1982.

Hallett, J. and Mossop, S. C.: Production of Secondary Ice Particles during the Riming Process, Nature, 249, 26–28, doi:10.1038/249026a0, 1974.

Hara, K., Yamagata, S., Yamanouchi, T., Sato, K., Herber, A., Iwasaka, Y., Nagatani,

M., and Nakata, H.: Mixing states of individual aerosol particles in spring Arctic troposphere during ASTAR 2000 campaign, Journal of Geophysical Research (Atmospheres), 108, 4209, doi:10.1029/2002JD002513, 2003.

Harrington, J. Y. and Olsson, P. Q.: A method for the parameterization of cloud optical properties in bulk and bin microphysical models. Implications for arctic cloudy boundary layers, Atmospheric Research, 57, 51–80, doi:10.1016/S0169-8095(00)00068-5, 2001.

Harrington, J. Y. and Olsson, P. Q.: On the potential influence of ice nuclei on surface-forced marine stratocumulus cloud dynamics, Journal of Geophysical Research (Atmospheres), 106(D21), 27 473–27 484, doi:10.1029/2000JD000236, 2001.

Harrington, J. Y., Meyers, M. P., Walko, R. L., and Cotton, W. R.: Parameterization of Ice Crystal Conversion Processes Due to Vapor Deposition for Mesoscale Models Using Double-Moment Basis Functions. Part 1: Basic Formulation and Parcel Model Results, Journal of the Atmospheric Sciences, 52, 4344–4366, doi:10.1175/1520-0469(1995)052<4344:POICCP>2.0.CO;2, 1995.

Harrington, J. Y., Reisin, T., Cotton, W. R., and Kreidenweis, S. M.: Cloud resolving simulations of Arctic stratus. Part II: Transition-season clouds, Atmospheric Research, 51, 45–75, doi:10.1016/S0169-8095(98)00098-2, 1999.

Hartmann, J., Kottmeier, C., and Raasch, S.: Roll Vortices and Boundary-Layer Development during a Cold Air Outbreak, Boundary-Layer Meteorology, 84, 45–65, doi:10.1023/A:1000392931768, 1997.

Heymsfield, A. J. and Parrish, J. L.: A Computational Technique for Increasing the Effective Sampling Volume of the PMS Two-Dimensional Particle Size Spectrometer, Journal of Applied Meteorology, 17, 1566–1572, doi:10.1175/1520-0450(1978)017<1566:ACTFIT>2.0.CO;2, 1978.

Hill, A. A., Field, P. R., Furtado, K., Korolev, A., and Shipway, B. J.: Mixed-phase clouds in a turbulent environment. Part 1: Large-eddy simulation experiments, Quarterly Journal of the Royal Meteorological Society, 140, 855–869, doi:10.1002/qj.2177, 2014.

Hobbs, P. V. and Alkezweeny, A. J.: The Fragmentation of Freezing Water Droplets in Free Fall, Journal of the Atmospheric Sciences, 25, 881–888, doi:10.1175/1520-0469(1968)025<0881:TFOFWD>2.0.CO;2, 1968.

Hobbs, P. V. and Rangno, A. L.: Microstructures of low and middle-level clouds over the Beaufort Sea, Quarterly Journal of the Royal Meteorological Society, 124, 2035–2071, doi:10.1002/qj.49712455012, 1998.

Hoose, C. and Möhler, O.: Heterogeneous ice nucleation on atmospheric aerosols: a review of results from laboratory experiments, Atmospheric Chemistry and Physics, 12, 9817–9854, doi:10.5194/acp-12-9817-2012, 2012.

Hoose, C., Kristjánsson, J. E., Chen, J.-P., and Hazra, A.: A Classical-Theory-Based Parameterization of Heterogeneous Ice Nucleation by Mineral Dust, Soot, and Biological Particles in a Global Climate Model, Journal of Atmospheric Sciences, 67, 2483–2503, doi:10.1175/2010JAS3425.1, 2010.

Intrieri, J. M., Fairall, C. W., Shupe, M. D., Persson, P. O. G., Andreas, E. L., Guest, P. S., and Moritz, R. E.: An annual cycle of Arctic surface cloud forcing at SHEBA, Journal of Geophysical Research (Oceans), 107, 2002.

Jackson, R. C., McFarquhar, G. M., Korolev, A. V., Earle, M. E., Liu, P. S. K., Lawson, R. P., Brooks, S., Wolde, M., Laskin, A., and Freer, M.: The dependence of ice microphysics on aerosol concentration in arctic mixed-phase stratus clouds during ISDAC and M-PACE, Journal of Geophysical Research (Atmospheres), 117, D15 207, doi:10.1029/2012JD017668, 2012.

Jacob, D. J., Crawford, J. H., Maring, H., Clarke, A. D., Dibb, J. E., Emmons, L. K., Ferrare, R. A., Hostetler, C. A., Russell, P. B., Singh, H. B., Thompson, A. M., Shaw, G. E., McCauley, E., Pederson, J. R., and Fisher, J. A.: The Arctic Research of the Composition of the Troposphere from Aircraft and Satellites (ARCTAS) mission: design, execution, and first results, Atmospheric Chemistry and Physics, 10, 5191–5212, doi:10.5194/acp-10-5191-2010, 2010.

Jiang, H., Cotton, W. R., Pinto, J. O., Curry, J. A., and Weissbluth, M. J.: Cloud Resolving Simulations of Mixed-Phase Arctic Stratus Observed during BASE:

Sensitivity to Concentration of Ice Crystals and Large-Scale Heat and Moisture Advection, Journal of Atmospheric Sciences, 57, 2105–2117, doi:10.1175/1520-0469(2000)057<2105:CRSOMP>2.0.CO;2, 2000.

Kandler, K., Schütz, L., Deutscher, C., Ebert, M., Hofmann, H., Jäckel, S., Jaenicke, R., Knippertz, P., Lieke, K., Massling, A., Petzold, A., Schladitz, A., Weinzierl, B., Wiedensohler, A., Zorn, S., and Weinbruch, S.: Size distribution, mass concentration, chemical and mineralogical composition and derived optical parameters of the boundary layer aerosol at Tinfou, Morocco, during SAMUM 2006, Tellus Series B, 61, 32–50, doi:10.1111/j.1600-0889.2008.00385.x, 2009.

Kandler, K., Lieke, K., Benker, N., Emmel, C., Küpper, M., Müller-Ebert, D., Ebert, M., Scheuvens, D., Schladitz, A., Schütz, L., and Weinbruch, S.: Electron microscopy of particles collected at Praia, Cape Verde, during the Saharan Mineral Dust Experiment: particle chemistry, shape, mixing state and complex refractive index, Tellus Series B, 63, 475–496, doi:10.1111/j.1600-0889.2011.00550.x, 2011.

Kapsch, M.-L., Graversen, R. G., and Tjernström, M.: Springtime atmospheric energy transport and the control of Arctic summer sea-ice extent, Nature Climate Change, 3, 744–748, doi:10.1038/nclimate1884, 2013.

Kay, J. E. and Gettelman, A.: Cloud influence on and response to seasonal Arctic sea ice loss, Journal of Geophysical Research (Atmospheres), 114, D18204, doi:10.1029/2009JD011773, 2009.

Khain, A., Ovtchinnikov, M., Pinsky, M., Pokrovsky, A., and Krugliak, H.: Notes on the state-of-the-art numerical modeling of cloud microphysics, Atmospheric Research, 55, 159–224, doi:10.1016/S0169-8095(00)00064-8, 2000.

Klein, S. A., McCoy, R. B., Morrison, H., Ackerman, A. S., Avramov, A., de Boer, G., Chen, M., Cole, J. N. S., Del Genio, A. D., Falk, M., Foster, M. J., Fridlind, A., Golaz, J.-C., Hashino, T., Harrington, J. Y., Hoose, C., Khairoutdinov, M. F., Larson, V. E., Liu, X., Luo, Y., McFarquhar, G. M., Menon, S., Neggers, R. A. J., Park, S., Poellot, M. R., Schmidt, J. M., Sednev, I., Shipway, B. J., Shupe, M. D., Spangenberg, D. A., Sud, Y. C., Turner, D. D., Veron, D. E., Salzen, K. v., Walker,

G. K., Wang, Z., Wolf, A. B., Xie, S., Xu, K.-M., Yang, F., and Zhang, G.: Intercomparison of model simulations of mixed-phase clouds observed during the ARM Mixed-Phase Arctic Cloud Experiment. I: Single-layer cloud, Quarterly Journal of the Royal Meteorological Society, 135, 979–1002, doi:10.1002/qj.416, 2009.

Korhonen, H., Carslaw, K. S., Spracklen, D. V., Ridley, D. A., and Ström, J.: A global model study of processes controlling aerosol size distributions in the Arctic spring and summer, Journal of Geophysical Research (Atmospheres), 113, D08211, doi:10.1029/2007JD009114, 2008.

Korolev, A. and Field, P. R.: The Effect of Dynamics on Mixed-Phase Clouds: Theoretical Considerations, Journal of Atmospheric Sciences, 65, 2008.

Korolev, A. and Isaac, G.: Phase transformation of mixed-phase clouds, Quarterly Journal of the Royal Meteorological Society, 129, 19–38, doi:10.1256/qj.01.203, 2003.

Korolev, A., Emery, E., and Creelman, K.: Modification and Tests of Particle Probe Tips to Mitigate Effects of Ice Shattering, Journal of Atmospheric and Oceanic Technology, 30, 690–708, doi:10.1175/JTECH-D-12-00142.1, 2013.

Lance, S., Brock, C. A., Rogers, D., and Gordon, J. A.: Water droplet calibration of the Cloud Droplet Probe (CDP) and in-flight performance in liquid, ice and mixed-phase clouds during ARCPAC, Atmospheric Measurement Techniques, 3, 1683–1706, doi:10.5194/amt-3-1683-2010, 2010.

Lawson, R. P., Baker, B. A., Schmitt, C. G., and Jensen, T. L.: An overview of microphysical properties of Arctic clouds observed in May and July 1998 during FIRE ACE, Journal of Geophysical Research (Atmospheres), 106, 2001.

Lawson, R. P., O'Connor, D., Zmarzly, P., Weaver, K., Baker, B., Mo, Q., and Jonsson, H.: The 2D-S (Stereo) Probe: Design and Preliminary Tests of a New Airborne, High-Speed, High-Resolution Particle Imaging Probe, Journal of Atmospheric and Oceanic Technology, 23, 1462–1477, doi:10.1175/JTECH1927.1, 2006.

Leck, C. and Bigg, E. K.: Aerosol production over remote marine areas-A new route, Geophysics Research Letters, 26, 3577–3580, doi:10.1029/1999GL010807, 1999.

Leck, C., Bigg, E. K., Covert, D. S., Heintzenberg, J., Maenhaut, W., Nilsson, E. D., and Wiedensohler, A.: Overview of the atmospheric research program during the International Arctic Ocean Expedition of 1991 (IAOE-91) and its scientific results, Tellus Series B, 48, 136–155, doi:10.1034/j.1600-0889.1996.t01-1-00002.x, 1996.

Levin, Z., Teller, A., Ganor, E., and Yin, Y.: On the interactions of mineral dust, sea-salt particles, and clouds: A measurement and modeling study from the Mediterranean Israeli Dust Experiment campaign, Journal of Geophysical Research (Atmospheres), 110, D20202, doi:10.1029/2005JD005810, 2005.

Liu, D., Quennehen, B., Darbyshire, E., Allan, J. D., Williams, P. I., Taylor, J. W., Bauguitte, S. J.-B., Flynn, M. J., Lowe, D., Gallagher, M. W., Bower, K. N., Choularton, T. W., and Coe, H.: The importance of Asia as a source of black carbon to the European Arctic during springtime 2013, Atmospheric Chemistry and Physics, 15, 11 537–11 555, doi:10.5194/acp-15-11537-2015, 2015.

Lloyd, G., Choularton, T. W., Bower, K. N., Crosier, J., Jones, H., Dorsey, J. R., Gallagher, M. W., Connolly, P., Kirchgaessner, A. C. R., and Lachlan-Cope, T.: Observations and comparisons of cloud microphysical properties in spring and summertime Arctic stratocumulus during the ACCACIA campaign, Atmospheric Chemistry and Physics, 15, 3719–3737, doi:10.5194/acp-15-3719-2015, 2015.

Mamane, Y. and Noll, K. E.: Characterization of large particles at a rural site in the eastern United States: Mass distribution and individual particle analysis, Atmospheric Environment, 19, 611–622, doi:10.1016/0004-6981(85)90040-X, 1985.

McClatchey, R. A., Fenn, R. W., Selby, J. E. A., Volz, F. E., and Garing, J. S.: Optical Properties of the Atmosphere, Air Force Cambridge Research Laboratories, Air Force Systems Command, United States Air Force, 1972.

McFarquhar, G. M., Zhang, G., Poellot, M. R., Kok, G. L., McCoy, R., Tooman, T., Fridlind, A., and Heymsfield, A. J.: Ice properties of single-layer stratocumulus during the Mixed-Phase Arctic Cloud Experiment: 1. Observations, Journal of Geophysical Research (Atmospheres), 112, D24201, doi:10.1029/2007JD008633, 2007.

McFarquhar, G. M., Ghan, S., Verlinde, J., Korolev, A., Strapp, J. W., Schmid, B., Tomlinson, J. M., Wolde, M., Brooks, S. D., Cziczo, D., Dubey, M. K., Fan, J., Flynn, C., Gultepe, I., Hubbe, J., Gilles, M. K., Laskin, A., Lawson, P., Leaitch, W. R., Liu, P., Liu, X., Lubin, D., Mazzoleni, C., MacDonald, A.-M., Moffet, R. C., Morrison, H., Ovchinnikov, M., Shupe, M. D., Turner, D. D., Xie, S., Zelenyuk, A., Bae, K., Freer, M., and Glen, A.: Indirect and Semi-direct Aerosol Campaign: The Impact of Arctic Aerosols on Clouds, Bulletin of the American Meteorological Society, 92, 183–201, doi:10.1175/2010BAMS2935.1, 2011.

Meyers, M. P., DeMott, P. J., and Cotton, W. R.: New Primary Ice-Nucleation Parameterizations in an Explicit Cloud Model., Journal of Applied Meteorology, 31, 708–721, doi:10.1175/1520-0450(1992)031<0708:NPINPI>2.0.CO;2, 1992.

Möhler, O., DeMott, P. J., Vali, G., and Levin, Z.: Microbiology and atmospheric processes: the role of biological particles in cloud physics, Biogeosciences, 4, 1059–1071, doi:10.5194/bg-4-1059-2007, 2007.

Morrison, H. and Pinto, J. O.: Intercomparison of Bulk Cloud Microphysics Schemes in Mesoscale Simulations of Springtime Arctic Mixed-Phase Stratiform Clouds, Monthly Weather Review, 134, 1880–1900, doi:10.1175/MWR3154.1, 2006.

Morrison, H., Curry, J. A., and Khvorostyanov, V. I.: A New Double-Moment Microphysics Parameterization for Application in Cloud and Climate Models. Part I: Description, Journal of Atmospheric Sciences, 62, 1665–1677, doi:10.1175/JAS3446.1, 2005.

Morrison, H., Zuidema, P., Ackerman, A. S., Avramov, A., de Boer, G., Fan, J., Fridlind, A. M., Hashino, T., Harrington, J. Y., Luo, Y., Ovchinnikov, M., and Shipway, B.: Intercomparison of cloud model simulations of Arctic mixed-phase boundary layer clouds observed during SHEBA/FIRE-ACE, Journal of Advances in Modeling Earth Systems, 3, M05 001, doi:10.1029/2011MS000066, 2011.

Morrison, H., de Boer, G., Feingold, G., Harrington, J., Shupe, M. D., and Sulia, K.: Resilience of persistent Arctic mixed-phase clouds, Nature Geoscience, 5, 11–17, doi:10.1038/ngeo1332, 2012.

Mossop, S. C.: The Origin and Concentration of Ice Crystals in Clouds., Bulletin of the American Meteorological Society, 66, 264–273, doi:10.1175/1520-0477(1985)066<0264:TOACOI>2.0.CO;2, 1985.

Murakami, M.: Numerical Modeling of Dynamical and Microphysical Evolution of an Isolated Convective Cloud - The July 19 1981 CCOPE Cloud, Journal of the Meteorological Society of Japan, 68, 107–128, 1990.

Murray, B. J., O'Sullivan, D., Atkinson, J. D., and Webb, M. E.: Ice nucleation by particles immersed in supercooled cloud droplets., Chemical Society Reviews, 41, 6519–54, doi:10.1039/c2cs35200a, 2012.

Neale, R., Gettelman, A., Park, S., Chen, C.-C., Lauritzen, P., Williamson, D., Conley, A., Garcia, R., Kinnison, D., Lamarque, J.-F., Marsh, D., Mills, M., Smith, A., Tilmes, S., Vitt, F., Morrison, H., Cameron-Smith, P., Collins, W., Iacono, M., Easter, R., Liu, X., Ghan, S., Rasch, P., and Taylor, M.: Description of the NCAR Community Atmosphere Model (CAM 5.0), Tech. rep., NCAR, 2010.

Nichman, L., Fuchs, C., Järvinen, E., Ignatius, K., Florian Höppel, N., Dias, A., Heinritzi, M., Simon, M., Tröstl, J., Wagner, A. C., Wagner, R., Williamson, C., Yan, C., Connolly, P. J., Dorsey, J. R., Duplissy, J., Ehrhart, S., Frege, C., Gordon, H., Hoyle, C. R., Bjerring Kristensen, T., Steiner, G., McPherson Donahue, N., Flagan, R., Gallagher, M. W., Kirkby, J., Möhler, O., Saathoff, H., Schnaiter, M., Stratmann, F., and Tomé, A.: Phase transition observations and discrimination of small cloud particles by light polarization in expansion chamber experiments, Atmospheric Chemistry and Physics, 16, 3651–3664, doi:10.5194/acp-16-3651-2016, 2016.

Niedermeier, D., Shaw, R. A., Hartmann, S., Wex, H., Clauss, T., Voigtländer, J., and Stratmann, F.: Heterogeneous ice nucleation: exploring the transition from stochastic to singular freezing behavior, Atmospheric Chemistry and Physics, 11, 8767–8775, doi:10.5194/acp-11-8767-2011, 2011.

Niemand, M., Möhler, O., Vogel, B., Vogel, H., Hoose, C., Connolly, P., Klein, H., Bingemer, H., DeMott, P., Skrotzki, J., and Leisner, T.: A Particle-Surface-Area-Based Parameterization of Immersion Freezing on Desert Dust Particles, Journal of Atmospheric Sciences, 69, 3077–3092, doi:10.1175/JAS-D-11-0249.1, 2012.

O'Sullivan, D., Murray, B. J., Malkin, T. L., Webb, M. E., Whale, T. F., Atkinson, J. D., and Baustian, K. J.: Atmospheric ice nucleation by fertile soil dusts particles: Relative importance of mineral and biological components, American Institute of Physics Conference Series, 1527, 871–874, doi:10.1063/1.4803409, 2013.

Ovchinnikov, M., Korolev, A., and Fan, J.: Effects of ice number concentration on dynamics of a shallow mixed-phase stratiform cloud, Journal of Geophysical Research (Atmospheres), 116, D00T06, doi:10.1029/2011JD015888, 2011.

Palm, S. P., Strey, S. T., Spinhirne, J., and Markus, T.: Influence of Arctic sea ice extent on polar cloud fraction and vertical structure and implications for regional climate, Journal of Geophysical Research (Atmospheres), 115, D21209, doi:10.1029/2010JD013900, 2010.

Parkinson, C. L. and Comiso, J. C.: On the 2012 record low Arctic sea ice cover: Combined impact of preconditioning and an August storm, Geophysics Research Letters, 40, 1356–1361, doi:10.1002/grl.50349, 2013.

Passarelli Jr, R. E.: An Approximate Analytical Model of the Vapor Deposition and Aggregation Growth of Snowflakes, Journal of Atmospheric Sciences, 35, 118–124, doi:10.1175/1520-0469(1978)035<0118:AAAMOT>2.0.CO;2, 1978.

Perovich, D. K., Richter-Menge, J. A., Jones, K. F., and Light, B.: Sunlight, water, and ice: Extreme Arctic sea ice melt during the summer of 2007, Geophysics Research Letters, 35, L11501, doi:10.1029/2008GL034007, 2008.

Pinto, J. O.: Autumnal Mixed-Phase Cloudy Boundary Layers in the Arctic, Journal of Atmospheric Sciences, 55, 2016–2038, doi:10.1175/1520-0469(1998)055<2016:AMPCBL>2.0.CO;2, 1998.

Pratt, K. A. and Prather, K. A.: Aircraft measurements of vertical profiles of aerosol mixing states, Journal of Geophysical Research (Atmospheres), 115, D11305, doi:10.1029/2009JD013150, 2010.

Pratt, K. A., DeMott, P. J., French, J. R., Wang, Z., Westphal, D. L., Heymsfield, A. J.,

Twohy, C. H., Prenni, A. J., and Prather, K. A.: In situ detection of biological particles in cloud ice-crystals, Nature Geoscience, 2, 398–401, doi:10.1038/ngeo521, 2009.

Prenni, A. J., Harrington, J. Y., Tjernström, M., DeMott, P. J., Avramov, A., Long, C. N., Kreidenweis, S. M., Olsson, P. Q., and Verlinde, J.: Can Ice-Nucleating Aerosols Affect Arctic Seasonal Climate?, Bulletin of the American Meteorological Society, 88, 541–550, doi:10.1175/BAMS-88-4-541, 2007.

Primm, K. M., Schill, G. P., Veghte, D. P., Freedman, M. A., and Tolbert, M. A.: Depositional ice nucleation on NX illite and mixtures of NX illite with organic acids, Journal of Atmospheric Chemistry, pp. 1–15, doi:10.1007/s10874-016-9340-x, 2016.

Pruppacher, H. R. and Klett, J. D.: Microphysics of Clouds and Precipitation, 2nd Edn., Kluwer Academic Publishers, Dordrecht, the Netherlands, 1997.

Quennehen, B., Schwarzenboeck, A., Matsuki, A., Burkhart, J. F., Stohl, A., Ancellet, G., and Law, K. S.: Anthropogenic and forest fire pollution aerosol transported to the Arctic: observations from the POLARCAT-France spring campaign, Atmospheric Chemistry and Physics, 12, 6437–6454, doi:10.5194/acp-12-6437-2012, 2012.

Rangno, A. L. and Hobbs, P. V.: Ice particles in stratiform clouds in the Arctic and possible mechanisms for the production of high ice concentrations, Journal of Geophysical Research (Atmospheres), 106(D14), 15 065–15 075, doi:10.1029/2000JD900286, 2001.

Rogers, R. R. and Yau, M. K.: A Short Course in Cloud Physics (Third Edition), Butterworth Heinemann, 1989.

Rosenberg, P. D., Dean, A. R., Williams, P. I., Dorsey, J. R., Minikin, A., Pickering, M. A., and Petzold, A.: Particle sizing calibration with refractive index correction for light scattering optical particle counters and impacts upon PCASP and CDP data collected during the Fennec campaign, Atmospheric Measurement Techniques, 5, 1147–1163, doi:10.5194/amt-5-1147-2012, 2012.

Savre, J. and Ekman, A. M. L.: Large-eddy simulation of three mixed-phase cloud events during ISDAC: Conditions for persistent heterogeneous ice formation, Journal of Geophysical Research (Atmospheres), 120, 7699–7725, doi: 10.1002/2014JD023006, 2015.

Schnell, R. C. and Vali, G.: Biogenic Ice Nuclei: Part I. Terrestrial and Marine Sources, Journal of Atmospheric Sciences, 33, 1554–1564, doi:10.1175/1520-0469(1976)033<1554:BINPIT>2.0.CO;2, 1976.

Schwarzenboeck, A., Shcherbakov, V., Lefevre, R., Gayet, J.-F., Pointin, Y., and Duroure, C.: Indications for stellar-crystal fragmentation in Arctic clouds, Atmospheric Research, 92, 220–228, doi:10.1016/j.atmosres.2008.10.002, 2009.

Seinfeld, J. H. and Pandis, S. N.: Atmospheric Chemistry and Physics: From Air Pollution to Climate Change, John Wiley and Sons, 1998.

Seinfeld, J. H., Bretherton, C., Carslaw, K. S., Coe, H., DeMott, P. J., Dunlea, E. J., Feingold, G., Ghan, S., Guenther, A. B., Kahn, R., Kraucunas, I., Kreidenweis, S. M., Molina, M. J., Nenes, A., Penner, J. E., Prather, K. A., Ramanathan, V., Ramaswamy, V., Rasch, P. J., Ravishankara, A. R., Rosenfeld, D., Stephens, G., and Wood, R.: Improving our fundamental understanding of the role of aerosol-cloud interactions in the climate system, Proceedings of the National Academy of Sciences, 113, 5781–5790, doi:10.1073/pnas.1514043113, 2016.

Serreze, M. C. and Barry, R. G.: Processes and impacts of Arctic amplification: A research synthesis, Global and Planetary Change, 77, 85–96, doi: 10.1016/j.gloplacha.2011.03.004, 2011.

Shaw, G. E.: The Arctic Haze Phenomenon, Bulletin of the American Meteorological Society, 76, 2403–2413, doi:10.1175/1520-0477(1995)076<2403:TAHP>2.0.CO;2, 1995.

Shupe, M. D. and Intrieri, J. M.: Cloud Radiative Forcing of the Arctic Surface: The Influence of Cloud Properties, Surface Albedo and Solar Zenith Angle, Journal of Climate, 17, 616–628, doi:10.1175/1520-0442(2004)017<0616:CRFOTA>2.0.CO;2, 2003.

Shupe, M. D., Matrosov, S. Y., and Uttal, T.: Arctic Mixed-Phase Cloud Properties Derived from Surface-Based Sensors at SHEBA., Journal of Atmospheric Sciences, 63, 697–711, doi:10.1175/JAS3659.1, 2006.

Shupe, M. D., Daniel, J. S., de Boer, G., Eloranta, E. W., Kollias, P., Long, C. N., Luke, E. P., Turner, D. D., and Verlinde, J.: A Focus On Mixed-Phase Clouds, Bulletin of the American Meteorological Society, 89, 1549–1562, doi:10.1175/2008BAMS2378.1, 2008.

Shupe, M. D., Walden, V. P., Eloranta, E., Uttal, T., Campbell, J. R., Starkweather, S. M., and Shiobara, M.: Clouds at Arctic Atmospheric Observatories. Part I: Occurrence and Macrophysical Properties, Journal of Applied Meteorology and Climatology, 50, 626–644, doi:10.1175/2010JAMC2467.1, 2011.

Solomon, A., Shupe, M. D., Persson, P. O. G., and Morrison, H.: Moisture and dynamical interactions maintaining decoupled Arctic mixed-phase stratocumulus in the presence of a humidity inversion, Atmospheric Chemistry and Physics, 11, 10 127–10 148, doi:10.5194/acp-11-10127-2011, 2011.

Solomon, A., Feingold, G., and Shupe, M. D.: The role of ice nuclei recycling in the maintenance of cloud ice in Arctic mixed-phase stratocumulus, Atmospheric Chemistry and Physics, 15, 10 631–10 643, doi:10.5194/acp-15-10631-2015, 2015.

Sotiropoulou, G., Sedlar, J., Tjernström, M., Shupe, M. D., Brooks, I. M., and Persson, P. O. G.: The thermodynamic structure of summer Arctic stratocumulus and the dynamic coupling to the surface, Atmospheric Chemistry and Physics, 14, 12 573–12 592, doi:10.5194/acp-14-12573-2014, 2014.

Staniforth, A., White, A., Wood, N., Thuburn, J., Zerroukat, M., Cordero, E., and Davies, T.: Joy of UM 6.3 Model Formulation, Unified Model Documentation Paper, No. 15, 2006.

Stocker, T., Qin, D., Plattner, G.-K., Alexander, L., Allen, S., Bindoff, N., Bréon, F.-M., Church, J., Cubasch, U., Emori, S., Forster, P., Friedlingstein, P., Gillett, N., Gregory, J., Hartmann, D., Jansen, E., Kirtman, B., Knutti, R., Krishna Kumar, K., Lemke, P., Marotzke, J., Masson-Delmotte, V., Meehl, G., Mokhov, I., Piao, S.,

Ramaswamy, V., Randall, D., Rhein, M., Rojas, M., Sabine, C., Shindell, D., Talley, L., Vaughan, D., and Xie, S.-P.: Technical Summary, in: Climate Change 2013 - The Physical Science Basis: Working Group I Contribution to the Fifth Assessment Report of the Intergovernmental Panel on Climate Change, edited by: Stocker, T.F., D. Qin, G.-K. Plattner, M. Tignor, S.K. Allen, J. Boschung, A. Nauels, Y. Xia, V. Bex and P.M. Midgley, pp. 31—-116, Cambridge University Press, Cambridge, United Kingdom and New York, NY, USA, doi:10.1017/CBO9781107415324.005, 2014.

Stroeve, J. C., Serreze, M. C., Fetterer, F., Arbetter, T., Meier, W., Maslanik, J., and Knowles, K.: Tracking the Arctic's shrinking ice cover: Another extreme September minimum in 2004, Geophysics Research Letters, 32, L04501, doi: 10.1029/2004GL021810, 2005.

Ström, J., Umegård, J., Tørseth, K., Tunved, P., Hansson, H.-C., Holmén, K., Wismann, V., Herber, A., and König-Langlo, G.: One year of particle size distribution and aerosol chemical composition measurements at the Zeppelin Station, Svalbard, March 2000-March 2001, Physics and Chemistry of the Earth, 28, 1181–1190, doi:10.1016/j.pce.2003.08.058, 2003.

Taylor, J. W., Choularton, T. W., Blyth, A. M., Liu, Z., Bower, K. N., Crosier, J., Gallagher, M. W., Williams, P. I., Dorsey, J. R., Flynn, M. J., Bennett, L. J., Huang, Y., French, J., Korolev, A., and Brown, P. R. A.: Observations of cloud microphysics and ice formation during COPE, Atmospheric Chemistry and Physics, 16, 799–826, doi:10.5194/acp-16-799-2016, 2016.

Tjernström, M., Leck, C., Persson, P. O. G., Jensen, M. L., Oncley, S. P., and Targino, A.: The Summertime Arctic Atmosphere: Meteorological Measurements during the Arctic Ocean Experiment 2001, Bulletin of the American Meteorological Society, 85, 1305–1321, doi:10.1175/BAMS-85-9-1305, 2004.

Tjernström, M., Žagar, M., Svensson, G., Cassano, J. J., Pfeifer, S., Rinke, A., Wyser, K., Dethloff, K., Jones, C., Semmler, T., and Shaw, M.: Modelling the Arctic Boundary Layer: An Evaluation of Six Arcmip Regional-Scale Models using

Data from the Sheba Project, Boundary-Layer Meteorology, 117, 337–381, doi: 10.1007/s10546-004-7954-z, 2005.

Tjernström, M., Leck, C., Birch, C. E., Bottenheim, J. W., Brooks, B. J., Brooks, I. M., Bäcklin, L., Chang, R. Y.-W., de Leeuw, G., Di Liberto, L., de la Rosa, S., Granath, E., Graus, M., Hansel, A., Heintzenberg, J., Held, A., Hind, A., Johnston, P., Knulst, J., Martin, M., Matrai, P. A., Mauritsen, T., Müller, M., Norris, S. J., Orellana, M. V., Orsini, D. A., Paatero, J., Persson, P. O. G., Gao, Q., Rauschenberg, C., Ristovski, Z., Sedlar, J., Shupe, M. D., Sierau, B., Sirevaag, A., Sjogren, S., Stetzer, O., Swietlicki, E., Szczodrak, M., Vaattovaara, P., Wahlberg, N., Westberg, M., and Wheeler, C. R.: The Arctic Summer Cloud Ocean Study (ASCOS): overview and experimental design, Atmospheric Chemistry and Physics, 14, 2823–2869, doi:10.5194/acp-14-2823-2014, 2014.

Tobo, Y., Prenni, A. J., DeMott, P. J., Huffman, J. A., McCluskey, C. S., Tian, G., Pöhlker, C., Pöschl, U., and Kreidenweis, S. M.: Biological aerosol particles as a key determinant of ice nuclei populations in a forest ecosystem, Journal of Geophysical Research (Atmospheres), 118, 10 100–10 110, doi:10.1002/jgrd.50801, 2013.

Tunved, P., Ström, J., and Krejci, R.: Arctic aerosol life cycle: linking aerosol size distributions observed between 2000 and 2010 with air mass transport and precipitation at Zeppelin station, Ny-Ålesund, Svalbard, Atmospheric Chemistry and Physics, 13, 3643–3660, doi:10.5194/acp-13-3643-2013, 2013.

Twohy, C. H., McMeeking, G. R., DeMott, P. J., McCluskey, C. S., Hill, T. C. J., Burrows, S. M., Kulkarni, G. R., Tanarhte, M., Kafle, D. N., and Toohey, D. W.: Abundance of fluorescent biological aerosol particles at temperatures conducive to the formation of mixed-phase and cirrus clouds, Atmospheric Chemistry and Physics, 16, 8205–8225, doi:10.5194/acp-16-8205-2016, 2016.

Twomey, S.: Pollution and the planetary albedo, Atmospheric Environment (1967), 8, 1251–1256, doi:10.1016/0004-6981(74)90004-3, 1974.

van Tricht, K., Lhermitte, S., Lenaerts, J. T. M., Gorodetskaya, I. V., L'Ecuyer, T. S., Noël, B., van den Broeke, M. R., Turner, D. D., and van Lipzig, N. P. M.:

Clouds enhance Greenland ice sheet meltwater runoff, Nature Communications, 7, 10266, doi:10.1038/ncomms10266, 2016.

Verlinde, J., Harrington, J. Y., McFarquhar, G. M., Yannuzzi, V. T., Avramov, A., Greenberg, S., Johnson, N., Zhang, G., Poellot, M. R., Mather, J. H., Turner, D. D., Eloranta, E. W., Zak, B. D., Prenni, A. J., Daniel, J. S., Kok, G. L., Tobin, D. C., Holz, R., Sassen, K., Spangenberg, D., Minnis, P., Tooman, T. P., Ivey, M. D., Richardson, S. J., Bahrmann, C. P., Shupe, M., DeMott, P. J., Heymsfield, A. J., and Schofield, R.: The Mixed-Phase Arctic Cloud Experiment, Bulletin of the American Meteorological Society, 88, 205–221, doi:10.1175/BAMS-88-2-205, 2007.

Vihma, T., Pirazzini, R., Fer, I., Renfrew, I. A., Sedlar, J., Tjernström, M., Lüpkes, C., Nygård, T., Notz, D., Weiss, J., Marsan, D., Cheng, B., Birnbaum, G., Gerland, S., Chechin, D., and Gascard, J. C.: Advances in understanding and parameterization of small-scale physical processes in the marine Arctic climate system: a review, Atmospheric Chemistry and Physics, 14, 9403–9450, doi:10.5194/acp-14-9403-2014, 2014.

Walsh, J. E., Chapman, W. L., and Portis, D. H.: Arctic Cloud Fraction and Radiative Fluxes in Atmospheric Reanalyses, Journal of Climate, 22, 2316–2334, doi:10.1175/2008JCLI2213.1, 2009.

Wang, Q., Jacob, D. J., Fisher, J. A., Mao, J., Leibensperger, E. M., Carouge, C. C., Le Sager, P., Kondo, Y., Jimenez, J. L., Cubison, M. J., and Doherty, S. J.: Sources of carbonaceous aerosols and deposited black carbon in the Arctic in winter-spring: implications for radiative forcing, Atmospheric Chemistry and Physics, 11, 12 453–12 473, doi:10.5194/acp-11-12453-2011, 2011.

Wegener, A.: Thermodynamik der Atmosphäre, J. A. Barth, Leipzig, Germany, 1911.

Weinbruch, S., Wiesemann, D., Ebert, M., Schütze, K., Kallenborn, R., and Ström, J.: Chemical composition and sources of aerosol particles at Zeppelin Mountain (Ny Ålesund, Svalbard): An electron microscopy study, Atmospheric Environment, 49, 142–150, doi:10.1016/j.atmosenv.2011.12.008, 2012.

Westbrook, C. D. and Illingworth, A. J.: Evidence that ice forms primarily in supercooled liquid clouds at temperatures $>$ -27°C, Geophysics Research Letters, 38, L14808, doi:10.1029/2011GL048021, 2011.

Westbrook, C. D. and Illingworth, A. J.: The formation of ice in a long-lived supercooled layer cloud, Quarterly Journal of the Royal Meteorological Society, 139, 2209–2221, doi:10.1002/qj.2096, 2013.

Wilson, T. W., Ladino, L. A., Alpert, P. A., Breckels, M. N., Brooks, I. M., Browse, J., Burrows, S. M., Carslaw, K. S., Huffman, J. A., Judd, C., Kilthau, W. P., Mason, R. H., McFiggans, G., Miller, L. A., Nájera, J. J., Polishchuk, E., Rae, S., Schiller, C. L., Si, M., Temprado, J. V., Whale, T. F., Wong, J. P. S., Wurl, O., Yakobi-Hancock, J. D., Abbatt, J. P. D., Aller, J. Y., Bertram, A. K., Knopf, D. A., and Murray, B. J.: A marine biogenic source of atmospheric ice-nucleating particles, Nature, 525, 234–238, doi:10.1038/nature14986, 2015.

Wu, D. L. and Lee, J. N.: Arctic low cloud changes as observed by MISR and CALIOP: Implication for the enhanced autumnal warming and sea ice loss, Journal of Geophysical Research (Atmospheres), 117, D07107, doi:10.1029/2011JD017050, 2012.

Yakobi-Hancock, J. D., Ladino, L. A., and Abbatt, J. P. D.: Feldspar minerals as efficient deposition ice nuclei, Atmospheric Chemistry and Physics, 13, 11 175–11 185, doi:10.5194/acp-13-11175-2013, 2013.

Yamaguchi, N., Ichijo, T., Sakotani, A., Baba, T., and Nasu, M.: Global Dispersion of Bacterial Cells on Asian Dust, Nature: Scientific Reports, 2, 525, doi:10.1038/srep00525, 2012.

Yamanouchi, T., Treffeisen, R., Herber, A., Shiobara, M., Yamagata, S., Hara, K., Sato, K., Yabuki, M., Tomikawa, Y., Rinke, A., Neuber, R., Schumachter, R., Kriews, M., Ström, J., Schrems, O., and Gernandt, H.: Arctic Study of Tropospheric Aerosol and Radiation (ASTAR) 2000: Arctic haze case study, Tellus Series B, 57, 141–152, doi:10.1111/j.1600-0889.2005.00140.x, 2005.

Zimmermann, F., Weinbruch, S., Schütz, L., Hofmann, H., Ebert, M., Kandler, K., and Worringen, A.: Ice nucleation properties of the most abundant mineral dust phases, Journal of Geophysical Research (Atmospheres), 113, D23 204, doi: 10.1029/2008JD010655, 2008.

A Cited campaigns and measurement sites

Several campaigns from various geographical regions are mentioned for comparison with observations made during ACCACIA. For clarity, key aspects from each campaign are summarised in Table A.1. Geographical locations of cited permanent measurement stations are also illustrated in Fig. A.1.

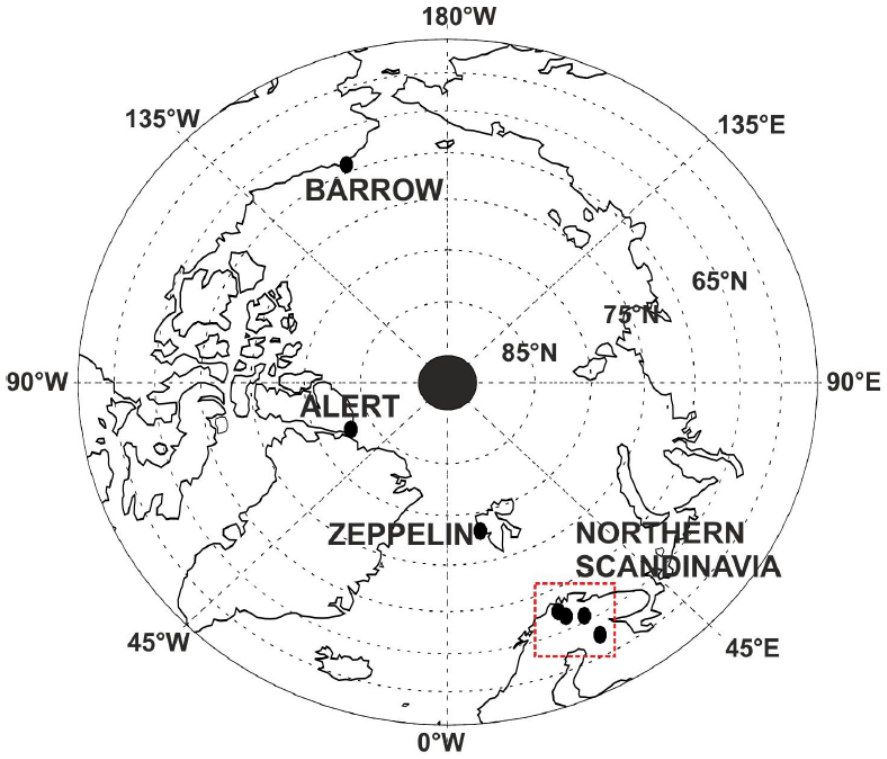

Figure A.1: Browse et al. (2012) Fig. 1: Locations of three of the permanent Arctic measurement stations often referred to in cited studies. Zeppelin, Svalbard (11.9°E, 78.9°N); Alert, Canada (62.3°W, 82.5°N); and Barrow, Alaska (156.8°W, 71.2°N) are shown. Permanent stations in Northern Scandinavia are also indicated; however, measurements from these locations are not referred to in the studies contained in this thesis.

Table A.1: List of observational campaigns mentioned for comparison throughout thesis. Key aspects of these campaigns – for example, seasonality and observational goals – are summarised. Approximate geographical location is listed for each campaign. Example citations are not exhaustive and other articles are available using data from these campaigns. **BL:** boundary layer, and **Spr/Sum/Aut/Win:** spring, summer, autumn, and winter respectively.

Abbreviation	Full Name	Season & Year	Location	Observational aims	Methods	Example source(s)
AOE-2001	Arctic Ocean Experiment 2001	Sum 2001	Svalbard	Interdisciplinary, BL structure	Ship-based, icebreaker *Oden*	Tjernström et al. (2004)
ARCTAS	Arctic Research of the Composition of the Troposphere from Aircraft and Satellites	Spr & Sum 2008	Alaska/ western Canada	Aerosol composition	Aircraft/ satellite	Jacob et al. (2010)
ASCOS	Arctic Summer Cloud Ocean Study	Sum 2008	Svalbard	Cloud BL structure	Ship-based icebreaker *Oden*	Tjernström et al. (2014)
ASTAR-2000	Arctic Study of Tropospheric Aerosol and Radiation	Spr 2000	Svalbard	Aerosol	In situ, aircraft	Hara et al. (2003), Yamanouchi et al. (2005)
ASTAR-2004	Arctic Study of Tropospheric Aerosol and Radiation	Spr-Sum 2004	Svalbard	Cloud microphysics	In situ, aircraft	Gayet et al. (2009)
ISDAC	Indirect and Semi-Direct Aerosol Campaign	Spr 2008	Barrow, Alaska	Aerosol-cloud interactions	In situ, aircraft	McFarquhar et al. (2011)
M-PACE	Mixed-Phase Arctic Cloud Experiment	Aut 2004	Barrow, Alaska	Cloud microphysics	In situ, aircraft	McFarquhar et al. (2007), Verlinde et al. (2007)
SHEBA	Surface Heat Budget of the Arctic Ocean	Aut 1997-1998	Barrow, Alaska (Beaufort Sea)	Radiative interactions, clouds	Ground-based, temporary station in sea ice	Intrieri et al. (2002), Shupe et al. (2006)

B Chapter 4: Supplementary Material

Supplementary material for the journal article titled ”Size-segregated compositional analysis of aerosol particles collected in the European Arctic during the ACCACIA campaign” is included as follows.

Table S1: Classification scheme adopted in this study. Similarly to Kandler et al. (2011), "All" stands for the sum of Na+Mg+Al+Si+P+S+Cl+K+Ca+Ti+Cr+Fe+Ni+Cu+Zn and square brackets indicate an interval of values. "All elements" represents each weight percentage unweighted. Kr2005: Krejci et al. (2005), K2007: Kandler et al. (2007), B2008: Behrenfeldt et al. (2008), G2010: Geng et al. (2010), H2010: Hand et al. (2010), K2011: Kandler et al. (2011). Source in bold: Direct copy of their criteria. Source in italics: Based upon their criteria.

Particle Class	Classification Criteria	Source
Carbonaceous	All elements/All<0.2, C+O>0.92 **OR** C+O>0.9, All elements/All<0.2 **AND** Mg/All≥0.1 **OR** Na/All≥0.1 **OR** S/All≥0.1	*G2010*
	Criteria for secondary Na-rich and Ammonium Sulphate	**K2011**
Biogenic	Criteria for biogenic	**K2011**
	C+O>0.9, Si/Cl0.2, Na/Cl0.3, Na/Si0.3 **AND** K/All≥0.2 **OR** P/All≥0.2 **OR** Cl/All≥0.2 **OR** (Ca+K)/All≥0.3 **OR** (Na+P+K)/All ≥ **OR** (Na+Mg+Zn)/All≥0.3	*Kr2005, G2010*
Sulphates	Criteria for NaS sulphates	**K2011**
Gypsum	(Ca+S)/All>0.5, Ca/S=[0.25;4], Si/Ca<0.5	**K2007**
	Criteria for Ca sulphates	**K2011**
Sulphates	S/All>0.4, Si/S<0.5, S>All elements	*K2007, H2010*
	Criteria for CaNaS	**K2011**
Ca-Rich	Ca/All>0.5, Si/Ca<0.5, Al/Ca<0.5, Ca>All elements	*H2010*
	Criteria for Ca- and CaMg-carbonates	**K2011**
	(Ca+Mg)/All>0.5, Mg/Ca=[0.33;3], Si/Ca<0.5, S/Ca<0.25, P/Ca<0.15	**K2007**
Phosphates	Criteria for phosphates	**K2011**
Fresh Chlorides	(Na+Cl)/All>0.5, S/Na<0.375, S/Cl<0.5, Si/Cl<0.2, Fe/Cl<0.5	**K2007**
	OR Na/Cl=[0.5;1.5], S/Cl<0.5, Si/Cl<0.2, S/Na<0.375, Fe/Cl<0.5	*Kr2005, G2010*
	Criteria for NaCl, KCl and other chlorides	**K2011**
Aged Chlorides	(Na+Cl)>0.4, S/Cl<5, S/Na<5, Si/Cl<0.5	*Kr2005, B2008*
	OR Cl/All=[0.1;1.1], Si/All<0.0699, Al/All<0.0099, Na/Cl<2, Mg/Cl<2, P/Cl<0.2, K/Cl<2, Ca/Cl<2, Ti/Cl<0.1, Cr/Cl<0.1, Fe/Cl<0.1	*K2011*
	Criteria for mixClS	**K2011**
Sulphates	Cl/S<0.5, Si/S<0.5, Ti/S<0.2, Cr/S<0.2, Fe/S<0.5, Ni/S<0.2, Cu/S<0.2, Zn/S<0.2	*K2007*
	Criteria for other sulphates	**K2011**
Metallic	Criteria for Fe, Ti, Fe-Ti and Al oxides	**K2011**
	OR Fe/All>0.3, Si/Fe<0.2, Al/Fe<0.2, Cl/Fe<0.2, Ti/Fe<1.33, Mg/Fe<0.2	**K2007**, *H2010*
	OR Ti/All>0.3, Na/Ti<1, Mg/Ti<1, Al/Ti<0.2, Si/Ti<0.2, S/Ti<1, Fe/Ti<1	**K2007**, *H2010*
Silicates	Criteria for quartz, SiAl, SiAlK, SiAlNa, SiAlNaCa, SiAlNaK, SiAlCaFeMg, SiAlKFeMg, SiAlFeMg, SiMgFe, SiMg, SiCaTi	**K2011**
	OR Si/All>0.2, Na/Si<0.7, Mg/Si<1.33, Al/Si<1.33, K/Si<0.5, Ca/Si<0.5, Ti/Si<0.5, Fe/Si<0.5, (P+S+Cl)/All<0.2	**K2007**
	OR Si/All≥0.6, S/Si<0.2, Cl/Si<0.2	*H2010*
	OR Si/All≥0.2, S/Si<0.2, Cl/Si<0.2 **AND** (Al+Si)/All≥0.6 **OR** (Si+Fe)/All≥0.6 **OR** (Al+Si+Fe)/All≥0.5 **OR** (Al+Si+Na)/All≥0.5 **OR** (Al+Si+Mg)/All≥0.5 **OR** (Al+Si+K)/All≥0.5 **OR** (Al+Si+Ca)/All≥0.5 **OR** (Al+Si+Ti)/All≥0.5	
	OR Si/All≥0.5, S/Si<0.2, Cl/Si<0.2 **AND** Mg/All≥0.1 **OR** K/All≥0.1 **OR** Ca/All≥0.1	
	OR (Si+Al)/All≥0.5, S/Si<0.2, Cl/Si<0.2 **AND** Mg/All≥0.1 **OR** K/All≥0.1 **OR** Ca/All≥0.1	
	OR (Si+Fe)/All≥0.5, S/Si<0.2, Cl/Si<0.2 **AND** Mg/All≥0.1 **OR** K/All≥0.1 **OR** Ca/All≥0.1	
	OR (Si+Al+Fe)/All≥0.5, S/Si<0.2, Cl/Si<0.2 **AND** Mg/All≥0.1 **OR** K/All≥0.1 **OR** Ca/All≥0.1	
Mixed Silicates	(Na+S+Mg+Al+Si+K+Ca)/All>0.7, S/Si=[0.6;2] **OR** (Al+Si)/All≥0.6, S/Si>0.2	**K2007**, *H2010*
	OR Si/All≥0.2, Na/Si<0.7, Mg/Si<1.33, Al/Si<1.33, K/Si<0.5, Ca/Si<0.5, Ti/Si<0.5, Fe/Si<0.5, (P+Cl)/All<0.2, S/All>0.2	*K2007*
	OR Si/All≥0.1, S/Si>0.2 **AND** (S+Si)/All≥0.5 **OR** (S+Si+Al)/All≥0.5 **OR** (Si+S+Fe)/All≥0.5 **OR** (Si+S+Al+Fe)/All≥0.5	
	OR Si/All≥0.1, (Si+S)/All≥0.4, S/Si>0.2 **AND** Mg/All≥0.1 **OR** K/All≥0.1 **OR** Ca/All≥0.1	
	OR Si/All≥0.1, (Si+S+Al)/All≥0.4, S/Si>0.2 **AND** Mg/All≥0.1 **OR** K/All≥0.1 **OR** Ca/All≥0.1	
	OR Si/All≥0.1, (Si+S+Fe)/All≥0.4, S/Si>0.2 **AND** Mg/All≥0.1 **OR** K/All≥0.1 **OR** Ca/All≥0.1	
	OR Si/All≥0.1, (Si+S+Fe+Al)/All≥0.4, S/Si>0.2 **AND** Mg/All≥0.1 **OR** K/All≥0.1 **OR** Ca/All≥0.1	
	OR Fe/All>0.15, Si/Fe<1, Ti/Fe<1.33, (Fe+S)/All>0.4 **OR** Ti/All>0.3, Na/Ti<1, Mg/Ti<1, Al/Ti<1, Si/Ti<1, Fe/Si<1, (Ti+S)/All>0.4 **OR** (Ti+S)/All>0.5	*K2007*
	Criteria for mixSiS, mixAlSiS, mixNaClSi, mixNaClSiAl, mixCaSi, mixCaAlSi	**K2011**
Fresh Chlorides	(Na+Cl+Ca)/All≥0.5, Na/Cl=[0.2;1.1], Si/Cl<0.2, S/Cl<0.2	
Aged Chlorides	(Na+Cl+Ca+S)/All≥0.5, Na/Cl=[0.1;1.1], Si/Cl<0.2, S/Cl>0.2	
	OR Cl/All=[0.1;1.1], Si/Cl<0.1, S/Cl>0.2, Cr/Cl<1	
Metallic	(Fe+Ni+Cr+Cu+Zn)/All>0.5, Si/(Fe+Ni+Cu+Zn)<0.05 **OR** Zn/All=[0.2;1.1] **OR** Cu/All=[0.2;1.1] **OR** Cr/All=[0.2;1.1] **OR** Ni/All=[0.2;1.1] **OR** Cu¿All elements	
Silicates	Mg/All=[0.35;1.1], Si≥0.1	*K2011*
Phosphates	P/All=[0.1;1.1], P>All elements	
Silicates	Si/All=[0.1;1.1]	**K2011**
Metallic	Al/All=[0.1;1.1]	
Silicates	(Al+Si)/All=[0.2;1.1], Si≥0.1	
Fresh Chlorides	Cl/All=[0.1;1.1]	
Biomass Tracers	K/All=[0.25;1.1]	**K2011**
Ca-Rich	Ca/All=[0.2;1.1]	*K2011*
Other	Particles not classified by these criteria	

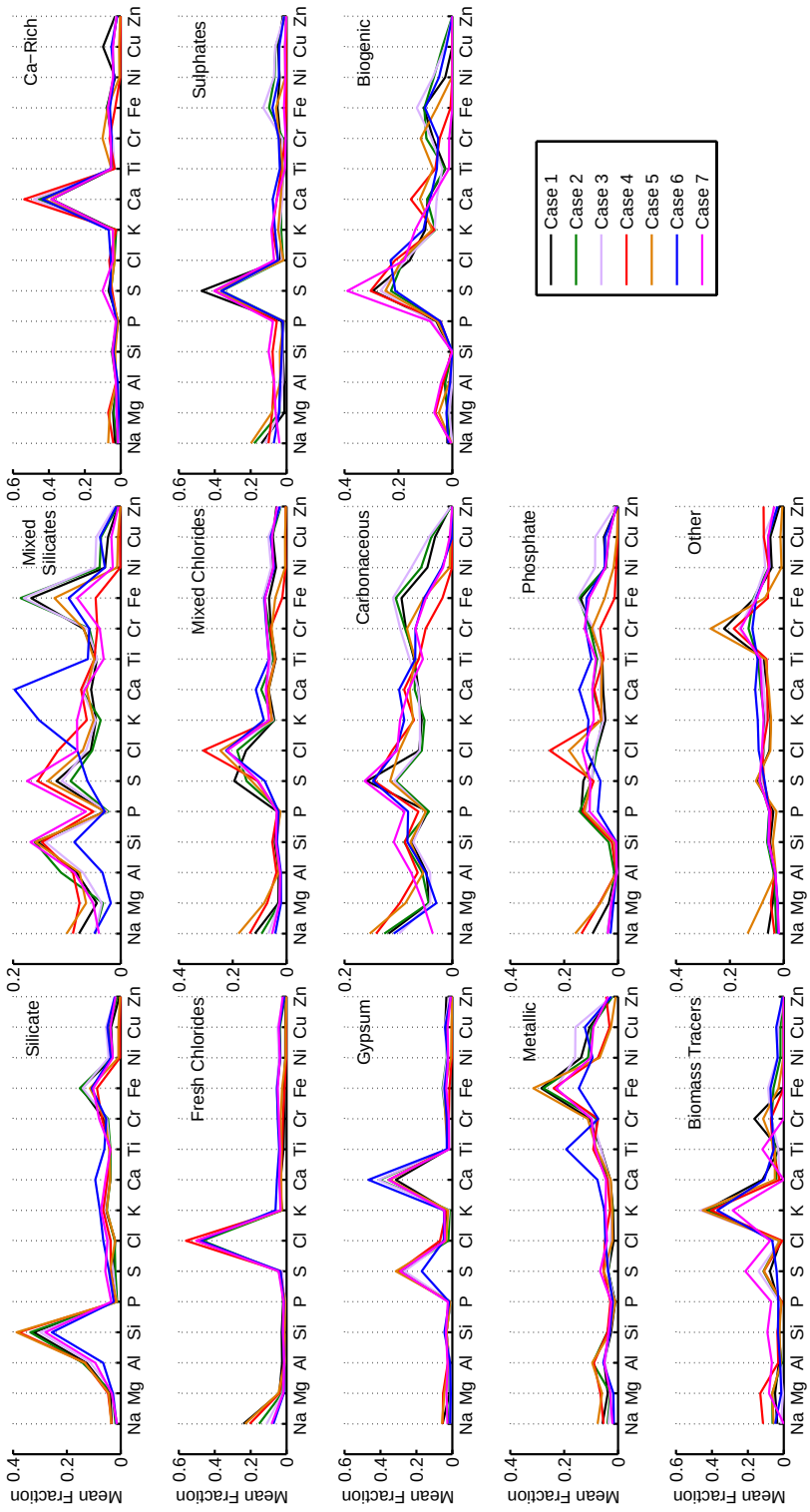

Figure S2: Mean elemental fractions of each particle category, normalised by the summed contributions from all elements except C and O. Variability is seen most clearly in the mixed categories, with consistency amongst the well-defined categories (e.g. Ca-rich)

C Chapter 5: Supplementary Material

Supplementary material for the journal article titled ”Observed microphysical changes in Arctic mixed-phase clouds when transitioning from sea ice to open ocean” is included as follows.

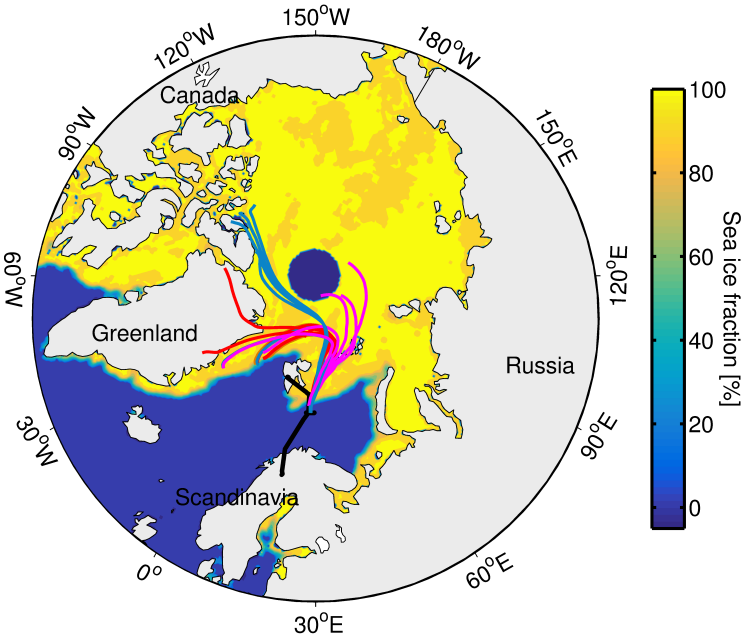

Figure S1: 3 day back trajectories for the B762 science period. Back trajectory analyses were calculated at 30 second intervals along each flight path using the National Oceanic and Atmospheric Administration HYbrid Single-Particle Lagrangian Integrated Trajectory (NOAA HYSPLIT 4.0) model (Draxler and Hess 1998), as described in Liu et al. (2015) and Young et al. (2016). GDAS reanalysis meteorology (Global Data Assimilation System; NOAA Air Resources Laboratory, Boulder, CO, USA) was used to simulate the 3D wind fields; however, turbulent motions are not resolved by the model and therefore some uncertainty is attached to the modelled trajectories (Fleming et al. 2012). A sample of trajectories modelled over the sea ice (red), MIZ (magenta) and ocean (blue) are shown. Sea ice fraction from the NSIDC is shown in colour, with the ocean and sea ice depicted in blue and yellow respectively. Sea ice data at the north pole are not included.

References

R. R. Draxler and G. D. Hess. An Overview of the HYSPLIT_4 Modelling System for Trajectories, Dispersion, and Deposition. Australian Meteorological Magazine, 47:295–308, 1998.

Z. L. Fleming, P. S. Monks, and A. J. Manning. Review: Untangling the influence of air-mass history in interpreting observed atmospheric composition. Atmospheric Research, 104:1–39, February 2012. doi: 10.1016/j.atmosres.2011.09.009.

D. Liu, B. Quennehen, E. Darbyshire, J. D. Allan, P. I. Williams, J. W. Taylor, S. J.-B. Bauguitte, M. J. Flynn, D. Lowe, M. W. Gallagher, K. N. Bower, T. W. Choularton, and H. Coe. The importance of asia as a source of black carbon to the european arctic during springtime 2013. Atmospheric Chemistry and Physics, 15(20):11537–11555, 2015. doi: 10.5194/acp-15-11537-2015.

G. Young, H. M. Jones, E. Darbyshire, K. J. Baustian, J. B. McQuaid, K. N. Bower, P. J. Connolly, M. W. Gallagher, and T. W. Choularton. Size-segregated compositional analysis of aerosol particles collected in the european arctic during the accacia campaign. Atmospheric Chemistry and Physics, 16(6):4063–4079, 2016. doi: 10.5194/acp-16-4063-2016.

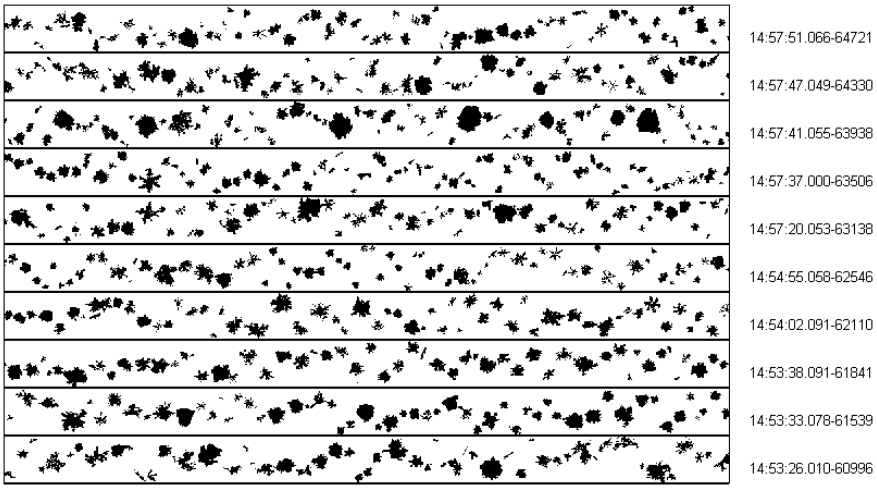

Figure S2: Example data from the CIP100 at cloud base over the ocean. Large dendrites are observed, with potential shattering events noted. Vertical width of image strip represents a size range of 6.4 mm.

D Chapter 6: Supplementary Material

Supplementary material for the journal article titled ”Microphysical sensitivity of coupled springtime Arctic stratocumulus to modelled primary ice over the ice pack, marginal ice, and ocean” is included as follows.

Supplementary Material

Bigg immersion-freezing and Meyers contact-freezing

The influence of immersion- and contact-freezing within the Morrison et al. (2005) microphysics scheme was tested to quantify their contribution to N_{ice}. Simulations with contact-freezing (Meyers et al. 1992 - hereafter, M92) and immersion-freezing (Bigg 1953 - hereafter, B53) switched either on or off are shown in Fig. S1. The addition of B53 and M92 produces a significantly larger ice crystal number concentration (up to $3\,L^{-1}$, $1.5\,L^{-1}$, and $10\,L^{-1}$ in cases 1, 2, and 3 respectively) than the mean observed ($0.47 \pm 0.86\,L^{-1}$, $0.35 \pm 0.20\,L^{-1}$, and $0.55 \pm 0.95\,L^{-1}$ respectively, Table 2).

Modelled ice number concentrations with and without B53 and M92 active are similar in case 1. Both representations cause glaciation, and liquid water is not modelled at any point during the simulations. No improvement can be seen in the liquid water mixing ratio when both the B53 and M92 nucleation mechanisms are disabled. Modelled ice number concentrations for case 2 peak at $\sim$1.5 L^{-1} and $\sim$0.8 L^{-1} with and without both B53 immersion- and M92 contact-freezing nucleation active. Both scenarios allow for liquid water to form in the cloud, with $\sim$0.2 g kg^{-1} modelled. When B53 and M92 are active in case 3, high ice number concentrations are rapidly simulated at approximately 12 h-14 h. This event causes the evaporation of all simulated liquid water, and the region of high ice number concentration dissipates back to the original sustained concentration of $\sim 2\,L^{-1}$ afterwards. This event is not simulated when B53 and M92 are disabled, suggesting these additional sources of ice number are the cause of this phenomenon.

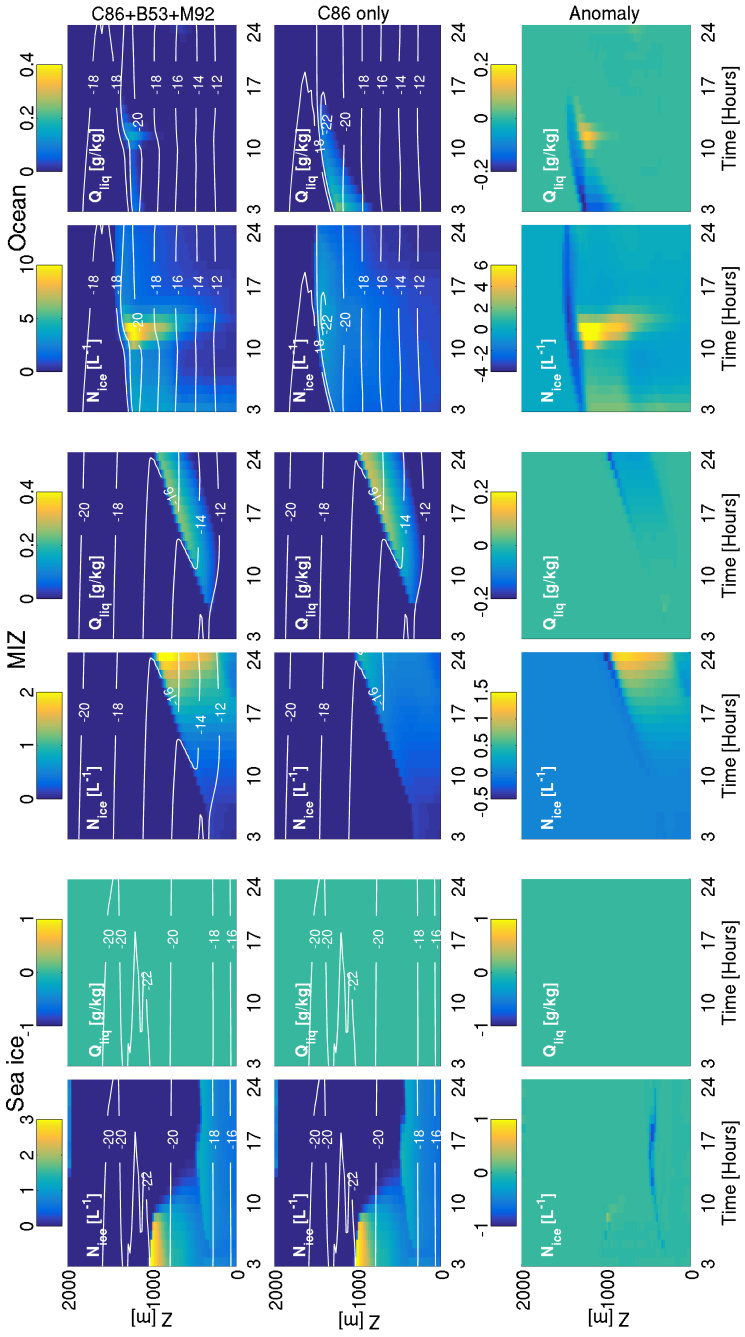

Figure S1. Simulated ice number concentrations (N_{ice}, **columns 1, 3, and 5**) and liquid water mixing ratios (Q_{liq}, **columns 2, 4, and 6**) using the Cooper (1986) parameterisation under default WRF conditions ($T < -8°C$, $S_w > 0.999$ or $S_i > 1.08$). **Top row:** B53, M92, and C86 active. **Middle row:** C86 deposition-condensation freezing only. **Bottom row:** Anomaly between simulations including B53 and M92 and those using C86 only. **Column 1-2:** Sea ice (case 1), **Column 3-4:** MIZ (case 2), **Column 5-6:** Ocean (case 3). Run length 24 hours. Temperature (°C) contours are overlaid in white. Note changing colour bars for each subfigure.

Supplementary figures

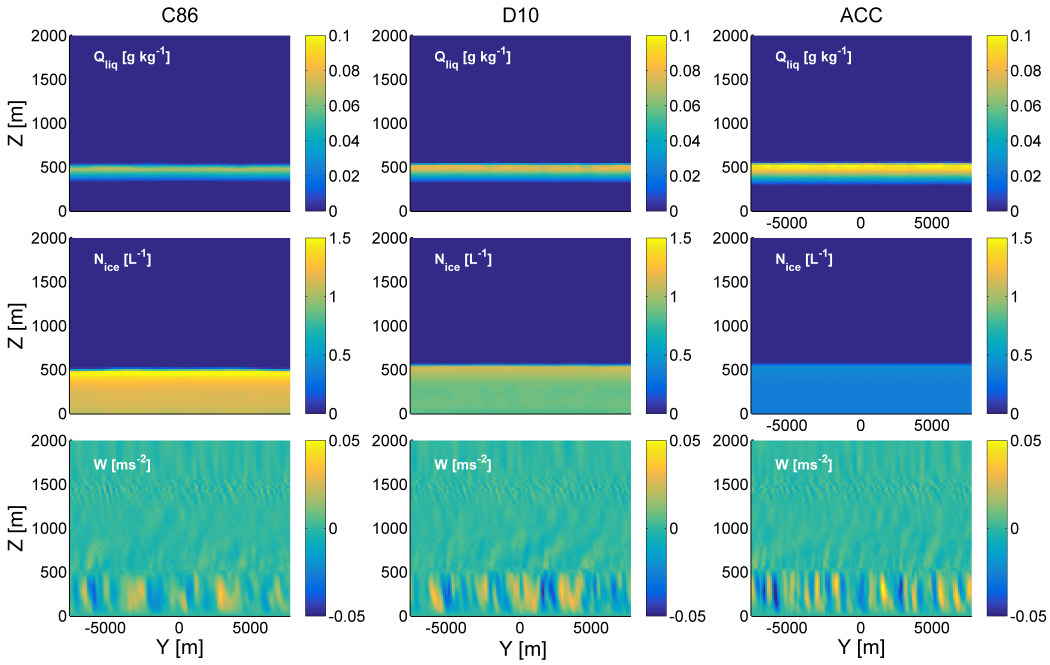

Figure S2. Z-Y slice of modelled Q_{liq} (**top row**), N_{ice} (**middle row**), and vertical velocity (**bottom row**) at 21 h over the sea ice (case 1). The N_{ice} and Q_{liq} fields are homogeneous, with liquid layer at cloud top and ice formation throughout. Enhanced turbulent activity, due to the comparatively larger liquid water content, is modelled with ACC. Note changing colour bars for each subfigure.

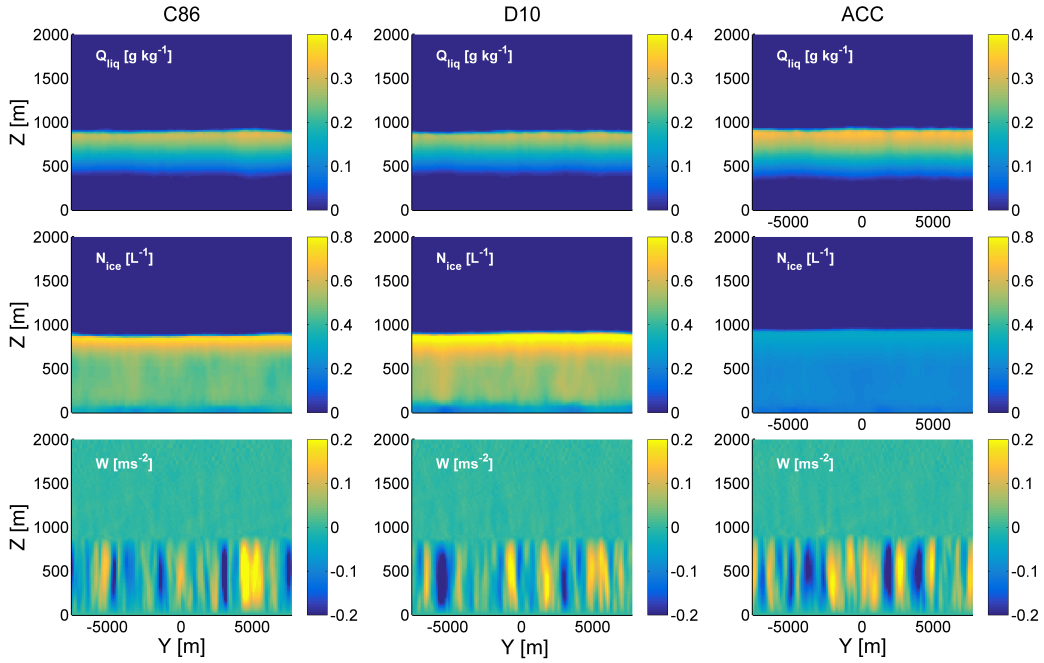

Figure S3. Z-Y slice of modelled Q_{liq} (**top row**), N_{ice} (**middle row**), and vertical velocity (**bottom row**) at 21 h over the MIZ (case 2). Significant turbulence is simulated within the cloudy layer (bottom row). With comparison to the sea ice case, the liquid layer at cloud top is more heterogeneous in all cases. This is particularly clear in the D10 simulations, where N_{ice} is enhanced in downdraughts. Note changing colour bars for each subfigure.

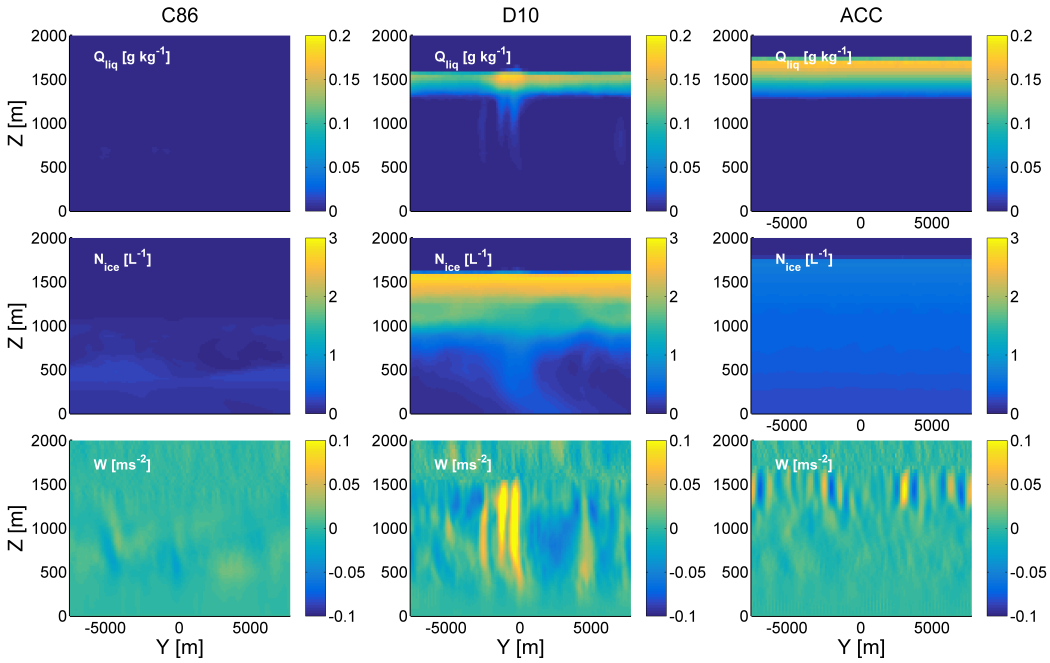

Figure S4. Z-Y slice of modelled Q_{liq} (**top row**), N_{ice} (**middle row**), and vertical velocity (**bottom row**) at 21 h over the ocean (case 3). Large updraught columns are simulated using D10, which correspond spatially with columns of high Q_{liq}. These updraughts are co-located with a precipitating (snow) region, evident from the N_{ice} figures (second row). C86 had dissipated by 21 h; therefore, little activity can be seen in this simulation. Similar to cases 1 and 2, ACC produces a homogeneous liquid layer at cloud top, with ice below.Note changing colour bars for each subfigure.

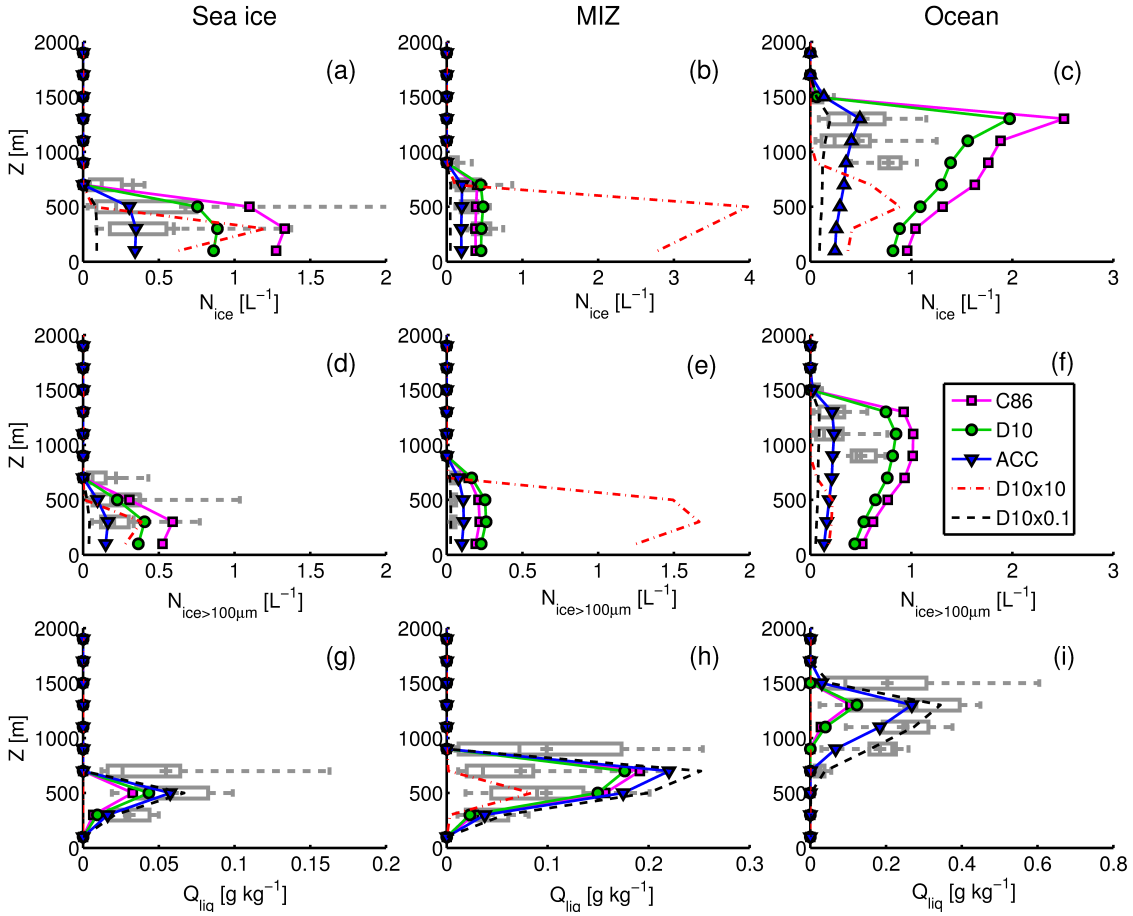

Figure S5. Observed N_{ice} (**top row**), $N_{ice>100\mu m}$ (**middle row**), and Q_{liq} (**bottom row**) for the sea ice (**column 1**), MIZ (**column 2**) and ocean (**column 3**) cases. Observations are shown as grey boxes. These boxes illustrate data similarly to those in Fig. 7. Modelled N_{ice}, $N_{ice>100\mu m}$, and Q_{liq} are overlaid from the C86 (magenta), D10 (green), ACC (blue), D10×10 (red), and D10×0.1 (black) simulations. Model time steps of 21 h, 17 h, and 7 h are again used for comparison with the sea ice, MIZ, and ocean observations respectively. Note changing colour bars for each subfigure.

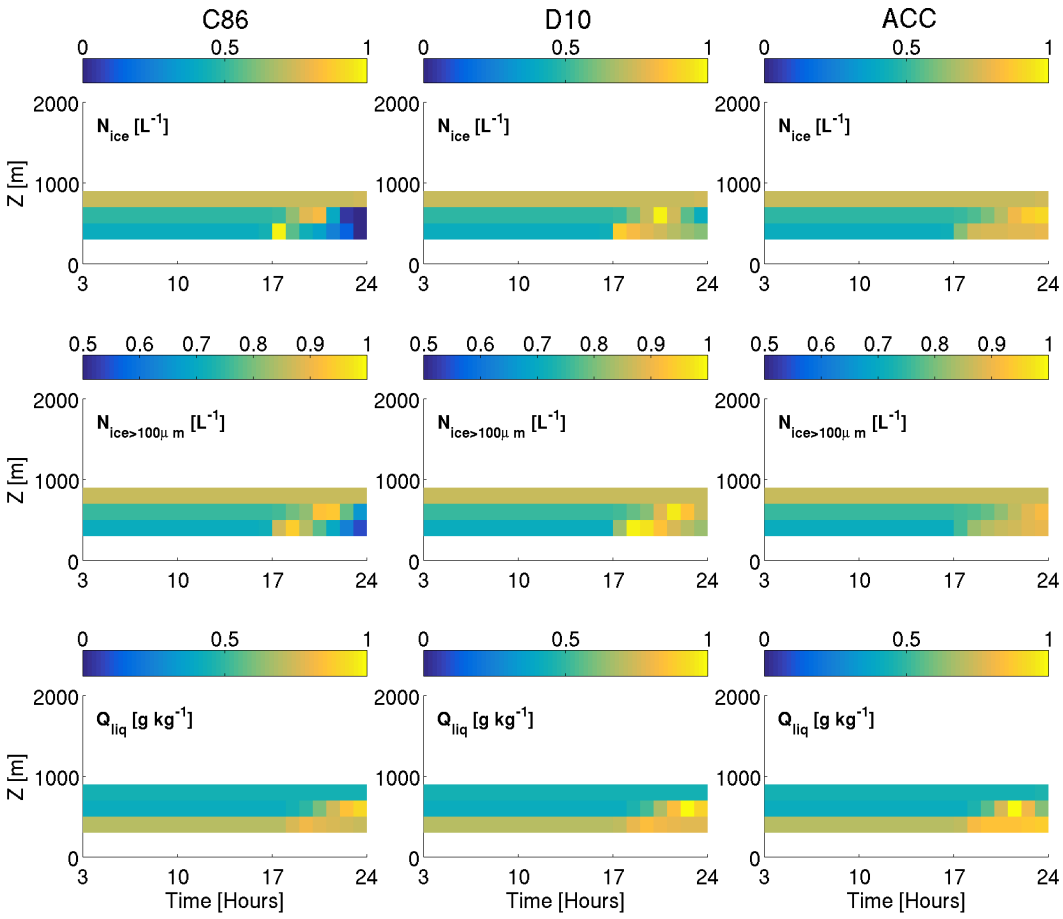

Figure S6. Residual comparison of modelled and observed N_{ice} (**top row**), $N_{ice>100\mu m}$ (**middle row**), and Q_{liq} (**bottom row**) in case 1 (sea ice) for each model time step. At each altitude bin, the mean observed quantity is subtracted from the mean modelled. The absolute magnitude of this fraction is then subtracted from 1. Therefore, better agreement between the mean observed and mean modelled values gives a larger fraction (with a maximum of 1). When two of the three parameterisations give good agreement with the N_{ice} observations at the same time step, that time step has been selected for comparison with the observations in Fig. 7. For the sea ice simulations, the chosen time step was 21 h. Note changing colour bars for each subfigure.

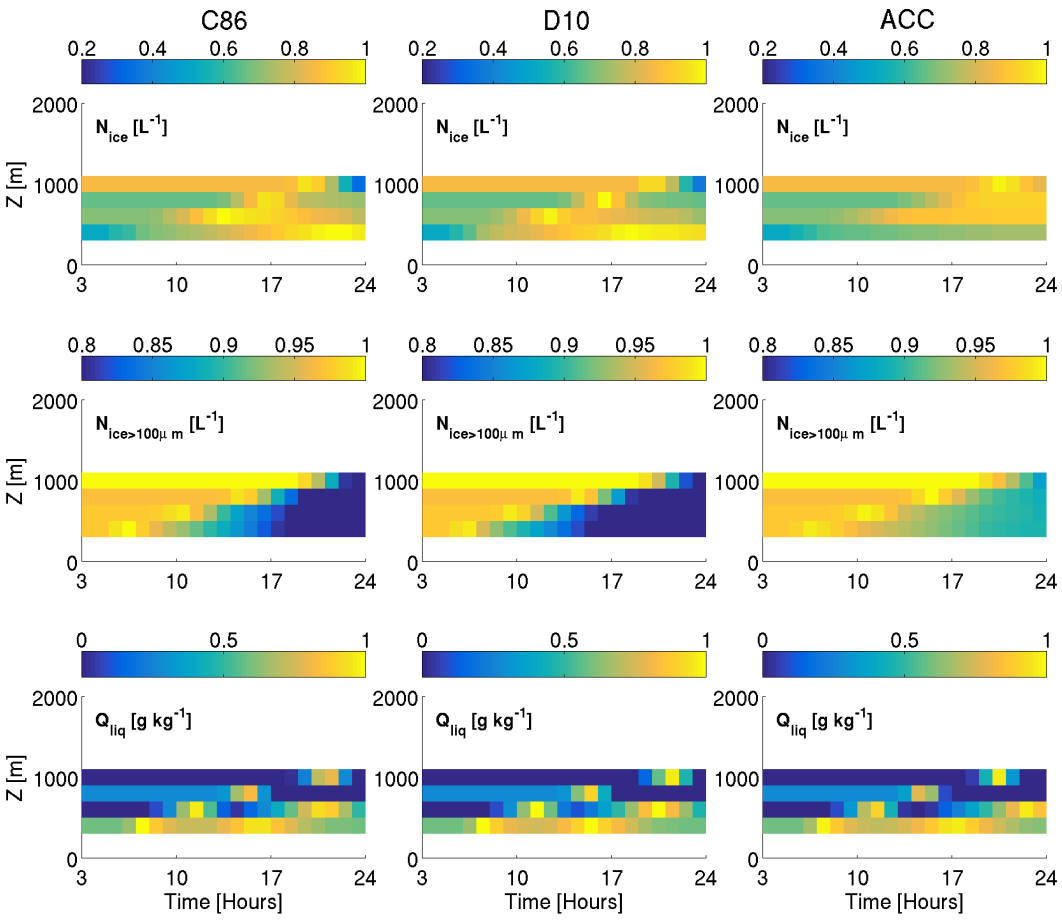

Figure S7. Residual comparison of modelled and observed N_{ice} (**top row**), $N_{ice>100\mu m}$ (**middle row**), and Q_{liq} (**bottom row**) in case 2 (MIZ) for each model time step. As with Fig. S6, better agreement with the mean observed value gives a larger fraction (with a maximum of 1). For the MIZ simulations, the chosen time step was 17 h. Note changing colour bars for each subfigure.

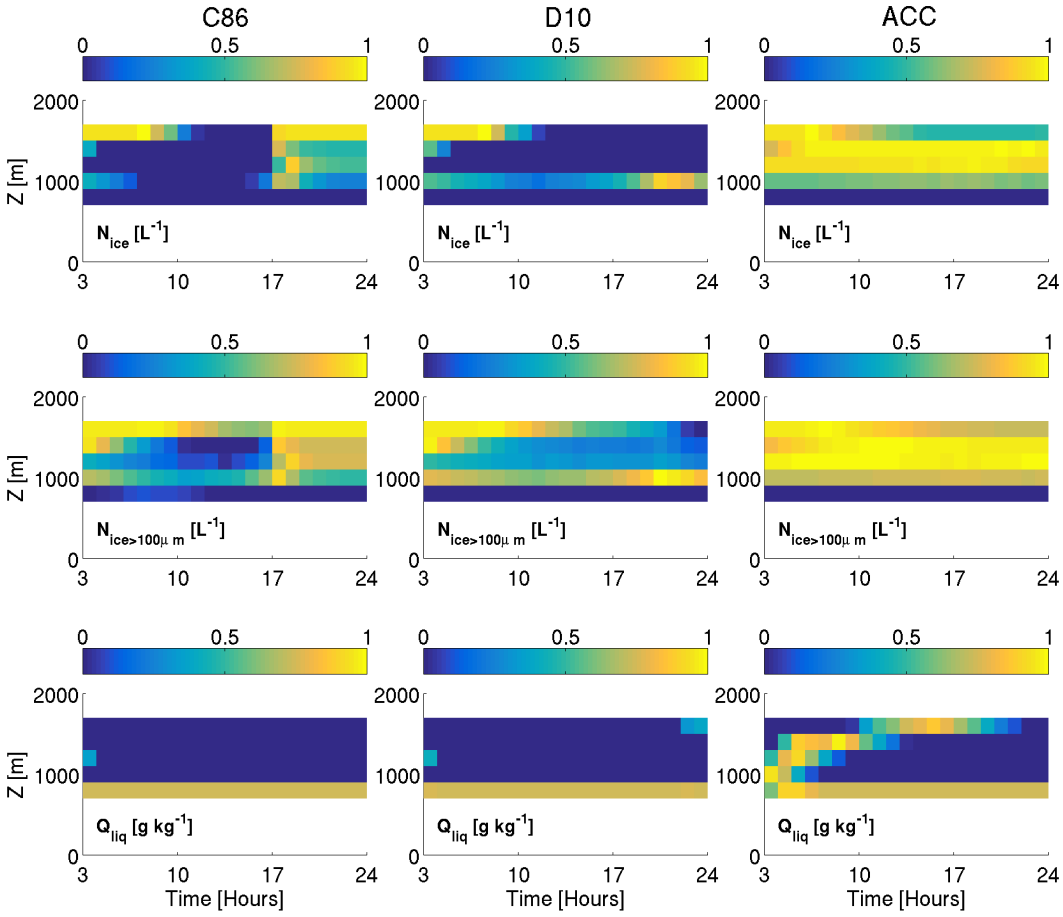

Figure S8. Residual comparison of modelled and observed N_{ice} (**top row**), $N_{ice>100\mu m}$ (**middle row**), and Q_{liq} (**bottom row**) in case 3 (ocean) for each model time step. As with Fig. S6, better agreement with the mean observed value gives a larger fraction (with a maximum of 1). For the MIZ simulations, the chosen time step was 7 h. Note changing colour bars for each subfigure.

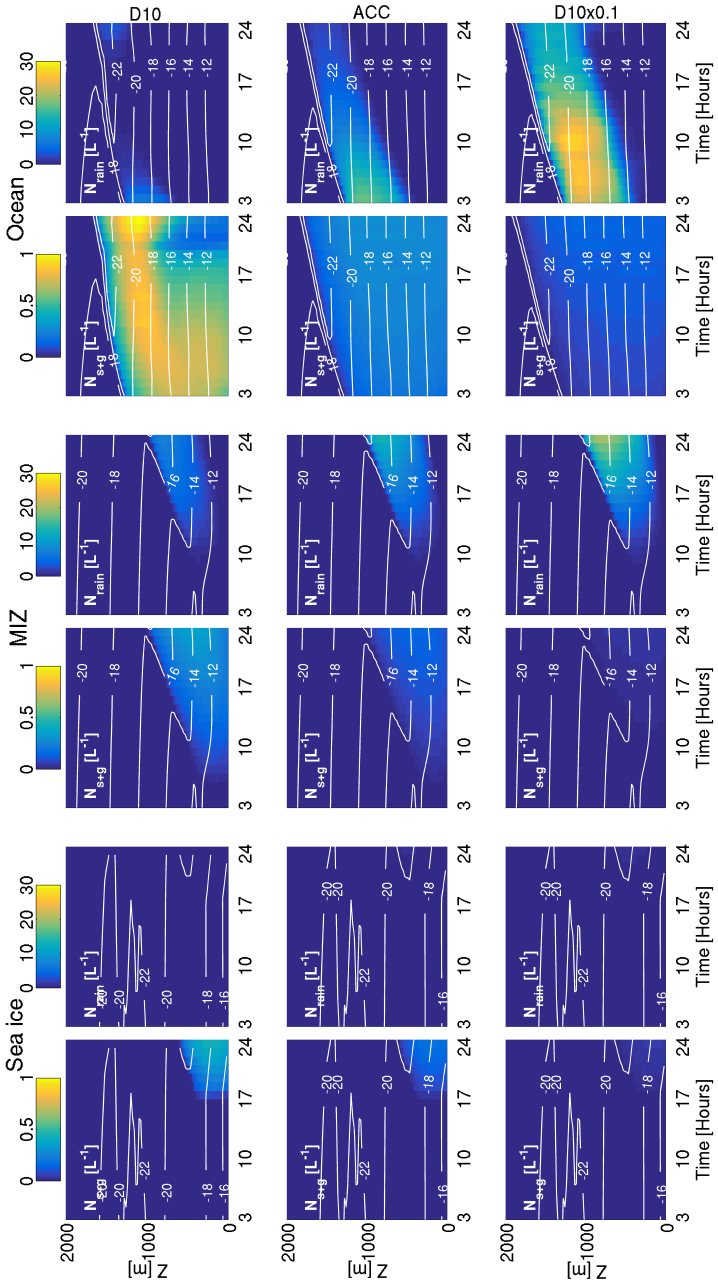

Figure S9. Summed snow and graupel number concentrations (N_{s+g}, **columns 1, 3, and 5**) and rain number concentration (N_{liq}, **columns 2, 4, and 6**) using D10 (**top row**), ACC (**middle row**) and D10×0.1 (**bottom row**). **Column 1-2:** Sea ice (case 1), **Column 3-4:** MIZ (case 2), **Column 5-6:** Ocean (case 3). Run length 24 hours. Solid precipitation increases with simulation time in all cases when using D10, and the rain number concentration behaves similarly in case 2 when applying D10×0.1. Overall, little solid and liquid precipitation is modelled during the ACC simulations, and almost no precipitation is modelled in case 1 with D10×0.1. Note changing colour bar for each column.

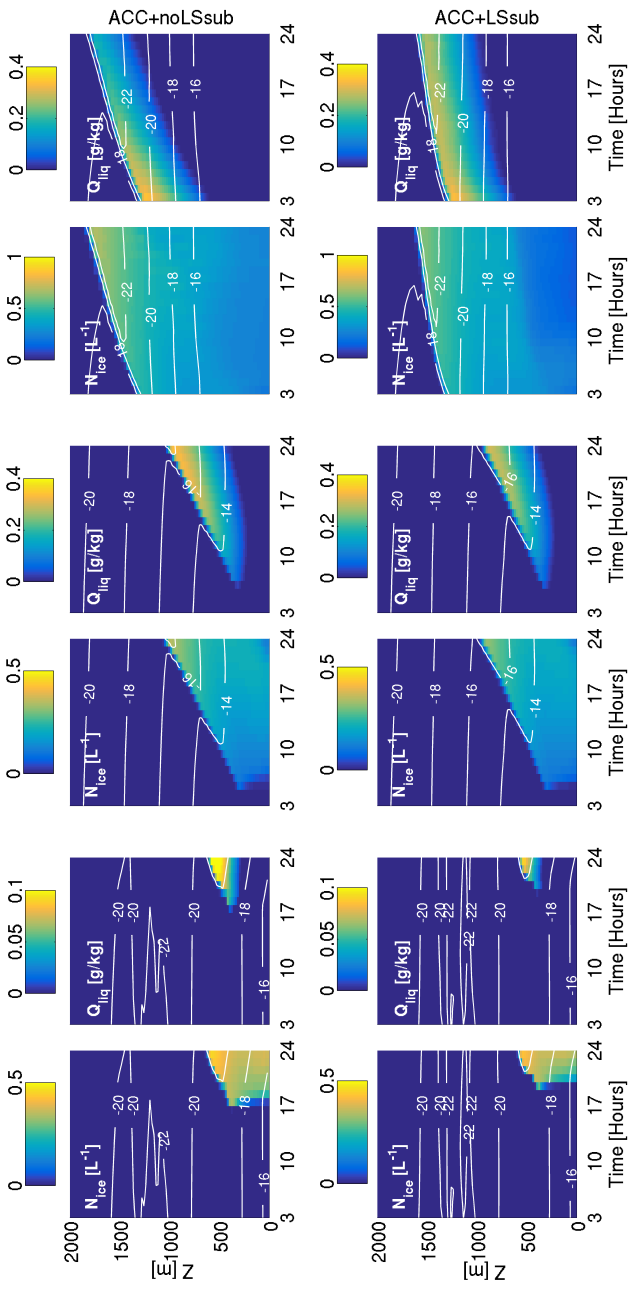

Figure S10. Simulated ice number concentrations (N_{ice}, **columns 1, 3, and 5**) and liquid water mixing ratios (Q_{liq}, **columns 2, 4, and 6**) using ACC without large-scale subsidence (**top row**) and with an imposed subsidence of $2.5\times10^{-6}\,s^{-1}$ (**bottom row**, as in Solomon et al., 2015). All are restricted to water-saturation. **Column 1-2:** Sea ice (case 1), **Column 3-4:** MIZ (case 2), **Column 5-6:** Ocean (case 3). Run length 24 hours. In all cases, cloud top height and Q_{liq} is suppressed when large-scale subsidence is imposed. Temperatures are also warmer; however, case 2 is still too cold with comparison to the observations. Note changing colour bars for each subfigure.

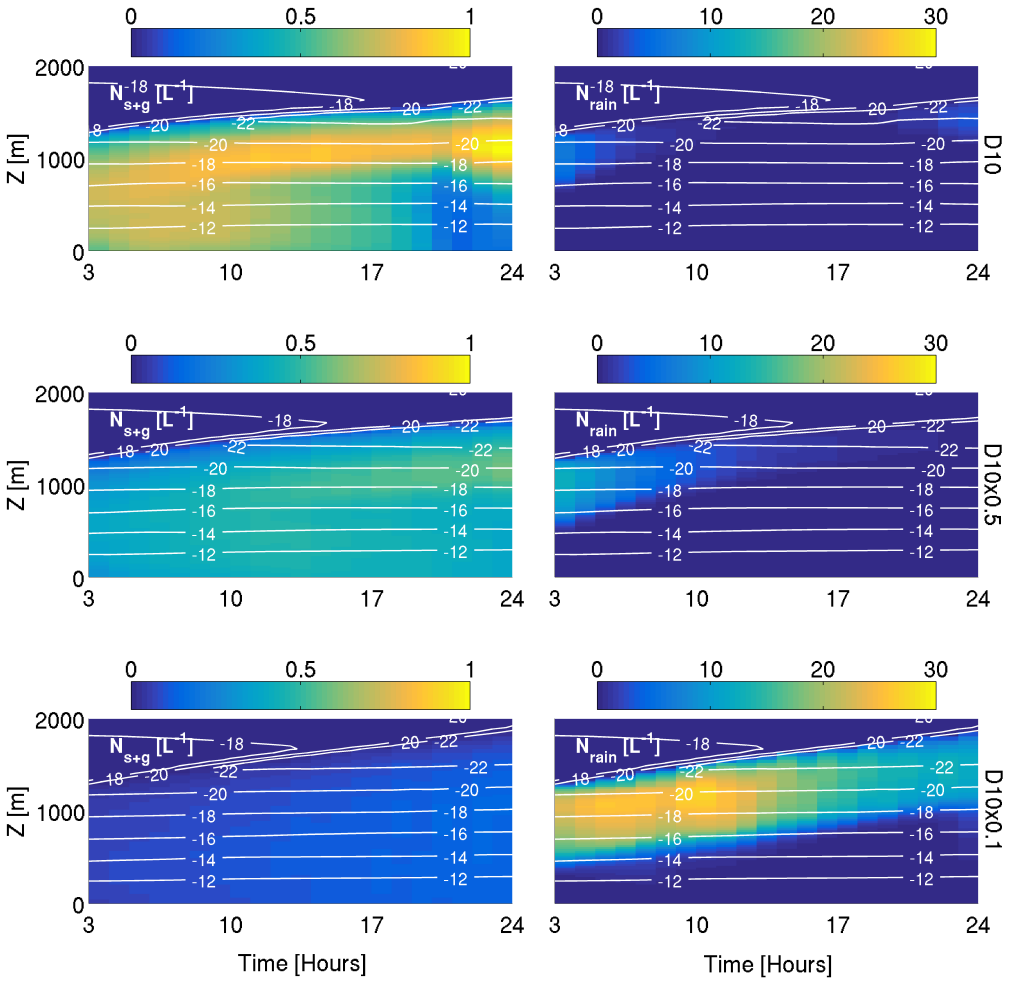

Figure S11. Number concentrations of solid (snow + graupel, N_{s+g}, **left column**) and liquid (rain, N_{rain}, **right column**) precipitation modelled during the D10, D10×0.5, and D10×0.1 simulations over the ocean (case 3). Note changing colour bars for each subfigure.

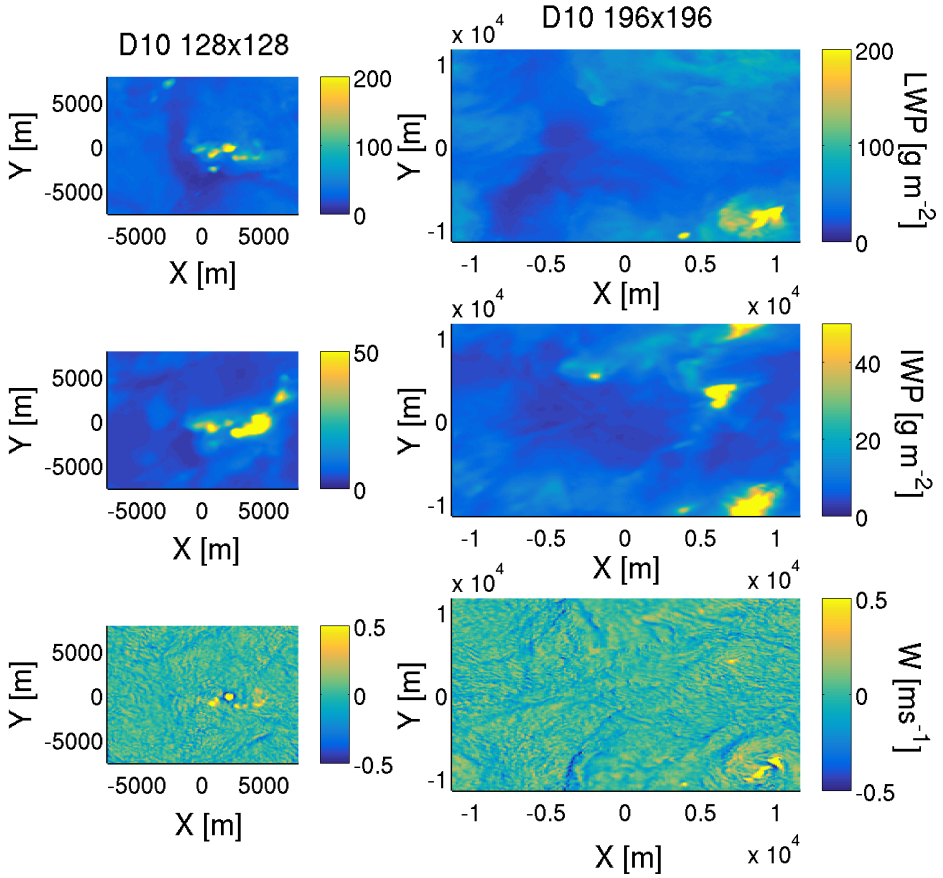

Figure S12. Modelled LWP (**top row**), IWP (**second row**), and W (at approximately 1500 m, **bottom row**) for domain sizes 128 × 128 grid points (**left column**) and 196 × 196 grid points (**right column**) at 21 h into the simulations. Both domains use X/Y resolution of 120 m and use the same vertical domain size and resolution; the only difference is the domain size in X/Y. Convective cells – as shown by the hot-spots in LWP, IWP, and W – form in both cases, suggesting that these phenomena were not a result of the original domain specifications. Note changing colour bars for each subfigure.

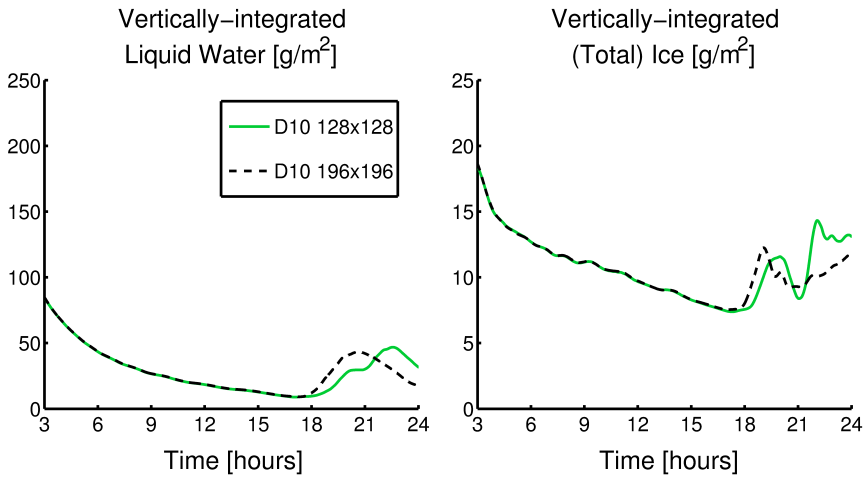

Figure S13. Modelled LWP (**left panel**) and IWP (**right panel**) with time for the original domain size (128 $\times$ 128 grid points, **green**) and the larger domain size (196 $\times$ 196 grid points, **black**). These traces diverge at approximately 18 h; however, similar trends are seen. The feedbacks associated with convection and precipitation formation affect the evolution of the cloud properties, leading to different LWP and IWPs. These differences are due to the influence of the domain size on, for example, cloud radiative cooling and entrainment, leading to the formation of different convective cells, of different sizes, to the original domain.

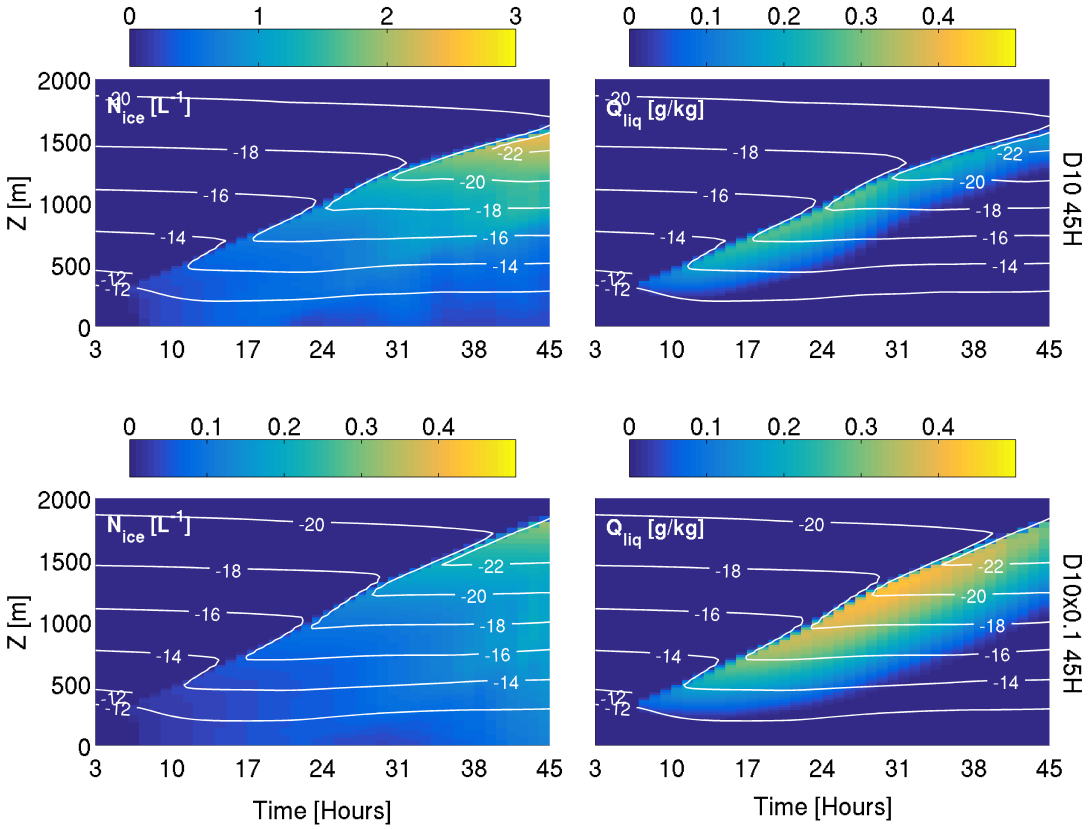

Figure S14. Modelled N_{ice} (**left column**) and Q_{liq} (**right column**) when using D10 (**top row**) and D10×0.1 (**bottom row**) to simulate case 2 over an extended run time of 45 h. Note changing colour bars for each subfigure.

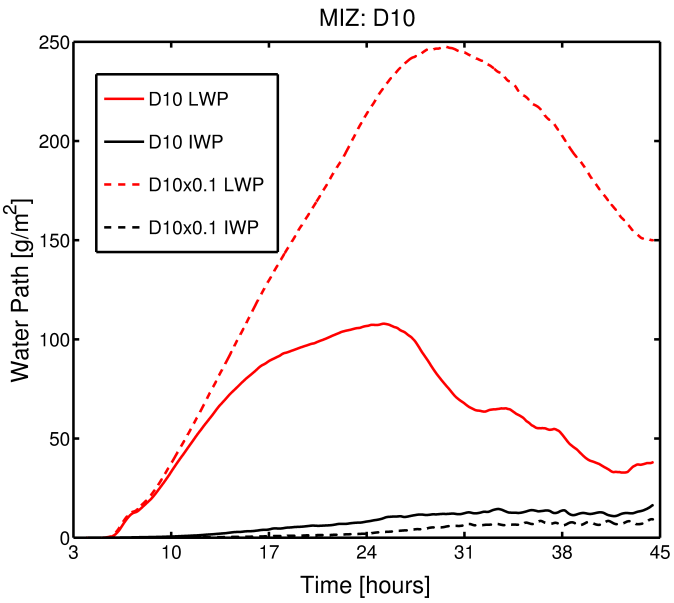

Figure S15. Modelled LWP (red) and IWP (black) when using D10 (**solid**) and D10×0.1 (**dashed**) to simulate case 2 over an extended run time of 45 h.

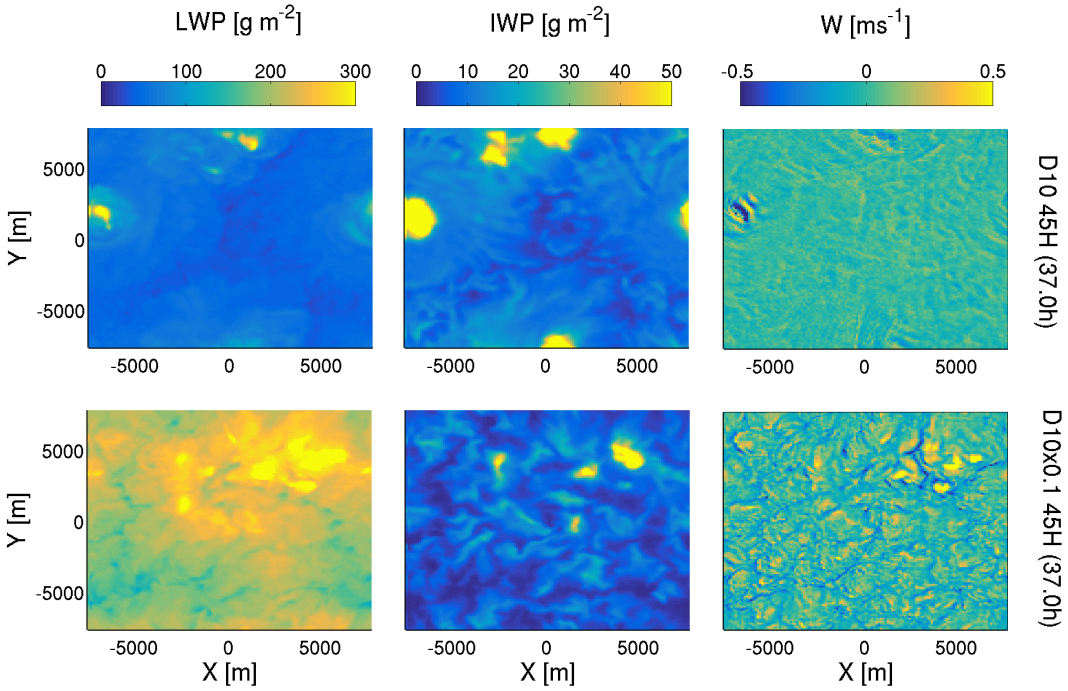

Figure S16. Modelled LWP (**first column**), IWP (**second column**), and vertical velocity (**third column**) at approximately 1500 m using D10 (**top row**) and D10×0.1 (**bottom row**) to simulate case 2. Planar X-Y slices are shown at 37 h. Note changing colour bars for each subfigure.

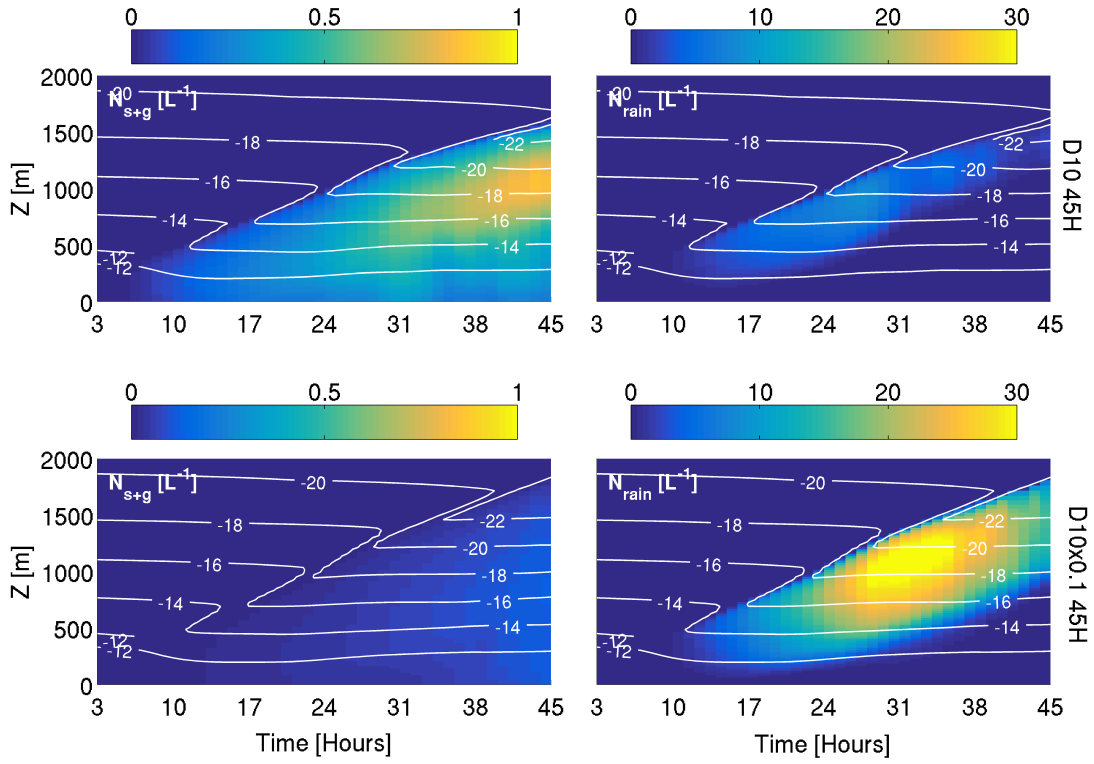

Figure S17. Modelled solid (N_{s+g}, **left column**) and liquid (N_{rain}, **right column**) precipitation when using D10 (**top row**) and D10×0.1 (**bottom row**) to simulate case 2 over an extended run time of 45 h. Note changing colour bars for each subfigure.